

A search for $W^{\pm}H \rightarrow \mu\nu b\bar{b}$ production at the
Tevatron

A search for $W^{\pm}H \rightarrow \mu\nu b\bar{b}$ production at the Tevatron

EEN WETENSCHAPPELIJKE PROEVE OP HET GEBIED VAN
NATUURWETENSCHAPPEN, WISKUNDE EN INFORMATICA

PROEFSCHRIFT

TER VERKRIJGING VAN DE GRAAD VAN DOCTOR
AAN DE RADBOD UNIVERSITEIT NIJMEGEN
OP GEZAG VAN DE RECTOR MAGNIFICUS PROF. MR. S.C.J.J. KORTMANN,
VOLGENS BESLUIT VAN HET COLLEGE VAN DECANEN
IN HET OPENBAAR TE VERDEDIGEN OP WOENSDAG 6 FEBRUARI 2008
OM 15.30 UUR PRECIES

DOOR

Carmen Miruna Anăstăsoaie

GEBOREN OP 27 MEI 1978
TE PLOIEȘTI (ROEMENIË)

Promotor: Prof. dr. S.J. de Jong

Co-promotor: Dr. F. Filthaut

Manuscriptcommissie: Prof. dr. S.C.M. Bentvelsen Universiteit van Amsterdam
Prof. dr. D. Froidevaux
Prof. dr. H.J. Kappen
Prof. dr. J. Qian University of Michigan, Ann Arbor
Prof. dr. F. Rizatdinova Oklahoma State University

ISBN: 978-90-9022640-8

The work described in this thesis is part of the research programme of the ‘Nationaal Instituut voor Kernfysica en Hoge-Energie Fysica’ (Nikhef) in Amsterdam, the Netherlands. The author was financially supported by the ‘Stichting voor Fundamenteel Onderzoek der Materie’ (FOM).

Contents

1	Introduction	1
2	Higgs Production and Decay in Hadron Collisions	3
2.1	Standard Model general aspects	3
2.2	Higgs Mechanism	7
2.3	Higgs production	9
2.4	Higgs mass	10
2.5	Higgs searches	14
2.5.1	Direct Searches	14
2.5.2	Indirect Experimental Measurements	15
2.6	Higgs search at the Tevatron	15
2.6.1	Higgs search strategy and backgrounds	16
3	Tevatron and the DØ detector	19
3.1	The Tevatron Accelerator	19
3.1.1	Proton Source	20
3.1.2	Antiproton Source: Target, Debuncher, Accumulator and Recycler . .	23
3.2	The DØ Detector	25
3.2.1	Coordinate System	25
3.2.2	The Luminosity Monitor System	27
3.2.3	The Central Tracking Detector	30
3.2.4	The Calorimeter System	34
3.2.5	The Muon System	37
4	Data Samples, Event Selection and Monte Carlo Simulation	39
4.1	Data sample	39
4.2	Event simulation	39
4.2.1	Monte Carlo Samples	40
4.2.2	Shifting, smearing and removing simulated jets - JSSR	41
4.3	The Trigger	42
4.3.1	Muon triggers	45
4.4	Object identification	47
4.4.1	Muons	47
4.4.2	Jets	50
4.4.3	Electrons, Positrons and Photons	55

4.4.4	Missing E_T	56
4.4.5	Tracks	56
4.4.6	Track jets	57
4.4.7	Vertices	57
5	Tagging of b-Jets	59
5.1	b Jet tagging algorithms	60
5.1.1	SVT	60
5.1.2	CSIP	60
5.1.3	JLIP	61
5.1.4	Soft lepton tag	61
5.1.5	Taggability	62
5.2	The Neural Network	62
5.2.1	Neural net architecture	62
5.2.2	Input variables	63
5.2.3	Neural net training	64
5.2.4	Input Selection Cuts	64
5.2.5	NN Performance on Monte Carlo	64
5.3	Data efficiency and studies	64
5.3.1	Operating Points	67
5.3.2	Data and MC Samples	67
5.3.3	Jet Samples	68
5.4	b-Efficiency Measurement	68
5.4.1	System8 Method	68
5.4.2	Determination of the Correlation Coefficients	71
5.4.3	System8 Efficiency and Systematic Errors	74
5.4.4	b-tagging and Scale Factor Parameterisation	77
5.4.5	Data/MC Scale Factor	78
5.4.6	Tag Rate Functions	78
5.4.7	Systematic Uncertainties	78
5.5	Fake Rate	86
5.5.1	Negative Tags	86
5.5.2	Negative Tag Rate	86
5.5.3	Parameterisation Systematic	88
5.5.4	MC Negative Tag Scale Factors	89
5.5.5	Fake Rate	93
5.5.6	Total Systematics	96
5.5.7	Total Errors	97
5.6	Performance on Data	97
6	Search for WH production in the Muon plus b-Jets Channel	101
6.1	Luminosity and Triggers	102
6.1.1	Triggers	102
6.1.2	Luminosity	102

6.2	Event selection	103
6.2.1	Data preselection	104
6.2.2	Muon isolation	104
6.2.3	Missing E_T requirement and W boson transverse mass	106
6.2.4	Jet properties	107
6.2.5	Second lepton veto	107
6.2.6	W selection cut	108
6.3	Simulated Event Samples	108
6.4	Multijet (QCD) background	110
6.5	b-Tagging	111
6.6	Systematic Uncertainties	114
6.7	Upper Limits on $W^{\pm}H$ Production	120
6.7.1	Limit calculations	121
6.7.2	Results for Higgs production	122
7	Conclusions	127
	References	129
	Summary	135
	Samenvatting	139
	Acknowledgements	143
	Curriculum Vitae	145

Chapter 1

Introduction

The quantum field theory developed to describe particles and their interactions, the Standard Model, is used to explain and calculate a vast variety of particle interactions and quantum phenomena. It describes the matter particles (quarks and leptons) and the forces acting on them as fields. The force fields are also associated with particles, the photon for the electromagnetic force, the W^\pm and Z bosons for the weak force and the gluons for the strong nuclear force. High-precision experiments are and were built to verify the subtle effects predicted by the Standard Model.

The Higgs boson is the only Standard Model particle not yet discovered. It plays a unique role in the Standard Model, and a key role in explaining the origin of mass of other elementary particles and the mass hierarchy between e.g. the massless photon and the very heavy W^\pm and Z bosons. Mass is a fundamental property of matter. If Nature does not provide a Higgs boson, other particles and forces are needed to save the predictions of the Standard Model components and to explain the origin of mass. Since 1964, when Peter Higgs developed the Higgs Field theory and proposed that the Universe is pervaded by this field [1], we have been looking for evidence of its existence with the help of high energy experiments.

The Higgs mechanism predicts that the Higgs field interacts more strongly with particles that have large masses. Through the interaction with the field, these particles become more “inert”. This inertia corresponds to the mass that we observe in every day life. High energy physicists carry out direct tests of the idea that mass arises from the interaction with one or more Higgs fields by looking for evidence of the existence of the Higgs boson. To carry out these tests we need appropriate particle colliders with sufficient energy to produce Higgs bosons, sufficient intensity to make enough of them and very good detectors to analyse what is produced.

While the Standard Model predicts that a Higgs boson should exist, it does not predict the exact mass of the Higgs boson. The most stringent direct lower limit on the Higgs boson mass is from a combination of searches at the four LEP experiments, yielding $m_H > 114.4$ GeV [2]. On the other hand, precision electroweak fits constrain the mass to $m_H < 144$ GeV [3].

At the moment, the DØ and CDF experiments at Fermilab are the only experiments in the world capable of observing enough Higgs bosons to allow discovery. DØ and CDF are detectors designed to study the collisions of protons and antiprotons at the Tevatron collider.

Like many other particles, the Higgs particle is not stable. Since the Higgs particle interacts stronger with particles with larger masses, it most often decays to heavy particles. If the Higgs mass is below about 140 GeV, it mostly decays into a bottom quark pair (“ $b\bar{b}$ ”). The identification of bottom quarks in collisions is therefore very important. At higher masses, the Higgs is heavy enough to decay into W^+W^- or ZZ pairs as well.

A very promising signature for light Higgs searches is the associated production with a heavy W^\pm or Z boson. The signature of leptonic W^\pm or Z boson decays can be used to select events. The presence of Higgs bosons can be determined by looking for their decay into $b\bar{b}$ pairs.

This thesis describes a search for the Higgs boson in $D\bar{O}$ data taken between April 2002 and February 2006. The search focuses on associated $W^\pm H$ production, where the W^\pm decays to a muon and a neutrino and the Higgs boson into a $b\bar{b}$ pair. Chapter 2 introduces the Standard Model and the Higgs mechanism. Chapter 3 describes the Tevatron particle accelerator and the $D\bar{O}$ detector. The methods and algorithms used to acquire and reconstruct the data used in the analysis are presented in Chapter 4. Since the Higgs boson most often decays into a $b\bar{b}$ pair, the identification of jets originating from bottom quarks is very important. Chapter 5 describes in detail a Neural Net-based tool used for the identification of b-jets. The tool uses information from previously developed tagging algorithms used in $D\bar{O}$ and improves the efficiency for finding b-jets. The $W^\pm H$ search is described in Chapter 6. A discussion of the results is given in Chapter 7.

Chapter 2

Higgs Production and Decay in Hadron Collisions

The Standard Model is the basic theory of elementary particles and interactions. The SM was tested up to high energy ranges at the LEP e^+e^- collider and at the Tevatron. It describes the fundamental particles and their interactions up to these energy scales. Three of the four fundamental forces — the strong force and the unified electroweak forces — are incorporated in the theory. The gravitational force is about 40 orders of magnitude weaker than the other three forces, so that the impact of the Standard Model on present experiments is not inhibited by the lack of a consistent quantum gravitation field theory. Nevertheless the Standard Model will ultimately break down at energy scales where gravity can no longer be neglected.

To explain particle masses in the SM, the Higgs mechanism was introduced. However, the corresponding Higgs particle has not yet been observed. Searches for the Higgs boson have high priority in high energy physics world.

This chapter contains a brief introduction to the Standard Model of particle physics in Section 2.1 and a more detailed description of the Higgs mechanism in Section 2.2. Higgs production is described in Section 2.3. The constraints on the mass of the SM Higgs are briefly discussed in Section 2.4. Search strategies at previous experiments are discussed in Section 2.5. Section 2.6 describes Higgs searches at the Tevatron.

2.1 Standard Model general aspects

The Standard Model (SM) is the theory of the electromagnetic (EM), weak and strong forces. The dynamics are described by gauge theories, in which symmetry transformations vary in time and space.

The Standard Model is based on the $SU(3)_C \otimes SU(2)_L \otimes U(1)_Y$ gauge symmetry group, where the $SU(3)_C$ group corresponds to the strong interaction and $SU(2)_L \otimes U(1)_Y$ corresponds to the electroweak interactions.

Matter particles are described by the theory as spin- $\frac{1}{2}$ *fermions*. The force carriers are spin-1 *gauge bosons*. For every fermion, there is also an anti-fermion, differing from its counterpart by opposite signs of the quantum numbers. The fermions are summarised in

	Generation			Quantum number			
	1 st	2 nd	3 rd	Q	T	T_3	Y
leptons	$\begin{pmatrix} \nu_e \\ e \end{pmatrix}_L$	$\begin{pmatrix} \nu_\mu \\ \mu \end{pmatrix}_L$	$\begin{pmatrix} \nu_\tau \\ \tau \end{pmatrix}_L$	0	1/2	+1/2	-1
	e_R	μ_R	τ_R	-1	1/2	-1/2	-1
				-1	0	0	-2
quarks	$\begin{pmatrix} u \\ d \end{pmatrix}_L$	$\begin{pmatrix} c \\ s \end{pmatrix}_L$	$\begin{pmatrix} t \\ b \end{pmatrix}_L$	+2/3	1/2	+1/2	+1/3
	u_R	c_R	t_R	-1/3	1/2	-1/2	+1/3
	d_R	s_R	b_R	+2/3	0	0	+4/3
				-1/3	0	0	-2/3

Table 2.1: The fermions of the Standard Model arranged in $SU(2)_L \otimes U(1)_Y$ multiplets and their quantum numbers; electrical charge Q , weak isospin T and hypercharge Y . The “colour” quantum number of the strong force is not included.

Symmetry	Gauge boson	Field	Interaction	Q	Mass [GeV]	Width [GeV]
	Photon γ	A_μ	electromag.	0	0	—
$SU(2)_L \otimes U(1)_Y$	Z-Boson	Z_μ	electroweak	0	91.2	2.5
	W^\pm -Boson	W_μ^\pm	weak	± 1	80.4	2.1
$SU(3)_C$	Gluon g	g_μ^a	strong	0	0	—

Table 2.2: The gauge bosons of the Standard Model and their electrical charge Q , mass and width [4]. The index a of the gluon field refers to the eight colour charges of the gluons.

Table 2.1.

By forcing the Lagrangian of a free particle to be invariant under local group transformations, it is necessary to introduce “gauge fields” to maintain the invariance of the Lagrangian. These gauge fields correspond to the force mediating spin-1 bosons. The gauge fields with their associated quantum numbers and $SU(2)_L$ and $SU(3)_C$ representations are given in Table 2.2.

All the matter particles are described by complex Dirac spinors $\Psi(x)$ and $\bar{\Psi} = \Psi^\dagger \gamma^0$, depending on the space-time coordinate x . The principle of local gauge invariance is best demonstrated using a free Dirac field, whose Lagrangian is given by

$$\mathcal{L}_{Dirac} = \bar{\Psi}(i\gamma^\mu \partial_\mu - m)\Psi, \quad (2.1)$$

where γ^μ are 4×4 gamma matrices (see e.g. [5]). A $U(x) \in U(1)$ local gauge transformation of the Dirac fields is defined as

$$\begin{aligned} \Psi &\rightarrow \Psi' = U(x)\Psi(x) = e^{i\theta(x)}\Psi \\ \bar{\Psi} &\rightarrow \bar{\Psi}' = e^{-i\theta(x)}\bar{\Psi}, \end{aligned} \quad (2.2)$$

where $\theta(x)$ is a function of the space-time co-ordinates. Substituting Equation 2.2 into Equation 2.1 demonstrates that the Lagrangian is clearly not invariant in its current form:

$$\mathcal{L}_{Dirac} \rightarrow \mathcal{L}'_{Dirac} = \mathcal{L}_{Dirac} - \bar{\Psi}\gamma^\mu \partial_\mu \theta(x)\Psi. \quad (2.3)$$

To maintain the invariance of the Lagrangian a real gauge field, A_μ , is introduced whose transformation exactly cancels out the extra term in Equation 2.3:

$$A_\mu \rightarrow A'_\mu = A_\mu - \frac{1}{e}\partial_\mu\theta(x). \quad (2.4)$$

An invariant kinetic term for the gauge field is also added to the Lagrangian:

$$\mathcal{L}^{K.E.} = -\frac{1}{4}F_{\mu\nu}F^{\mu\nu}, \quad (2.5)$$

where $F_{\mu\nu} = \partial_\mu A_\nu - \partial_\nu A_\mu$. Replacing the derivative with the covariant derivative, D_μ , defined as:

$$D_\mu \equiv \partial_\mu + ieA_\mu, \quad (2.6)$$

ensures that the extra term is cancelled and the Lagrangian is invariant under the U(1) local gauge transformation. The resulting Lagrangian now describes the interactions of electrons and photons - quantum electrodynamics (QED). By requiring the invariance of a free Dirac field under a U(1) local gauge transformation, the free system has been changed into an interacting one. The final QED Lagrangian is given by:

$$\begin{aligned} \mathcal{L}_{QED} &= \bar{\Psi}(i\gamma^\mu D_\mu - m)\Psi - \frac{1}{4}F_{\mu\nu}F^{\mu\nu} \\ &= \bar{\Psi}(i\gamma^\mu \partial_\mu - m)\Psi - \underbrace{e\bar{\Psi}\gamma^\mu\Psi A_\mu}_{\text{Interaction Term}} - \frac{1}{4}F_{\mu\nu}F^{\mu\nu}. \end{aligned} \quad (2.7)$$

A mass term for A_μ is not included, as a term such as $m^2 A_\mu A^\mu$ is not invariant. In the SM the gauge bosons of the weak and strong forces are introduced in an analogous way, but using different group structures to represent the different symmetries. For instance, the strong force is introduced into the SM Lagrangian by requiring invariance under SU(3)_C local gauge transformations. The 8 generators¹ of the SU(3) group correspond to the 8 gluons.

Quantum electrodynamics (QED) was united with the weak force within the Glashow-Salam-Weinberg (GSW) model [6, 7], which is represented by a SU(2)_L⊗U(1)_Y gauge group. The index *L* denotes the weak isospin and *Y* denotes the weak hypercharge. The Lie group U(1)_{EM} describing the quantum electrodynamics is a subgroup of the GSW group U(1)_{EM} ⊂ SU(2)_L⊗U(1)_Y. The associated spin-1 gauge boson is the photon A_μ . The generator and coupling strength is the electric charge *Q*. The photon is electrically neutral and has no self-interaction, because U(1) is Abelian. Though U(1)_{EM} is mathematically identical to U(1)_Y it has a different physical meaning. In the GSW-model the generator of the U(1)_{EM} group, the electric charge *Q* is replaced by the U(1)_Y weak hypercharge *Y*. The electric charge is then defined by the Gell-Mann-Nishijima equation, involving the third component of the SU(2)_L weak isospin T_3 and the hypercharge *Y*:

$$Q = T_3 + \frac{Y}{2}. \quad (2.8)$$

¹SU(*n*) groups have $n^2 - 1$ generators.

The three generators of the $SU(2)_L$ group correspond to the W_μ^1 , W_μ^2 and W_μ^3 gauge bosons with a coupling g , and the single generator of the $U(1)_Y$ group to the B_μ boson with a coupling g' . The weak mixing angle θ_w is defined by the relation of the couplings $g' = g \tan \theta_w$. The physical bosons (photon, W^\pm and Z) exist as linear superpositions of the gauge fields, and are given by:

$$W^\pm : W^\pm = \frac{1}{\sqrt{2}}(W_\mu^1 \mp W_\mu^2), \quad (2.9)$$

$$Z : Z^0 = -B_\mu \sin \theta_w + W_\mu^3 \cos \theta_w, \quad (2.10)$$

$$\gamma : A_\mu = B_\mu \cos \theta_w + W_\mu^3 \sin \theta_w. \quad (2.11)$$

While the photon has a pure vectorial coupling to the charged fermions, the charged weak current W^\pm couplings have a vector minus axial-vector ($V - A$) structure. The interactions mediated by the W^\pm involve only left-handed fermions (and right-handed anti-fermions). The left-handed and right-handed parts of a generic fermion field, $\Psi_L = P_L \cdot \Psi$ and $\Psi_R = P_R \cdot \Psi$ are defined through the two chirality operators

$$P_L = \frac{1 - \gamma^5}{2} \quad \text{and} \quad P_R = \frac{1 + \gamma^5}{2}. \quad (2.12)$$

The left-chiral fields Ψ_L are given by

$$\Psi_{Li}^{\text{lepton}} = P_L \begin{pmatrix} \nu_i \\ l_i \end{pmatrix} \quad \Psi_{Li}^{\text{quark}} = P_L \begin{pmatrix} u_i \\ d_i \end{pmatrix}, \quad (2.13)$$

where $i = 1, 2, 3$ are the three generations of fermions. For massive fermions there is always a frame of reference, in which the fermion field has a left-handed part. The chirality corresponds to definite helicity states only in the case of massless fermions.

The left-chiral eigenstates of the down-type quarks d' arise from the mass eigenstates d_i by applying the Cabibbo-Kobayashi-Maskawa mixing matrix $V_{CKM} : d'_i = \sum_j V_{ij} d_j$. The off-diagonal elements of the CKM matrix give rise to family-changing charged weak interactions.

The field strength tensors of the electro-weak GSW theory are:

$$\vec{W}_{\mu\nu} = \partial_\mu \vec{W}_\nu - \partial_\nu \vec{W}_\mu - g \vec{W}_\mu \times \vec{W}_\nu \quad (2.14)$$

and

$$B_{\mu\nu} = \partial_\mu B_\nu - \partial_\nu B_\mu. \quad (2.15)$$

Mathematically, all the particles of the SM, fermions and bosons and their interactions are described by a Lagrangian density with four different contributions:

$$\mathcal{L}_{\text{SM}} = \mathcal{L}_{\text{Fermion}} + \mathcal{L}_{\text{Yang-Mills}} + \mathcal{L}_{\text{Yukawa}} + \mathcal{L}_{\text{Higgs}} \quad (2.16)$$

with

$$\mathcal{L}_{\text{Fermion}} = \bar{\Psi}_L i \gamma^\mu D_\mu \Psi_L + \bar{\Psi}_R i \gamma^\mu D_\mu \Psi_R, \quad (2.17)$$

$$\mathcal{L}_{\text{Yang-Mills}} = -\frac{1}{4} G_a^{\mu\nu} G_{\mu\nu}^a - \frac{1}{4} W_i^{\mu\nu} W_{\mu\nu}^i - \frac{1}{4} B^{\mu\nu} B_{\mu\nu}, \quad (2.18)$$

$$\mathcal{L}_{\text{Yukawa}} = -g_f \bar{L} \Phi R - g_f \bar{R} \Phi^\dagger L, \quad \text{and} \quad (2.19)$$

$$\mathcal{L}_{\text{Higgs}} = (D^\mu \Phi)^\dagger (D_\mu \Phi) - V(\Phi^\dagger \Phi)^2. \quad (2.20)$$

$\mathcal{L}_{\text{Fermion}}$ are the kinematic terms of the fermion fields Ψ and their interactions with the gauge boson fields using the covariant derivative D_μ for the given representation:

$$\partial_\mu \quad \rightarrow \quad D_\mu = \partial_\mu - ig_3 G_\mu^a \lambda_a + ig_2 T_i \cdot W_\mu^i + i\frac{g_1}{2} Y \cdot B_\mu. \quad (2.21)$$

The $\mathcal{L}_{\text{Yang-Mills}}$ terms contain the kinetic-energy and self-interaction terms of the gauge bosons associated with the local symmetry groups. The terms $\mathcal{L}_{\text{Yukawa}}$ provide mass terms for fermions via Yukawa couplings of the Higgs to the fermions, where the L denotes left-handed doublets and the R right-handed singlets.

Gauge invariance implies that the theory is renormalisable for massless bosons [8] as well as for massive bosons [9].

The gauge bosons cannot be massive because a mass term of the form $m_A^2 A^\mu A_\mu$ is not invariant under gauge transformations. Similarly, the fermion mass term also violates gauge invariance. However, the observed masses of the fermions and the massive Z and W^\pm bosons ought to be included in the theoretical framework. So an independent mechanism responsible for giving mass to the bosons must exist. In the Standard Model, this is the Higgs mechanism, named after P.W. Higgs, who developed this mechanism of mass generation in non-Abelian gauge theories, based on earlier work of Nambu, Goldstone, Englert, Brout and Anderson. The last term in Equation 2.20 is the Higgs Lagrangian and will be explained in the next section.

2.2 Higgs Mechanism

In 1967, Steven Weinberg and Abdus Salam proposed the hypothesis of ‘‘spontaneous symmetry breaking’’. In 1971, Gerard ’t Hooft proved that this theory was renormalisable [8, 9]. Twelve years later, the W^\pm and Z particles were discovered at CERN and the model was placed on a firm footing.

The electroweak gauge bosons W^\pm and Z have non-zero masses, but mass terms of type $m^2 W_\mu W^\mu$ are not allowed in the Lagrangian, because they would destroy the local gauge invariance. The Higgs mechanism [1] provides a solution. As shown in Equations 2.16 and 2.20, an additional term $\mathcal{L}_{\text{Higgs}}$, which is invariant under the gauge transformations, is added to the Standard Model Lagrangian:

$$\mathcal{L}_{\text{Higgs}} = (D^\mu \Phi)^\dagger (D_\mu \Phi) - V(\Phi^\dagger \Phi),$$

where Φ is a two-component complex scalar field

$$\Phi = \begin{pmatrix} \phi^+ \\ \phi^0 \end{pmatrix} = \frac{1}{\sqrt{2}} \begin{pmatrix} \phi_1 + i\phi_2 \\ \phi_3 + i\phi_4 \end{pmatrix}. \quad (2.22)$$

The first term is the kinetic term and the second term $V(\Phi)$ is the potential term. Its most general renormalisable form is given by

$$V(\Phi) = \mu^2 \Phi^\dagger \Phi + \lambda (\Phi^\dagger \Phi)^2. \quad (2.23)$$

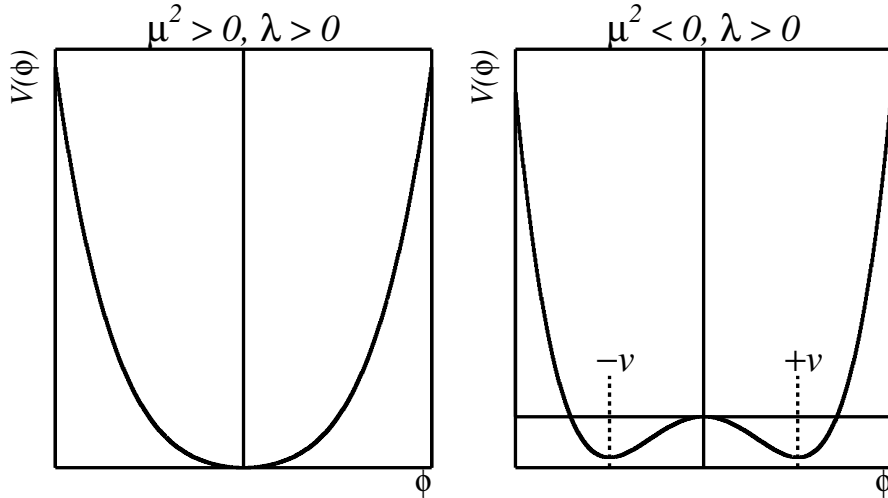


Figure 2.1: Representation of a potential of type $V(\phi)$ where $\phi = \sqrt{\Phi^\dagger \Phi}$ and v indicates the vacuum expectation value.

The parameter λ is a “running” coupling constant, as it depends on the energy scale. It has to be positive, since the potential may not be arbitrarily negative for large Φ . If the parameter μ^2 is negative, a non-trivial minimum of the Higgs potential exists, as shown in Fig. 2.1. The set of minima form a hypersurface which is parameterised by:

$$\phi_{1,min}^2 + \phi_{2,min}^2 + \phi_{3,min}^2 + \phi_{4,min}^2 = v^2 \quad (2.24)$$

with

$$v = \sqrt{\frac{-\mu^2}{\lambda}}, \quad (2.25)$$

where v is the vacuum expectation value. The perturbative expansion of the Lagrangian has to be performed around the classical minimum, and by choosing a specific minimum we are breaking the symmetry of the theory. This is “spontaneous symmetry breaking”; by choosing a particular minimum the symmetry of the theory has been broken.

The $SU(2)_L \otimes U(1)_Y$ symmetry of the Higgs potential is spontaneously broken. If the vacuum expectation value for the charged Higgs field $\phi^+ = \frac{1}{\sqrt{2}}(\phi_1 + i\phi_2)$ is set to 0 then the resulting state is invariant under $U(1)_{EM}$ and the photon field A_μ remains massless. By choosing one ground state, e.g. $\phi_1 = \phi_2 = \phi_4 = 0$ and $\phi_3 = v$, the vacuum expectation value for the neutral Higgs field becomes $\langle \phi^0 \rangle = \frac{v}{\sqrt{2}}$. Even then the Lagrangian as such is symmetric, only the ground state is not. Expanding the scalar field $\Phi(x)$ around the ground state gives:

$$\Phi(x) = \frac{1}{\sqrt{2}} \begin{pmatrix} 0 \\ v + h(x) \end{pmatrix}, \quad (2.26)$$

where the only remaining degree of freedom, $h(x)$, corresponds to the physical Higgs boson H . The other three degrees of freedom of the $SU(2)$ doublet field $\Phi(x)$ reappear as mass

terms, leading to longitudinal polarisation degrees of freedom of the three heavy electroweak gauge bosons. Using the representation of the Higgs field as given by Equation (2.26), the boson mass terms can be identified in the Higgs Lagrangian $\mathcal{L}_{\text{Higgs}}$. The $\text{SU}(2)_L \otimes \text{U}(1)_Y$ eigenstates mix to the mass eigenstates W^\pm , Z and A_μ as discussed previously:

$$m_{W^\pm} = \frac{v}{2} g_2 \quad (2.27)$$

and

$$m_Z = \frac{v}{2} \sqrt{g_1^2 + g_2^2}. \quad (2.28)$$

A priori v , and therefore the masses of the bosons, are not known. However, the boson masses as well as the electroweak mixing angle θ_w can be measured and allow for a precise test of the Standard Model, as these values are related by

$$\cos \theta_w = \frac{m_W}{m_Z}. \quad (2.29)$$

From measurements of m_{W^\pm} and m_Z , v is precisely known, so λ is the only parameter for which no experimental measurement is available. The mass of the Higgs boson itself is not predicted by the theory and not measured yet. The Standard Model fermions obtain mass via Yukawa couplings to the Higgs doublet field Φ . This is discussed in detail in Ref. [10]. For one generation, the fermion mass terms in the SM Lagrangian are:

$$\mathcal{L}_{\text{Yukawa}} = -\frac{v+h}{\sqrt{2}} (g_\nu \bar{\nu}\nu + g_l \bar{l}l + g_u \bar{u}u + g_d \bar{d}d), \quad (2.30)$$

where the mass of the fermion f is given by $m_f = \frac{v}{\sqrt{2}} g_f$. This means that the strength of the coupling of particles to the Higgs field is proportional to the particle mass.

2.3 Higgs production

Higgs boson production cross sections in the SM at Tevatron energies are of the order of 0.1–1 pb depending on the production mechanism and the Higgs boson mass. The Higgs boson can be produced through several mechanisms at the Tevatron presented in Fig. 2.2. One of the most sensitive Higgs boson production mechanism at the Tevatron is the Higgs-strahlung process of Fig. 2.2(b),

$$q\bar{q} \rightarrow HV$$

where V can be a W^\pm or a Z . While the gluon fusion cross section is higher, that process is almost impossible to distinguish from the large background, especially in the low mass region where Higgs bosons primarily decay into $b\bar{b}$ pairs (see Fig. 2.3). The associated production with a heavy vector boson decaying into a lepton pair, especially a W^\pm boson decaying into a $l\nu_l$ pair, gives a much clearer experimental signature. These channels rely on efficient b-tagging and lepton identification as well as precise Monte Carlo (MC) modelling of backgrounds.

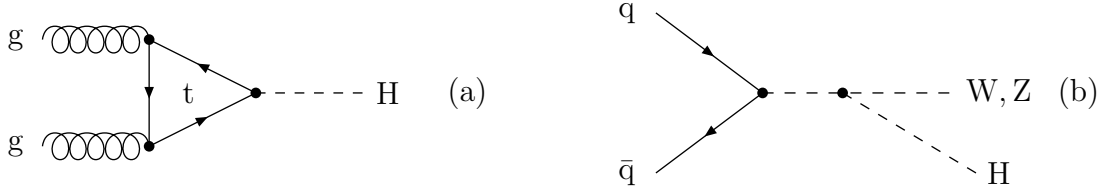


Figure 2.2: Higgs production processes at the Tevatron: gluon-gluon fusion through a top loop (a), and Higgs-strahlung of a W^\pm or Z boson (b).

The associated production of Higgs and gauge bosons can be viewed simply as the Drell-Yan production of a virtual W^\pm or Z boson, which then splits into a real vector boson and a Higgs particle. The cross section times branching ratio for $p\bar{p} \rightarrow W^\pm \rightarrow W^\pm H$ (summed over both charge states) reaches values of 0.3–0.02 pb for $m_H \sim 100$ GeV to ~ 200 GeV. The cross section for $p\bar{p} \rightarrow ZH$ is roughly a factor two lower for the same Higgs mass range. The QCD contribution to $\sigma(p\bar{p} \rightarrow VH)$ (e.g. from radiative corrections [12]) coincides with that of the Drell-Yan process and increases the cross section by about 30%. The cross sections as a function of the Higgs mass are shown in Fig. 2.4. The theoretical uncertainty is estimated to be about 15% from the remaining scale dependence. The dependence on different sets of parton distribution functions leads to another variation of the production cross-section of about 15%.

2.4 Higgs mass

While the Higgs mechanism is introduced to explain the masses of particles in the SM, the mass of the Higgs particle itself is unknown. In theory, the mass is given by

$$m_H = \sqrt{2\lambda} \times v, \quad (2.31)$$

but the value of λ is unknown. In this section the theoretical constraints will be reviewed.

In higher order calculations the λ parameter becomes energy scale dependent, as most other parameters in a quantum field theory. In the Standard Model, most divergences in the running of λ cancel, except for the ones that are logarithmic in the energy. However, these logarithmic terms can be re-summed giving:

$$\lambda(Q^2) = \frac{\lambda(\mu^2)}{1 - \beta \ln\left(\frac{Q^2}{\mu^2}\right)}, \quad (2.32)$$

where Q^2 is the energy scale of the process considered, usually given by the relevant exchanged four-momentum Q , μ is some low energy scale at which the value of $\lambda(\mu^2)$ is fixed, and β is the beta function of the renormalisation group equation. To next to leading order

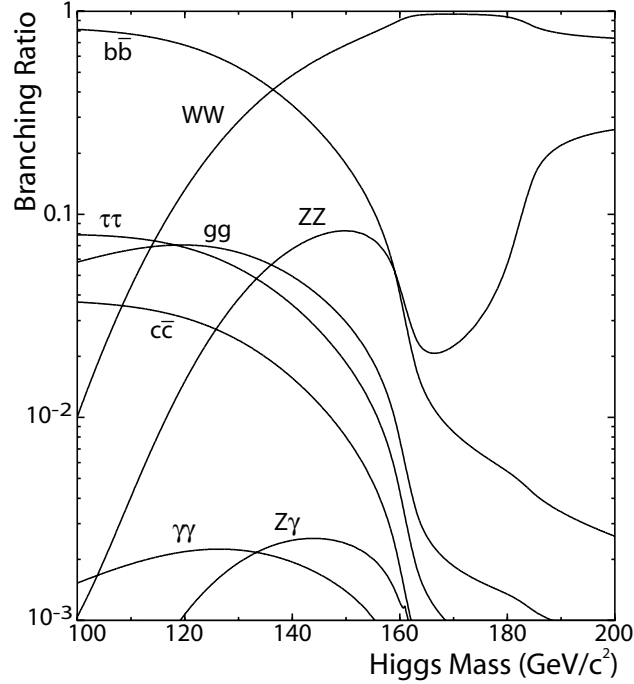


Figure 2.3: The branching ratios for the SM Higgs boson as a function of m_H , calculated using the HDECAY program [11].

β is given by:

$$\beta = \frac{12\lambda(\mu^2)}{16\pi^2}. \quad (2.33)$$

For the low energy scale at which the value is to be determined, the vacuum expectation value ($\mu = v$) is a natural scale.

The value of λ explodes if the denominator in Equation 2.32 goes to zero. The energy scale at which this happens is called the Landau scale, denoted by Λ_{Landau} . The theory only makes sense for energy scales below the Landau scale. Addition to the theory or a new theory must kick in at or below the Landau scale.

For the Landau scale it follows that:

$$\ln\left(\frac{\Lambda_{\text{Landau}}^2}{v^2}\right) = \frac{1}{\beta} = \frac{16\pi^2}{12\lambda(v^2)}, \quad (2.34)$$

or formulated in terms of the value of $\lambda(v^2)$:

$$\lambda(v^2) = \frac{16\pi^2}{12 \ln\left(\frac{\Lambda_{\text{Landau}}^2}{v^2}\right)} \quad (2.35)$$

For any energy scale below the Landau scale, $Q^2 < \Lambda_{\text{Landau}}^2$, the Higgs mass squared is given by:

$$m_H^2 = 2\lambda(Q^2)v^2 < 2\lambda(v^2)v^2 = \frac{2v^2 16\pi^2}{12 \ln\left(\frac{\Lambda_{\text{Landau}}^2}{v^2}\right)}. \quad (2.36)$$

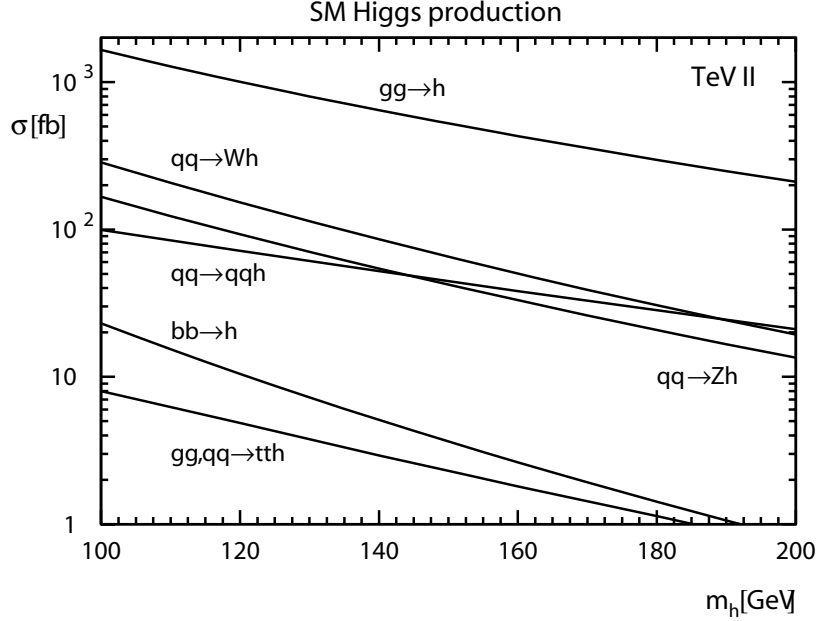


Figure 2.4: The production cross section for the SM Higgs boson in proton-antiproton collisions at $\sqrt{s} = 1.96$ TeV [12].

Hence, it follows for the Higgs mass that:

$$m_H < \frac{2\sqrt{2}\pi}{\sqrt{3}} \frac{v}{\sqrt{\ln\left(\frac{\Lambda_{\text{Landau}}^2}{v^2}\right)}}. \quad (2.37)$$

Vacuum stability forces λ to be positive at any acceptable energy scale, to ascertain that the Higgs potential always goes up to infinity with increasing field strength. At small values of λ the coupling to the top quark, with its Yukawa coupling constant nearly equal to one, dominates in the running of λ and the derivative of λ with respect to the energy scale behaves as:

$$\frac{\partial\lambda}{\partial(\ln Q^2)} \propto -g_t^4, \quad (2.38)$$

with $g_t = \sqrt{2}m_t/v$, the top Yukawa coupling and m_t the top quark mass. To first order this means that up to the energy scale $\Lambda_{\text{unstable}}$:

$$\lambda(\Lambda_{\text{unstable}}^2) = \lambda(v^2) - \frac{12g_t^4}{16\pi^2} \ln\left(\frac{\Lambda_{\text{unstable}}^2}{v^2}\right) > 0. \quad (2.39)$$

Using again that $m_H^2 = 2\lambda v^2$ a bound on the Higgs mass squared can be given as:

$$m_H^2 > \frac{12g_t^4 2v^2}{16\pi^2} \ln\left(\frac{\Lambda_{\text{unstable}}^2}{v^2}\right). \quad (2.40)$$

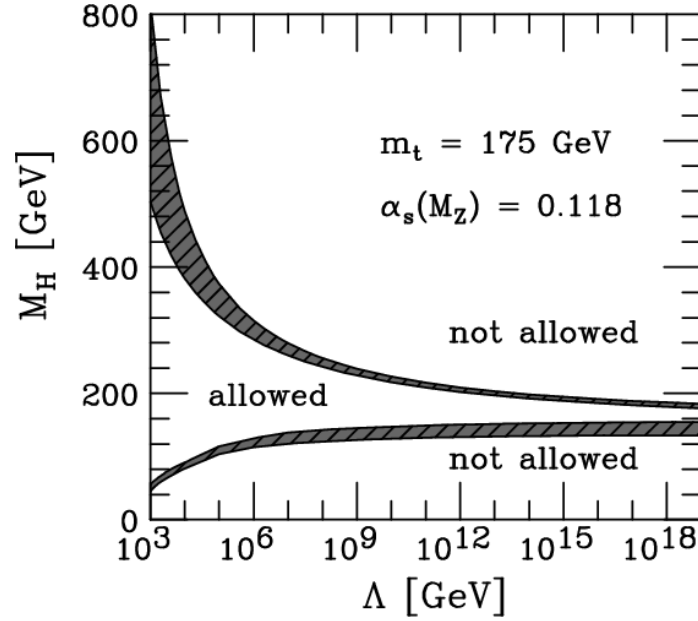


Figure 2.5: The theoretical limits on the mass of the Higgs (m_H) as a function of Λ , the energy where new physics appears [13].

The lower bound on the Higgs mass is then:

$$m_H > \sqrt{\frac{3}{2}} \frac{m_t^2}{\pi v} \sqrt{\ln \left(\frac{\Lambda_{\text{unstable}}^2}{v^2} \right)}. \quad (2.41)$$

Identifying both Λ_{Landau} and $\Lambda_{\text{unstable}}$ with a breakdown scale for the Standard Model, $\Lambda_{\text{breakdown}}$, the range of valid Higgs masses can be written as:

$$\sqrt{\frac{3}{2}} \frac{m_t^2}{\pi v} \sqrt{\ln \left(\frac{\Lambda_{\text{breakdown}}^2}{v^2} \right)} < m_H < \frac{2\sqrt{2} \pi}{\sqrt{3}} \frac{v}{\sqrt{\ln \left(\frac{\Lambda_{\text{breakdown}}^2}{v^2} \right)}}. \quad (2.42)$$

Figure 2.5 shows the theoretical limits on the mass of the Higgs as a function of Λ , taking into account higher orders of the β function [13]. The theoretical limits allow a Higgs boson up to the Planck scale³. If $\Lambda_{\text{breakdown}} \approx 1$ TeV, the Higgs mass is constrained to be in the range $78 < m_H < 754$ GeV, using a vacuum expectation value $v = 246$ GeV and a mass of the top quark of $m_t = 170.9$ GeV [14].

³The Planck scale is the energy at which quantum gravity becomes important, and corresponds to 10^{19} GeV.

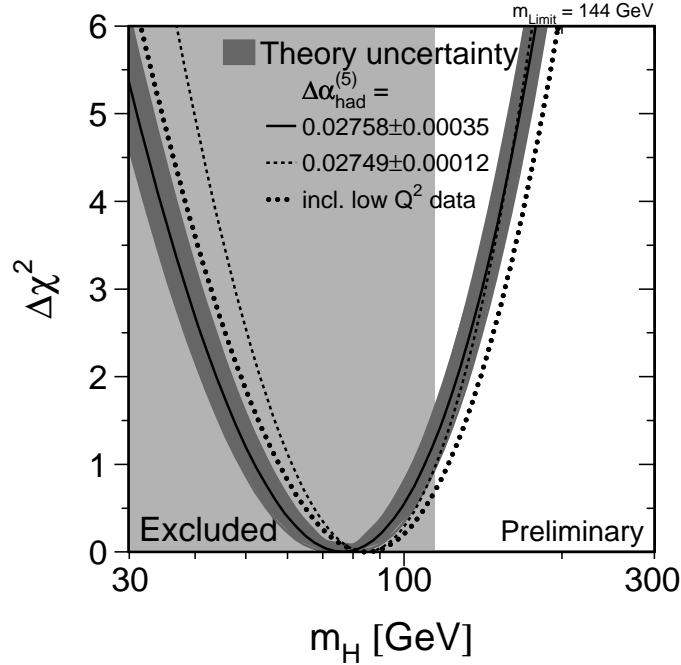


Figure 2.6: The $\Delta\chi^2(m_H) = \chi_{min}^2(m_H) - \chi_{min}^2$ of the fit to the electroweak parameters and the Higgs mass as a function of the Higgs mass [3]. The band represents the theoretical uncertainty, and the vertical band shows the 95% confidence level exclusion limit found from the direct searches at LEP [2].

2.5 Higgs searches

2.5.1 Direct Searches

Direct searches for the Higgs must exploit the Higgs production mechanisms and decay channels that are most suitable to the collider where the study is performed. Searches have been performed at both LEP and the Tevatron.

The most stringent limit on the mass of the Higgs particle has been set by direct searches carried out at CERN. At the LEP e^+e^- collider, the primary production process is $e^+e^- \rightarrow ZH$. The four LEP experiments performed a direct search for the Higgs boson using 2461 pb^{-1} , for all four LEP experiments combined, of data collected at centre of mass energies from 189 to 209 GeV. All Z decays were included for the $H \rightarrow b\bar{b}$ channel, but only Z decays to quarks were included for the $H \rightarrow \tau^+\tau^-$ channel. A lower limit was set on the Higgs boson mass of 114.4 GeV at 95% confidence level (CL) [2].

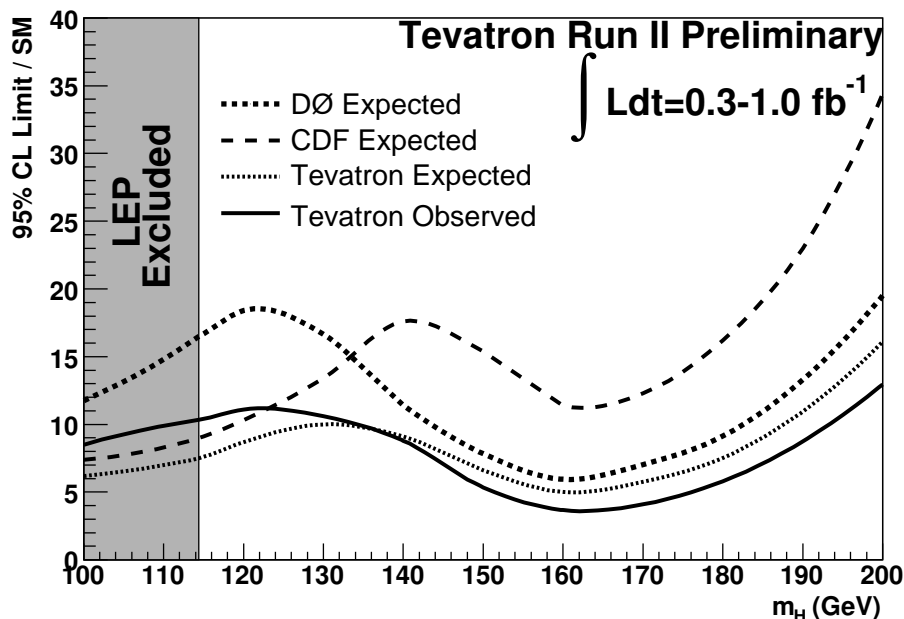


Figure 2.7: The ratio of the expected and observed 95% CL limits to the SM cross section for the combined CDF and DØ analyses [15].

2.5.2 Indirect Experimental Measurements

Most electroweak parameters are sensitive to the Higgs mass via higher order loop corrections and it is thus possible to use these corrections to place indirect constraints on the mass of the Higgs. Precision measurements of 18 electroweak parameters, such as the mass and width of the W boson, have been combined in a global fit with the Higgs mass, using high- Q^2 data from LEP, SLC and the Tevatron. The $\Delta\chi^2(m_H) = \chi_{min}^2(m_H) - \chi_{min}^2$ of the fit as a function of Higgs mass is shown in Fig. 2.6. The minimum of the $\Delta\chi^2$ curve corresponds to 76^{+33}_{-24} GeV at 68% CL and an upper limit is set on the Higgs mass of $m_H < 144$ GeV at 95% CL [3]. The largest sources of error in the fit are due to the mass of the W-boson and the mass of the top quark.

Combined with the lower limit of 114.4 GeV from the direct searches, this means that the most likely mass range for the Higgs boson is $114.4 < m_H < 144$ GeV. This is also the range in which the Tevatron gives a good opportunity to observe the Higgs boson.

2.6 Higgs search at the Tevatron

Direct searches have also been carried out by both the DØ and CDF experiments. Upper limits have been set on the production cross section as a function of the SM Higgs mass, in associated production ($ZH \rightarrow \nu\nu b\bar{b}$, $W^\pm H \rightarrow e\nu_e b\bar{b}$, $W^\pm H \rightarrow \mu\nu_\mu b\bar{b}$ and $W^\pm H \rightarrow W^\pm W^+ W^-$) and gluon fusion ($H \rightarrow W^+ W^-$) production channels. The current combined limit from both experiments for all search channels is shown in Fig. 2.7 [15]. The expected limit indicates the limit setting potential of the experiment, and is derived from the background and signal

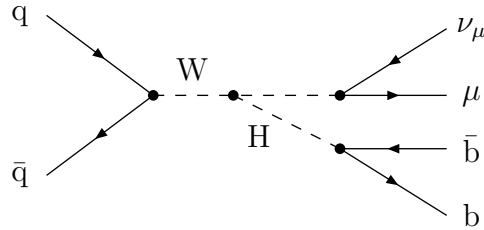


Figure 2.8: The search channel $q\bar{q} \rightarrow W^\pm H \rightarrow \mu\nu\bar{b}b$.

distributions assuming no signal production. The observed limit is the actual limit on signal production derived when also taking into account the experimental data. The observed cross section limit at the Tevatron is currently a factor of 10 (4) above the SM cross section at a mass of 115 (160) GeV, although with the expected increases in luminosity and improved analysis techniques (see for example the b-tagging improvements in Chapter 5) this factor will decrease rapidly.

Previous studies have indicated that 2 fb^{-1} is sufficient to set a limit on the SM Higgs mass of about 115 GeV [16]. The Higgs boson could even be discovered at the Tevatron during Run II if its mass is relatively low, $m_H < 200 \text{ GeV}$, as described by fits to the high-precision electroweak data, and if sufficient data is collected. Higgs bosons with masses up to $m_H \sim 1 \text{ TeV}$, beyond which value perturbation theory in the SM is no longer possible, can be probed at the LHC.

Two Higgs mass ranges are of particular interest:

- $110 \text{ GeV} < m_H < 130 \text{ GeV}$
- $130 \text{ GeV} < m_H < 180 \text{ GeV}$

In the lowest mass range, the Higgs boson mass lies above the present direct LEP search limit. If the Higgs boson is discovered in this range, the theoretical limits would imply $\Lambda_{\text{breakdown}} < m_{\text{Planck}}$. A Higgs mass in the range 130 – 180 GeV would imply $\Lambda_{\text{breakdown}} = m_{\text{Planck}}$. In this case, the SM could in principle remain viable all the way up to the Planck scale.

2.6.1 Higgs search strategy and backgrounds

In this analysis we study Higgs bosons with masses below 150 GeV. The search channel is the associated production of a Higgs boson with a W^\pm boson, with the Higgs boson decaying to a $b\bar{b}$ pair and the W^\pm boson to a $\mu\nu_\mu$ pair. The diagram is shown in Fig. 2.8.

A basic event selection that follows the expected topology is used. First, events are selected that are consistent with the decay of a W boson to a charged lepton (either μ or $\tau \rightarrow \mu$) and a neutrino, indicated by an energy imbalance in the detector. Next, since the Higgs boson is expected to decay primarily to a $b\bar{b}$ pair, the presence of jets is required. The

presence of b quarks in the jets is determined by looking for evidence of the decays of the relatively long-lived b-flavoured hadrons.

Substantial backgrounds still exist. The backgrounds are $t\bar{t}$, $W^\pm/Zb\bar{b}$, $W^\pm Z$, ZZ , single top quark production and background from QCD processes. In most of these background processes real leptons from W^\pm/Z decays and real pairs of b quarks are present in the final state. Then, we should rely on the detailed event characteristics in order to improve the signal to background ratio.

To discover a Higgs signal in $p\bar{p} \rightarrow W^\pm H \rightarrow W^\pm b\bar{b}$ at the Tevatron, one must be able to separate the signal from an irreducible SM $W^\pm b\bar{b}$ background. The kinematic properties of the signal and background are not identical, so by applying appropriate cuts, a statistically significant signal can be extracted given sufficient luminosity.

Although the SM $W^\pm b\bar{b}$ signal can be studied experimentally, a reliable theoretical computation of the predicted $W^\pm b\bar{b}$ differential cross-section is an essential ingredient of the Tevatron Higgs search. At lowest order in QCD perturbation theory, the rate for $W^\pm b\bar{b}$ production is proportional to $(\alpha^2(m_Z^2))$. The appropriate energy scale of the strong coupling constant is not fixed at lower order, leading to a significant uncertainty in the theoretical predictions. The higher order corrections greatly reduce the scale dependence of the predicted rate. However, the NLO calculations also change the shape of kinematic distributions from the lowest order results. In particular, the NLO calculations describe more accurately the kinematics of the $b\bar{b}$ pair and thus permit an extrapolation of the $b\bar{b}$ invariant mass distribution $m_{b\bar{b}}$ to higher values than have been measured. Unfortunately, the NLO cross-sections are generally not reliable for describing details of the final state distributions, since these are sensitive to the details of the hadronisation and fragmentation processes. To overcome this deficiency, a consistent treatment that combines the NLO calculations with the Monte Carlo parton shower simulations is required.

Chapter 3

Tevatron and the DØ detector

Since the shutdown of CERN's LEP (Large Electron Positron) collider in 2000, the Tevatron at Fermilab has taken over the most prominent position to search for the Higgs boson and particles beyond the Standard Model. General aspects of Fermilab's Tevatron accelerator and the upgraded DØ detector will be described in this chapter.

3.1 The Tevatron Accelerator

The Tevatron accelerator is a proton-antiproton collider, located on the Fermilab site about 60 km west of Chicago, USA. The accelerator division of Fermilab maintains a chain of accelerators, needed for proton and antiproton production, pre-acceleration, accumulation and storage. A schematic overview of the accelerator chain is presented in Fig. 3.1. The particle production and acceleration processes are very complex and difficult operations and subject to continuous research and improvements. In this section only the general aspects will be covered, for more information the reader is referred to a more detailed introduction which can be found in e.g. [17].

At the moment the Tevatron is the highest-energy operational particle accelerator in the world. It is a circular accelerator with a circumference of roughly 6.3 km and collides beams of protons and antiprotons. The beams are accelerated to 980 GeV each in the same beam pipe, but in opposite directions, and are brought to collision at two designated points in the accelerator: BØ and DØ, respectively the locations of the CDF and DØ detectors.

Run I of the Tevatron took place between 1992-1996. During this period of data-taking the centre-of-mass energy was $\sqrt{s} = 1.8$ TeV and the total integrated luminosity delivered was 120 pb^{-1} . After a shutdown of five years during which Fermilab's whole accelerator chain and the DØ and CDF experiments were upgraded, the Tevatron resumed operation and data-taking in early 2001 at an approximately 9% higher center-of-mass energy compared to Run I. Both beams now have an energy of 980 GeV, giving a centre-of-mass energy of the Tevatron of $\sqrt{s} = 1.96$ TeV. This phase of data taking is known as Run II. The numbers of bunches of protons and antiprotons used in the Tevatron were increased from 6 to 36 and the beam intensities were much higher than in Run I. This led to considerably higher instantaneous luminosities.

Run II began in early 2001 and is split into two parts, Run IIa and Run IIb. Run IIa

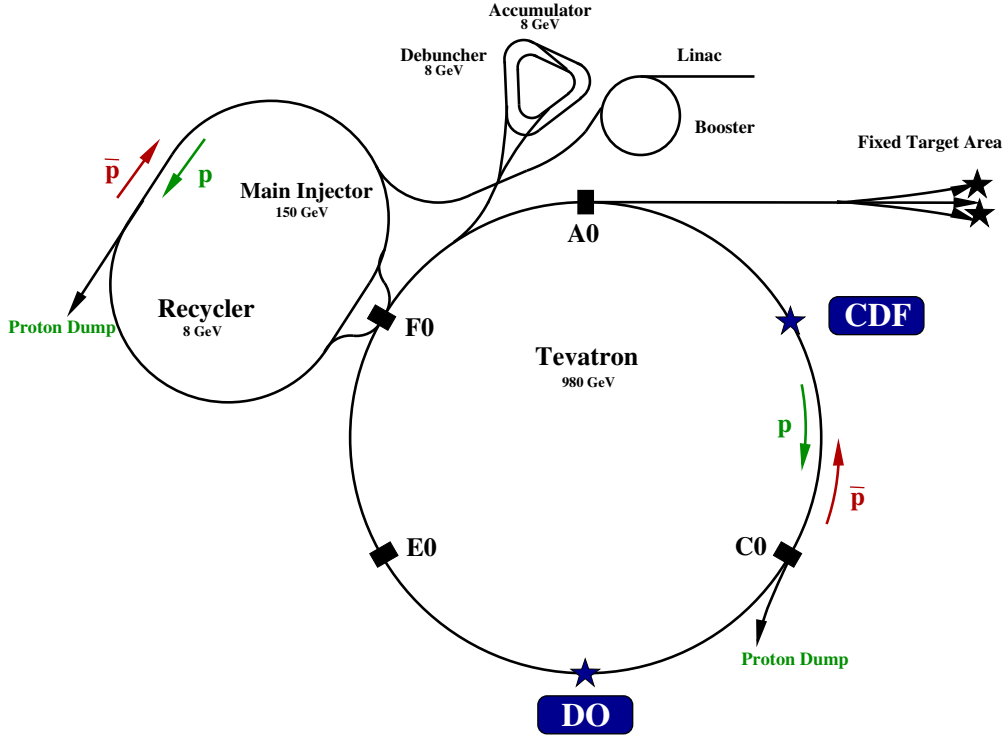


Figure 3.1: The accelerator chain of Fermilab.

finished in April 2006, and all data used in this thesis were collected during this run. Both detectors were upgraded to operate at the higher instantaneous luminosities expected in Run IIb, which began in June 2006. Run II is currently planned to last until the end of 2009, with a final total integrated luminosity of up to 8 fb^{-1} .

A comparison of the operating parameters for the Tevatron used in Run I and Run II is presented in Table 3.1. Figure 3.2 shows the peak instantaneous luminosity achieved during Run IIa. Through incremental improvements, typical peak luminosities in Run IIb are expected to be $\sim 3 - 4 \cdot 10^{32} \text{ cm}^{-2}\text{s}^{-1}$.

The accelerator systems used in proton and antiproton production and acceleration presented in Fig. 3.1 will be briefly described in the following sections.

3.1.1 Proton Source

The Pre-accelerator, the LINAC and the Booster together form the proton source. The high energetic particle beams of the Tevatron start from a small bottle of hydrogen located in an electrostatic Cockcroft-Walton pre-accelerator. A magnetron creates negative hydrogen ions H^- . The H^- ions are accelerated in the Cockcroft-Walton linear accelerator to an energy of 750 keV and passed to the LINAC. The LINAC boosts the particles to 400 MeV. From the LINAC, the negative hydrogen ions can go to any of three destinations: two are dump lines that allow for measurements of either the momentum spread or the transverse emittance, and the third line goes to the Booster.

The Booster is the first circular accelerator, a rapid cycling synchrotron, where protons

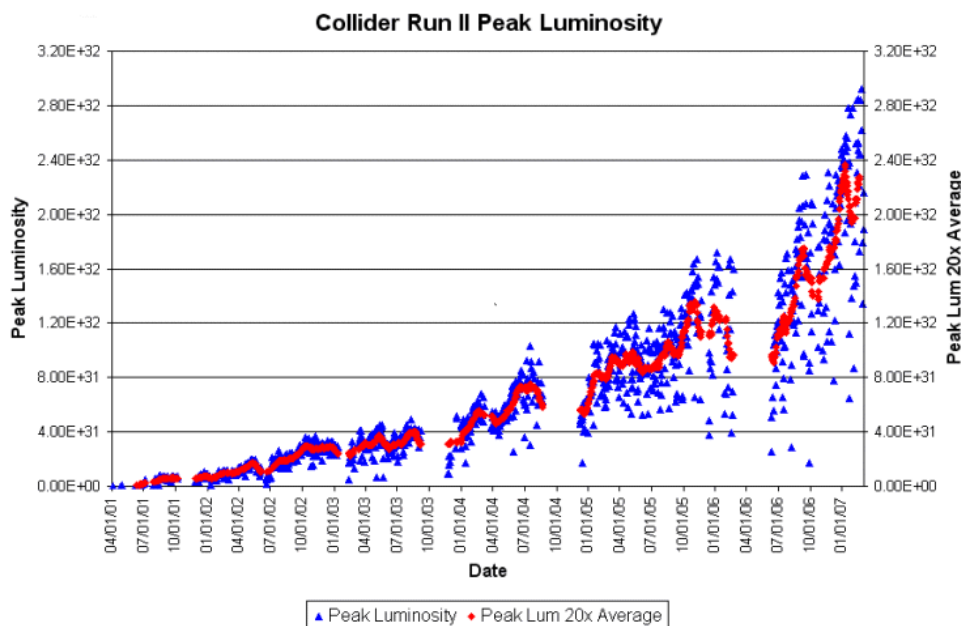


Figure 3.2: The peak instantaneous luminosity delivered by the Tevatron during Run IIa [18].

are accelerated from 400 MeV to 8 GeV. It consists of a series of magnets arranged around a circle with a circumference of about 475 m. Contrary to the magnets in the Main Injector, all Booster magnet are so-called combined function magnets, which bend the beam and focus it either horizontally or vertically (horizontal defocusing). The usage of alternating gradients to keep the proton bunches tightly constrained inside the vacuum chamber of the beam pipe is usually referred to as strong focusing and it is very similar to alternating concave and convex optical lenses.

Compared to the Booster's revolution time of only 2.2 ms, the LINAC pulses are rather long at 40 ms. This means that the LINAC beam has to be injected continuously into the Booster without kicking out the protons that are already inside the Booster. Before reaching the next magnet, though, the merged beam of protons and hydrogen ions is passed through a thin carbon foil, where the weakly bound electrons are stripped off the H^- ions to leave bare protons. Since the foil is very thin, the high energy protons are not affected at all.

The 8 GeV protons from the Booster are transferred to the Main Injector, another synchrotron with a circumference of roughly 3.3 km, more than half the circumference of the Tevatron and about seven times that of the Booster. The tunnel of the Main Injector houses two separate rings: the Main Injector (the lower ring), which can perform a multitude of operations and the Recycler (the upper ring), a storage ring for 8 GeV antiprotons. Since recycling is too time consuming and the achieved efficiency is low, the Recycler is used only to store antiprotons, in order to unload the antiproton accumulator. The Recycler beam pipe is equipped with permanent magnets, making it more robust against e.g. power failures, to store 8 GeV antiprotons. The Main Injector beam line makes use of separate large dipole

Accelerator	Initial energy	Final energy	Destination
Cockcroft Walton	0 keV	750 keV	LINAC
LINAC	750 keV	400 MeV	Booster
Booster	400 MeV	8 GeV	Main Injector, MiniBooNE
Main Injector	8 GeV	(studies) 8 GeV	Recycler, Antiproton source
		120 GeV	Antiproton source
		120 GeV	NuMI target
		120 GeV	Switchyard, fixed target exp.
		150 GeV	Tevatron
Antiproton source	8 GeV	(accumulates) 8 GeV	Main injector, Recycler
Recycler	8 GeV	8 GeV	Main injector (same tunnel)
Tevatron	150 GeV	(stores) 980 GeV	Collisions at $D\bar{O}$ and CDF

	Run I		Run II
TEVATRON characteristics	1992-1996	current	design for December 2007
energy per particle	900 GeV		980 GeV
number of bunches	6×6		36×36
p per bunch [10^{10}]	24.0		24.0
\bar{p} per bunch [10^{10}]	5.5	10.0	13.0
inst. lumi. [$10^{30} \text{ cm}^{-2}\text{s}^{-1}$]	16	290	290

Table 3.1: Basic characteristics of the accelerator chain [17] and the Tevatron in Run I and after the upgrade in Run II.

magnets populating the ring segments to bend the beam, while special focusing/defocusing quadrupole magnets are utilised to keep the beam restricted to the beam pipe. The beam does not form a continuous stream, but it is bunched. Since the Main Injector is much larger than the Booster, 84 bunches are required to fill all the available RF slots (or buckets) around the circumference of the Main Injector; the total sum of the bunches, i.e. all available buckets, constitutes a batch.

The Main Injector accepts 8 GeV protons from the Booster, or 8 GeV antiprotons from the Antiproton Source, and accelerates the 8 GeV protons to either 120 GeV or 150 GeV depending on their destination. The Main Injector and the Tevatron ring were designed to allow simultaneous operation. If the Main Injector is used to inject protons or antiprotons into the Tevatron, its final beam energy is 150 GeV; if it is used to supply protons for production of antiprotons during a physics store in the Tevatron, which lasts typically around 24 hours, the Main Injector will continuously accelerate protons from 8 to 120 GeV. These are then delivered to fixed target experiments and to the antiproton source.

Furthermore, the 150 GeV proton and antiproton bunches delivered to the Tevatron must be superbunches, more intense than any individual bunch that can be accelerated by the Booster. To meet this requirement, the Main injector coalesces 7 to 11 Booster bunches into one superbunch, before transferring them to the Tevatron.

Fixed target experiments at Fermilab include the NuMI [19] Beamline, which uses protons from the Main Injector to produce an intense beam of neutrinos for the MINOS experiment, and MiniBooNE. MINOS and MiniBooNE are designed to observe and test the phenomenon

of neutrino oscillations, an effect which is related to neutrino mass. MINOS is a long-baseline experiment using two detectors, one located at Fermilab, at the source of the neutrinos, and the other located 450 miles away in northern Minnesota. MiniBooNE looks for electron neutrinos in beams of muon-neutrinos or muon-antineutrinos produced using protons from the Booster.

3.1.2 Antiproton Source: Target, Debuncher, Accumulator and Recycler

An important point in the operation of a proton-antiproton collider is the time needed to accumulate the required numbers of antiprotons. This is why the performance of the antiproton production facility greatly affects the quality and the duration of stores in the Tevatron. Anti-proton production is inherently inefficient; for every one million protons on target, typically only about 10 to 20 antiprotons can be captured and stored.

The Antiproton Source consists of a target station, two triangular shaped rings called the Debuncher and the Accumulator, and the transport lines between those rings and the Main Injector. The Debuncher and the Accumulator are synchrotrons with a mean radius of about 90 m and are divided into 6 sectors.

The antiproton source is a nickel-copper target (about 1.3 cm thick) with properties optimised for antiproton production. Protons of 120 GeV from the Main Injector are fired onto the nickel-copper target. The Debuncher captures the antiprotons coming from the target and the Accumulator continuously stores them.

The antiprotons are selected from the interaction products of the proton – fixed target collisions. The energy spectrum of the selected antiprotons peaks at 8 GeV and is monochromised by stochastic cooling in the Debuncher and Accumulator. The method of stochastic cooling was developed by Simon van der Meer in the late 1970s to increase the accumulation of antiprotons for their usage in the Sp \bar{p} S (Super Proton and Antiproton Synchrotron) collider at CERN. In 1984, Van der Meer was awarded the Nobel Prize in Physics for this work, together with C. Rubbia, who initiated the construction of the Sp \bar{p} S and led one of the experimental collaborations that discovered the W and Z bosons. Stochastic cooling consists of picking up a signal from the circulating antiprotons on one side of the ring indicating a deviation from the ideal orbit, amplifying it, and applying the appropriate correction to the antiproton beam on the other side of the ring to move it back towards the ideal orbit.

The stacking efficiency depends on the amount of already stacked antiprotons. Therefore some fraction of the particles are transferred to the Recycler, which was designed to store antiprotons. The recycler has no special features except for the use of mostly permanent magnets and it is used to store antiprotons from the Accumulator to allow a higher production and stack rate in the latter. Until Fall 2005, the Recycler only used stochastic cooling as described earlier in this section. Since then a second type of cooling, electron cooling, is additionally used in the Recycler and enables it to store even more antiprotons at a higher beam density. Electron cooling is based on the exchange of energy in elastic collisions between a beam of cold electrons and the hot antiproton beam. The electrons interact with the antiprotons, cooling the beam and reducing the spread around the longitudinal momentum:

antiprotons travelling too fast are slowed down when they bump into electrons and slow antiprotons are sped up as they are hit by faster electrons. It turned out that since the use of electron cooling, the increased number of antiprotons stored in the recycler led to a higher antiproton production rate in the Accumulator and an increase in the luminosity of the Tevatron collider.

After the transfer of 36 proton bunches with an energy of 150 GeV per particle from the Main Injector to the Tevatron main ring, the antiprotons are transferred. First from the Accumulator and the Recycler to the Main Injector and then after acceleration from 8 to 150 GeV, to the Tevatron. The reason for this sequence is to keep the antiprotons safe as long as possible, because of the significantly larger operating expense to produce antiprotons, compared to the more simple proton acceleration. As soon as all 36 antiproton bunches are in the Tevatron beam pipe, the energy is increased to 980 GeV per particle. Finally, the low-beta magnets are ramped up, to focus the proton and antiproton beams into the interaction zones in the DØ and CDF detectors.

The beam intensity and therefore the luminosity drops exponentially, since the particle loss rate is approximately proportional to the particle flux $\dot{p} \sim p$. If the Tevatron luminosity drops below $10 \times 10^{30} \text{ cm}^{-2} \text{ s}^{-1}$ or as soon as enough antiprotons are stacked in the Accumulator or in the Recycler, the old beams are dumped. The beam circulation can be stopped unintentionally if a magnet quenches. A quench is the local break-down of superconductivity in a magnet coil, e.g. triggered by a temperature fluctuation of the liquid helium coolant. This can result in an accidental particle loss. The magnetic field in the quenched magnet will break down, however this is in general slow compared to the circulation frequency, so that the beams can be kicked out of the beam pipe and dumped in time to avoid further damage. An unnoticed change of the beam orbit can result in the quenching of a large number of magnets.

The Tevatron is in *shot setup* mode, when new particles are to be inserted. In total 36 bunches of protons and 36 antiproton bunches are filled. The bunches are grouped in three trains with a $7 \mu\text{s}$ separation. The bunch to bunch separation, or the interaction frequency is 396 ns. A proton bunch contains about $2.4 \cdot 10^{11}$ protons, the antiproton bunch about two to five times less depending on the number of available antiprotons. The length of the bunches is 37 cm; the number of particles per bunch and the bunch size is limited due to the repelling Coulomb forces. During normal operation the beams are stored with an energy of 980 GeV per particle for up to two days. During test runs a maximum energy of 1.012 TeV per particle has been attained. Some basic characteristics of the Tevatron are summarised in Tab. 3.1.

The Tevatron main ring is divided into six sections, named A through F, clockwise starting in the west section. Each section is divided into five buildings. Each “Ø” location has a long straight section with special functions. At AØ the Tevatron is connected to the Fixed Target Area and the beam abort is located here. The CDF detector is located at position BØ, and a second beam abort (for protons only) is located at CØ. The DØ detector is named after its position in the ring. At EØ the transfer line from the old main ring to the Tevatron – which is now obsolete – was located. The Tevatron RF cavities are located at FØ, as well as the proton and antiproton connection beam lines to the Injector and a transfer line to the antiproton source.

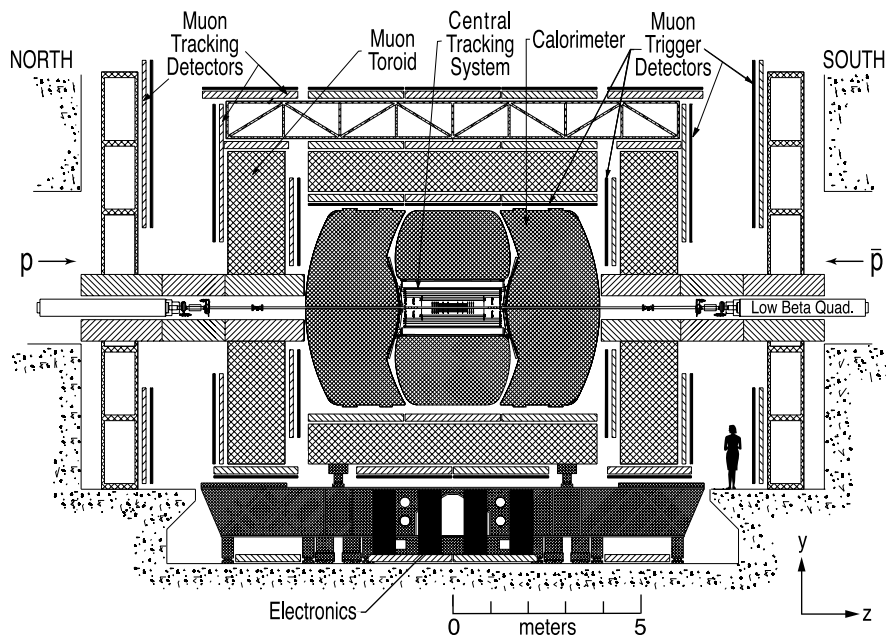


Figure 3.3: A longitudinal view of the $D\bar{O}$ detector. The central tracking region is shown in more detail in Fig. 3.4.

3.2 The $D\bar{O}$ Detector

The $D\bar{O}$ detector, shown in Fig. 3.3, has a symmetric design of concentric cylindrical sub-detectors centred around the collision point, like the layers of an onion. The innermost layer is the central tracking system, shown in Fig. 3.4. It is immersed in a solenoid magnetic field, which allows to determine the momentum of charged particles through their bending radius. The tracking system is followed by the calorimeter and then the muon detectors in a toroid magnetic field. With its three major subsystems, the $D\bar{O}$ detector is capable of detecting all kinds of physics objects, either directly or at least indirectly as for example neutrinos that leave no signal in the detector but can be reconstructed through the missing, unmeasured energy. All sub-detectors are described in more detail in the following sections. Full details can be found in [20]. The $D\bar{O}$ detector functions with an average data-taking efficiency¹ of between 85 – 90% as shown in Fig. 3.5.

3.2.1 Coordinate System

In the Tevatron main ring the proton beam circulates clockwise and the antiproton beam counter-clockwise. The protons enter the $D\bar{O}$ detector from the north. The proton direction defines the positive z -axis. The x -axis points out of the ring and the y -axis points up, defining a right-handed Cartesian coordinate system. The origin of the coordinate system is in the centre of the detector. Since neither the beams, nor the beam interaction products have a preferred direction in the $x - y$ plane, often a cylindrical coordinate system, symmetric

¹Data taking efficiency is defined as the ratio of the recorded to the delivered luminosities.

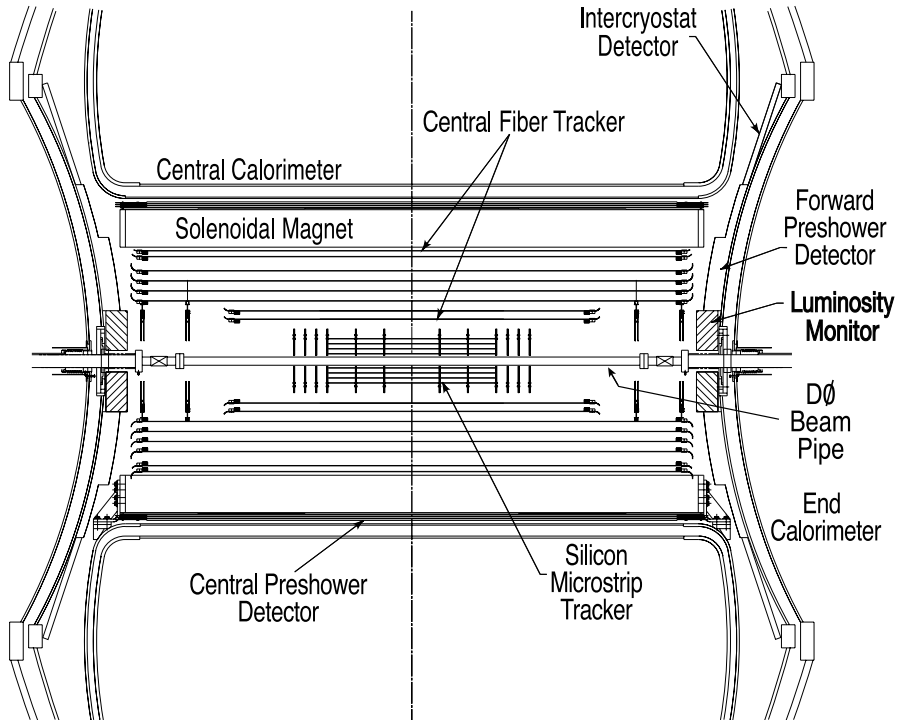


Figure 3.4: The central tracking region in the $D\bar{O}$ detector.

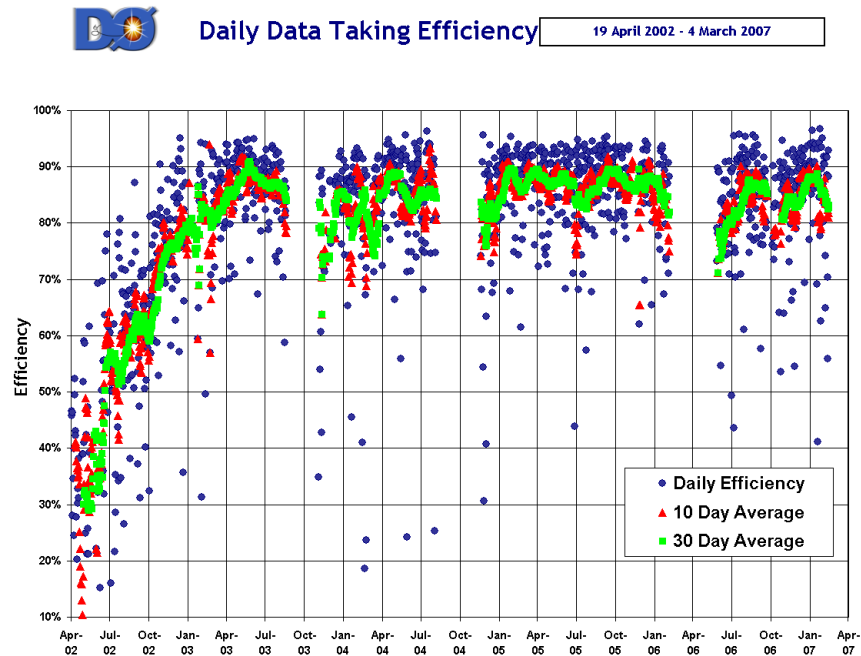


Figure 3.5: The data-taking efficiency of the $D\bar{O}$ detector during Run IIa [21]. The efficiency for each day and the running 10- and 30-day averages are shown.

with respect to the z -axis is used. The azimuthal angle $\phi = [0..2\pi]$ is measured in the $x - y$ plane, $\phi = 0$ is the positive x -axis, and $\phi = \pi/2$ is the positive y -axis. The polar angle θ is often replaced by the pseudo-rapidity η ,

$$\eta = -\ln \tan \frac{\theta}{2}. \quad (3.1)$$

The pseudo-rapidity for physics objects is calculated from the primary vertex z -coordinate and from the r , z -position in e.g. the calorimeter. For high energies, $E \gg m$ and therefore $E \approx |\vec{p}|$, the pseudo-rapidity approaches the true rapidity y ,

$$y = \frac{1}{2} \ln \left(\frac{E + p_z}{E - p_z} \right), \quad (3.2)$$

where E is the particle's energy and p_z the momentum in z -axis direction. Differences in rapidity are invariant under Lorentz boosts along the z -axis. This is especially important at hadron colliders, where the centre-of-mass system of the colliding partons is not the lab rest frame. Rapidity is only a meaningful variable if the mass is known.

The interaction volume of the proton and antiproton beams is an ellipsoidal shaped density distribution with a typical radius r in ϕ -direction of $\sigma_{x,y} \approx 30 \mu\text{m}$ and a length in the z -direction of $\sigma_z \approx 25 \text{ cm}$. The position of the interaction region ellipsoid is not stable; changes of the beam optics due to maintenance or upgrades cause shifts in all directions by the order of several $100 \mu\text{m}$. The vertex distribution over the relevant runtime is shown in Fig. 3.6. The luminosity depends on the particle density in this interaction volume, but the density is limited by the beam optics, the number of particles in the bunches and the repelling Coulomb forces.

3.2.2 The Luminosity Monitor System

The luminosity is an important number to normalise the recorded data. The luminosity can be measured by counting events of a specific process, if the cross section of this process is known. However, to measure a cross section of a certain process one needs to know the luminosity.

The Luminosity Monitor (LM) is used to determine the luminosity (\mathcal{L}) at the DØ interaction point by detecting inelastic $p\bar{p}$ collisions.

The luminosity detector consists of two arrays of 24 plastic scintillation counters and photo multiplier tubes (PMT). A schematic drawing of an array is shown in Fig. 3.7 (left). The location of the PMT is marked by solid dots. The luminosity detectors are located at $z = \pm 140 \text{ cm}$, Fig. 3.7 (right), between the silicon tracker and the forward calorimeter. The scintillation counters are 15 cm long and cover a pseudo-rapidity range of $2.7 \leq |\eta| \leq 4.4$.

To detect an event of the elastic and inelastic scattering reference process, both luminosity detectors have to be fired. Background from beam-halo is suppressed by requiring that the z -coordinate z_v of the interaction vertex be within 100 cm of the detector centre. The vertex coordinate is calculated as $z_v = \frac{c}{2}(t_- - t_+)$, where t_{\pm} is the time-of-flight measurement at the detectors at $\pm 140 \text{ cm}$.

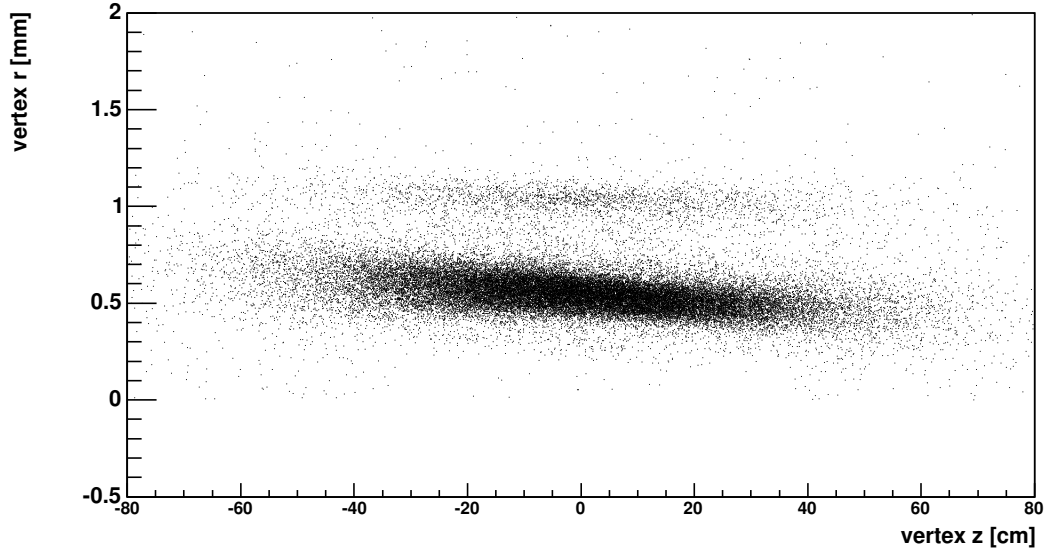


Figure 3.6: The vertex distribution at $D\bar{O}$, where z is the distance from the detector centre and r the distance from the beam-pipe centre. The imperfect adjustment of the low-beta focusing magnets at $D\bar{O}$ and the imperfect Gaussian particle density in the proton and antiproton bunches lead to shifts and the slight angle of the vertex distribution. The upper band originates from a period of running when the beams were displaced significantly from the detector centre. The image was taken from [22].

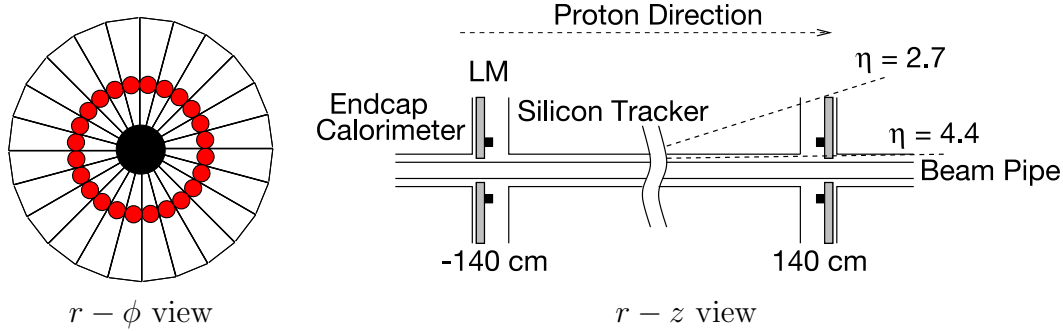


Figure 3.7: Both luminosity detectors LM (left) are located between the silicon tracking detector and the forward calorimeter (right) at $z = \pm 140$ cm.

The luminosity \mathcal{L} is measured by counting the rate of inelastic $p\bar{p}$ collisions recorded by the $D\bar{O}$ LM

$$\mathcal{L} = \frac{1}{\sigma_{\text{eff}}} \frac{dN}{dt}(\text{p}\bar{\text{p}}) \quad (3.3)$$

where σ_{eff} is the effective cross section into the LM, derived from a base inelastic cross section of 60.7 ± 2.4 mb[23] used by both the $D\bar{O}$ and CDF collaborations for Run II[24]. In

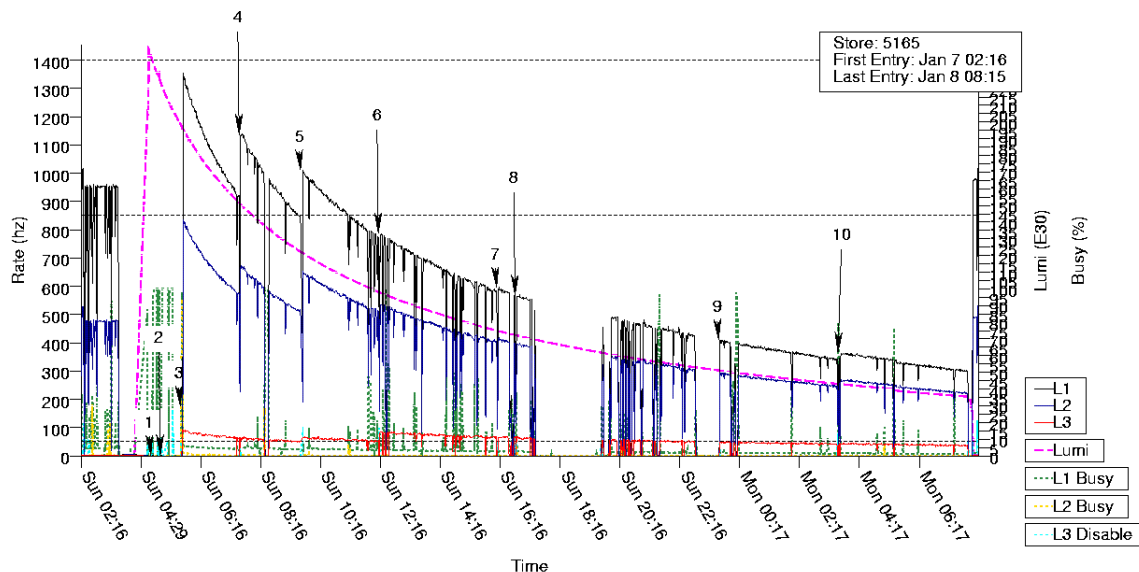


Figure 3.8: A typical physics store [26]. The dashed line refers to the instantaneous luminosity, $135 \cdot 10^{30} \text{ cm}^2\text{s}^{-1}$ at the beginning. The solid lines are the Level 1, Level 2 and the Level 3 output rates. Each run, referred to by numbers, is ended after approximately two hours and the set of triggers (the trigger list) is changed to account for the changed luminosity. DØ has recorded 3.96 pb^{-1} in this store with an absolute data taking efficiency of 89.4%.

Spring 2005, DØ installed a new custom VME readout electronics for the LM. They have a large dynamic range and they are fully incorporated into the DØ data acquisitions system providing pulse height and timing information for every channel in each triggered beam crossing. This information was not available before spring 2005. In Autumn 2005, DØ began reporting luminosity with the new readout system. The new luminosity measurement was initially scaled to equal old luminosity. The data taken with the new system is used to make an improved determination of the absolute scale of the DØ luminosity measurement [25].

The luminosity is measured over short periods of time, called luminosity blocks. The time period of at most 60 seconds is short enough so that the instantaneous luminosity is effectively constant during each luminosity block, introducing negligible uncertainty on the measurement of the luminosity due to the width of the time slice. Events from blocks with a bad luminosity measurement can be easily rejected to ensure a good luminosity measurement.

Besides the detection of elastic and inelastic scattering events, the luminosity detector measures the beam-halo rates and provides a fast measurement of the z -coordinate of the interaction vertex.

The luminosity detectors are always on when the Tevatron is running, even when the DØ detector is not taking data. This means that the luminosity delivered by the accelerator can be measured.

In Fig. 3.8 the data taking profile of a typical store is shown, and in Fig. 3.9 the total integrated luminosity recorded by DØ can be seen.

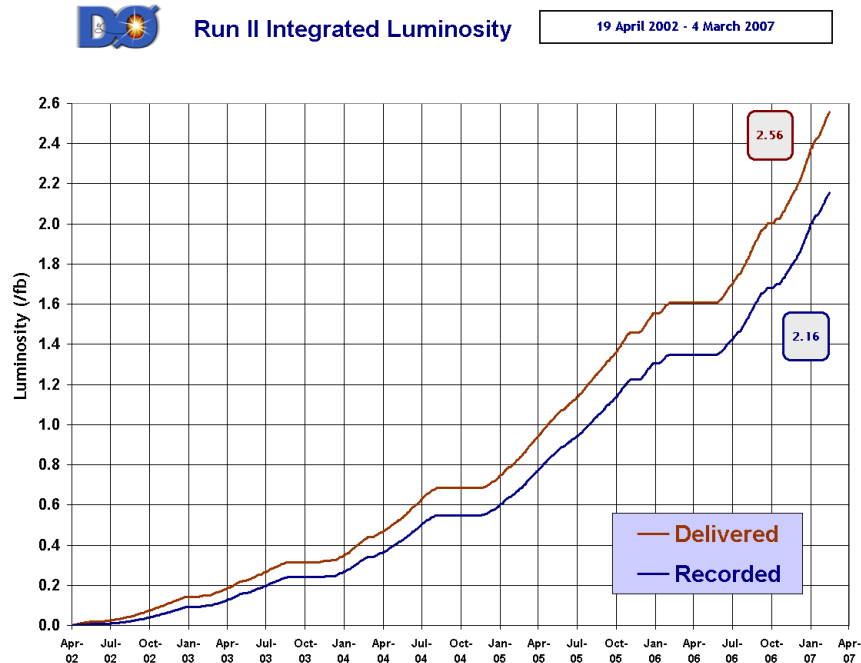


Figure 3.9: Total integrated $D\bar{O}$ luminosity. The upper curve shows the delivered luminosity, the lower curve the recorded luminosity.

3.2.3 The Central Tracking Detector

Excellent tracking, and by extension vertex reconstruction, is essential for a wide range of physics studies including Higgs, top, B, electroweak and new phenomena. The central tracking system at $D\bar{O}$ in Run II, shown in Fig. 3.4, consists of a high precision silicon microstrip tracker (SMT) and a central fibre tracker (CFT) and is embedded in a superconducting solenoid magnet with radius $r = 50$ cm and length $l = 2.70$ m. The magnetic field is 2 Tesla and is approximately homogeneous inside the magnet. Charged particles are forced onto a helical trajectory and will lose energy on their way through the tracker material. This energy deposition, in the form of ionisation in the silicon sensors or in the form of light in the fibres, is detected. The five helix parameters, such as origin, direction and curvature are calculated. Momentum information can be extracted from these parameters. Both tracking detectors combined locate the primary interaction vertex and secondary decay vertices with a resolution of $35 \mu\text{m}$. The impact parameter resolution, for example useful in the identification of b-quarks, is better than $15 \mu\text{m}$ for tracks with $p_t > 10$ GeV. Together, the silicon microstrip and the central scintillating fibre tracker achieve a momentum resolution of $(2 + 0.15p_T)\%$, with p_T in GeV.

The Silicon Microstrip Tracker

The Silicon Microstrip Tracker (SMT) uses silicon sensors with readout strips placed at a distance (“pitch”) of 50 to $153.5 \mu\text{m}$ of each other, depending on the location in the SMT.

The readout strips are made of n^+ -doped silicon on one side of the sensor, and of p^+ -doped silicon on the other. A bias voltage is applied to the sensors so that the bulk is depleted of charge carriers. When a charged particle traverses the silicon, extra charge carriers are created, leading to an electric signal on the nearest readout strips. By combining “hits” in several sensors, the trajectory of the particle is reconstructed.

The design of the SMT was dictated by the length of the nominal interaction region, which is quite long: of the order of 50 cm. The tracks coming from the interaction region should penetrate the sensors approximately perpendicularly, to minimise multiple scattering and to allow for the most precise measurements. The SMT provides tracking and vertex reconstruction for almost the full η range of the calorimeter and muon detectors. An isometric view of the SMT is shown in Fig. 3.10. The detector consists of six barrels, with sensors parallel to the beam line, and 16 disks orthogonal to the beam line. The layout of each of these parts is as follows:

Barrels - There are three barrels on each side of the origin, each made from 4 concentric layers of single- and double-sided rectangular silicon wafers (called *ladders*) providing information in $r - \phi$ (p-side) and $r - z$ (n-side). There are 12 wafers in the inner layers 1 and 2, and 24 in the outer layers 3 and 4, for a total of 432 ladders. The barrel detectors cover $2.7 \text{ cm} < r < 10.5 \text{ cm}$ and $|z| < 38 \text{ cm}$, providing tracking in the region $|\eta| < 2.4$.

F-Disks - Each barrel section is capped at the extreme- z end with an “F-disk” made of twelve double-sided wedge detectors. Three more F-disks at each end complete the central part of the detector, so there are twelve F-disks in total. Thanks to a stereo angle of 30 deg, they provide a measurement of $r - z$ as well as ϕ . The F-disks are located at $|z| = 12.5, 25.3, 38.2, 43.1, 48.1$ and 53.1 cm .

H-Disks - Tracking at high $|\eta|$ is provided by four “H-disks”, two at each end of the tracking volume. Each H-disk is made from 24 wedges; each wedge is constructed from two single sided silicon modules positioned back-to-back, with a stereo angle of 15 deg. The disks are located at $|z| = 100.4$ and 121.0 cm . They extend the coverage of the SMT tracking in the forward region up to $|\eta| < 3.0$ with a large lever arm.

The barrel detectors primarily measure the $r - \phi$ coordinate, but in the 1st and 3rd layers, ladders with a 90° stereo angle also measure the z -coordinate. The disk detectors measure $r - z$ as well as ϕ . The precise knowledge of the tracks’ ϕ -component is more important than the z -component, because the momentum reconstruction depends on the measurement of the track curvature, and a solenoid field bends tracks only in the $r - \phi$ plane.

The SMT has 912 readout modules with a grand total of 792,576 channels. The pitch of the strips on the double-sided sensors is predominantly $50 \mu\text{m}$ (p-side) and $62.5 \mu\text{m}$ (n-side), with hit resolutions of $\sim 10 \mu\text{m}$. The signal to noise ratio varies from 12:1 to 18:1 depending on the detector type. Towards the end of Run IIa $\sim 15\%$ of the barrel, $\sim 5\%$ of the F-disk and $\sim 15\%$ of the H-disk silicon modules were disabled.

The SMT resides in an area of high radiation. It was designed to resist a radiation dose of about 2 Mrad, which corresponds to a delivered luminosity of about $3.5 - 6 \text{ fb}^{-1}$ at the

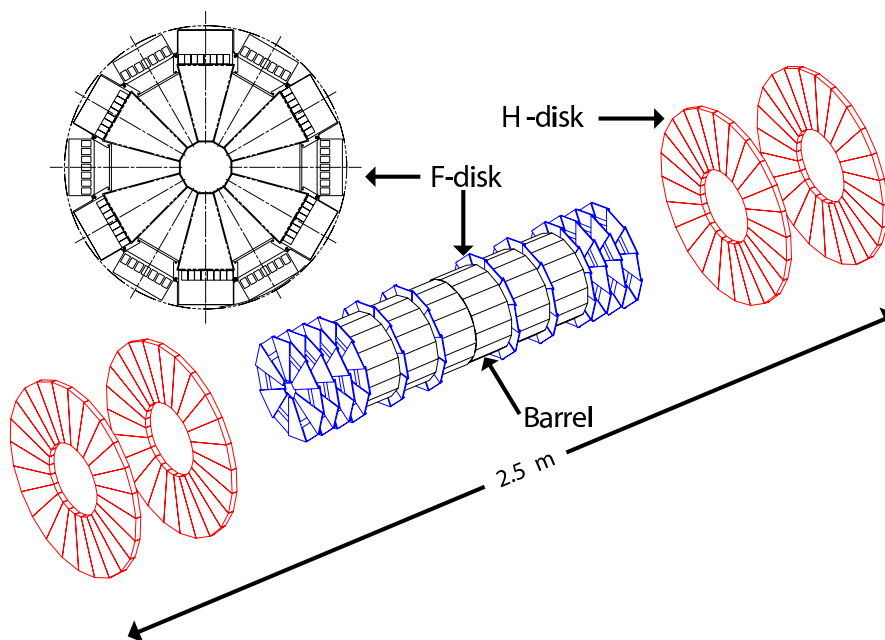


Figure 3.10: The silicon microstrip tracker.

inner layer. It is expected that microdischarges in the sensors will limit the lifetime of the SMT. As part of the Run IIb upgrade in Summer 2006 the SMT has been upgraded with a new barrel layer. This *Layer 0* was inserted between the first barrel layer and a new, smaller radius beryllium beam pipe. Especially the secondary vertex tagging is expected to benefit from this upgrade. Layer 0 will ensure the $D\bar{O}$ tracking capability even if parts of the present SMT die of radiation.

The Radiation Monitor

Extended exposure to high radiation levels will damage the SMT, mainly in the form of displacement damage to the crystal structure of the sensors. The radiation originates mainly from two sources:

1. Non ionising energy loss in the silicon by particles produced in the $p\bar{p}$ interactions and the beam halo [27]. The flux of these particles follows the charged particle $r^{-1.68}$ dependence measured by CDF [28], where r is the distance to the beam line;
2. A neutron flux, approximately independent of r , originating mainly from interactions with the calorimeter.

The radiation dose at the smallest radii is mostly due to the charged particle flux (about 0.4 MRad per fb^{-1} [29]). Radiation damage will cause the leakage current to rise linearly with the total fluence. In addition, type inversion of the initially n type silicon bulk will occur after 0.3 – 0.4 MRad, corresponding to about 1 fb^{-1} . After type inversion, the depletion voltage will rise to high values which limits the useful lifetime of the detector. Biasing the sensors from both sides, a total bias voltage of 120 to 130 V can be applied. Because a

good charge collection efficiency requires the bias voltage to be about 20 V higher than the depletion voltage, the maximum depletion voltage at which the sensors can be operated is expected to be about 100 V. Significant loss of channels in Layer 1 is expected after about $3\text{--}4\text{ fb}^{-1}$ [30]. Operation of the second layer could also become compromised at a higher integrated luminosity; however, the loss of the innermost layer already severely impairs the detector performance for b tagging.

A significant part of the radiation exposure of the SMT may come from unexpected beam deviations and losses. To prevent unnecessary exposure to accidental radiation and to monitor the total radiation dose received by the SMT, two radiation monitoring and alarm systems have been installed. Four Beam Loss Monitors (BLMs) [31] are mounted at each end of the detector, just outside the calorimeter end caps. Their main function is to provide an abort signal to the Beams Division if radiation levels are too high. A system consisting of 48 silicon diodes is located in the SMT volume itself [32]. This system, similar to one previously used by the OPAL collaboration [33], provides an integrated dose measurement as well as a precise radiation history in the case of an abort. The diodes are known as the “radiation monitors”. The radiation monitors can also send alarm signals to the control room and to the Beams Division.

The Beam Loss Monitors have been used successfully by both CDF and the Beams Division in Run I [34]. The monitors are large argon filled gas counters with a large diameter anode cylinder, so no amplification occurs. The BLMs operate at 2 kV, well above their plateau region, to ensure a fast response time. This system is very robust and well understood, but not as sensitive to low radiation levels as the Radiation Monitors. In addition, their location makes it hard to correlate the measured dose to the dose at the SMT.

The sensors for the Radiation Monitors are small ($1 \times 1\text{ cm}^2$) silicon diodes, cut from the SMT production wafers. They are mounted on small flexible circuits which are laminated onto beryllium support plates. Two diodes are mounted on one plate or “finger”, one at the inner radius of the detector and one near the mounting point of the plate on the support ring. Six such modules are placed on each of the outer F- and H-disks, uniformly distributed in ϕ , for a total of 24 fingers. Charged particles traversing the $300\text{ }\mu\text{m}$ thick diodes generate a charge signal of about 3 fC which is amplified on the fingers. The flexible circuits contain two separate analog amplification circuits providing high and low gain output for each diode. The low gain signal provides an alarm signal for high radiation doses, while the high gain signal allows precise monitoring of the integrated dose. Both signals are integrated in a custom electronics crate. The high gain signal is used to measure individual MIPs (Minimum Ionising Particles) and to calibrate the signal. In addition, a precise record of the total received dose is kept (see e.g. [35]). The $D\bar{O}$ detector accumulated about 3fb^{-1} so far and type inversion has been observed, but no indication for lost channels or deteriorated performance due to radiation damage.

The Central Fibre Tracker (CFT)

The CFT provides tracking in the region $|\eta| < 1.6$. Fibres are arranged in concentric layers around the beam pipe. A doublet layer is made from 256 fibres divided into two layers of 128 fibres offset by half the diameter of a fibre. A ‘super layer’ is made from two doublet

layers, one parallel to the beam pipe providing $r - \phi$ information and one at an angle of $+2^\circ$ or -2° providing $r - z$ information through a stereo measurement. There are 8 super layers covering $20 \text{ cm} < r < 52 \text{ cm}$, $|z| < 1.26 \text{ m}$ in the outer 6 super layers and $|z| < 0.88 \text{ m}$ in the two inner super layers.

The scintillating fibres are constructed from doped polystyrene surrounded by a double cladding with a total diameter of $835 \mu\text{m}$. High-energetic charged particles cause excitations of the polystyrene. When the molecules fall back to the ground state, light of a characteristic wavelength is emitted. The scintillating fibres are connected to clear fibre waveguides which carry the light to visible light photon counters (VLPC) where the light is converted to an electrical signal. The VLPCs have a fast response time, a quantum efficiency of greater than 75% and a high gain of 22,000 - 65,000. The single hit efficiency per doublet layer is $\sim 99.0\%$ for cosmic muon tracks.

3.2.4 The Calorimeter System

The $D\bar{O}$ Calorimeter was designed to provide energy measurements for electrons, photons, and jets, and to assist in the identification of electrons, photons, jets and muons. It was inherited from $D\bar{O}$ Run I and the calorimeter itself is unchanged. However, more material was inserted in front of the calorimeter: the tracking system and the solenoid magnet, equal to 2–4 radiation lengths² X_0 . The readout electronics were replaced to cope with the increased readout frequency of 2.5 MHz. The calorimeter detector is divided into four parts; three liquid-argon sampling calorimeters, each housed in its own cryostat, and an intercryostat detector (ICD). The central calorimeter (CC) covers $|\eta| \lesssim 1$ and the two end-cap calorimeters ECN (north) and ECS (south) extend the coverage up to $|\eta| \lesssim 4$. The ICD fills the space between the barrel and endcap cryostats, where there is a lot of dead material, with scintillators. A sketch of the calorimeter system is shown in Fig. 3.11.

Using the shower profile (the width of the shower in the calorimeter as a function of the depth) and information from the tracking system, the identification of electrons (using E/p) and photons (by the absence of a charged particle track) is possible. Muons are minimal ionising particles (MIP) and can be identified by the typical MIP signal, an energy deposition of 2 – 3 GeV along their track in the calorimeter, divided over the depth samplings. Since the transverse energy of the initially colliding partons is approximately zero, the transverse energy of not-interacting particles, like neutrinos, can be reconstructed from the energy balance of the hermetically closed calorimeter. This is not possible for the total energy, since the longitudinal momentum fraction of the initial partons is unknown at hadron colliders.

The Liquid Argon Calorimeter

The $D\bar{O}$ Liquid Argon Calorimeter is segmented in 18 layers, while each layer has 74 segments in η and 64 segments in ϕ ³, for a grand total of 47,032 readout cells. The calorimeter cells are arranged in pseudo-projective towers, as shown in Fig. 3.12. Different absorber plates are

²One radiation length X_0 is the distance an electron can travel in material, until its energy E drops to $1/e \cdot E$ on average.

³Parts of the electromagnetic(EM) calorimeter have a finer granularity, while outer parts of the hadronic calorimeter have a coarse granularity.

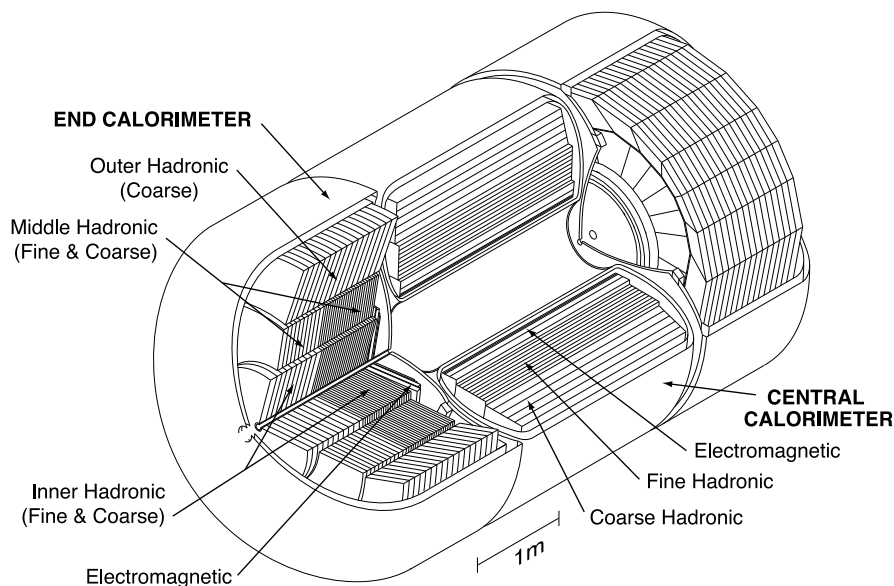


Figure 3.11: Isometric view of the central and the two endcap calorimeters.

used in different locations, in order to achieve a similar energy response of the calorimeter for electro-magnetic and hadronic particles. The inner electro-magnetic part of the calorimeter, layer 1–4, uses 3 mm (4 mm) thin plates in the CC (EC) made from pure, depleted uranium. All 4 layers together have about 20 radiation lengths X_0 . The absorber plates in the fine hadronic sections are made from 6 mm uranium-niobium alloy. The coarse hadronic modules contain 46.5 mm thick plates of copper in the CC and stainless steel in the EC. The total thickness of the hadronic calorimeter is about six nuclear interaction lengths λ_I in the CC and up nine in the EC.

A typical calorimeter cell consists of the absorber plate, the liquid argon active medium and a signal board. The signal boards are made from two 0.5 mm thick G-10 sheets. The outer surfaces facing the liquid argon gap are coated with carbon-loaded epoxy with high resistivity. The electric field is established between the grounded absorber plate and the high voltage (typically +2.0 kV) epoxy electrode. The inner surface of one G-10 sheet is uncoated while the other is coated with copper. The copper pad is divided into a pattern, as necessary for the segmented readout. Charged particles in the showers traversing the liquid argon gap ionise the argon atoms. The electric field forces the drift electrons onto the charge collecting signal boards. The maximal electron drift time across the 2.3 mm liquid argon gap is 450 ns, which provides a challenge for the signal charge integration, as the beam crossing interval in Run II is 396 ns.

The inner four layers of the calorimeter are called the electro-magnetic section, because of the electro-magnetic shower range from electrons or photons. On average, the longitudinal shower of a hadronic jet reaches its maximum far behind the electro-magnetic layers of the calorimeter in the hadronic section due to the larger nuclear interaction length $\lambda_I \gg X_0$, while the shower from electro-magnetic objects reaches its maximum in the third layer. The size of most readout cells is $\Delta\eta \times \Delta\phi = 0.1 \times 0.1$ and is therefore of the order of the transverse

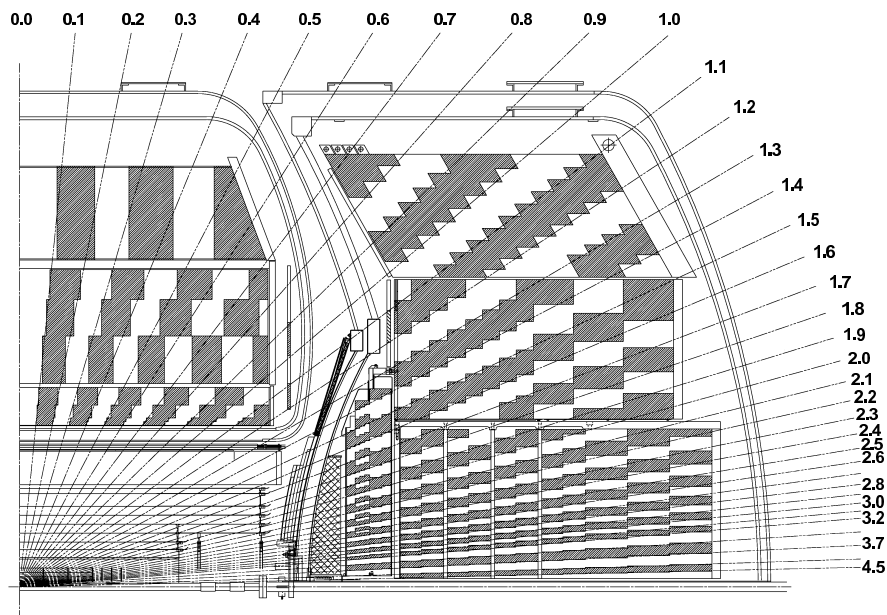


Figure 3.12: Side view of the calorimeter showing the segmentation and coverage in η .

shower radius of hadronic jets $\mathcal{O}(10 \text{ cm})$ and electro-magnetic objects $\mathcal{O}(2 \text{ cm})$. To improve the spatial resolution of electrons and photons the third layer, where the EM showers are maximal, has a finer segmentation $\Delta\eta \times \Delta\phi = 0.05 \times 0.05$.

The Intercryostat Detector

Since the Liquid Argon Calorimeter is divided into three cryostats, it has incomplete coverage in the region $0.8 \leq |\eta| \leq 1.4$. To cope with this problem an intercryostat detector (ICD) is installed, covering $1.1 \leq |\eta| \leq 1.4$. A twice as large $|\eta|$ region was covered by the ICD in Run I, but the space is now needed for the cabling of the tracking system. The ICD is a ring of 16 trapezoid shaped, 1.27 cm thick scintillating tiles enclosed in light-tight aluminium boxes. Each tile covers an area of $\Delta\phi \times \Delta\eta = 0.4 \times 0.3$ and is divided into 12 cells which cover $\Delta\phi \times \Delta\eta = 0.1 \times 0.1$ each. The scintillator tiles are connected by optical fibres to photomultiplier tubes contained in a drawer system in a low magnetic-field region. See Fig. 3.4 and Fig. 3.12 for the location of this detector.

Calorimeter Performance

For Run I, the energy resolution of the $D\bar{O}$ calorimeter was studied in a test beam with pions, electrons and muons with energies between 10 and 150 GeV [36]. However, the jet energy resolution obtained in Run II differs from the pre-Run I testbeam pion resolution. Beside physical arguments for different calorimeter responses for hadronic jets depending on the neutral pion content ($\pi^0 \rightarrow \gamma\gamma$) and therefore the electromagnetic energy fraction, Run II upgrades are responsible for a degrading energy resolution:

- The 5 times higher beam crossing frequency leads to a shorter time over which the

accumulated signal charge can be integrated. This results in larger fluctuations, leading to larger sampling uncertainty.

- The additional material from the solenoid and the tracking system also affect the sampling uncertainty.
- The Run II calorimeter signal amplifiers were found to increase noise.

More detailed information, estimation of the DØ Run II jet energy resolution, the Jet Energy Scale (JES) calibration and jet reconstruction efficiencies will be discussed in Section 4.4.2

3.2.5 The Muon System

The muon system is the outermost subsystem of the detector and provides efficient muon triggering and identification up to $|\eta| \sim 2$. The detector is divided in three regions: the central muon system up to $|\eta| < 1$ and the forward muon systems in the regions $1 < |\eta| < 2$. Each section has three layers of drift tubes (A, B and C, where A is closest to the interaction point). Solid iron toroid magnets with a field strength of 1.8 T are located between the A and B layers. Scintillators in each region provide timing and triggering information. The spatial and the momentum resolution of the muon system allow matching with central tracks with an efficiency close to 1 (see Section 4.4.1 for details.) A detailed drawing of the complete system can be seen in Fig. 3.13. Detailed information on the DØ Run II muon system can be found in [37].

The central muon system uses large Proportional Drift Tubes (PDT), which were also used in Run I, and the forward system uses smaller Mini Drift Tubes (MDT). A-layers have 4 decks of drift tubes and the B/C-layers have 3. The PDTs, which have a drift cell width of 10.1 cm, have a maximum drift time of 500 ns. The MDT drift cells have a cross section of only $9.4 \times 9.4 \text{ mm}^2$ and have a maximum drift time of 60 ns.

The central muon system has two scintillator counters, one in front of Layer A and one behind Layer C. The forward muon system has three scintillator counters located in front of Layers A and C, and one behind Layer B. The scintillator counters are used to trigger on muons, and to provide accurate timing information for track reconstruction in the drift chambers.

The central muon system has 98.6% of the 8k tubes active and 99.8% of the scintillator counters. In the forward region 99.7% of the 50k wires and 99.9% of the 4608 scintillator counters are active. The muon system is stable over time to $\sim 1\%$. The scintillator counters have a time resolution of $\sim 2 \text{ ns}$, and both the PDT and MDT have a hit resolution of $\sim 1 \text{ mm}$. The resolution of the MDTs is limited by the bin size of the drift time digitisation. The momentum resolution for the muons is dominated by the central tracking system for muons with momentum up to 100 GeV, after this the muon systems improve the resolution. The central muon system has a momentum resolution of $\sigma(p) = 0.36(p - 3.1)/p \oplus 0.03p\%$ (where p is in GeV) and the forward muon system of $\sim 20\%$.

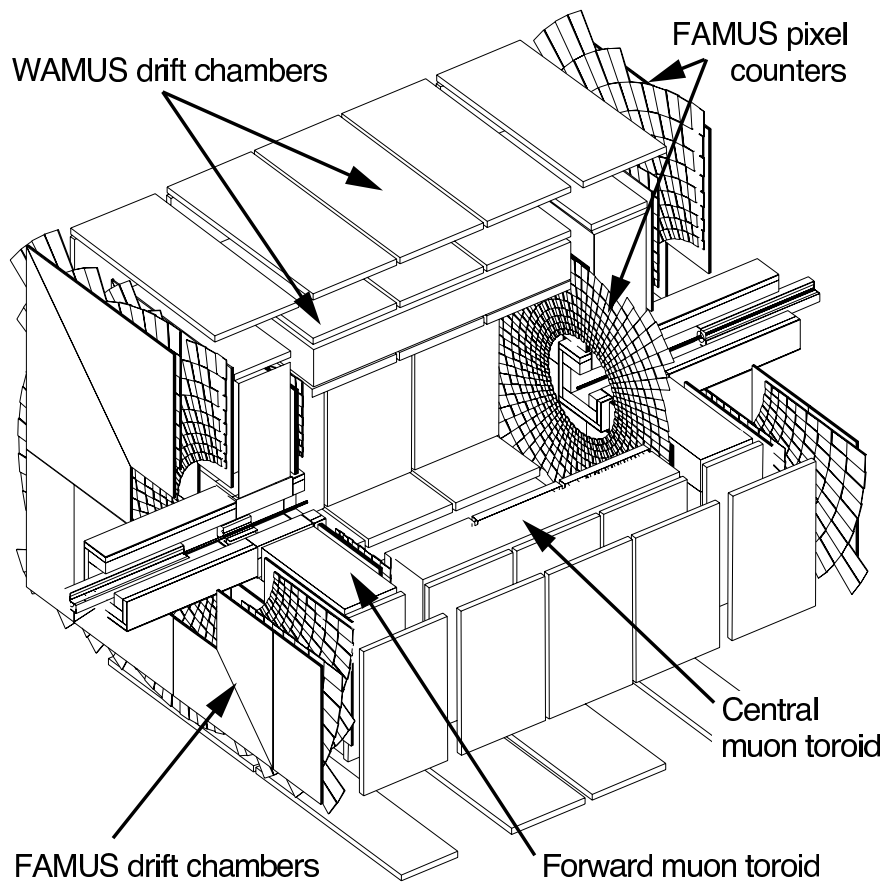


Figure 3.13: Cutaway view of the DØ Muon Spectrometer.

Chapter 4

Data Samples, Event Selection and Monte Carlo Simulation

In this chapter the reconstruction and identification algorithms are described that are necessary for the selection and analysis of WH events. Section 4.1 presents the total data sample and the version of the reconstruction code used in this analysis. Section 4.2 describes the generation of the background and signal MC samples. Section 4.3 presents the general aspects of triggering at DØ. Section 4.4 describes the reconstruction of physics objects such as jets and muons.

4.1 Data sample

The present analysis for the $W^{\pm}H$ search used DØ data collected between November 2002 and April 2006. The integrated luminosity for the total dataset is 1.05 fb^{-1} .

The various versions of DØ software which are used to reconstruct the offline physics objects are referred to by the terminology pXX, where the XX is an integer which is incremented for each new major release of the code. All the work in this analysis uses p17 version reconstruction code which provides the final reconstruction for Run II data.

4.2 Event simulation

Data events can be simulated using Monte Carlo simulations. In addition to the main event generation (the “hard scatter” interaction) which is based on leading order (LO) or next-to-leading order (NLO) and even next-to-next-to-leading order (NNLO) matrix elements, several other steps are performed. The distributions of quarks and gluons in the colliding proton and antiproton are given by parton distribution functions (PDF). Initial and final state showering of particles taking part in the “hard scatter” interaction and the hadronisation process are also simulated.

To prove good understanding of Standard Model processes and of the detector, simulated data must be in agreement with the recorded data. All simulated events have been processed through the DØ detector simulation `dØgstar` [38] based on the detailed detector material

Process	Generator	# events (μ)	$\sigma(\times\text{BR})[\text{pb}]$
$\text{HW}^\pm \rightarrow \text{b}\bar{\text{b}} + \ell\nu$	$m_{\text{H}} = 105 \text{ GeV}$	32.5k	0.0222
	$m_{\text{H}} = 115 \text{ GeV}$	47.8k	0.0150
	$m_{\text{H}} = 125 \text{ GeV}$	52.1k	0.0093
	$m_{\text{H}} = 135 \text{ GeV}$	32.8k	0.0045
	$m_{\text{H}} = 145 \text{ GeV}$	47.3k	0.0022
$\text{HW}^\pm \rightarrow \text{b}\bar{\text{b}} + \tau\nu, \tau \rightarrow \ell$	$m_{\text{H}} = 105 \text{ GeV}$	30.3k	0.0039
	$m_{\text{H}} = 115 \text{ GeV}$	46.7k	0.0026
	$m_{\text{H}} = 125 \text{ GeV}$	46.8k	0.0016
	$m_{\text{H}} = 135 \text{ GeV}$	48.0k	0.00078
	$m_{\text{H}} = 145 \text{ GeV}$	45.8k	0.00038

Table 4.1: List of simulated signal processes, along with the generator that was used for production, number of events and cross section times branching ratio. ℓ is to be understood as either e or μ .

simulation package `GEANT` [39], the electronics simulation `d0sim`, the reconstruction software `d0reco`.

A good determination of key efficiencies and resolutions for both simulated and recorded data is crucial. The physics and detector simulation is constantly checked by comparing real data with Monte Carlo data and determining correction factors in case the agreement is not satisfactory.

4.2.1 Monte Carlo Samples

Several Monte Carlo samples were used for this analysis. The samples used for the W^\pmH search described in Chapter 6 are described here. The samples used to determine the performance of the neural network-based tagging algorithm in Chapter 5 are described there.

Several Monte Carlo samples were generated for the WH analysis. The WH signal samples and the di-boson background samples have been produced with the `PYTHIA` event generator [40] making use of the leading order parton distribution functions `CTEQ6L` [41]. The number of generated events and their corresponding cross sections are given in Tables 4.1 and 4.2. The cross sections calculated at next-to-leading order are scaled to NNLO using a “K-factor” [42].

The $\text{t}\bar{\text{t}}$ and $\text{W} + \text{jets}$ events have been generated with the matrix element generator `ALPGEN` [43], cf Tables 4.3 and 4.4, interfaced to `PYTHIA` for subsequent parton shower and hadronisation. The single-top sample was produced using `CompHep` [44] as shown in Table 4.3.

The cross sections used in the analysis are calculated at NLO (NNLO for $\text{t}\bar{\text{t}}$). The WH limit is however compared to the NNLO prediction in Chapter 7 (the NNLO cross section is ~ 0.95 times the NLO cross section.) The `ALPGEN` samples have been produced in exclusive bins of “light” (i.e. gluons or u,d,s quarks) parton multiplicity except for the “highest” bin obtained in an inclusive way, i.e. it includes higher multiplicities as well. `ALPGEN` use the matching prescription as described in [45].

All `ALPGEN` $\text{W} + \text{jets}$, $\text{W} + \text{b}\bar{\text{b}}$ and $\text{W} + \text{c}\bar{\text{c}}$ have undergone a process of heavy-flavour (HF)

Process	Generator	# events	$\sigma \times \text{K-factor} \times \text{BR}[\text{pb}]$
$W^+W^- \rightarrow e\nu_e jj$	PYTHIA	87k	$2.04 \times 1.31 \times 0.39$
$W^+W^- \rightarrow \mu\nu_\mu jj$	PYTHIA	107k	$2.04 \times 1.31 \times 0.39$
$WZ \rightarrow e\nu_e jj$	PYTHIA	96k	$0.61 \times 1.35 \times 0.39$
$WZ \rightarrow \mu\nu_\mu jj$	PYTHIA	47k	$0.61 \times 1.35 \times 0.39$
$WZ \rightarrow jj e^+ e^-$	PYTHIA	92k	$0.18 \times 1.35 \times 0.44$
$WZ \rightarrow jj \mu^+ \mu^-$	PYTHIA	96k	$0.18 \times 1.35 \times 0.44$
ZZ inclusive	PYTHIA	95k	1.43

Table 4.2: List of simulated di-boson processes, along with the generator that was used for production, number of events and cross section times branching ratio for the leptonic decays. The K-factor is used to scale the NLO cross section to the NNLO cross section.

Process	Generator	# events	$K \times (\sigma \times \text{BR})[\text{pb}]$
$t\bar{t} \rightarrow b\bar{b} + \ell^+ \nu \ell'^- \bar{\nu}_{\ell'}$	+ 0 light parton	224k	1.39×0.3241
	+ 1 light parton	96k	1.39×0.1507
	+ 2 light partons	50k	1.39×0.1035
$t\bar{t} \rightarrow b\bar{b} + 2j + \ell\nu$	+ 0 light parton	283k	1.41×1.2840
	+ 1 light parton	98k	1.41×0.6249
	+ 2 light partons	92k	1.41×0.3978
Single-top s -channel ($tb \rightarrow \ell\nu b\bar{b}$)	CompHEP + PYTHIA	291k	0.0978
Single-top t -channel ($tqb \rightarrow \ell\nu bqb$)	CompHEP + PYTHIA	385k	0.22

Table 4.3: List of simulated $t\bar{t}$ and single-top processes, along with the generator that was used for production, number of events and K-factor times cross section times branching ratio. The K-factor for $t\bar{t}$ scales the $t\bar{t}$ cross section to 6.8 pb. No K-factor is given for single-top since the cross section given is already at NLO. $\ell = e, \tau$ or μ .

skimming; that is, additional heavy-flavoured partons generated by PYTHIA have been removed so as not to bias the sample. Z+jets samples used in this analysis have not been HF-skimmed. W+jets and $t\bar{t}$ samples include all three lepton flavours. Other samples, such as Z+HF and single-top, have been produced in bins of lepton flavour; they have been grouped in the tables for enhanced readability.

4.2.2 Shifting, smearing and removing simulated jets - JSSR

The purpose of the JSSR procedure is to simulate in Monte Carlo the biases stemming from jet reconstruction inefficiency, resolution and possible difference in Data-Monte Carlo Jet Energy Scale and resolution. In a nutshell, MC jets are oversmeared using $\sigma_{\text{smear}}^2 = \sigma_{\text{Data}}^2 - \sigma_{\text{MC}}^2$. Then we remove jets using resolution and reconstruction efficiencies from Data. JSSR is only applied to Monte Carlo [46].

Process	Generator	# events	$\sigma(\times\text{BR})[\text{pb}]$
$W^\pm jj \rightarrow \ell\nu jj$	+ 0 light parton	2.3M	4574.4
	+ 1 light parton	2.8M	1273.9
	+ 2 light partons	1.6M	298.6
	+ 3 light partons	790k	70.6
	+ 4 light partons	780k	15.8
	+ 5 light partons	58k	11.3
$W^\pm b\bar{b} \rightarrow \ell\nu b\bar{b}$	+ 0 light parton	740k	19.2
	+ 1 light parton	261k	7.9
	+ 2 light partons	171k	2.6
	+ 3 light partons	164k	1.7
$W^\pm c\bar{c} \rightarrow \ell\nu c\bar{c}$	+ 0 light parton	482k	71.1
	+ 1 light parton	336k	29.9
	+ 2 light partons	333k	10.3
	+ 3 light partons	372k	18.4
$Zjj \rightarrow e^+e^-jj$	+ 0 light parton	1.0M	139.2
	+ 1 light parton	187k	41.8
	+ 2 light partons	93k	10.3
	+ 3 light partons	93k	5.3
$Zjj \rightarrow \mu^+\mu^-jj$	+ 0 light parton	839k	139.5
	+ 1 light parton	209k	41.6
	+ 2 light partons	104k	10.3
	+ 3 light partons	104k	5.3
$Zjj \rightarrow \tau^+\tau^-jj$	+ 0 light parton	795k	139.4
	+ 1 light parton	209k	41.7
	+ 2 light partons	97k	10.3
	+ 3 light partons	104k	5.3
$Zb\bar{b} \rightarrow \ell^+\ell^-b\bar{b}$	+ 0 light parton	604k	0.97
	+ 1 light parton	271k	0.36
	+ 2 light partons	144k	0.21
$Zc\bar{c} \rightarrow \ell^+\ell^-c\bar{c}$	+ 0 light parton	152k	3.0
	+ 1 light parton	143k	1.06
	+ 2 light partons	172k	0.6

Table 4.4: List of simulated W+jets and Z+jets and single-top processes, along with the generator that was used for production, number of events and cross section times branching ratio (the light partons are requested to have $p_T > 8$ GeV and $|\eta| < 5$). The LO cross sections given in the table are corrected by the following K-factors correcting the cross section to the NLO value: 1.35 for $W^\pm jj$, Zjj , and 1.75 for $W^\pm c\bar{c}$, $b\bar{b}$, $Zc\bar{c}$, $b\bar{b}$. ALPGEN samples have been produced in bins of light parton multiplicity. Bins must be understood as exclusive except the last bin, which is inclusive. ℓ must be understood as lepton, i.e. either e , τ or μ .

4.3 The Trigger

Triggering is a very important aspect of physics at hadron colliders. The vast majority of all collisions at hadron colliders result in what are considered to be “background” events.

	Rate	Latency
Collisions	1.7 MHz	n/a
L1	1.6 kHz	3.6 μ s
L2	800 Hz	\sim 100 μ s
L3	50 Hz	\sim 150 ms

Table 4.5: Approximate trigger rates and latency for the three trigger levels.

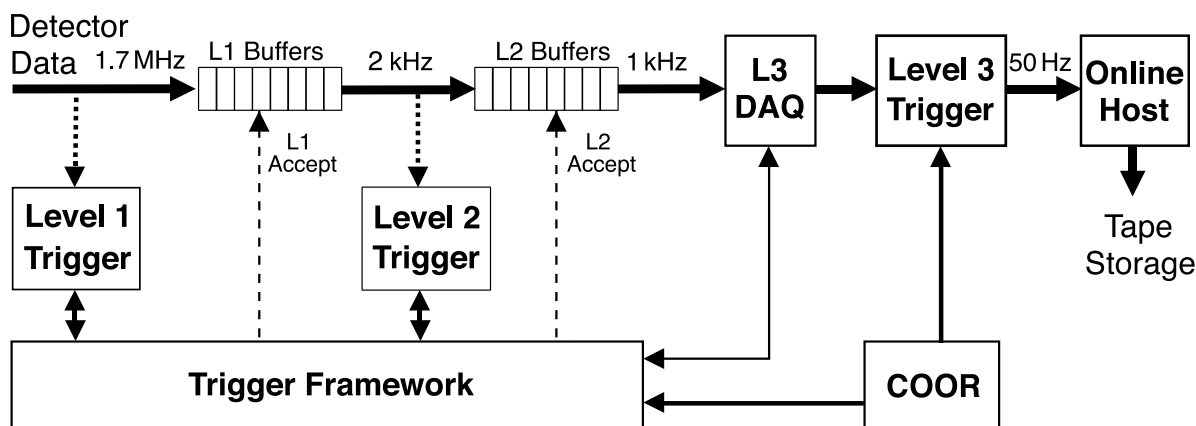


Figure 4.1: The DØ trigger and data acquisition systems. The rates are the maximum design rates.

The production cross section for background processes is several orders of magnitude larger than that for the signal process. The trigger system is an online event filter that is designed to select and save only potentially interesting signal events. By triggering the data readout, the number of signal events can be increased with respect to the background. The trigger decision is based on inputs from all subdetectors and must be made within the short time defined by the size of the readout buffers.

The DØ trigger is divided into three layers referred to as Level 1 (L1), Level 2 (L2) and Level 3 (L3). Each level has increasingly sophisticated event reconstruction, and an event will proceed through each of the trigger levels depending on conditions being met. All front-end systems are pipelined and store information until the Level 1 trigger decision is made. The trigger framework issues Level 1 accept and reject decisions for every bunch-crossing after collecting the trigger information from all participating trigger subsystems. The L1 latency, i.e. the time between the original bunch-crossing and the trigger decision, is 3.6 μ s. The trigger rate and the latency at each level are shown in Table 4.5. An overview of the DØ trigger and data acquisition systems is shown in Fig. 4.1.

Level 1

The L1 trigger is based entirely on hardware and firmware (i.e. programmable hardware). It examines every bunch crossing and decides if the event is worth looking at in more detail

by the second and third level triggers. It uses a reduced form of the detector readout, using only information from the luminosity system, the central fibre tracker, the calorimeter and the muon chambers.

The calorimeter trigger decision is based upon the transverse energy (E_T) sum in $\Delta\eta \times \Delta\phi \sim 0.2 \times 0.2$ towers of calorimeter cells called “trigger towers”. The trigger towers are summed to give a total E_T for the calorimeter, and the number of trigger towers with an E_T deposit above a given threshold can be calculated and used to trigger events. This is done both for the calorimeter as a whole and for the EM layers separately.

The Level 1 central track trigger (L1CTT) reconstructs the trajectories of charged particles using fast information provided by the scintillator-based central fibre tracker and preshower detector. The Level 1 triggers require tracks with transverse momenta above certain thresholds (1.5, 3, 5 and 10 GeV). A list of up to 480 Level 1 tracks per bunch crossing is stored for later L2/L3 readout and are used as seeds for other trigger systems.

The muon trigger looks for patterns consistent with muons using the scintillator hits and timing information as well as wire hits.

If the Level 1 trigger issues an accept, the event is passed into a buffer for evaluation by the L2 trigger.

Level 2

The L2 trigger is firmware based and uses the results derived in the L1 trigger, with the addition of the SMT data. The second trigger stage not only triggers on individual detector objects like tracks and detector towers, but also on correlations between these objects. To this end, the L2 preprocessors collect data from the L1 trigger system and from each sub-detector and combine the data into physics objects (muons, jets, charged particles, and EM objects like photons) which are then passed onto a global processor. The global processor creates global physics objects from one or more of the sub-detector physics objects, e.g. matching a track to an EM object to make an electron object, and allows event wide correlations between all L2 objects to be tested.

Each L1 trigger bit corresponds to one or more L2 triggers. If a L1 trigger bit is set, each of the corresponding L2 triggers is processed. This involves generating all the physics objects required by the trigger, and checking them against the thresholds defined for that trigger. Based on L1 decisions and additional script-controlled L2 trigger criteria the global L2 processor selects events, which are then tagged for full readout and sent to L3 for further analysis.

Level 3

The Level 3 trigger is a fully programmable software based event filter and reconstructs events based upon the full detector readout on a farm of standard PCs. The L3 trigger performs a fast event reconstruction, so that its decision to reject or accept a given event is based on the complete physics objects and relationships between objects (e.g. the angle between two objects, invariant masses etc.).

A set of parameters is defined at runtime to control the reconstruction algorithm’s behaviour. A limited number of parameter sets is defined for each tool; these are the only

instances of the tool that triggers can call.

Each L2 trigger bit corresponds to one or more L3 triggers. If a L2 trigger bit is set, the corresponding L3 triggers are processed. Each L3 trigger consists of a filter script which contains one or more filters, and each filter defines a condition. For a trigger to pass an event, the condition of each of the filters in the filter script has to be met. There are two kinds of filters:

- Physics object filters, which compare the value for a physics objects to predefined thresholds;
- Relational filters, which execute other filters and combine the results.

If an event passes a trigger, the event is written to tape for offline processing. The collection of all the filter scripts, reconstruction parameter sets and trigger criteria is referred to as a “trigger list”.

The L3 data acquisition system (L3DAQ) receives fully digitised data from up to 63 single board computers (SBCs), housed in the VME crates which are connected to the various subdetectors. The Routing Master (RM) specifies routing instructions, which direct the SBCs whether and to which L3 trigger farm node the data, typically 1 to 20 kB, is to be send. The event fragments are built into complete events on the L3 farm nodes. Events that pass the L3 trigger criteria are sent via a separate network to tape storage devices. The typical size of unreconstructed “raw” events is 250 kB. The L2 accept rate of 1 kHz is reduced to 50 Hz, which is mainly limited by tape storage. L3 software algorithms (tools and filters) running on the L3 farm nodes reconstruct the physics objects, calculate relations between them and perform trigger decisions, specified by the triggerlist. To limit the rate at the different trigger levels in accordance with the trigger and DAQ capabilities, specific triggers can be prescaled with a prescale factor N , such that only one out of every N triggers is accepted. The triggerlist and more importantly the trigger prescales can be changed by the DAQ shifter to account for changes in the instantaneous luminosity. It contains thresholds and parameters, such as jet cone radius, and trigger prescales and is downloaded to each farm node via the L3 supervisor node.

4.3.1 Muon triggers

The data used for the Higgs search in this thesis were acquired with muon triggers. At Level 1, muon triggers use the scintillator and wire hits. At Level 2, basic cuts on the muon quality can be made. At Level 3, the local muon information is refined and combined with a central track.

The L1, L2 and L3 requirements together form a complete muon trigger. The complete trigger is referenced by a name which indicates the trigger requirements. Typically, the first part of the name indicates the L1 requirement, the middle part the L2 requirement and the last part the L3 requirement.

Epochs	Single Muon Triggers
v8.00 - v10.3	MU_W_L2M5_TRK10, MU_W_L2M0_TRK3, MUW_W_L2M5_TRK10, MU_W_L2M0_TRK10
v10.3 - v13.0	MU_W_L2M3_TRK10, MUW_W_L2M3_TRK10
v13.0 - v14.0	MUH1_TK12, MUH1_TK10, MUH1_LM15, MUH1_TK12_TLM12, MUH2_LM15, MUH2_LM10_TK12, MUH2_LM6_TK12, MUH2_LM3_TK12, MUH3_LM15, MU_W_A_L2M3_TRK10, MUH3_LM6_TK12, MUH3_LM10_TK12, MUH3_LM3_TK10, MUH4_LM15, MUH4_TK10, MUH5_LM15, MUH6_LM15, MUH6_TK10, MUH7_TK10, MUH7_TK12, MUH7_LM15
v14.0 - v15.0	MUH1_ILM15, MUH1_ITLM10, MUH1_TK12_TLM12, MUH5_LM15, MUH6_LM15, MUH6_TK12_TLM12, MUH7_TK12, MUH7_LM15, MUH8_TK12_TLM12, MUH8_ILM15, MUH8_ITLM10

Table 4.6: List of all the single muon triggers (Run IIa) that have been considered for the OR (split in four main trigger list epochs).

“OR” Combination of triggers

The single muon triggers used for the Higgs search are combined as a logical “OR” of the individual triggers listed in Table 4.6. The efficiencies for the individual trigger terms are determined using a “tag and probe” method (see Section 4.4.1). The trigger efficiency for the “OR” trigger is determined from the efficiencies of the individual trigger terms, taking into account the prescales [47]. The trigger efficiency is determined separately for four running periods in Run IIa (see Table 4.6).

A consequence of including the prescale inefficiencies is the introduction of correlations between the tag muon and the probe muon. This leads to an overestimate of the efficiency of the OR trigger. To cancel this effect, the tag muon is required to only have fired unprescaled (single muon) triggers.

The efficiency gain of the OR trigger compared to the single muon trigger efficiencies is shown in Fig. 4.2. The plot on the left hand side shows the increase in acceptance, especially in the forward region, thanks to the contribution of MUH5_LM15. The combination of MUH1_TK12_TLM12 and MUH1_LM15 also contributes to the gain, as the former requires L3 muon, tracking and central matching criteria and the latter requires a tighter L3 muon.

The right hand side plot shows the influence of the prescales. At low luminosity, most triggers are unprescaled, and thus offer the greatest contribution to the OR efficiency. This behaviour is confirmed when not requiring the L1 requirements to have fired (dashed lines), i.e. by releasing the requirement that the tag muon fired unprescaled triggers only. In this case, no prescales are taken into account and the efficiencies do not fall at high luminosity.

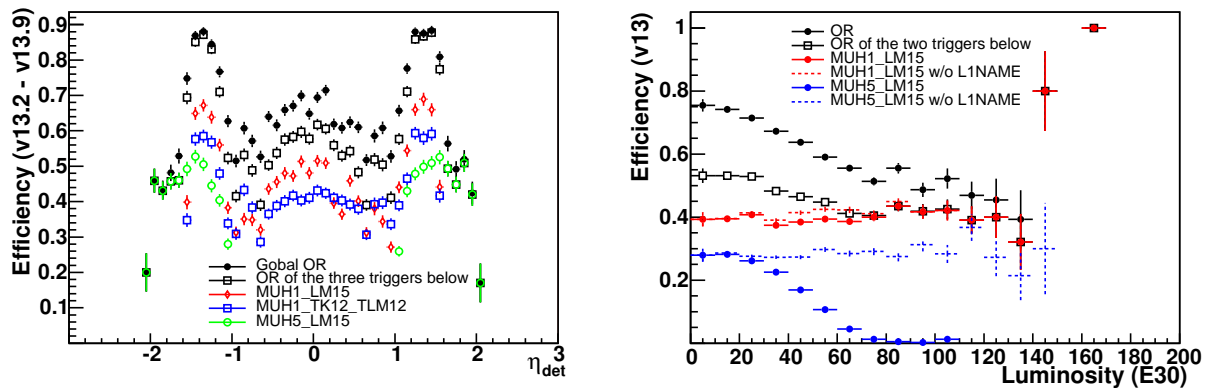


Figure 4.2: Dependence of the single muon “OR” trigger as a function of η^{det} (left) and instantaneous luminosity (right), compared to several individual single muon triggers. Only results from the v13 trigger epoch are shown.

4.4 Object identification

After an event has been passed by the trigger system and written to tape, it will undergo a full offline event reconstruction. The basic reconstructed data (tracks, calorimeter clusters, etc.) are used to reconstruct physics objects, such as muons, parton jets etc. In this section, the reconstruction algorithms used for the identification of muons, jets and other objects are described in more detail.

4.4.1 Muons

In this analysis some of the most important objects are the muons, of which one is required in the final state. The efficiencies to identify and reconstruct muons will be presented in detail, as well as those of some basic muon properties, isolations and quality.

Identification

Muons are identified based on hits in the central or forward muon drift chambers and scintillators. Track segments are first fitted using the drift chamber hits in each separate layer. In a second step these segments are interpolated in between two or all three layers of the muon system, to form a local muon candidate. While the scintillator hits are primarily used for triggering purposes (especially at L1), the timing information also provides an excellent possibility for the rejection of out-of-time background, like cosmic muons. Additionally, a matching inner track, measured with the inner tracker, or a matching energy deposit in the calorimeter provide possibilities to define effective isolation criteria for muons.

Quality

The muon ID criteria are given in [48]. Muons can be designated “tight”, “medium” or “loose”. Only “medium” and “loose” criteria are used in this analysis. A “medium” muon candidate is required to satisfy the following criteria:

- at least two A layer wire hits and at least one A layer scintillator hit;
- at least two BC layer wire hits;
- at least one BC layer scintillator hit (except for central muons with less than four BC wire hits).

If the muon candidate has only wire and scintillator hits in the BC layer, it can still be “medium” if it is located in the bottom part of the detector (octant 5 and 6 with $|\eta^{\text{detector}}| < 1.6$) and has a matched central track. If it has hits only in the A layer, it can still be “medium” if it is located in the bottom part of the detector and has a matched central track, and if it has a low probability to reach the BC layer [48].

A “loose” muon candidate without a central track match is required to satisfy the same criteria as a “medium” muon, but one of the tests is allowed to fail. The A level wire and scintillator requirement count as one test, and one scintillator hit is always required. A “loose” muon candidate with a central track has to satisfy the following requirements:

- at least one BC layer scintillator hit and at least two BC layer wire hits; or
- at least one scintillator hit and at least two A layer wire hits.

In addition to these requirements, the scintillator hit times must be within 10 ns of the beam crossing to reject cosmic muon background.

Efficiency

The muon efficiencies are estimated using a “tag and probe” method [49]. $Z/\gamma^* \rightarrow \mu^+\mu^-$ events are selected from data, since the production and decay of Z bosons is a well understood and measured process. In addition, the signature of such events is very clean and only little background from other processes is expected, which makes this type of events very suitable for efficiency studies, giving us a meaningful comparison of simulated MC data and real data.

The “tag and probe” method requires two muons in the event. The “tag” muon should satisfy tight selection criteria. Efficiencies can then be determined by “probing” the other muon for the quantity of interest, e.g. muon isolation or the existence of a track matching the probe muon. If the second muon also satisfies the “tag” criteria, the roles of the two muons are reversed and the process is repeated. The efficiency is then given by the number of successful “probes” and the number of “tags”:

$$\epsilon = \frac{2 \times N_{tag+tag} + N_{tag+probe}}{2 \times N_{tag+tag} + N_{tag+pass} + N_{tag+fail}}, \quad (4.1)$$

with *tag*, *probe* and *fail*, respectively for a muon satisfying either the *tag* criteria, or the *probe* criteria, or failing both sets of criteria. The distinction between *tag* and *probe* is due

	central $ \eta \leq 1.6$	forward $ \eta > 1.6$
scale S	$0.9910^{+0.0026}_{-0.0026}$	$0.9962^{+0.0051}_{-0.0077}$
width σ	$0.0025^{+0.0001}_{-0.0002}$	$0.0043^{+0.0001}_{-0.0006}$

Table 4.7: Muon momentum smearing coefficients [50].

to the fact that the requirements for the *probe* muon are usually softer than the criteria used to *tag* a muon. In case the *tag* and *probe* criteria are the same, the terms (*tag* + *probe*) have to be omitted from the equation written above.

The efficiency is measured separately for data and for a $Z/\gamma^* \rightarrow \mu^+\mu^-$ Monte Carlo sample. In case of the collision data, another difficulty is found when determining efficiencies: any efficiency could be biased, if the event had been recorded due to exactly the property under study. For example, if events were selected using a special trigger for isolated muons, the measurement would be biased towards higher efficiencies because the probe muon could have fired this trigger. Exactly the opposite effect, i.e. a bias towards lower efficiencies, would be the result if the probe muon is required *not* to have fired this trigger. There are two ways of avoiding this bias: by using only events selected by a completely independent trigger, or by matching the *tag* muon to the trigger requirement. In case of track matching efficiency, which shows how well a local muon can be matched to an inner track, the second method is used. For this efficiency measurement the tag muon can be matched to a L3 track object.

Muon momentum smearing

Since the transverse momentum resolution of the muon and central tracking system is worse than that expected from MC simulations, the p_T of each muon candidate in MC events is smeared to force better agreement. The smearing corresponds to an artificial broadening of the p_T distribution in $Z/\gamma^* \rightarrow \mu^+\mu^-$ MC events until the distribution matches that measured in reconstructed $Z/\gamma^* \rightarrow \mu^+\mu^-$ collision data. Assuming the inverse momentum follows a Gaussian distribution, this is achieved by applying a Gaussian function to the p_T of each muon candidate:

$$\frac{1}{p_T} = \frac{1}{p'_T \times S} + \frac{1}{\sqrt{2\pi}\sigma} \cdot e^{-\frac{1}{p_T} - \frac{1}{p'_T}} \frac{1}{2\sigma^2}, \quad (4.2)$$

where S is a scale factor to the unsmeared muon momentum p'_T and the second term is a Gaussian distribution with mean 0 and width σ . The values of S and σ are given in Table 4.7 for the central and the forward muon system. For more details see [50].

The uncertainties on S and σ as given in Table 4.7 are considered as systematic error sources.

4.4.2 Jets

Jet finding algorithm

A jet is defined as a cluster of particles or energy deposits, originating from the hadronisation and decay of particles produced in a collision.

Jets are reconstructed in DØ using the so-called “Improved Legacy Cone Algorithm” (ILCA). This Run II cone algorithm has three steps: clustering, addition of midpoints, and merging and splitting [51]. The algorithm can be carried out using either (Monte Carlo) particles, leading to a “particle jet”, or using energy depositions in the detector, leading to a “detector jet”.

The jet is enclosed by a cone with radius R in the $\eta \times \phi$ plane. The radius is invariant under boosts along the z -axis. The cone axis coincides with the jet direction as defined by the $E_T = E \times \cos \theta$ weighted centroid of the particles within the cone¹.

The jet reconstruction algorithm starts with a number of “seeds” corresponding to the most energetic particles in the event. Calorimeter towers exceeding a threshold energy of typically a few hundred MeV are used. A calorimeter tower consists of all calorimeter cells with the same (η, ϕ) coordinate and covers an area in the $\eta - \phi$ plane of $\Delta\eta \times \Delta\phi = 0.1 \times 0.1$ (except in the third layer of the EM calorimeter, where the segmentation is 0.05×0.05 in the not too-forward region). The E_T -weighted centroids are calculated for the particles in each seed cone and the centroids are used as centres for new cones. This process is iterated until the cone axis matches the E_T -weighted centre. The *stable cones* are called *proto-jets*.

Ideally, the trajectories of all particles originating from the original parton created in the collision lie in the area defined by the cone size, and the reconstructed jet energy corresponds to the original parton’s energy. However, in practise many problems have to be solved by the jet reconstruction algorithm. The jet algorithm needs to find the same solutions independent of boosts in the longitudinal direction, particularly important at hadron colliders. There should not be any dependence on the detector performance, detector region, cell type, or cell size. The influence of the instantaneous luminosity should be under control and finally a reliable calibration of the kinematic properties of the jet must be found. In particular, the algorithm must be *collinear safe* and *infrared safe*.

Collinear problems can arise when the energy of a particle is shared among several detector towers, or if the jet algorithm is sensitive to the E_T -ordering of the seeds. If the energy of a particle is split among several detector towers (see Fig. 4.3), it might fail to produce a seed for the cone algorithm. If the seeds are treated in order of decreasing energy, a different cone may also be reconstructed if the energy of the most energetic particle is split among several towers and a different particle serves as the new seed (see Fig. 4.4). Using seed thresholds of $E_T > 1$ GeV, the seed-based jet algorithm at DØ was found to be fully collinear safe for jets with $E_T > 20$ GeV.

Another important requirement is the infrared safety of the algorithm. As illustrated in Fig. 4.5, two clearly separated particles can be merged into one cone if one particle radiates a soft gluon, which serves as a seed. Jet algorithms that only look for seed towers exceeding a minimum amount of energy are not infrared safe.

¹Since the determination of E_T requires the vertex coordinates, track and vertex reconstruction are performed first.

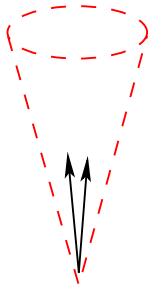


Figure 4.3: Seed collinear sensitivity

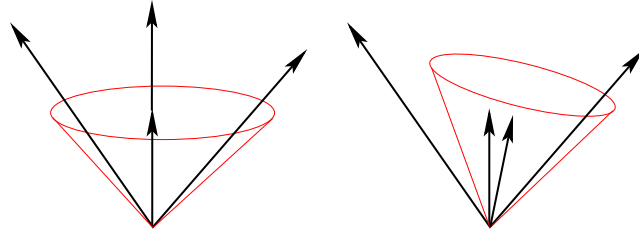


Figure 4.4: E_T ordering sensitivity

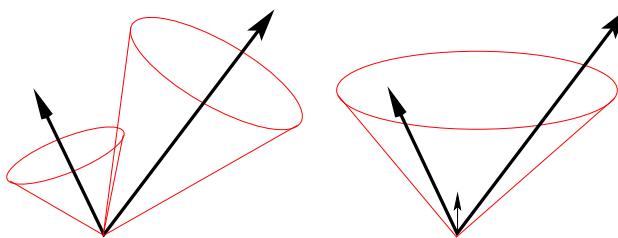


Figure 4.5: Infrared sensitivity

The problems described above arise from seed based algorithms. To accomplish an unbiased set of seeds, each calorimeter tower should be considered to be a seed. For the DØ detector, with a fiducial volume of $-4 \leq \eta \leq 4$ and $0 \leq \phi \leq 2\pi$, and a segmentation of 0.1×0.1 , this translates into the order of $5 \cdot 10^3$ seed towers. The efficiency to detect physically meaningful jets is maximal for seedless algorithms, but the necessary computing effort is too large.

Seed-based cone algorithms are more efficient, by considering only towers that pass a seed cut

$$E_T^{\text{tower}} > E_T^{\text{seed}} \quad (4.3)$$

as starting points for the initial jet cones. The seedless algorithm can be approximated by the addition of “midpoints”. The *infrared* sensitivity to soft radiation as shown in Fig. 4.5 is essentially removed by adding a starting point for clustering at the position given by the midpoint between two proto-jets for each pair of proto-jets separated by less than

$$\Delta R < 2.0 \times R_{\text{cone}}. \quad (4.4)$$

The last step in jet finding is the recombination or splitting of the proto-jets. Two independent proto-jets can share one or more calorimeter towers (particles) and need to be split, or two proto-jets belong to the same source and need to be recombined. The proto-jets, in descending order of transverse energy E_T , are tested for calorimeter towers that are shared with other proto-jets. Proto-jets sharing one or more towers are merged if the shared E_T is larger than a given fraction f of the total E_T of the lowest-energy jet; if the shared E_T

cone size $R = \sqrt{\Delta\eta + \Delta\phi}$	0.5
seed threshold p_T	1.0 GeV
split/merge fraction f	0.5
jet threshold E_T	8 GeV

Table 4.8: DØ Run II cone jet specifications

is smaller, the shared towers are assigned to the nearest proto-jet. In both cases the cones need to be recalculated as described above, and will be added to the list of proto-jets. When a proto-jets shares no more towers with other proto-jets, it is named “final” and is removed from the list. This procedure is iterated until no proto-jets are left. Once all jets are final, the jets with E_T less than the jet E_T threshold are discarded.

In Table 4.8 the cone algorithm specifications as used for this analysis are listed.

Noise reduction

To reduce jets originating from calorimeter noise, the T42 algorithm (T-four-two = threshold $4 - 2\sigma$, pronounced *tea-for-two*) [52–54] is applied. Calorimeter cells with less than 4σ energy above threshold, or with less than 2σ , if an adjacent cell has at least 4σ energy above threshold, are rejected. Between 30% and 60% of the cells in an event are rejected by the T42 algorithm. In the main part of the calorimeter, $|\eta| < 3.2$, the number of rejected cells corresponds to the number of expected noise cells, while in the very forward calorimeter region more cells are rejected due to pile-up effects, which accumulate close to the beampipe. The T42 algorithm is applied before jet clustering.

Jet identification

Further quality criteria are posed onto the found jets to remove fake jets, which were not created by hadronic particles, but by calorimeter noise or by electromagnetic particles created in the collision like electrons, photons or taus:

- The number of calorimeter towers containing 90% of a jet’s energy ($n90$) has to be larger than one, to reduce noise jets resulting from a single hot cell;
- Jets clustered from hot cells are removed by requiring the ratio of the highest to next-to-highest E_T cell (“HotF”) to be less than 10.
- To reject electromagnetic and noise-like jets, the electromagnetic fraction (EMF) of the energy deposition in the calorimeter is required to be $5\% < EMF < 95\%$.
- The coarse hadronic fraction (CHF) of the energy deposition in the coarse hadronic layers compared to all layers of the calorimeter is required to be less than 40%, because of the higher noise level in the coarse hadronic part of the calorimeter.
- To reduce the noise influence of the calorimeter readout, a L1 trigger confirmation is required, since the L1 trigger uses a different readout chain. Jets have to pass the

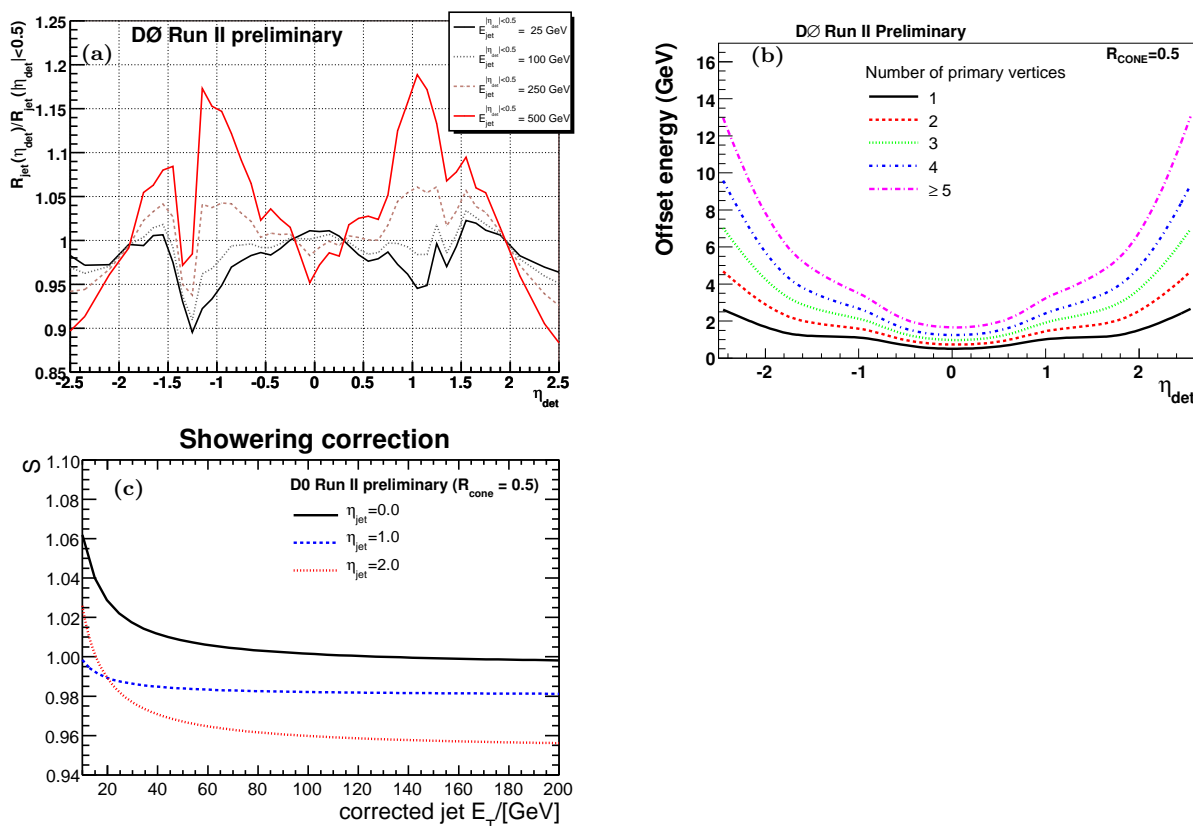


Figure 4.6: (a) Relative response correction in data. (b) Offset energy for different primary vertex multiplicities, as a function of jet η . (c) Showering correction for jets in data as a function of corrected jet transverse energy.

following cut:

$$\frac{L1SET}{E_T^{\text{reco}} \times (1 - CHF)} > \text{cut}, \quad (4.5)$$

where $L1SET$ is the scalar sum of the E_T of all trigger towers within the jet cone. The value of the cut is 0.4 for the Central Calorimeter, 0.2 for the InterCryostat Detector and 0.4 for the Endcap Calorimeters.

Jet Energy Scale

In the previous sections the ILCA cone algorithm has been discussed, which finds jets in the calorimeter. The measured jet energy E_{meas} is the sum of the energy contents of all calorimeter cells within a cone of size Δ around the jet axis, above a certain threshold. E_{meas} deviates from the true energy of the initial parton that created the jet and needs calibration. This is provided by the Jet Energy Scale (JES) correction [55]. The jet energy scale correction relating the reconstructed jet energy E_{meas} to the original parton energy

E_{corr} is parameterised by the following equation:

$$E_{\text{corr}} = \frac{E_{\text{meas}} - O}{R \times S}, \quad (4.6)$$

where R is the calorimeter response, O is the offset energy and S is the showering correction.

The *calorimeter response* can be distorted for different partons, different calorimeter regions, e.g. a strong η -dependence, inhomogeneous instrumentation, dead material and a non-linear response to the particle energies. R is determined by the examination of QCD Compton events, i.e. $qg \rightarrow q\gamma$. The purely electromagnetic energy of the photon can be reconstructed with high precision, due to the accurate EM energy scale calibration, for example on the $Z \rightarrow e^+e^-$ peak. The photon energy is used as an estimator for the parton energy, if q and γ are back to back. This is the largest relative correction and can be as large as 30% (see Fig. 4.6(a)).

The *energy offset* corresponds to additional energy in the calorimeter cells within the jet cone, due to underlying events (beam remnants and multiple parton interactions), energy pile-up or noise from the electronics or the uranium absorber material. This offset has to be subtracted from the reconstructed energy. O is determined in “minimum bias” events, which are triggered by the luminosity detectors but have no other trigger requirements. The energy offset depends on η as well as on the number of primary vertices and is typically of the order of a few GeV (see Fig. 4.6(b)).

The *showering corrections* are necessary because some amount of the original energy might escape the cone. For example, low energetic, charged hadrons can curl out of the jet cone due to the magnetic field. S is measured from jet energy profiles and is typically smaller than 4% for jet momenta larger than 20 GeV (see Fig. 4.6(c)).

The JES correction and its uncertainty depend on the initial parton p_T as well as on η . Since the jet energies in the data are not correctly described by the Monte Carlo, a different correction is applied on simulated events.

The total systematic uncertainty assigned for the JES correction arises from the statistical and the systematic error of both data and Monte Carlo added in quadrature:

$$\sigma_{\text{JES}} = \sqrt{\sigma_{\text{stat,data}}^2 + \sigma_{\text{syst,data}}^2 + \sigma_{\text{stat,MC}}^2 + \sigma_{\text{syst,MC}}^2}. \quad (4.7)$$

The JES correction depends on the flavor of the initial parton. In particular, b -quark jets that decay semileptonically and that are tagged by a muon within the jet cone are corrected with twice the muon energy (as the neutrino energy is approximated to be equal to the muon’s).

Jet Energy Resolution

The jet energy resolution was studied in a di-jet event sample, taken with the jet triggers JT_8TT, JT_15TT, JT_25TT_NG, JT_45TT, JT_65TT, JT_95TT and JT_125TT. Only events which pass these jet triggers are used.

Both jets were required to pass the standard jet ID cuts, as discussed previously in Sec. 4.4.2. Both jets are required to be back-to-back; $|\Delta\phi - \pi| \leq 5$ degrees. The details of this study can be found in [56].

The sample is split into bins of 20 GeV width, in the variable of average momentum of the two jet system $\langle p_T \rangle = \frac{1}{2}(p_T^{\text{jet1}} + p_T^{\text{jet2}})$. This binning was chosen to reduce jet p_T smearing related effects. Then the momentum asymmetry A is calculated:

$$|A| = \frac{|p_T^{\text{jet1}} - p_T^{\text{jet2}}|}{p_T^{\text{jet1}} + p_T^{\text{jet2}}}. \quad (4.8)$$

The jet p_T resolution is directly related to the asymmetry resolution σ_A , which is obtained by a Gaussian fit of the A distribution, with a mean value set to zero.

$$\frac{\sigma_{p_T}}{p_T} = \sqrt{2} \cdot \sigma_A, \quad (4.9)$$

when both jets are in the same rapidity bin. If only one jet is required to be in the rapidity bin and the other is allowed to be in some larger reference region, the jet resolution can be calculated as:

$$\frac{\sigma_{p_T}}{p_T} = \sqrt{4\sigma_A^2 - 2\sigma_{A\text{ref}}^2}, \quad (4.10)$$

where $\sigma_{A\text{ref}}$ is the resolution on the asymmetry for that reference region.

The resolutions are fitted using the following formula also used in Run I:

$$\frac{\sigma_{p_T}}{p_T} = \sqrt{\left(\frac{N}{p_T}\right)^2 + \left(\frac{S}{\sqrt{p_T}}\right)^2 + C^2}, \quad (4.11)$$

where N , S and C are the contributions from noise, statistical sampling fluctuations and calibration errors, respectively.

The jet energy resolution as a function of jet p_T as well as the obtained χ^2 -fit results for the parameters N , S , and C are shown in Fig. 4.7 for different bins in η of width 0.4.

4.4.3 Electrons, Positrons and Photons

Electrons, positrons and photons, which only interact with the detector electromagnetically, can be recognised by the shower pattern in the calorimeter, as they deposit most of their energy in the EM layers. The reconstruction of electron candidates starts with clusters, which are defined as a set of towers in a cone of radius $R = 0.2$ around an initial tower. For electrons and positrons, reconstruction can also start from central tracks. Each EM object must satisfy the following criteria to be considered an electron:

- $EMF > 0.9$;
- Calorimeter isolation $iso = \frac{E_{0.4}^{\text{tot}} - E_{0.2}^{\text{EM}}}{E_{0.2}^{\text{EM}}} < 0.2$, where $E_{0.4}^{\text{tot}}$ is the total energy in the calorimeter within a cone of size $\Delta R = 0.4$ around the cluster axis and $E_{0.2}^{\text{EM}}$ is the energy in a cone of size $\Delta R = 0.2$ in the EM layers of the calorimeter;
- A matching track within $|\eta^{\text{det}}| < 3$;

- A shower shape compatible with an electron, determined by the HMx7 variable and an electron likelihood described below;
- $p_T > 5$ GeV.

The HMx7 variable defines the longitudinal and lateral shape of the shower [57]. It is the inverse of a covariance matrix of seven correlated variables, of which the HMx7 variable forms a kind of χ^2 test in which the measured shape of a candidate shower is compared to MC simulations. The electron likelihood used to identify the EM objects is described in [58]. It uses five variables describing the isolation and shape of the EM object in the calorimeter:

- N_{tracks} in a $\Delta R = 0.05$ cone around the cluster axis;
- $\sum p_T^{\text{track}}$ between $\Delta R = 0.05$ and $\Delta R = 0.04$;
- χ_{spatial}^2 , the χ^2 of the spatial match between the track and the cluster;
- f_{iso} , describing the isolation of the cluster in the calorimeter;
- E_T/p_T .

4.4.4 Missing E_T

Information about particles that do not interact with the detector material, like neutrinos, can be found indirectly by calculating the missing transverse energy \cancel{E}_T . The initial longitudinal energy along the beam axis of both interacting partons is unknown at hadron-hadron colliders, so that the z -component of the missing energy cannot be reconstructed. The transverse missing energy \cancel{E}_T is a vector in the transverse plane and is calculated by the negative sum of the transverse energy contents of all calorimeter cells with an energy content of at least 100 MeV above threshold. The transverse energy component of each cell is calculated using the reconstructed vertex z -component to calculate the polar angle. If muons were reconstructed in the muon system, then the reconstructed muon momentum is added to the visible calorimeter energy. Muons are minimum ionising particles and leave only little energy, typically 2 – 3 GeV, in the calorimeter.

Corrections to the jet energy scale, muon momentum smearing, or noise suppression by the T42 algorithm are passed through to the \cancel{E}_T calculation. The systematic uncertainties on JES and muon p_T smearing have a significant effect on the missing E_T and are considered in this analysis.

4.4.5 Tracks

Tracks are reconstructed using a combination of three algorithms. Two track finding algorithms search for potential track candidates, and the third algorithm propagates the track candidates through the full detector.

The first track finding algorithm [59, 60] searches for tracks starting from seeds of 3 SMT or CFT hits. The seed tracks are then propagated through the SMT and CFT detectors and

at each layer a new seed track is created for every hit within the predicted trajectory. The second algorithm [61] uses a histogram based Hough transform [62] to locate tracks.

Both the track finding algorithms are run by default, and all the track candidates from both algorithms are ranked together according to quality criteria. All the tracks which fulfil minimum quality criteria are kept and the tracks are fitted using the third algorithm [63], based on a Kalman Track Fitter, which propagates the candidates through the detector taking account of the variations in the magnetic field, multiple scattering and energy loss [64].

4.4.6 Track jets

Instead of energy deposits or MC particles, jets can also be clustered from tracks. In $D\bar{O}$, track jets are reconstructed by finding tracks within $\Delta R < 0.5$ of a seed track. The tracks must have at least 2 SMT hits, and the seed track should have $p_t > 1$ GeV. A track jet consists of at least two tracks with $p_t > 0.5$ GeV. Requiring a track jet matched to a calorimeter jet helps reduce the number of fake jets due to calorimeter noise. Track jets are also used to define “taggable jets” in Section 5.1.5.

4.4.7 Vertices

Primary vertex

By extrapolating the tracks back to a common point of origin, the production vertex of the particles can be reconstructed. In $D\bar{O}$, the Adaptive Primary Vertex algorithm [65,66] is used to find primary vertices. In the adaptive fitting algorithm, track errors are re-weighted according to their χ^2 contribution to the vertex. This way, tracks origination from a different point like the decay of a B hadron contribute less to the position of the primary vertex. The algorithm can be described as follows:

1. All track candidates are fitted using the Kalman Filter algorithm. Each track is initially assigned a weight of 1. At the following iterations, the weight of a track depends on the distance to the vertex in the previous iteration;
2. For each track the weight is recomputed according to the χ^2 distance to the new fitted vertex;
3. These steps are repeated until the weights converge.

Finally, the primary vertex must be separated from additional vertices due to overlaid minimum-bias events. For this, a probabilistic approach is used [67] that assigns a probability to each vertex to come from a minimum bias interaction, using the fact that tracks from minimum bias interactions have smaller transverse momenta.

Secondary vertices

The decays of long-lived particles (including B hadrons) lead to “secondary vertices” that are removed from the primary vertex. These vertices are found using a 2-pass algorithm [68]. In the first pass, tight criteria are used to find vertices of high quality. A looser second pass is then used to increase the performance. The first and second pass each use a Kalman Fitter algorithm described in [69].

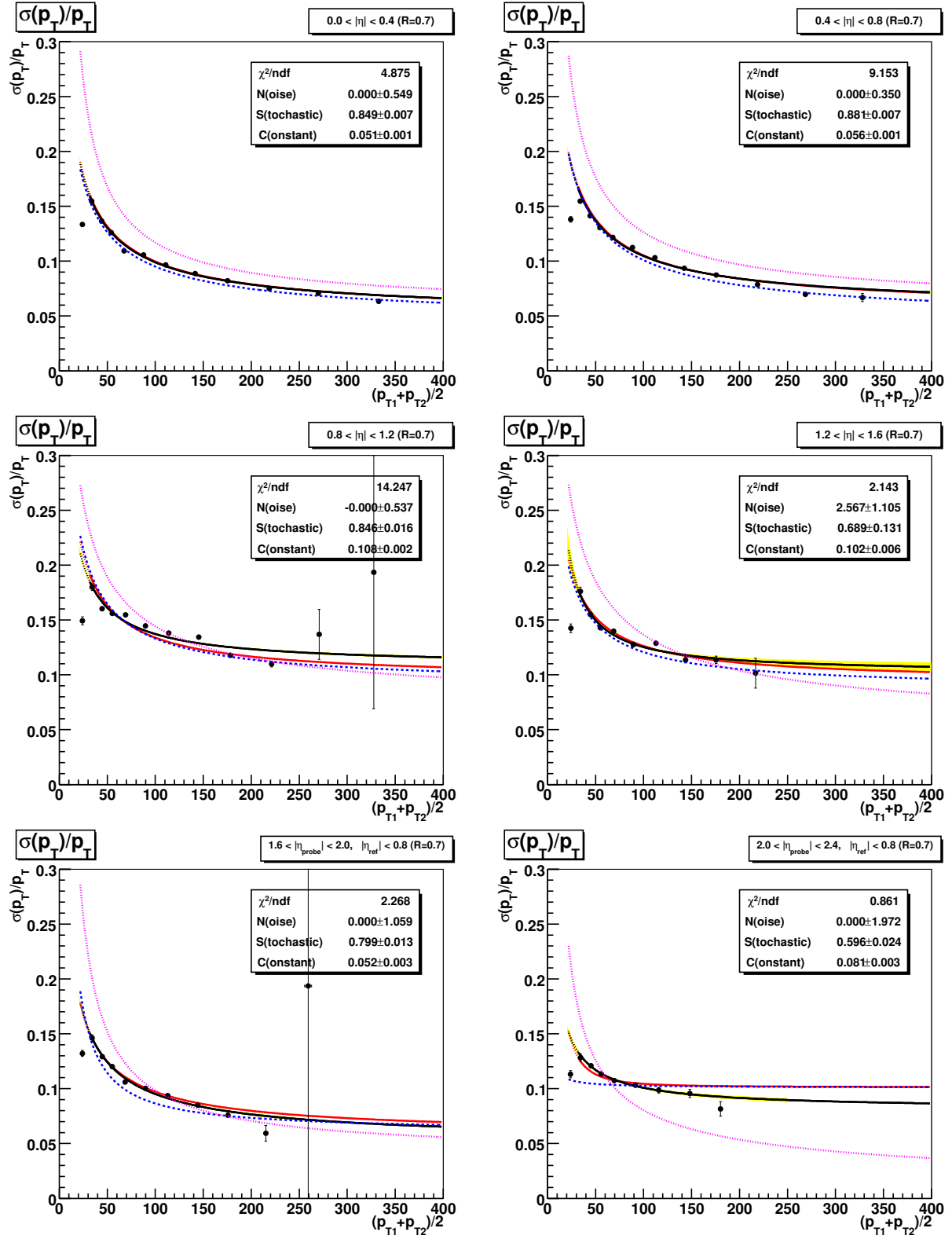


Figure 4.7: Jet resolution for JETCORR v7.1 with T42 in different rapidity bins after soft radiation corrections and particle imbalance corrections, for jets with cone size $R = 0.7$. Statistical error bands are shown as well [56].

Chapter 5

Tagging of b-Jets

Since a low mass Higgs will predominantly decay to two b-quarks, a good and accurate b-tagging algorithm is crucial for Higgs searches. This chapter describes the work of developing and testing the first Neural Network (NN) b-tagging tool at DØ.

The b-jets can be identified (“tagged”) using the properties of the particles coming from the b-quark decay. The average lifetime for B hadrons is $\tau = 1.564 \pm 0.014$ ps [4]. Because of this long lifetime, their decay vertex is on average a short but measurable distance from the primary vertex. By reconstructing the secondary decay vertex, B hadron decays can be identified. In addition, because of the large mass of the b-quark, the decay particles have a large transverse momentum relative to the jet axis. This also means that the particle tracks do not point back to the primary vertex, but have a large “impact parameter”, the distance of shortest approach of the track to the primary vertex.

Based on these properties of B-hadron decays, three tagging algorithms have been developed at DØ: a secondary vertex-based tagging algorithm SVT, and two impact parameter-based algorithms, JLIP and CSIP. The SVT algorithm uses the distance from the secondary vertex to the primary vertex to identify b-jets. The CSIP algorithm simply places a cut on the number of tracks in a jet that have large impact parameters. The JLIP algorithm uses the impact parameters of the tracks in a jet to calculate the probability that the jet is a b-jet.

The secondary vertex and impact parameters by themselves do not always lead to the most performant b-tagging. The NN tagger combines properties of the secondary vertex like mass, decay length and the number of tracks, and the results of the CSIP and JLIP algorithms in an optimal way to tag b-jets. It was developed and optimised on Monte Carlo (MC), but the efficiency and fake rate were determined in data.

The outline of this chapter is as follows: Section 5.1 describes the SVT, CSIP and JLIP b-tagging algorithms. Section 5.2 describes the architecture and optimisation of the NN. Section 5.3 describes the data samples used to determine the efficiency of the NN. Section 5.4 describes the method used to determine the efficiency in collision data and its results. Section 5.5 describes the fake-tag efficiency in collision data. Section 5.6 summarises the results of the studies presented in this chapter and shows the overall performance of the NN in collision data.

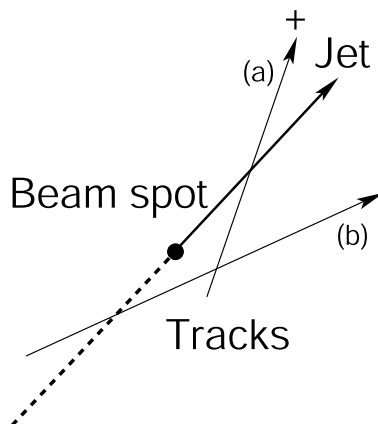


Figure 5.1: Definition of the physics signed impact parameter b_0 . The impact parameter is defined as positive if the track crosses the jet axis downstream of the beam position (a). If the track crosses the jet axis behind the beam position, the impact parameter is negative (b).

5.1 b Jet tagging algorithms

Three algorithms were developed that use the long lifetime of B hadrons to identify b -jets: the Secondary Vertex Tag (SVT), the Counting Signed Impact Parameter algorithm (CSIP), and the Jet Lifetime Probability algorithm (JLIP).

Both JLIP and CSIP taggers use the *physics signed 2D* impact parameter significance. The sign is based on the position of the point where the track and the jet cross in the $r - \varphi$ plane, with respect to the primary vertex (see Fig. 5.1). It is positive if the track crosses the jet axis in front of the primary vertex, and negative if the track crosses the jet axis behind the primary vertex. For background particles, the distribution of the physics signed impact parameter is expected to be symmetric around zero, but for b -decay particles it has a long positive tail. The significance is obtained by dividing the impact parameter by its error.

A fourth method uses the large relative momentum of a lepton resulting from the b decay with respect to the jet axis. The algorithms are briefly described in this section.

5.1.1 SVT

The SVT algorithm uses the decay length significance of secondary vertices to identify b -jets. The secondary vertices are reconstructed using a Kalman Fitting algorithm (see Section 4.4.7.) The decay length significance is defined as the distance from the secondary vertex to the primary vertex in the transverse plane, divided by the error.

5.1.2 CSIP

The CSIP algorithm [70] looks at the number of tracks with impact parameter significance larger than a certain cutoff. The impact parameter significance is defined as the impact parameter defined by the error. Four CSIP variables are used in this analysis:

CSIP 3s - The number of tracks with an impact parameter significance greater than 3.

CSIP 2s - The number of tracks with an impact parameter significance greater than 2.

CSIP 3w - The number of tracks with a negative impact parameter significance greater than 3 and an angle to the jet axis of less than 1.15 radians.

CSIP 2w - The number of tracks with a negative impact parameter significance greater than 2 and an angle to the jet axis of less than 1.15 radians.

A combined variable CSIP *Comb* is constructed from these variables and used as input for the NN.

5.1.3 JLIP

The JLIP algorithm [71] uses the impact parameters of tracks in a jet to calculate the probability that the jet comes from the primary vertex. To calculate the JLIP probability, the probability that each track comes from the primary vertex is determined by comparing the impact parameter significance to the distribution for background tracks:

$$P(S) = \frac{\int_S^\infty f_{\text{res}}(S')dS'}{\int_0^\infty f_{\text{res}}(S')dS'}, \quad (5.1)$$

where S is the impact parameter significance of the track and f_{res} is the resolution function determined from the distribution of negative impact parameter tracks. The probabilities for all the tracks associated with a jet within $\Delta R < 0.5$ are then combined to calculate the probability that all particles in the jet come from the primary vertex:

$$\mathcal{P}_{\text{jet}} = \Pi \cdot \sum_{i=0}^{N-1} \frac{(-\ln \Pi)^i}{i!}, \quad (5.2)$$

where Π is the product of the track probabilities. The smaller this probability, the more likely that the jet was a b-quark. If there was not enough information in the event to calculate a probability this value was set to 1.

5.1.4 Soft lepton tag

The SLT (Soft Lepton Tagging) method does not use the long lifetime of B hadrons but looks at the transverse momentum of a muon relative to the jet axis. Because of the large b-quark mass, this relative transverse momentum (P_T^{Rel}) is on average larger for b-jets. A cut on P_T^{Rel} can be used to increase the fraction of b-jets in a sample. The SLT tagger is not strongly correlated with the jet lifetime tags [72], so it can be used to determine the efficiency of the NN tagger (see Section 5.4.1.)

5.1.5 Taggability

The lifetime-based tagging algorithms are sensitive to the efficiency of the tracking algorithms. If not enough tracks can be found, the SVT, JLIP and CSIP algorithms will have much lower efficiency as well. To be able to compare the NN with other tagging algorithms, the efficiency is determined for *taggable* jets. A jet is taggable if it is matched to a track jet (see Section 4.4.6) within a distance of $\Delta R < 0.5$. The requirement also helps protect against fake jets due to calorimeter noise.

5.2 The Neural Network

When developing an optimised NN several attributes related to the design and training of the NN need to be studied. Important design parameters are the structure or architecture of the NN and the number and type of input variables. Important training parameters are the training samples and the input selection criteria, the training algorithm and the number of training epochs. The NN specifications are outlined in Table 5.1. They are discussed in more detail below.

Parameter	Value
NN structure	7:24:1:1
Jet input selection cuts (failure results in NN output of 0)	$SVT_{SL} DLS > 2.5$ or JLIP Prob < 0.02 or CSIP $Comb > 8$
Number of training epochs	400
Number of b -jets used in training (after jet selection cuts)	270,000 (220,000)
Number of light flavour jets used in training (after jet selection cuts)	470,000 (40,000)

Table 5.1: NN parameters.

5.2.1 Neural net architecture

The basic neural net structure is $N_{input} : N_{hidden} : N_{output}$. The number of input node is the number of input variables, and the number of output nodes in this case is 1. The number of hidden layers was chosen to be one, as one layer of sigmoid functions or ‘‘S-curves’’ should be sufficient to model any function, and it is advantageous to keep the NN as simple as possible. A sigmoid function is defined by the formula:

$$f(t) = \frac{1}{1 + e^{-t}}, \quad (5.3)$$

where $f(t)$ is the output of the node and t is the input. The number of hidden nodes in this layer was initially set to twice the number of input nodes. Since a single layer NN does

not produce an output normalised between 0 and 1, an extra hidden layer was added to constrain the NN between 0 and 1. By adding an extra hidden layer with 1 node the output is correctly normalised and the extra sigmoid does not alter the actual performance of the NN. The number of hidden nodes was optimised after choosing the input variables. Varying the number of hidden nodes from 7 to 34 for each operating point showed that the optimal number of hidden nodes was 24.

5.2.2 Input variables

The choice of input variables is crucial for the performance of the NN. Because of that, before creating the NN several studies were performed on the input variables. The initial variable sets, which were later re-optimised, were tested with a NN structure $N:2N:1$, where N is the number of input variables, using 500 training epochs and selection cuts of (SVT $DLS > 2$ or CSIP $Comb > 8$ or JLIP $prob < 0.02$).

Seven input variables were selected for their good discrimination between b-jets and non-b jets. Five of the variables are based on secondary vertices. The other two are based on tracks associated with the jet. The names of these variables are based on two other lifetime-based taggers, the JLIP and CSIP algorithms. The input variables are:

SVT DLS - The decay length significance (the decay length in the transverse plane divided by its uncertainty) of the secondary vertex with respect to the primary vertex.

SVT χ_{dof}^2 - The χ^2 per degree of freedom of the secondary vertex fit.

SVT N_{Tracks} - The number of tracks used to reconstruct the secondary vertex.

SVT $Mass$ - The mass of the secondary vertex. The mass is calculated from the combined momentum four-vectors of the tracks, assuming all particles were pions.

SVT Num - The number of secondary vertices reconstructed in the jet.

JLIP $Prob$ - The probability that the jet originated from the primary vertex. The probability is calculated based on the impact parameter significance of the tracks associated with the jet.

CSIP $Comb$ - A combined variable based on the number of tracks with an impact parameter significance greater than some value.

Since more than one secondary vertex can be found for each jet, vertex variables are ranked in order of the most powerful discriminator, the decay length significance (DLS). The secondary vertex with the largest DLS in a jet is used to provide the input variables. If no secondary vertex is found, the SVT values are set to 0, apart from the SVT χ_{dof}^2 which is set to 75 corresponding to the upper bound of χ_{dof}^2 values.

The CSIP $comb$ variable is based on the four CSIP variables described in Section 5.1.2. Neural Networks tend to perform best when provided with continuous values spread over a range. Since the CSIP variables have small integer values which are not very good as inputs,

they are combined in one variable which brings the advantage of reducing the number of input variables, hence simplifying the NN:

$$\text{CSIP Comb} = 6 \times 3s + 4 \times 2s + 3 \times 3w + 2 \times 2w \quad (5.4)$$

The weights were determined in an empirical manner to give optimum performance for this variable alone.

The distributions for the input variables to the NN in Monte Carlo and QCD data are shown in Fig. 5.2.

5.2.3 Neural net training

The training samples and training algorithms were optimised prior to the input variable optimisation as they did not depend on the input variable optimisation. The NN was trained on QCD light jet and $b\bar{b}$ samples, weighted to give an equal number of jets after input selection cuts. The signal sample of 270,000 $b\bar{b}$ events and the background sample of 470,000 light jet QCD events were each split in half, with one half used for the training sample and the other half for the test sample.

The number of training epochs was varied from 50 up to 2000. After testing different training versions, the number of training epochs was set to 400.

5.2.4 Input Selection Cuts

Another important attribute of the NN is the selection of the jets which are used to train the NN to separate the background and signal. A selection which is too loose can cause a loss of performance and resolution as the NN is learning a signal from background separation which could have been carried out with a simple cut. At the same time a selection which is too tight will cause a significant loss of b -jets and therefore limit the NN training.

The input selection cuts were optimised by considering each variable in turn, optimising SVT DLS first, then JLIP $Prob$ and finally CSIP $Comb$. The NN was trained on the QCD $b\bar{b}$ and QCD light jet samples and the optimisation plots were produced from the high p_t ALPGEN $t\bar{t}$ sample and cross checked with the QCD $b\bar{b}$ sample to ensure there was no sample, p_t or MC generator dependence in the optimisation.

5.2.5 NN Performance on Monte Carlo

The output from the optimised NN b -tagger on $b\bar{b}$ and light jet QCD MC is shown in Fig 5.3. The NN b -tagger shows significant separation between signal and background samples and demonstrates similar performance on different samples tested. The difference could be attributed to the difference in p_t spectra of the samples.

5.3 Data efficiency and studies

The MC simulation of the $D\emptyset$ detector is not always a realistic simulation of real detector data. For example, it is too optimistic in the quality and number of tracks found. Because

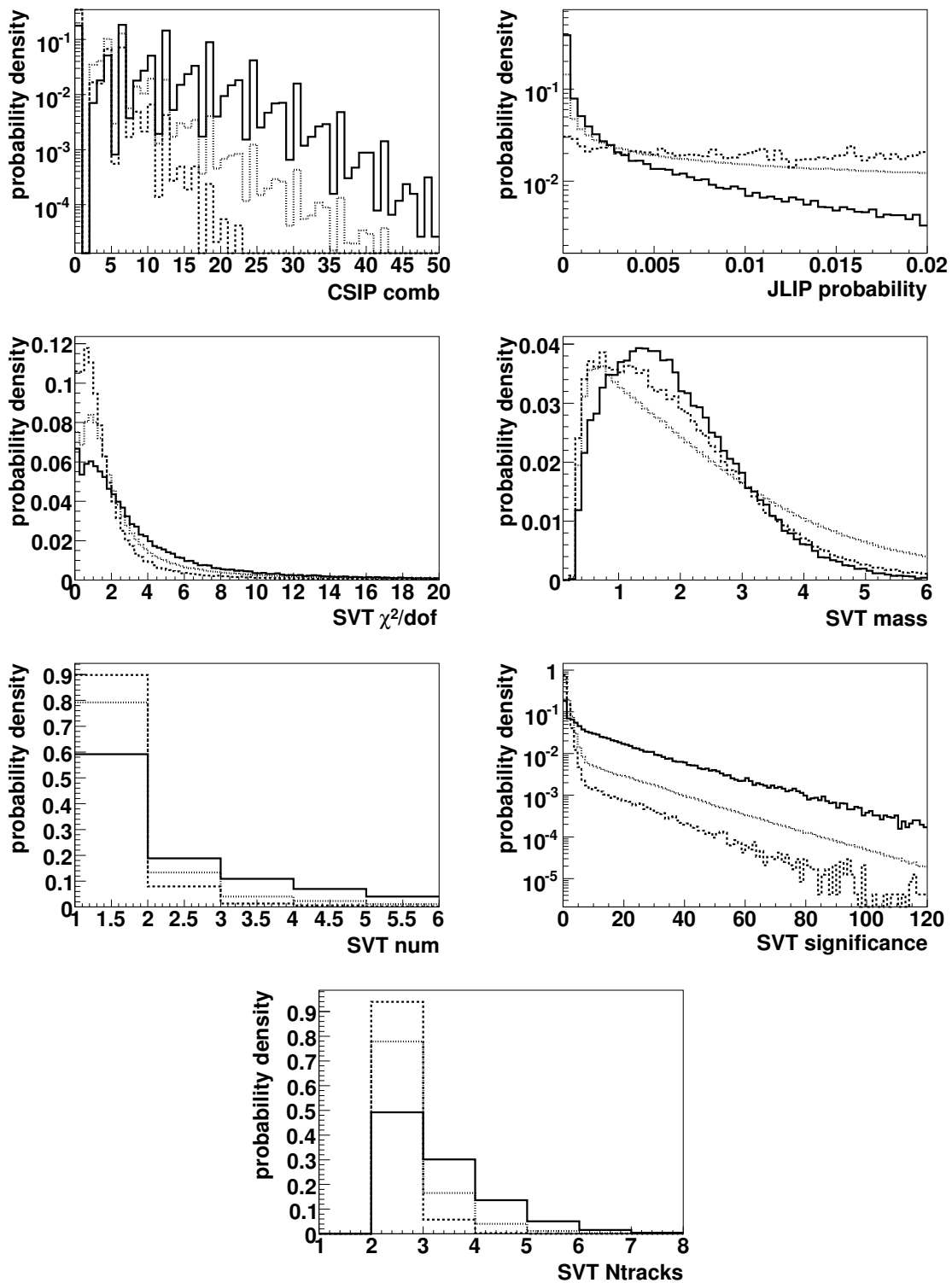


Figure 5.2: The NN variables CSIP *Comb*, JLIP *Prob*, SVT χ^2/dof , *Mass*, *Num*, *DLS* and N_{Tracks} for QCD $b\bar{b}$ MC (solid lines), light jet QCD MC (dashed lines) and data (dotted lines). All histograms are normalised to a surface of 1.

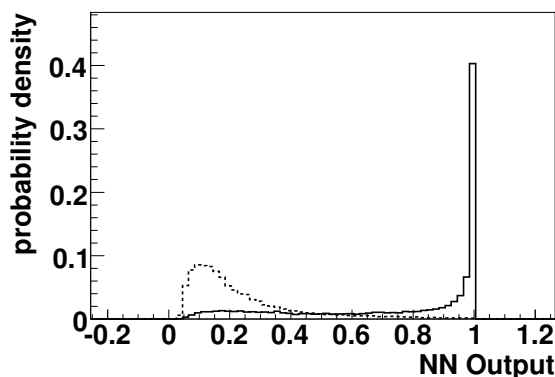


Figure 5.3: The NN output for the light jet QCD MC (dashed line) compared to the QCD $b\bar{b}$ MC (solid line). Both histograms are normalised to an area of 1.

of this the performance of the NN is measured directly in collision data.

When comparing data and MC studies, the b -tagging algorithm is applied directly to the data, and the jets either pass or fail a particular cut on the NN output. The performance in MC is overestimated compared to data and we need to apply different corrections for the MC at the tagging level.

When measuring the data performance, “Tag Rate Functions” (TRFs) and “Scale Factors” (SFs) are defined. The TRFs are used to predict the probability that the b -, c - and light jets in the event are tagged. Scale factors between data and MC are determined to more accurately simulate the data performance in the MC. The functions described above are:

TRF _{b} - The efficiency to tag a b -jet in data.

TRF _{c} - The efficiency to tag a c -jet in data.

Fake-Tag Rate (FTR)¹ - The efficiency to tag a light-flavour (uds or gluon) jet in data.

Scale Factor (SF) - The factor by which the b and c MC tagging efficiencies have to be multiplied by to obtain the data tagging efficiencies.

These functions are parameterised in terms of the p_T and η of the jets. To compare data and MC for various cuts on the NN output, they are measured for various fixed “operating points”, each representing a specific cut on the NN output. The NN tagger’s performance on data was measured with minimal input from MC. A system of eight independent equations was set up by equating the number of tags found by two independent tagging algorithms in two data samples with different b -quark content. By solving the system of equations, the efficiency was determined. The method and results are described in Section 5.4.

¹This can also be referred to as the light-jet TRF.

5.3.1 Operating Points

The NN tagger performance was evaluated for 12 operating points. The operating points are outlined in Table 5.2. To obtain the results presented in this thesis are the Tight and L3 operating point. Only plots for those operating points will be shown in this chapter.

Name	MegaTight	UltraTight	VeryTight	Tight	Medium	oldLoose
NN Cut	> 0.925	> 0.9	> 0.85	> 0.775	> 0.65	> 0.5
Name	Loose	L2	L3	L4	L5	L6
NN Cut	> 0.45	> 0.325	> 0.25	> 0.2	> 0.15	> 0.1

Table 5.2: The NN tagger’s operating points.

5.3.2 Data and MC Samples

The performance of the NN tagger was measured on data taken from July 2002 to February 2006. Data with bad luminosity blocks or runs that were marked as bad in the run quality database were not used. Three data samples were defined: a BID sample with higher b-jet content, an EM background sample and a QCD background sample. The selection criteria for the samples are outlined in Table 5.3, together with the number of events for each sample. In addition to these cuts, events in the EM sample had a missing transverse energy (\cancel{E}_T) cut of $\cancel{E}_T < 10$ GeV. A larger “COMB” sample combining all the selected jets in the EM and QCD samples was also created.

In addition, to reduce bias from electrons in the EM, QCD and combined samples, jets with a distance to the closest EM cluster smaller than $\Delta R < 0.4$ were removed. This cut is not part of the standard “good jet” selection (see Section 4.4.2) and removes many good jets, so it was not used in the BID sample. The effect of this cut in the QCD sample is studied separately in Section 5.5.2.

To avoid bias due to the online event selection, events that were only triggered by a lifetime-based trigger at L3 were excluded.

Skim	Skim Criteria	Events
EM	1 Electron with $p_T > 4$ Gev	177M
QCD	Jet Triggers	72M
COMB	Combination of the QCD and EM skims	249M
BID	One loose μ $p_T > 4$ GeV inside a 0.7 cone jet	141M

Table 5.3: The Run II full data skims used in the certification of the NN tagger.

The MC samples used are outlined in Table 5.4.

For the selection of events used for the performance estimation, medium quality muons were used with $p_t > 4$ GeV, a global fit $\chi^2 < 100$ and matched to a good jet within $\Delta R < 0.5$.

Sample	Number of Events
inclusive $t\bar{t}$	571,750
$Z \rightarrow b\bar{b}$	105,250
$Z \rightarrow b\bar{b}$ with μ	105,750
$Z \rightarrow c\bar{c}$	107,250
$Z \rightarrow c\bar{c}$ with μ	107,750
$Z \rightarrow q\bar{q}$ ($q = u,d,s$)	103,750
$Z \rightarrow q\bar{q}$ with μ ($q = u,d,s$)	107,000
QCD $p_T = 20 - 40, 40 - 80, 80 - 160, 160 - 320$	972,500
QCD $b\bar{b}$ $p_T = 20 - 40, 40 - 80, 80 - 160, 160 - 320$	265,000
QCD $c\bar{c}$ $p_T = 20 - 40, 40 - 80, 80 - 160, 160 - 320$	239,287

Table 5.4: The MC samples used in certification of the NN tagger.

5.3.3 Jet Samples

The number of jets available in the MC samples after data processing and physics object and jet cut selections is outlined in Table 5.5.

Only taggable jets (see Section 5.1.5) were used, and only events with at least two taggable jets were considered. A jet is taggable if it is matched to a track jet (see Section 4.4.6) within a distance of $\Delta R < 0.5$. In MC events, jets were identified as b-jets if there was a B-hadron within $\Delta R < 0.5$ of the jet. Jets were identified as c-jets if there was a C-hadron but no B-hadron within $\Delta R < 0.5$. Light jets include uds-quark and gluon jets, and had no heavy flavour particles associated with the jet at all.

The different energy QCD samples were merged into a continuous p_T ‘‘QCD Merged’’ sample by weighting the different energy samples so that a continuous fall-off in the jet p_T spectrum was obtained. Larger b and c-jets samples were created by combining all the appropriate jets from the different production channels.

The number of jets available in the data samples after data processing and physics object and jet selection cuts (including the presence of an away jet, see Section 5.4.1) is outlined in Table 5.6.

5.4 b-Efficiency Measurement

The efficiency of the NN tagger on data is measured in this section for inclusive b and c-jets; the statistical and systematic error associated with the measurement are also derived.

5.4.1 System8 Method

The b-jet efficiency on data was measured using the System8 (S8) formalism[73]. A system of 8 equations with 8 unknowns was constructed by equating the number of tags found by two different taggers on two different samples. The solutions to the equations included the efficiencies of the two taggers on b-jets.

Flavour	Sample	Number of Jets
b	$Z \rightarrow b\bar{b}$	130,220
	$t\bar{t} \rightarrow b$	1,662,929
	QCD $b\bar{b}$ (Merged)	90,252
	b (Combined)	2,349,755
$b \rightarrow \mu$	$Z \rightarrow b\bar{b} \rightarrow \mu$	42,726
	$t\bar{t} \rightarrow b \rightarrow \mu$	175,579
	$b \rightarrow \mu$ (Combined)	273,281
c	$Z \rightarrow c\bar{c}$	137,740
	$t\bar{t} \rightarrow c$	404,753
	QCD $c\bar{c}$ (Merged)	90,441
	c (Combined)	1,076,054
$c \rightarrow \mu$	$Z \rightarrow c\bar{c} \rightarrow \mu$	47,986
	$t\bar{t} \rightarrow c \rightarrow \mu$	17,715
	$c \rightarrow \mu$ (Combined)	91,824
uds	$Z \rightarrow q\bar{q}$	152,590
	QCD Fake (Merged)	239,118
All	QCD All	2,086,603

Table 5.5: Number of MC jets of each flavour available in each of the samples after data processing and jet selection.

Sample	Number of Jets
BID	15,277,180
EM	48,055,113
QCD	106,417,629
COMB	154,472,742

Table 5.6: Number of data jets available in each skim after data processing and jet selection.

The S8 equations were symmetric in nature and in order that the equations were (numerically) solvable the two taggers needed to be uncorrelated with different b -efficiencies and the two data samples needed to have different b -contents.

The two taggers used were the NN and SLT (“Soft Lepton Tag”) taggers. A SLT tag was defined as a muonic jet where the muon satisfied a cut of $P_T^{Rel} > 0.5$ GeV with respect to the jet axis. The SLT tagger is not strongly correlated with the jet lifetime tag, so it can be used for the S8 method. A low cut was required to ensure that the NN b -efficiency remained different from the SLT b -efficiency for all operating points. The efficiency for the SLT cut was about 80% in the $b\bar{b}$ MC sample.

The two data samples used were the BID muonic jet sample and a b -enriched subset consisting of muonic jets with an away tag of JLIP Prob < 0.005 . An “away tag” is an indirect method of tagging a jet without actually performing any cuts on the jet and thereby biasing the jet sample. A jet was defined as having an away tag if it was taggable and in an event with only one other taggable jet which had passed JLIP Prob cut. The away-tagged sample has a higher heavy-flavour content, as b -jets are predominantly produced as $b\bar{b}$ -pairs.

Correlation coefficients were introduced into the S8 formulation to account for the following effects:

α - Ratio of the $udsgc$ -tagging efficiencies in the two samples.

β - Ratio of the b -tagging efficiencies in the two samples.

κ_b - Correlations between the NN tagger and the SLT tagger on b -jets.

κ_{udsgc} - Correlations between the NN tagger and the SLT tagger on light-flavour (including charm) jets.

The values of the correlation coefficients were measured using MC samples. The statistical errors on the measurements were used to estimate systematic errors due to the uncertainty with which the correlation coefficients were known. The S8 equations were defined as

$$n = n_b + n_{udsgc}, \quad (5.5)$$

$$p = p_b + p_{udsgc}, \quad (5.6)$$

$$n^{SLT} = \varepsilon_b^{SLT} n_b + \varepsilon_{udsgc}^{SLT} n_{udsgc}, \quad (5.7)$$

$$p^{SLT} = \varepsilon_b^{SLT} p_b + \varepsilon_{udsgc}^{SLT} p_{udsgc}, \quad (5.8)$$

$$n^{NN} = \varepsilon_b^{NN} n_b + \varepsilon_{udsgc}^{NN} n_{udsgc}, \quad (5.9)$$

$$p^{NN} = \beta \varepsilon_b^{NN} p_b + \alpha \varepsilon_{udsgc}^{NN} p_{udsgc}, \quad (5.10)$$

$$n^{SLT,NN} = \kappa_b \varepsilon_b^{SLT} \varepsilon_b^{NN} n_b + \kappa_{udsgc} \varepsilon_{udsgc}^{SLT} \varepsilon_{udsgc}^{NN} n_{udsgc}, \quad (5.11)$$

$$p^{SLT,NN} = \kappa_b \beta \varepsilon_b^{SLT} \varepsilon_b^{NN} p_b + \kappa_{udsgc} \alpha \varepsilon_{udsgc}^{SLT} \varepsilon_{udsgc}^{NN} p_{udsgc}, \quad (5.12)$$

where n was the number of jets in the muonic jet sample, p was the number in the b -enriched sample and ε was the efficiency of the tagger. The superscripts referred to the NN and SLT taggers and the subscripts referred to the flavour of the jets, b or $udsgc$.

5.4.2 Determination of the Correlation Coefficients

Away tag correlation factor for light jets

The α correlation coefficient, which represented the differences between the tagging efficiency on udsgc jets in the two samples, was calculated from MC. The value determined from the combined QCD All MC sample is shown in Fig. 5.4 together with p_t and η parameterisations. The QCD All MC sample was derived from the inclusive QCD sample by simply rejecting all b-jets. The statistical error on α was calculated taking into account the correlated numbers of events between the two efficiencies. The systematic error on the efficiency was estimated by varying the value of α within its statistical error.

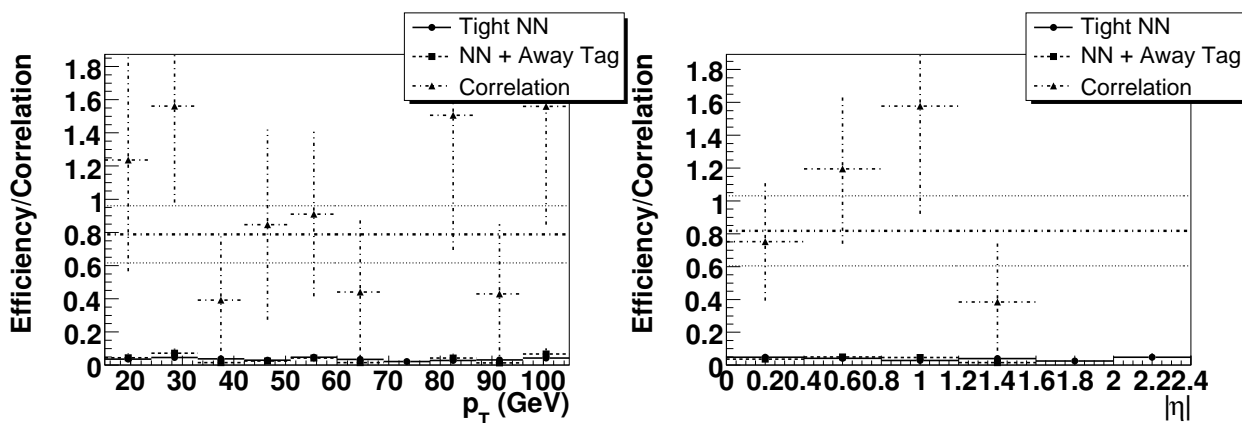


Figure 5.4: α in the QCD inclusive c combined sample as a function of jet p_T (left) and η (right), for the Tight operating point. The black dotted line represents the error on the straight line fit.

Away tag correlation factor for b-jets

β was introduced to represent differences between the b-efficiencies in the two different samples. β was calculated from the ratio of the muonic b-jet to the muonic b-jet with an away tag tagging efficiencies. The value determined from the combined $b \rightarrow \mu$ MC sample is shown in Fig. 5.5. The statistical error on β was calculated taking into account the correlated numbers of events between the two efficiencies. Another source of error exists due to the sample dependence of β . The ratio of the β value calculated in the $Z \rightarrow b\bar{b}$ and the $t\bar{t} \rightarrow b$ samples was calculated for each operating point. An error was attributed to the sample dependence by taking half the average deviation from unity in the η and p_T projections. The sample dependence error was added to the statistical error in quadrature to give the total error on β . The systematic error was estimated by varying the value of β within its error.

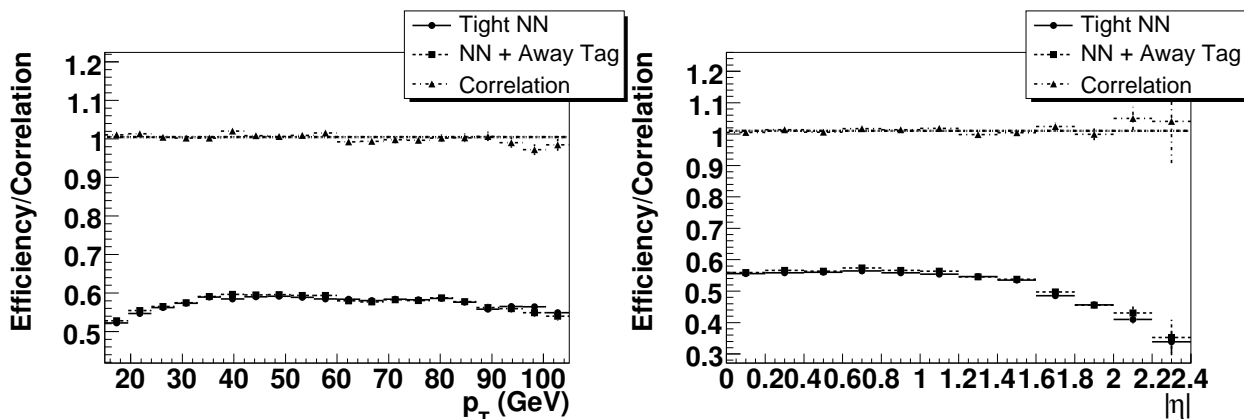


Figure 5.5: β in the $b \rightarrow \mu$ combined sample as a function of jet p_T (left) and η (right), for the Tight operating point. The black dotted line represents the error on the straight line fit. Sample in p_T (left) and η (right) projections.

Soft lepton tag correlation factor

κ_b and κ_{udsgc} which represented the correlations between the NN and SLT taggers on muonic jets were determined from the following relationship

$$\kappa_{b,\text{udsgc}} = \frac{\varepsilon_{b,\text{udsgc}}^{NN\&SLT}}{\varepsilon_{b,\text{udsgc}}^{NN} \times \varepsilon_{b,\text{udsgc}}^{SLT}}, \quad (5.13)$$

where ε was the efficiency, the subscripts referred to the jet flavour, the superscripts referred to the taggers and the ampersand to both tags being present.

κ_b was measured in the combined $b \rightarrow \mu$ MC sample and is shown in Fig. 5.6. The κ_b statistical error was calculated taking into account the correlated numbers of events. A linear dependence was observed in p_T and a straight line was used to model the coefficient. The error on the fit was determined from the covariance matrix and was therefore also a function of p_T . As the fit value and error were a function of p_T the systematic error due to the uncertainty in the measurement of κ_b also became a function of p_T .

Another source of error exists due to the sample dependence of κ_b . The ratio of the κ_b value calculated in the $Z \rightarrow b\bar{b}$ and the $t\bar{t} \rightarrow b$ samples was calculated for each operating point. An error was attributed to the sample dependence by taking half the average deviation from unity in the η and p_T projections. The η projection was restricted to a limited range in p_T due to the p_T dependence of κ_b and the difference in the p_T spectra in the two samples. The sample dependence error was added to the statistical error in quadrature to give the total error on κ_b .

κ_{udsgc} was measured using the combined $c \rightarrow \mu$ MC sample and is shown in Fig. 5.7. The κ_{udsgc} statistical error was calculated taking into account the correlated numbers of events.

As in the previous measurements another source of error exists due to the sample dependence of κ_{udsgc} . The ratio of the κ_{udsgc} value calculated in the $Z \rightarrow c\bar{c}$ and the $t\bar{t} \rightarrow c$ samples was calculated for each operating point. An error was attributed to the sample dependence

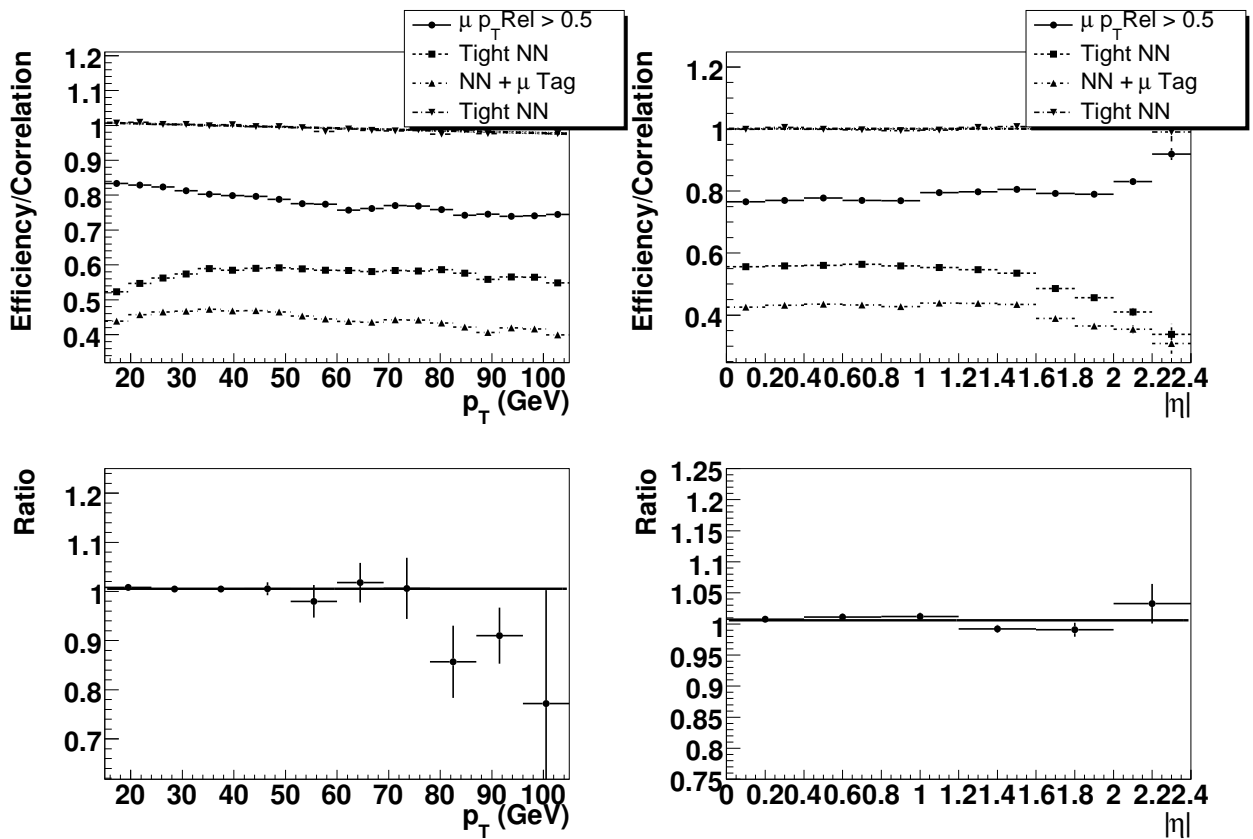


Figure 5.6: Correlation coefficient κ_b between the NN and the SLT tagger as measured in the combined $b \rightarrow \mu$ MC sample in jet p_T (left) and η (right) projections, for the Tight operating point. The black dotted line represents the error on the fit calculated from the full covariant fit error matrix. The bottom plots show the ratio between κ_b as found in the $Z \rightarrow b\bar{b} \rightarrow \mu$ and $t\bar{t} \rightarrow b \rightarrow \mu$ MC samples in p_T (left) and η (right).

by taking half the average deviation from unity in the η and p_T projections. The sample dependence error was added to the statistical error in quadrature to give the total error on κ_{udsgc} .

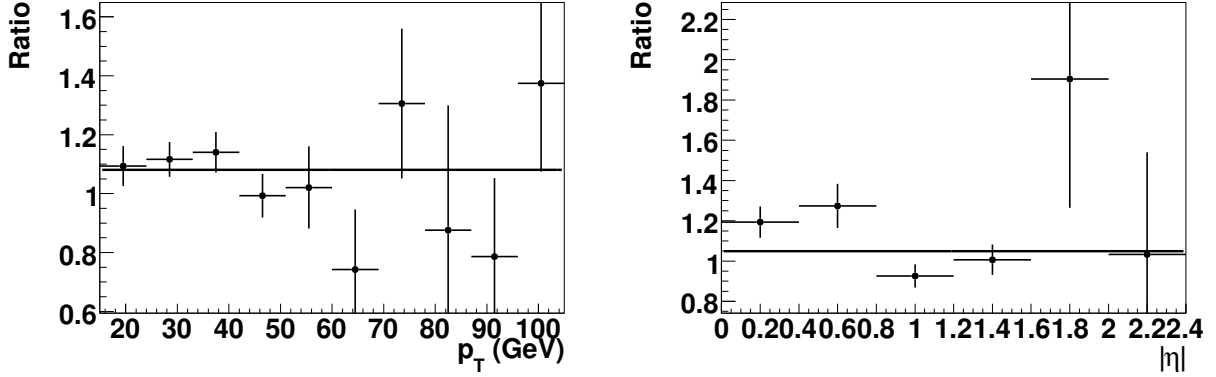


Figure 5.7: The ratio between κ_{udsgc} as found in the $Z \rightarrow c\bar{c} \rightarrow \mu$ and $t\bar{t} \rightarrow c \rightarrow \mu$ MC samples in p_T (left) and η (right), for the Tight operating point.

P_T^{Rel} Variation

The dependence of the efficiency on the chosen value of the p_T^{Rel} cut, due to the differences between SLT tagging efficiency on band udsgc-jets, was not represented in the S8 equations as a correlation coefficient. Instead the uncertainty due to the choice of the cut was evaluated by recalculating the S8 efficiency at different SLT operating points. The SLT p_T^{Rel} cut was varied from 0.3 to 0.7 GeV. The values of κ_b and κ_{cl} were dependent on the value of the SLT p_T^{Rel} cut. Therefore both these values were recalculated at the different SLT operating points.

Correlation Coefficient Values

The values of the correlation coefficients are given in Tables 5.7 and 5.8. The values and errors were consistent between the η and p_T parameterisations. The κ_b value and error were p_T dependent so the value was evaluated at the average jet p_T value for the sample. When solving the S8 equations in various bins in p_T and η the S8 correlation coefficients were evaluated for the average jet p_T value in that bin.

5.4.3 System8 Efficiency and Systematic Errors

The S8 equations were solved numerically, and the calculation was carried out on the entire sample and in several p_T and η regions to create a profile over the p_T and η phase space. The systematic uncertainties in the calculated b-efficiency, due to the errors in the correlation coefficients, were determined by varying the coefficients by their aforementioned errors and

Coefficients	L6	L5	L4	L3
α	0.967 ± 0.096	0.937 ± 0.102	0.957 ± 0.116	0.918 ± 0.124
β	1.010 ± 0.001	1.010 ± 0.001	1.010 ± 0.001	1.010 ± 0.002
κ_b	0.999 ± 0.002	0.999 ± 0.001	1.000 ± 0.001	1.000 ± 0.001
κ_{cl}	1.000 ± 0.018	0.998 ± 0.022	0.999 ± 0.026	1.000 ± 0.025
Coefficients	L2	Loose	oldLoose	Medium
α	0.766 ± 0.127	0.819 ± 0.152	0.840 ± 0.160	0.791 ± 0.183
β	1.010 ± 0.001	1.010 ± 0.001	1.010 ± 0.002	1.010 ± 0.002
κ_b	1.000 ± 0.002	1.000 ± 0.002	1.000 ± 0.003	1.000 ± 0.003
κ_{cl}	1.000 ± 0.022	1.000 ± 0.021	0.999 ± 0.025	0.995 ± 0.027
Coefficients	Tight	VeryTight	UltraTight	MegaTight
α	0.816 ± 0.213	0.904 ± 0.245	1.070 ± 0.326	0.951 ± 0.338
β	1.010 ± 0.005	1.010 ± 0.006	1.010 ± 0.007	1.010 ± 0.008
κ_b	1.000 ± 0.003	1.000 ± 0.002	1.000 ± 0.002	1.000 ± 0.001
κ_{cl}	0.987 ± 0.033	0.979 ± 0.025	0.958 ± 0.026	0.942 ± 0.029

Table 5.7: The S8 correlation coefficients with associated errors as derived in the MC samples from the η parameterisation.

Coefficients	L6	L5	L4	L3
α	1.060 ± 0.079	1.010 ± 0.086	0.921 ± 0.091	0.897 ± 0.098
β	1.000 ± 0.001	1.000 ± 0.001	1.010 ± 0.001	1.000 ± 0.002
κ_b	1.000 ± 0.002	1.000 ± 0.001	1.000 ± 0.001	1.000 ± 0.001
κ_{cl}	1.000 ± 0.018	1.000 ± 0.022	1.000 ± 0.027	1.010 ± 0.025
Coefficients	L2	Loose	oldLoose	Medium
α	0.786 ± 0.104	0.864 ± 0.126	0.789 ± 0.125	0.829 ± 0.156
β	1.010 ± 0.002	1.000 ± 0.002	1.000 ± 0.002	1.000 ± 0.002
κ_b	1.000 ± 0.002	1.000 ± 0.002	1.000 ± 0.003	1.000 ± 0.003
κ_{cl}	1.010 ± 0.022	1.010 ± 0.021	1.000 ± 0.025	0.998 ± 0.027
Coefficients	Tight	VeryTight	UltraTight	MegaTight
α	0.796 ± 0.174	0.940 ± 0.205	0.877 ± 0.224	0.904 ± 0.249
β	1.000 ± 0.005	1.000 ± 0.006	1.010 ± 0.007	1.010 ± 0.008
κ_b	1.000 ± 0.003	0.999 ± 0.002	0.999 ± 0.002	0.999 ± 0.001
κ_{cl}	0.989 ± 0.033	0.981 ± 0.025	0.960 ± 0.026	0.943 ± 0.030

Table 5.8: The S8 correlation coefficients with associated errors as derived in the MC samples from the p_T parameterisation evaluated at $p_T = 37$ GeV.

resolving the equations. The relative differences in efficiencies between the solutions provided the systematic errors.

The S8 efficiencies along with the systematic errors for the whole BID muonic jet sample are shown in Table 5.9. The efficiency is seen to vary from 37% for the tightest operating point to 77% for the loosest operating point. The relative systematic errors, when calculated for the entire sample, vary from 1.3% to 1.7%.

Error	L6	L5	L4	L3	L2	Loose
Efficiency	77%	74.9%	72.2%	69.6%	65.9%	60.8%
Total syst.	1.67%	1.58%	1.47%	1.31%	1.29%	1.37%
α	0.035%	0.022%	0.019%	0.028%	0.021%	0.027%
β	0.135%	0.142%	0.168%	0.205%	0.181%	0.181%
κ_b	0.657%	0.505%	0.557%	0.483%	0.728%	0.976%
κ_{cl}	0.66%	0.657%	0.589%	0.46%	0.293%	0.254%
p_T^{Rel}	1.38%	1.33%	1.21%	1.11%	1.01%	0.914%

Error	oldLoose	Medium	Tight	VeryTight	UltraTight	MegaTight
Efficiency	59.3%	53.7%	47.6%	43.3%	39.5%	37.1%
Total syst.	1.45%	1.34%	1.52%	1.51%	1.33%	1.43%
α	0.019%	0.003%	0.015%	0.037%	0.074%	0.114%
β	0.198%	0.257%	0.554%	0.777%	0.803%	0.957%
κ_b	1.23%	1.21%	1.21%	0.959%	0.699%	0.597%
κ_{cl}	0.254%	0.232%	0.218%	0.175%	0.156%	0.164%
p_T^{Rel}	0.691%	0.455%	0.696%	0.854%	0.784%	0.856%

Table 5.9: Relative systematic uncertainties on the NN tag efficiency determined with the System8 method. The total systematic uncertainty was determined by adding the individual uncertainties in quadrature.

The error due to the uncertainties in the correlation coefficients was measured separately for each η bin and each p_T bin in which the S8 equations were used. Primarily this was necessary because of κ_b , as its error varied as a function of p_T . Additionally, as each of the regions had different solutions there was no guarantee that the S8 errors would be the same in each region and would not be dependent on either p_T or η . Any such dependence would be overlooked if the systematic error was only evaluated for the entire sample.

The S8 errors were evaluated for each bin in the p_T and η projections and are shown in Fig. 5.8 for the L3 and Tight operating points. Evaluating the S8 errors in each bin produced overall larger systematic errors than calculating the S8 errors for the entire sample. The S8 errors appeared to have very little η dependence except at high η where the p_T^{Rel} uncertainty was substantially higher. The systematic errors demonstrate a downwards trend with increasing p_T . The constant fit for the total S8 systematic errors in both projections compared to that for the entire sample also suggested that only using the S8 error calculated from the entire sample would have been an underestimate of the systematic uncertainty.

The S8 error calculated for each bin was combined quadratically with the fit error on the b-efficiency. The combined error was assigned as the total uncertainty with which the

b-efficiency was known in each bin.

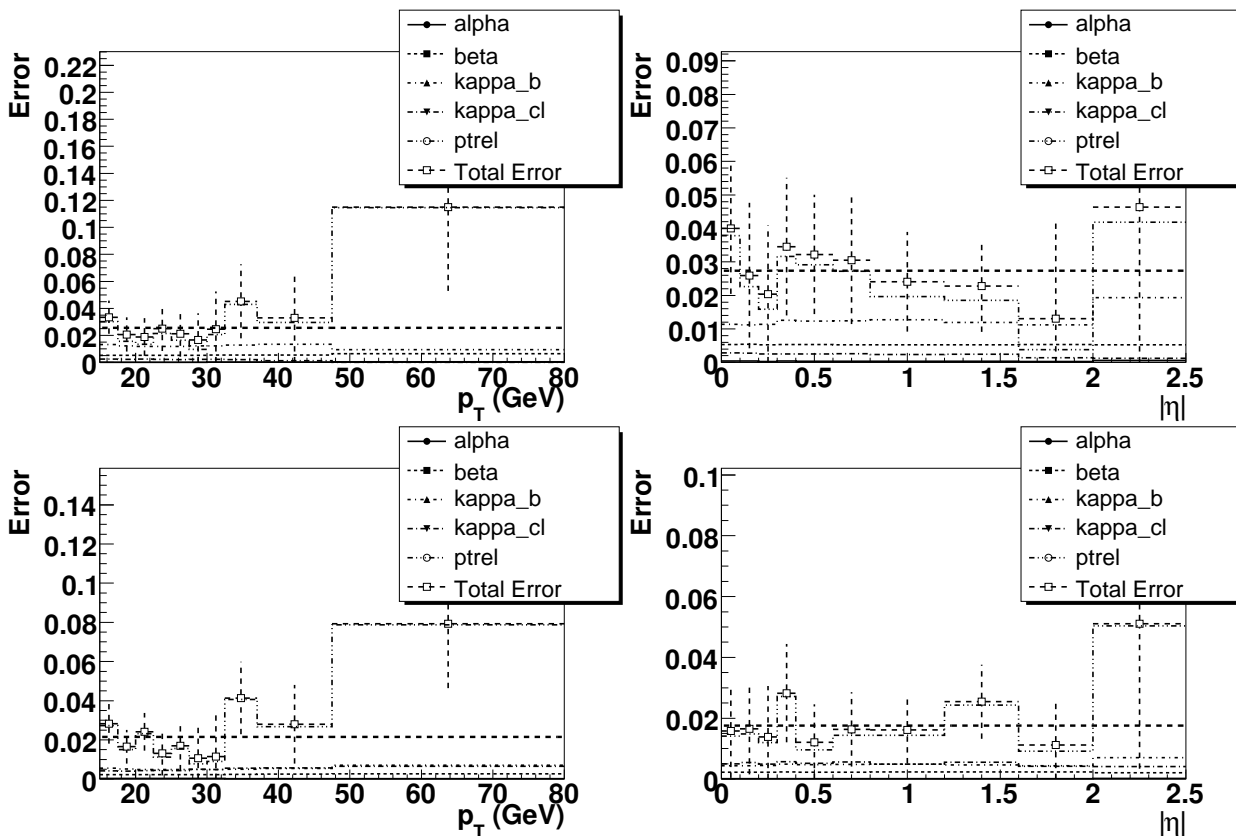


Figure 5.8: S8 systematic error calculated for each bin in p_T (left) and η (right) for the Tight operating point (top) and the L3 operating point (bottom). The dashed lines indicate the mean value for the whole range. The other operating points also show minimal dependence on p_T and η .

5.4.4 *b*-tagging and Scale Factor Parameterisation

The efficiencies were parameterised as a function of p_t using

$$\varepsilon(p_T) = \frac{c}{1 + ae^{-bp_T}}, \quad (5.14)$$

where ε was the efficiency and a , b , and c were constants to be determined. The efficiency was parameterised in $|\eta|$ using

$$\varepsilon(|\eta|) = d + e|\eta| + f|\eta|^2 + g|\eta|^3 + h|\eta|^4, \quad (5.15)$$

where ε was the efficiency and d , e , f , g and h were constants to be determined. To create a 2D parameterisation it was assumed that the efficiency could be factorised into η and p_T

components. A 2D parameterisation was given by the product of the two projections scaled by the total efficiency of the sample

$$\varepsilon(p_T, \eta) = \frac{1}{\varepsilon^{All}} \left(\frac{c}{1 + ae^{-bp_T}} \right) \times (d + e|\eta| + f|\eta|^2 + g|\eta|^3 + h|\eta|^4), \quad (5.16)$$

where ε^{All} was the efficiency on the entire sample. The efficiencies calculated from the S8 equations are shown in Fig. 5.9 along with the combined MC $b \rightarrow \mu$ sample efficiency and the data/MC SF produced by dividing the data efficiency by the MC efficiency.

5.4.5 Data/MC Scale Factor

The data/MC SF was measured in the previous section as

$$(\text{Data muonic } b\text{-efficiency}) / (\text{MC muonic } b\text{-efficiency}).$$

The SF measures the effect on the tagging rate caused by the differences in tracking between data and MC. The profile of the SF in p_T and η allows tagging rates to be corrected over the full p_T and η phase space.

It was assumed that the SF could be applied to any MC tagging efficiency to correct from a MC to a data tagging efficiency. In making this assumption it was assumed that the SF, which was measured only on muonic jets, was applicable to all jets. The validity of this assumption was not tested and it was assumed that any systematic error it caused was small in relation to the other errors.

5.4.6 Tag Rate Functions

The inclusive b -jet data TRF was calculated by multiplying the inclusive b -jet MC TRF (produced from the combined inclusive b -jet MC sample) by the SF. The inclusive b -jet data and MC TRFs (TRF_b) are shown in Fig. 5.10. A similar procedure was used to determine the inclusive c -jet data TRF (TRF_c). The inclusive c -jet MC TRF (produced from the combined inclusive c MC sample) was multiplied by the SF to give the TRF_c as shown in Fig. 5.11.

5.4.7 Systematic Uncertainties

RMS Closure Tests

Two main sources of systematic uncertainties are the dependence on the parameterisation of the TRFs and the dependence on the samples used to determine the TRFs. Both the parameterisation and MC sample dependence systematic errors, which result from the use of TRFs derived from generic combined samples of MC b , c and muonic b jets, can be quantified in one measurement. By carrying out closure tests, where we compare the percentage difference between the number of actual tags (N_{Obs}) and the predicted number (N_{Pred}) in various bins in p_T and η regions, we can ascertain a total error on the TRF from the spread of the percentage differences.

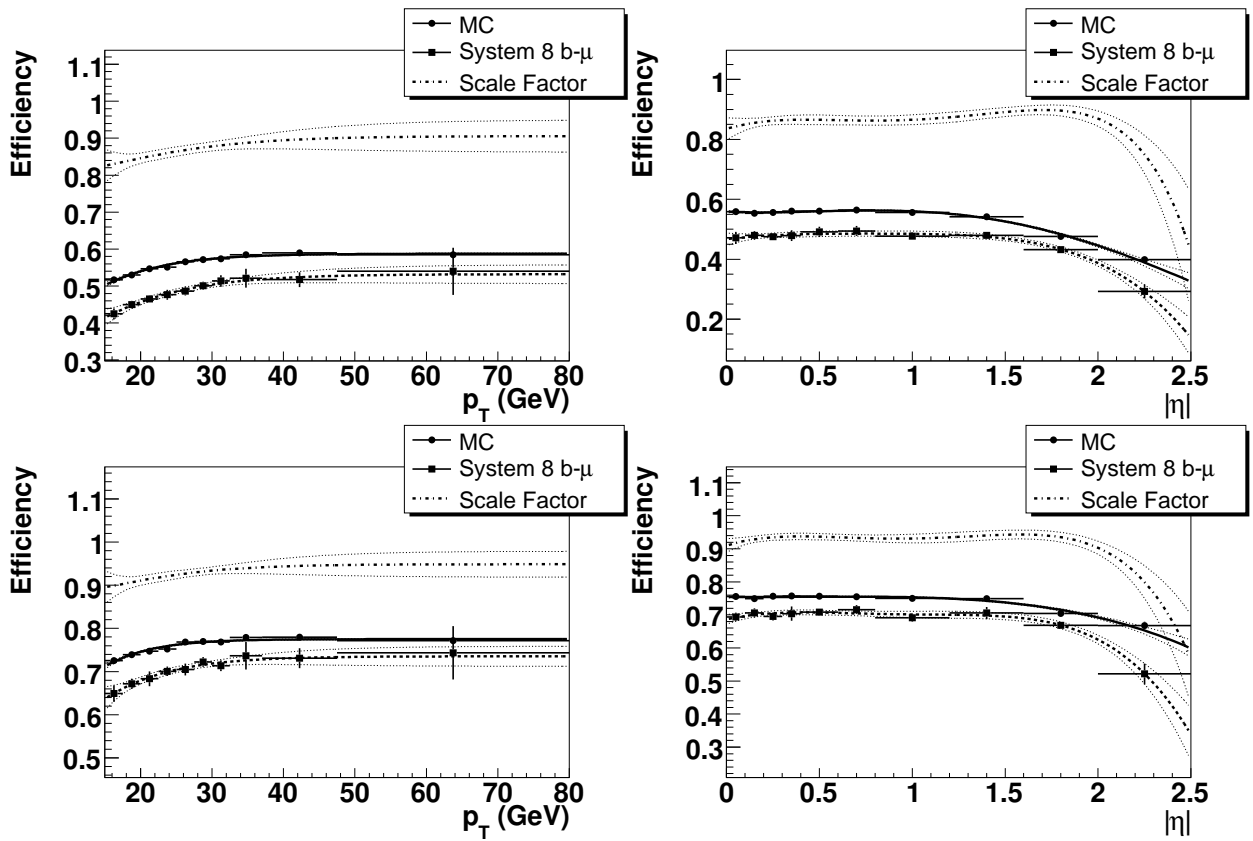


Figure 5.9: NN tagger muonic b-jet efficiency as a function of p_T (left) and η (right) in the BID μ -jet data sample for the Tight (top) and L3 (bottom) operating points. The functions used for the parameterisation are outlined in the text and the black dotted curves represent the fit error as calculated from the full covariant error matrix.

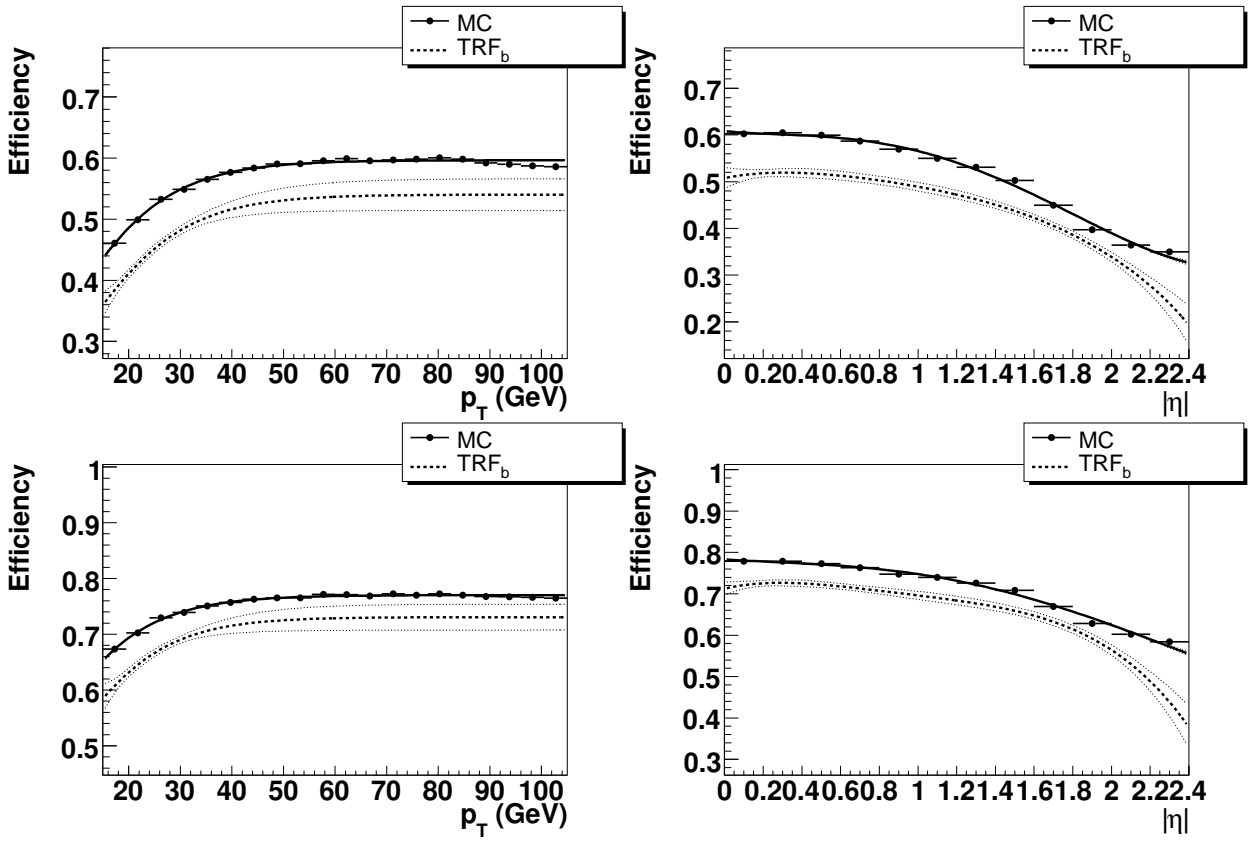


Figure 5.10: NN tagger b -jet efficiency as a function of p_T (left) and η (right) in the combined b -jet MC sample and the TRF_b derived from multiplying the MC b -jet efficiency by the data/MC SF for the Tight (top) and L3 (bottom) operating points. The dotted black lines represent the error on the fit which were almost entirely inherited from the error on the scale factor. The functions used for the parameterisation are outlined in the text.

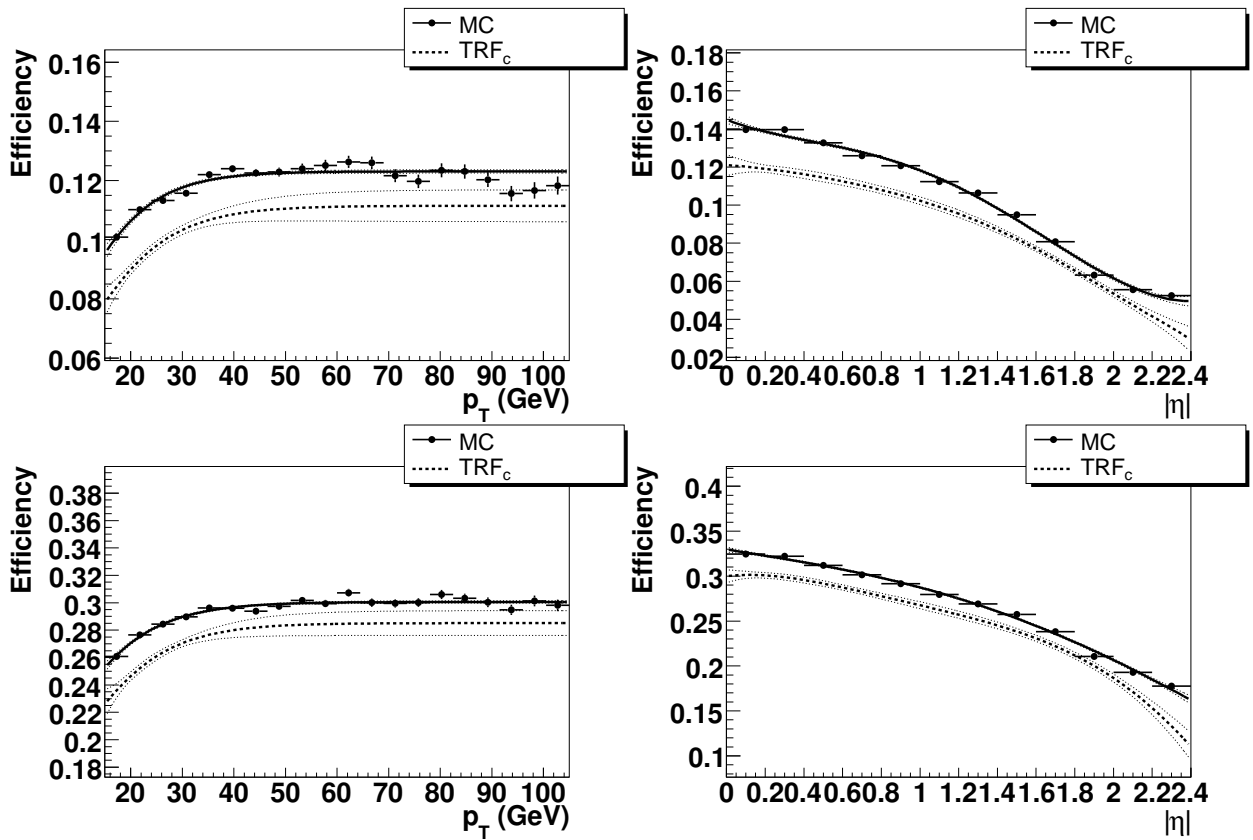


Figure 5.11: NN tagger c-jet efficiency as a function of p_T (left) and η (right) in the combined c-jet MC sample and the TRF_c derived from multiplying the MC c-jet efficiency by the data/MC SF for the Tight (top) and L3 (bottom) operating points. The dotted black lines represent the error on the fit which were almost entirely inherited from the error on the scale factor. The functions used for the parameterisation are outlined in the text.

The closure tests were carried out for each of the MC samples used to construct the TRFs. The percentage differences were calculated in p_T bins in the CC, ICR and EC calorimeter regions, and the percentage differences were binned weighted by the number of actual tags in the region. The RMS of the resulting distributions were used to quantify the total error on each of the TRFs.

The error values derived from the RMS of the percentage differences are shown in Tables 5.10, 5.11 and 5.12 for the b , muonic b and c -jet TRFs respectively. The total error derived from the RMS is larger than either individual or the combination of the systematic errors derived previously and therefore the RMS will be used as the error on the parameterised MC TRFs. The TRF error was taken from the constituent MC sample which produced the largest error.

RMS	L6	L5	L4	L3	L2	Loose
b	1.14%	1.28%	1.43%	1.58%	1.79%	2.11%
QCD $b\bar{b}$	1.19%	1.22%	1.22%	1.2%	1.32%	1.68%
$t\bar{t} \rightarrow b\bar{b}$	0.95%	1.03%	1.19%	1.33%	1.51%	1.79%
$Z \rightarrow b\bar{b}$	1.16%	1.19%	1.24%	1.33%	1.44%	1.54%
Max	1.19%	1.28%	1.43%	1.58%	1.79%	2.11%
RMS	oldLoose	Medium	Tight	VeryTight	UltraTight	MegaTight
b	2.2%	2.54%	2.84%	3.17%	3.45%	3.45%
QCD $b\bar{b}$	1.63%	1.64%	1.76%	2.09%	2.36%	2.45%
$t\bar{t} \rightarrow b\bar{b}$	1.84%	2.19%	2.43%	2.74%	2.98%	3.14%
$Z \rightarrow b\bar{b}$	1.59%	1.95%	2.01%	2.07%	2.4%	2.36%
Max	2.2%	2.54%	2.84%	3.17%	3.45%	3.45%

Table 5.10: The RMS b -jet TRF closure test errors for the combined b -jet sample and each of the constituent MC samples. The sample with the largest error was used as the error on the TRF.

System8 Systematic Errors

For each bin in η and p_t , the S8 systematic error for that bin was added in quadrature with the fit error. This gave an overall uncertainty with which the efficiency was known for each bin. This was repeated for the S8 efficiency of the entire sample. The combined errors were then used to fit the parameterised curves in p_T and η , with the S8 error folded into the statistical errors.

Total Systematic Errors

Each of the TRFs and the SF had an individual total systematic error constructed from the systematic errors calculated above as detailed below. The total systematic errors are shown in Table 5.13 and are added in quadrature to the statistical error to give the total error as detailed in the next sections.

RMS	L6	L5	L4	L3	L2	Loose
$b \rightarrow \mu$	1.2%	1.44%	1.63%	1.82%	1.96%	2.33%
QCD $b\bar{b} \rightarrow \mu$	0.298%	0.217%	0.165%	0.322%	0.466%	0.844%
$t\bar{t} \rightarrow b \rightarrow \mu$	1.29%	1.45%	1.59%	1.7%	1.83%	2.13%
$Z \rightarrow b\bar{b} \rightarrow \mu$	1.44%	1.77%	1.98%	2.12%	2.39%	2.92%
Max	1.44%	1.77%	1.98%	2.12%	2.39%	2.92%
RMS	oldLoose	Medium	Tight	VeryTight	UltraTight	MegaTight
$b \rightarrow \mu$	2.38%	2.64%	2.81%	2.86%	3.15%	3.35%
QCD $b\bar{b} \rightarrow \mu$	1.03%	1.5%	1.94%	2.39%	2.67%	2.55%
$t\bar{t} \rightarrow b \rightarrow \mu$	2.27%	2.35%	2.61%	2.66%	2.92%	3.05%
$Z \rightarrow b\bar{b} \rightarrow \mu$	3.08%	3.51%	3.47%	3.58%	3.36%	3.09%
Max	3.08%	3.51%	3.47%	3.58%	3.36%	3.35%

Table 5.11: The RMS muonic b-jet TRF closure test errors for the combined muonic b-jet sample and each of the constituent MC samples. The sample with the largest error was used as the error on the TRF.

RMS	L6	L5	L4	L3	L2	Loose
c	2%	2.1%	2.35%	2.56%	2.92%	3.25%
QCD $c\bar{c}$	2.39%	1.8%	1.95%	2.04%	2.17%	2.97%
$t\bar{t} \rightarrow c \rightarrow \mu$	2.01%	2.09%	2.36%	2.52%	2.71%	2.95%
$Z \rightarrow c\bar{c}$	1.99%	2.04%	2.27%	2.67%	2.86%	2.99%
Max	2.39%	2.1%	2.36%	2.67%	2.92%	3.25%
RMS	oldLoose	Medium	Tight	VeryTight	UltraTight	MegaTight
c	3.48%	3.81%	3.78%	3.31%	3.56%	3.55%
QCD $c\bar{c}$	2.9%	3.16%	2.5%	3.73%	2.97%	3.96%
$t\bar{t} \rightarrow c \rightarrow \mu$	3.25%	3.27%	3.73%	4.17%	3.81%	3.8%
$Z \rightarrow c\bar{c}$	2.95%	3.18%	3.88%	3.88%	3.87%	4.03%
Max	3.48%	3.81%	3.88%	4.17%	3.87%	4.03%

Table 5.12: The RMS c-jet TRF closure test errors for the combined c-jet sample and each of the constituent MC samples. The sample with the largest error was used as the error on the TRF.

Error	L6	L5	L4	L3	L2	Loose
MC $b \rightarrow \mu$	1.44%	1.77%	1.98%	2.12%	2.39%	2.92%
MC b	1.19%	1.28%	1.43%	1.58%	1.79%	2.11%
MC c	2.39%	2.1%	2.36%	2.67%	2.92%	3.25%
SF	1.44%	1.77%	1.98%	2.12%	2.39%	2.92%
TRF_b	1.87%	2.18%	2.44%	2.64%	2.98%	3.6%
TRF_c	2.79%	2.74%	3.08%	3.41%	3.77%	4.37%
Error	oldLoose	Medium	Tight	VeryTight	UltraTight	MegaTight
MC $b \rightarrow \mu$	3.08%	3.51%	3.47%	3.58%	3.36%	3.35%
MC b	2.2%	2.54%	2.84%	3.17%	3.45%	3.45%
MC c	3.48%	3.81%	3.88%	4.17%	3.87%	4.03%
SF	3.08%	3.51%	3.47%	3.58%	3.36%	3.35%
TRF_b	3.79%	4.34%	4.48%	4.78%	4.81%	4.81%
TRF_c	4.65%	5.18%	5.2%	5.5%	5.13%	5.24%

Table 5.13: Total systematic errors on the MC sample parameterisations, the SF and the TRFs.

Statistical Error

The overall relative statistical errors were calculated by evaluating

$$\sigma_{stat} = \frac{f^{+1\sigma}(p_T) \times f^{+1\sigma}(\eta)}{f_{All}^{+1\sigma}} - \frac{f(p_T) \times f(\eta)}{f_{All}}, \quad (5.17)$$

where σ_{stat} is the statistical error, f was the parameterised fit in p_T , η and for the entire sample (All) and $+1\sigma$ were the $+1$ sigma fits from the central function value. This was also repeated with the -1 sigma curves with the largest deviation taken as the statistical error.

Total Error

The total errors, given by the statistical and systematic errors combined in quadrature, for the SF, TRF_b and TRF_c are shown in Fig. 5.12. The relative error increases rapidly at high η , due to limited statistics in that region and because the value of the scale factor drops rapidly for $|\eta| > 2$.

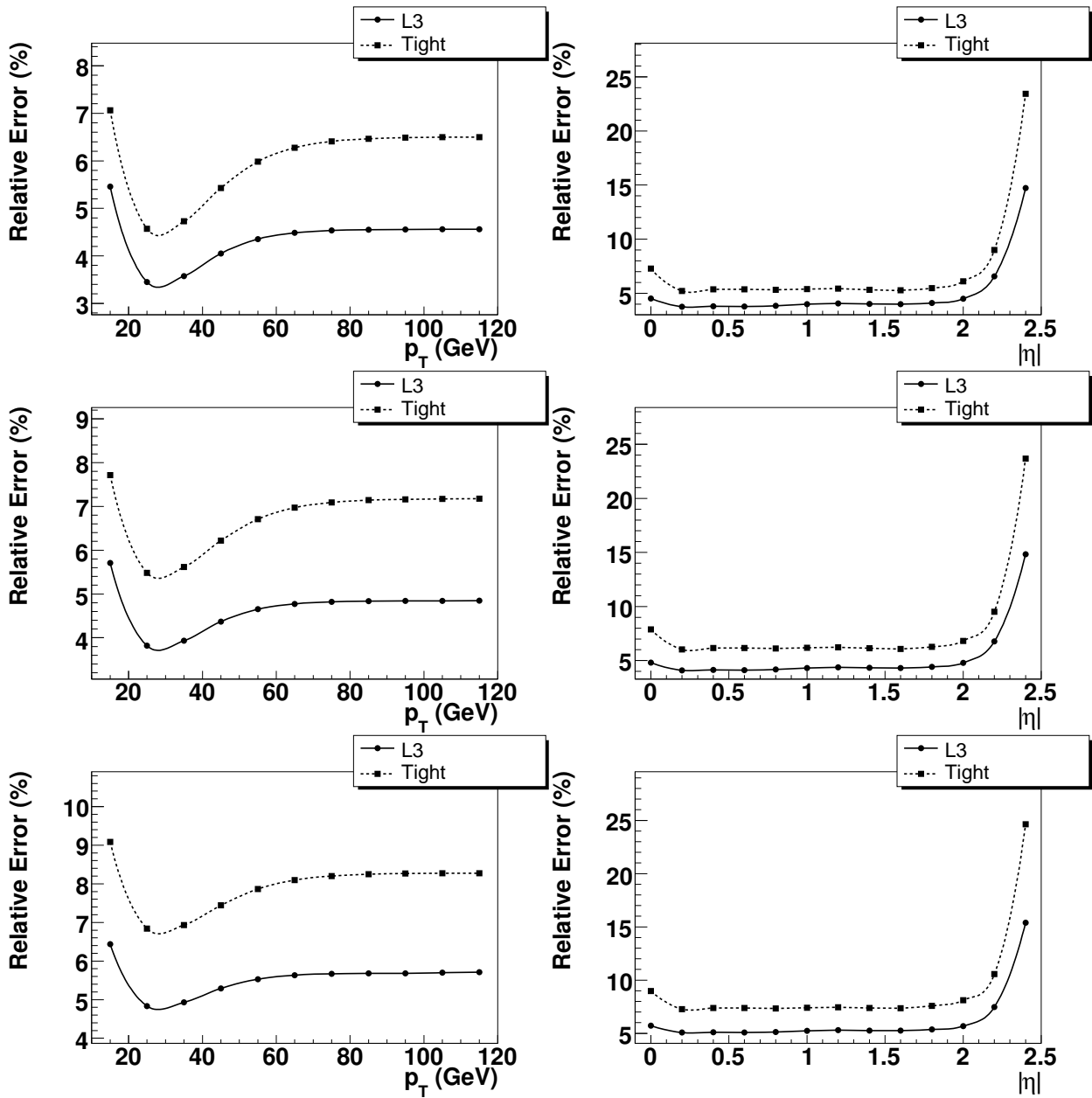


Figure 5.12: The total relative error (combined systematic and statistical) for the Scale Factor (SF) (top), TRF_b (middle) and TRF_c (bottom) in terms of p_T (left) when $\eta = 1.2$ and η (right) when $p_T = 45$ GeV.

5.5 Fake Rate

5.5.1 Negative Tags

The majority of fake tags are due to resolution effects affecting the reconstruction of the PV and tracks. The impact parameters (IP) of background tracks should be symmetrically distributed around zero (there will actually be slightly more with positive IP due to some long lived ‘light’ particles), whereas tracks from b and c particles will predominantly have positive IPs due to the long lifetimes and large masses of the decaying hadrons.

The symmetric distribution of the track IPs from light flavour and the asymmetric distribution from heavy-flavour jets can be used to construct two types of tag. Tags constructed from tracks with negative IPs have very little contribution from heavy flavour and therefore approximately describe the distribution for background tracks. Tags constructed from tracks with positive IPs will contain the vast majority of the heavy flavour signal.

Each lifetime tagging algorithm provides negative tag (NT) and positive tag (PT) results for each jet. The definition of what constitutes a NT result varies for each algorithm:

CSIP NT - Calculated in the same way as CSIP *Comb*, using tracks with negative IP significance instead of positive IP significance.

JLIP NT - Calculated in the same way as JLIP *Prob*, using tracks with negative IP significance instead of positive IP significance.

SVT NT - Secondary vertices (SV) which had a negative decay length and a $\Delta R < 0.5$ with respect to the jet.

All jets had a NT and a PT result for each of the algorithms. For the NN tagger a NT result was defined as the output from the NN when the NT results for each input variable were used as NN inputs.

5.5.2 Negative Tag Rate

The negative tag rates (NTRs) produced from the combined EM and QCD skims were used to estimate the fake tag rates (FTRs) on data. The shape of the p_T distributions were different in the forward and central calorimeter regions and so it was therefore not deemed valid to assume that the FTR factorised into p_T and η when parameterising the NTR. Thus, instead of factorising the NTR parameterisation in η and p_T , as for the S8 efficiencies (there was insufficient statistics to repeat this procedure in the S8 analysis), the NTR was parameterised in p_T in the three η regions $0 < |\eta| < 1.2$ (CC), $1.2 < |\eta| < 1.8$ (ICR) and $1.8 < |\eta| < 2.4$ (EC).

The NTRs for the NN tagger are outlined in Table 5.14 for the COMB skim and are shown for the EM, QCD and COMB samples for the Tight operating point in Fig. 5.13 along with the negative tag ratios between the QCD and EM samples.

A small discrepancy was observed between the NTRs in the QCD and EM skims, due to a bias in the EM sample from electrons and photons. To reduce the bias, jets close to EM clusters are removed. After removing these jets the difference is small enough to allow

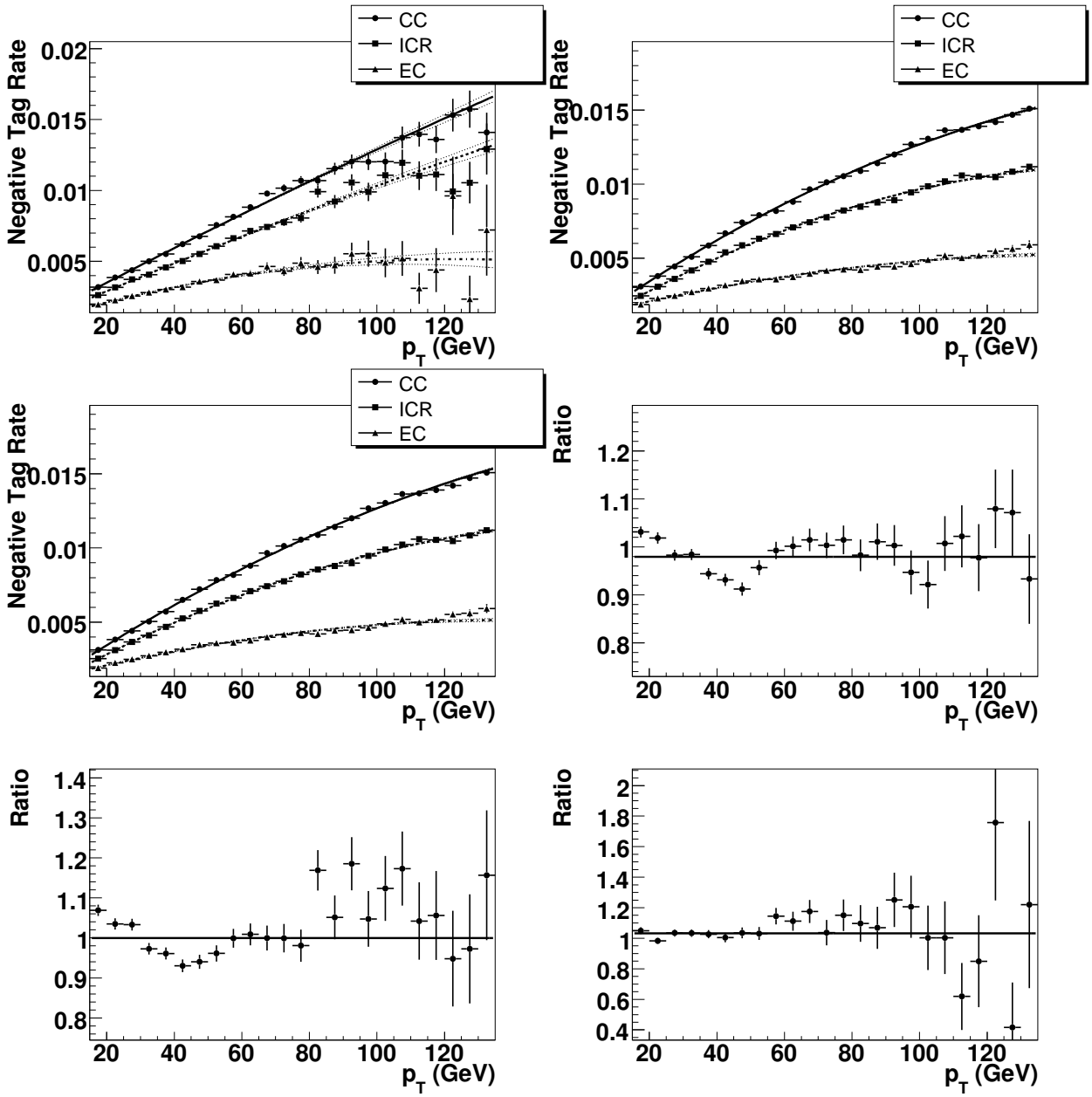


Figure 5.13: The NTR parameterisation for the EM skin (top left), QCD skin (top right), the COMB skin (middle left) and the ratio of the EM and QCD NTR in the CC (middle right), ICR (bottom left) and EC (bottom right) η regions, for the Tight operating point. The NTR was parameterised with a second order polynomial and the dotted lines show the fit error calculated using the full fit covariant error matrix.

CAL Region	L6	L5	L4	L3	L2	Loose
CC	12.4%	9.3%	7.02%	5.49%	3.97%	2.51%
ICR	11.2%	8.3%	6.16%	4.74%	3.35%	2.05%
EC	10.4%	7.6%	5.44%	4.03%	2.73%	1.55%
CAL Region	oldLoose	Medium	Tight	VeryTight	UltraTight	MegaTight
CC	2.11%	1.23%	0.717%	0.471%	0.322%	0.25%
ICR	1.7%	0.955%	0.533%	0.34%	0.227%	0.173%
EC	1.25%	0.627%	0.303%	0.172%	0.103%	0.073%

Table 5.14: Negative tag rates for the COMB skim.

Region	L6	L5	L4	L3	L2	Loose
CC	0.125%	0.147%	0.172%	0.189%	0.244%	0.301%
ICR	0.035%	0.041%	0.048%	0.055%	0.066%	0.085%
EC	0.049%	0.059%	0.077%	0.107%	0.147%	0.206%
Region	oldLoose	Medium	Tight	VeryTight	UltraTight	MegaTight
CC	0.317%	0.383%	0.47%	0.516%	0.571%	0.603%
ICR	0.093%	0.124%	0.165%	0.205%	0.25%	0.286%
EC	0.229%	0.37%	0.514%	0.54%	0.599%	0.723%

Table 5.15: Error assigned due to the EM and QCD skim NTR difference.

the combination of the QCD and EM skims to determine the fake tag rate. The NTR was determined using the COMB skim, with a systematic error assigned due to the difference between the constituent QCD and EM skims. The systematic error was calculated from a constant fit to the EM and QCD ratio. Half the difference between the fit value and unity was taken as the systematic error, or if the ratio was consistent with unity within the fit error scaled by $\sqrt{\chi^2/NDF}$, then the scaled fit error was taken as the error. The systematic errors are shown in Table 5.15.

In addition to the difference between the QCD and EM skims, the effect of removing jets close to EM clusters in the QCD sample must also be taken into account. The negative tag rate in the QCD sample with the jets removed is slightly slower than in the full QCD sample. The effect is small, ranging from 0.2% for the loosest and almost 1% for the tightest operating point, and does not depend on jet p_t . A systematic error was assigned in the same way as that for the difference between the EM and QCD skims. The systematic errors are shown in Table 5.16.

5.5.3 Parameterisation Systematic

To test the parameterisation of the NTR in the three η regions a comparison was made between the number of tags found by the tagger and the number predicted from the NTR. Figure 5.14 shows the expected number of tags and the predicted number of tags as a function of p_T in each of the η regions. A systematic error due to the parameterisation of the NTR

Region	L6	L5	L4	L3	L2	Loose
CC	0.19%	0.24%	0.28%	0.33%	0.37%	0.46%
ICR	0.17%	0.19%	0.25%	0.28%	0.29%	0.39%
EC	0.11%	0.16%	0.21%	0.26%	0.30%	0.39%
Region	oldLoose	Medium	Tight	VeryTight	UltraTight	MegaTight
CC	0.49%	0.62%	0.72%	0.78%	0.87%	0.95%
ICR	0.45%	0.55%	0.67%	0.76%	0.82%	0.86%
EC	0.39%	0.49%	0.63%	0.58%	0.67%	0.74%

Table 5.16: Error assigned due to the difference between the QCD skim with jets close to EM clusters removed, and the inclusive QCD skim.

Region	L6	L5	L4	L3	L2	Loose
CC	0.057%	0.062%	0.067%	0.071%	0.081%	0.094%
ICR	0.073%	0.080%	0.086%	0.093%	0.11%	0.13%
EC	0.063%	0.073%	0.085%	0.099%	0.12%	0.16%
Region	oldLoose	Medium	Tight	VeryTight	UltraTight	MegaTight
CC	0.097%	0.11%	0.15%	0.19%	0.22%	0.25%
ICR	0.13%	0.15%	0.20%	0.25%	0.30%	0.35%
EC	0.17%	0.25%	0.35%	0.47%	0.61%	0.72%

Table 5.17: The systematic uncertainties on the COMB skim parameterisation.

was calculated from the straight line fit to the ratio of the actual and predicted number of tags. The error was taken as the deviation of the ratio from 1, or if the ratio was consistent with 1 within the error scaled by $\sqrt{\chi^2/NDF}$, the error was taken to be the scaled fit error. The systematic errors are shown in Table 5.17.

As a cross check the actual and predicted number of tags from the COMB parameterisation were also compared with those in the QCD and EM skims and are shown in Figs. 5.15 and 5.16 with the errors outlined in Tables 5.18 and 5.19. These results should be compared to the errors assigned due to the difference between the EM and QCD skims in Table 5.15. The differences are well within the larger ratio assigned to account for the discrepancies between the skims.

5.5.4 MC Negative Tag Scale Factors

The NTR was not a perfect approximation for the PT fake rate as a contribution existed in the NTR from c and b-quarks and an asymmetry existed between the NTs and PTs due to long-lived light particles like K_S^0 , K_L^0 and Λ and due to γ conversions. An attempt is made to remove such particles [72], but tracks from unreconstructed particles still affect the results. To correct the NTR to the PT fake rate two NT correction scale factors (NT SF) were applied, both of which were measured in QCD MC.

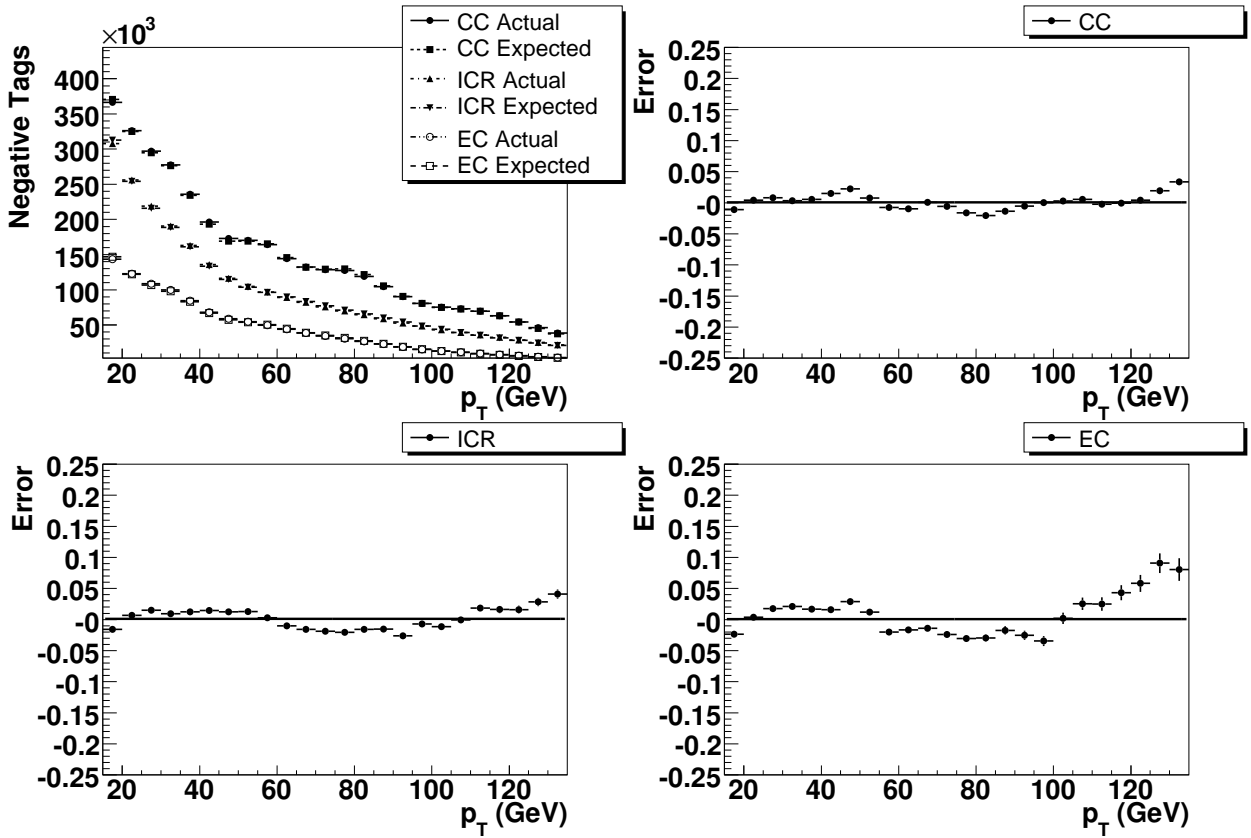


Figure 5.14: The predicted and actual number of NT in the three $|\eta|$ regions for the L3 operating point on the COMB skim (top left) and the relative difference between the actual and predicted number of NTs in the CC (top right), ICR (bottom left) and EC (bottom right) $|\eta|$ regions.

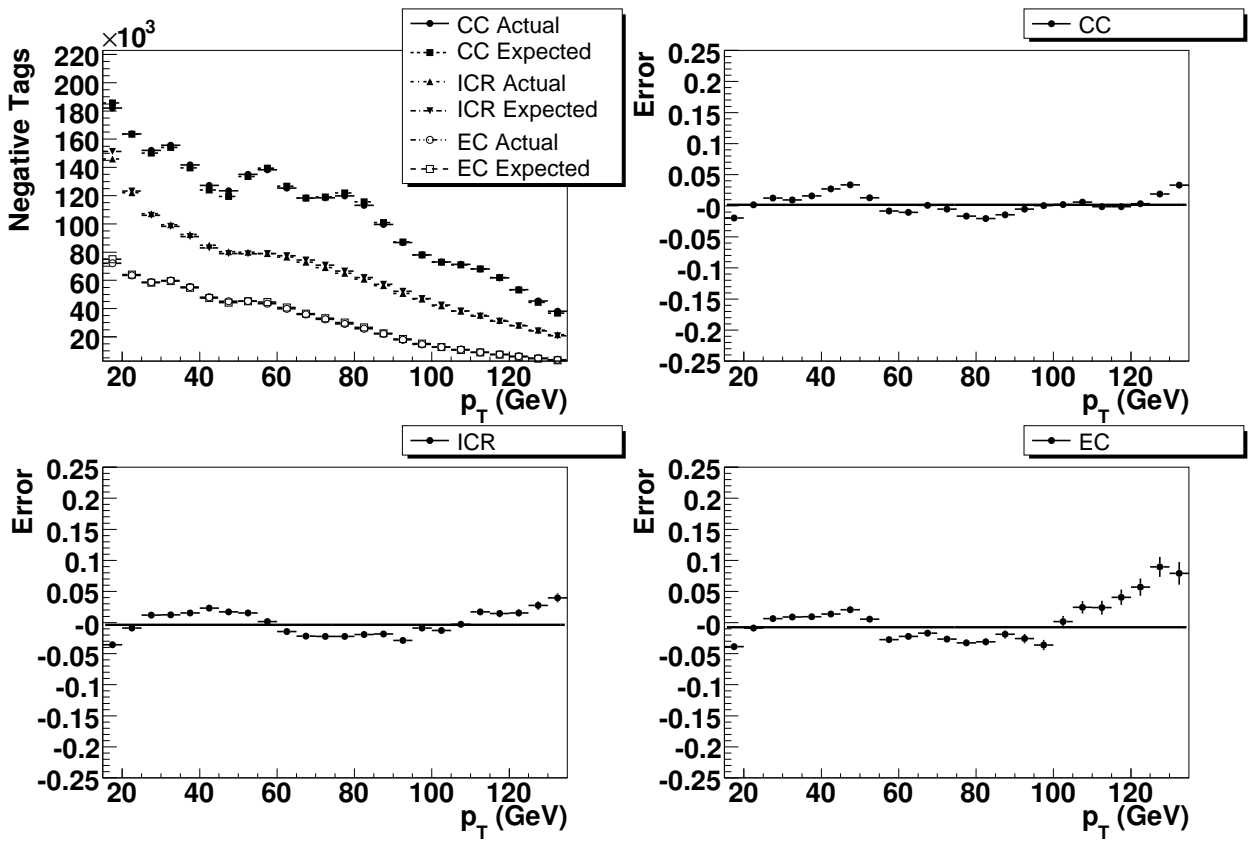


Figure 5.15: The predicted and actual number of NT in the three $|\eta|$ regions for the L3 operating point on the QCD skim (top left) and the relative difference between the actual and predicted number of NTs in the CC (top right), ICR (bottom left) and EC (bottom right) $|\eta|$ regions.

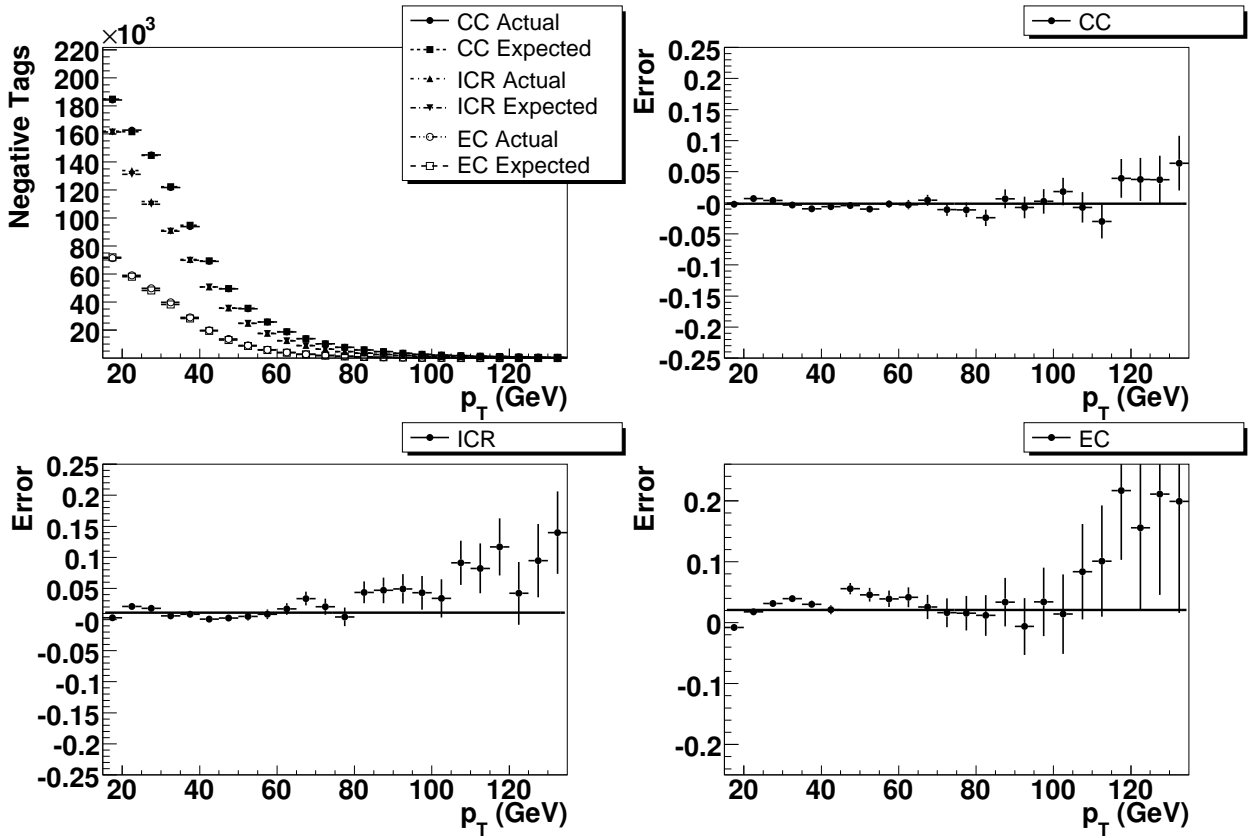


Figure 5.16: The predicted and actual number of NT in the three $|\eta|$ regions for the L3 operating point on the EM skim (top left) and the relative difference between the actual and predicted number of NTs in the CC (top right), ICR (bottom left) and EC (bottom right) $|\eta|$ regions.

Region	L6	L5	L4	L3	L2	Loose
CC	0.087%	0.11%	0.12%	0.15%	0.19%	0.23%
ICR	0.21%	0.32%	0.40%	0.38%	0.35%	0.40%
EC	0.61%	0.68%	0.74%	0.74%	0.79%	0.81%
Region	oldLoose	Medium	Tight	VeryTight	UltraTight	MegaTight
CC	0.29%	0.45%	0.47%	0.47%	0.55%	0.68%
ICR	0.32%	0.17%	0.23%	0.29%	0.35%	0.40%
EC	0.84%	0.93%	0.83%	1.1%	1.3%	1.4%

Table 5.18: The systematic uncertainties on the QCD skim parameterisation.

Region	L6	L5	L4	L3	L2	Loose
CC	0.07%	0.0801%	0.092%	0.16%	0.26%	0.34%
ICR	0.65%	0.96%	1.1%	1.1%	1.1%	1.3%
EC	1.7%	1.9%	2.06%	2.09%	2.3%	2.4%
Region	oldLoose	Medium	Tight	VeryTight	UltraTight	MegaTight
CC	0.50%	1.0%	1.1%	1.1%	1.5%	2.0%
ICR	1.1%	0.78%	0.40%	0.48%	0.60%	0.70%
EC	2.5%	2.8%	2.6%	3.5%	2.2%	4.7%

Table 5.19: The systematic uncertainties on the EM skim parameterisation.

SF_{hf} - The ratio of the light jet NTR to the total NTR.

SF_u - The ratio between the light jet PTR and the light jet NTR.

Applying these two correction factors to the NTR yielded the data FTR,

$$FTR = SF_{hf} \times SF_u \times NTR, \quad (5.18)$$

The NT SFs as a function of p_T in the three η regions are shown in Fig. 5.17 for the L3 operating point. The fit error on the NT SFs were scaled up by the $\sqrt{\chi^2/NDF}$ of the fit to account for the uncertainty in the fit parameterisations. A constant fit was used for all three regions.

5.5.5 Fake Rate

The NN tagger FTRs are shown in Fig. 5.18 and the rates for the COMB skim are shown in Table 5.20.

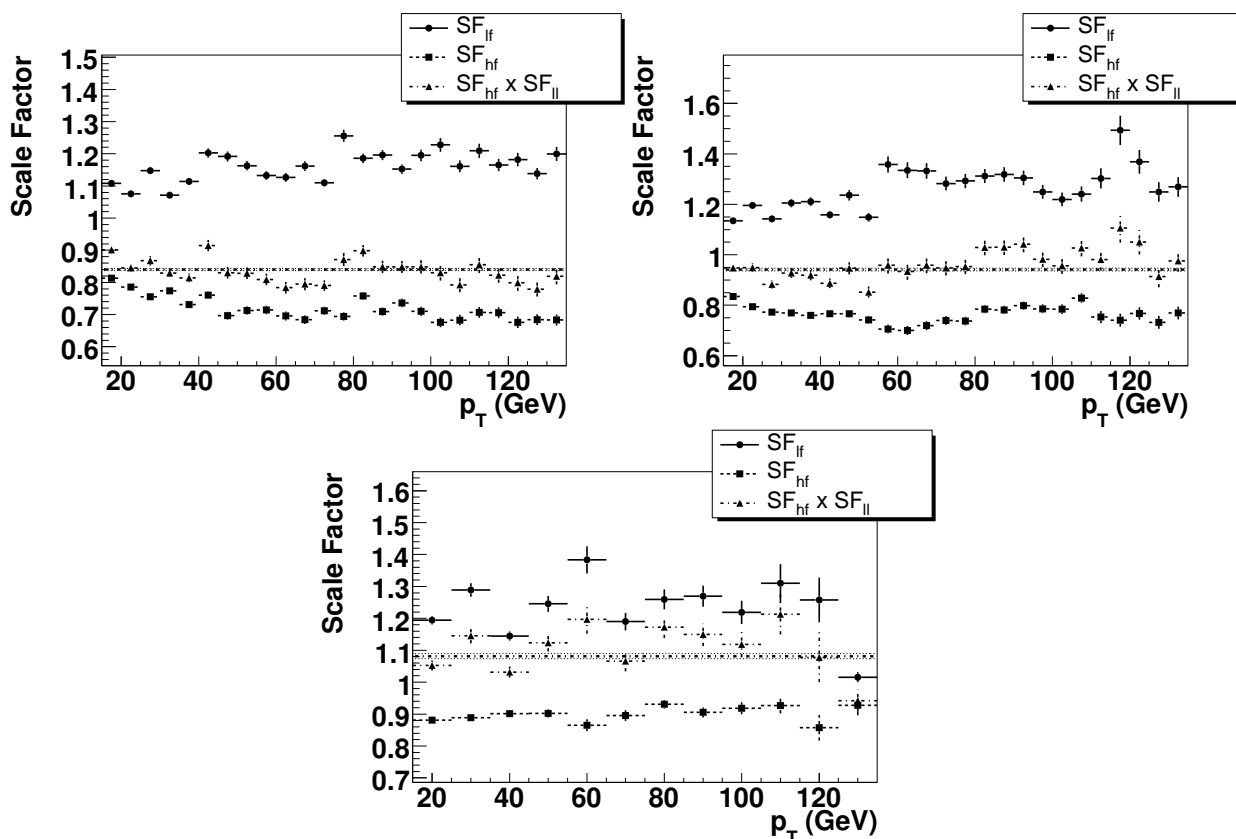


Figure 5.17: The heavy flavour correction (SF_{hf}), light jet asymmetry correction (SF_{ll}) and total NT SF correction in the CC (top left), ICR (top right) and EC regions (bottom) for the L3 operating point.

Region	L6	L5	L4	L3	L2	Loose
CC	11.1%	8.16%	6.06%	4.66%	3.28%	2.02%
ICR	10.8%	7.93%	5.86%	4.48%	3.12%	1.84%
EC	10.9%	8.08%	5.92%	4.35%	2.98%	1.69%
Region	oldLoose	Medium	Tight	VeryTight	UltraTight	MegaTight
CC	1.68%	0.958%	0.546%	0.343%	0.226%	0.169%
ICR	1.5%	0.803%	0.413%	0.244%	0.17%	0.127%
EC	1.35%	0.655%	0.299%	0.17%	0.0918%	0.0547%

Table 5.20: The data FTR calculated from the COMB NTR corrected for the presence of heavy flavour and light quark PT/NT asymmetry.

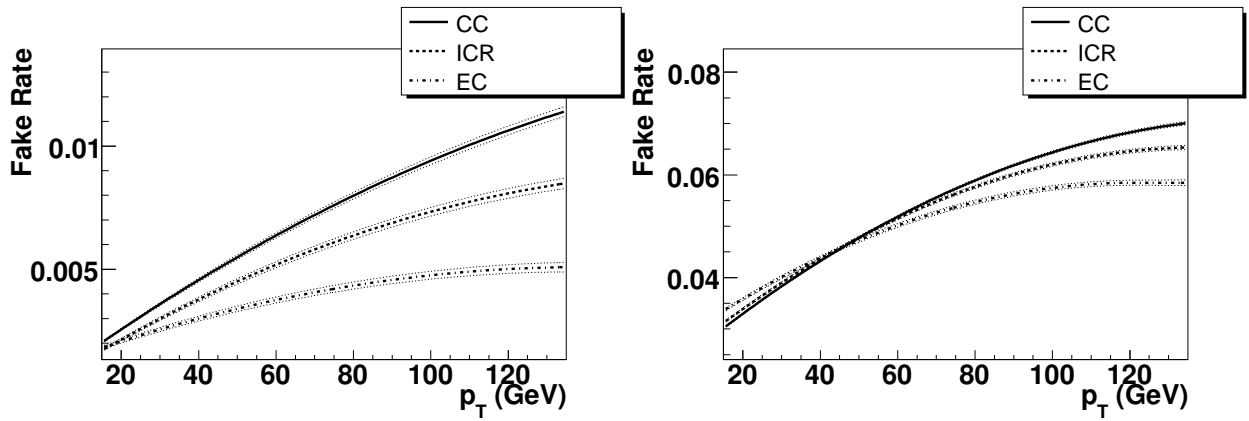


Figure 5.18: The FTRs parameterised in the three η regions for the Tight (left) and L3 (right) operating points. The fake rate was parameterised with a second order polynomial, and the dotted black lines represent the fit error calculated using the full error matrix.

Correcting the NTR with the MC SF correction introduced another systematic error due to the uncertainty in the proportions of *b* and *c* in the simulation. To estimate a systematic error the number of *b* and *c* quarks present in the MC was varied by $\pm 20\%$ and the fake rate recalculated with the largest discrepancy taken as the systematic error on the *b/c* content. The errors are outlined in Tables 5.21 and 5.22.

Region	L6	L5	L4	L3	L2	Loose
CC	1.96%	2.24%	2.57%	2.88%	3.25%	3.84%
ICR	1.56%	1.78%	2.14%	2.45%	2.8%	3.22%
EC	0.677%	0.761%	0.859%	0.929%	1.08%	1.34%
Region	oldLoose	Medium	Tight	VeryTight	UltraTight	MegaTight
CC	4.05%	4.94%	5.64%	6.08%	6.45%	6.67%
ICR	3.38%	4.1%	5.09%	5.65%	6.73%	7.07%
EC	1.38%	1.43%	1.55%	2.6%	3.68%	3.41%

Table 5.21: The systematic error in the FTR due to the uncertainty in the *b*-content in the MC.

Region	L6	L5	L4	L3	L2	Loose
CC	1.74%	1.89%	2.06%	2.22%	2.35%	2.48%
ICR	1.46%	1.6%	1.77%	1.88%	2.01%	2.15%
EC	0.874%	0.926%	1.04%	1.02%	1.03%	1.07%
Region	oldLoose	Medium	Tight	VeryTight	UltraTight	MegaTight
CC	2.48%	2.63%	2.66%	2.56%	2.48%	2.39%
ICR	2.22%	2.46%	2.4%	2.44%	2.28%	2.4%
EC	1.04%	1.14%	0.872%	1.37%	0.957%	0.935%

Table 5.22: The systematic error in the FTR due to the uncertainty in the *c*-content in the MC.

5.5.6 Total Systematics

The total systematic error for the FTR was calculated by adding the systematic uncertainties on the *b* and *c* content (as they were likely to be highly correlated) and then adding this in quadrature with the parameterisation and EM/QCD ratio systematic errors. The combined systematics are shown in Table 5.23. This error takes into account the uncertainty from the comparison of the full QCD and EM skims given in Table 5.15 and the difference between the inclusive QCD skim and the QCD skim with jets close to EM clusters removed given in Table 5.16.

Region	L6	L5	L4	L3	L2	Loose
CC	3.71%	4.15%	4.65%	5.13%	5.64%	6.36%
ICR	3.04%	3.42%	3.98%	4.4%	4.85%	5.44%
EC	1.99%	2.17%	2.44%	2.5%	2.72%	3.01%
Region	oldLoose	Medium	Tight	VeryTight	UltraTight	MegaTight
CC	6.59%	7.68%	8.41%	8.73%	9.05%	9.23%
ICR	5.66%	6.6%	7.54%	8.14%	9.07%	9.53%
EC	3.07%	3.39%	3.1%	4.76%	5.71%	5.6%

Table 5.23: Total systematic errors on the FTR, using the sample uncertainty from the full QCD and EM sample comparison (Table 5.15).

5.5.7 Total Errors

The total error on the FTR was given by adding in quadrature the total systematic error for the appropriate region to the statistical error given by the difference between the FTR central value and the $+1/-1$ sigma fit curves. The total systematic errors are given in Table 5.23. The dominant error is the systematic error although the statistical error on the fits has an increasing contribution as the operating point becomes tighter.

5.6 Performance on Data

The Run II data performance of the NN and JLIP taggers as measured on data including full statistical and systematic errors on the measurement is shown in Fig. 5.19 for all jets and also for jets with $|\eta| < 0.8$ and $p_T > 30$ GeV. The NN tagger demonstrates considerable improvement over the JLIP tagger, which was the most-used tagger before the NN tagger was developed, for all operating points.

The data performance of the NN tagger was also evaluated on two MC samples with the tagging performance and error calculated jet by jet using the derived data TRFs for b, c and light flavour jets. This demonstrates the overall performance and error of the NN tagger when the data TRFs are applied jet by jet to a MC sample. The performance is shown for all jets in the $Z \rightarrow b\bar{b}$ and $Z \rightarrow q\bar{q}$ MC and also for jets in the with $|\eta| < 1.2$ and with $p_T > 30$ GeV for QCD b and uds-jets in Fig. 5.20.

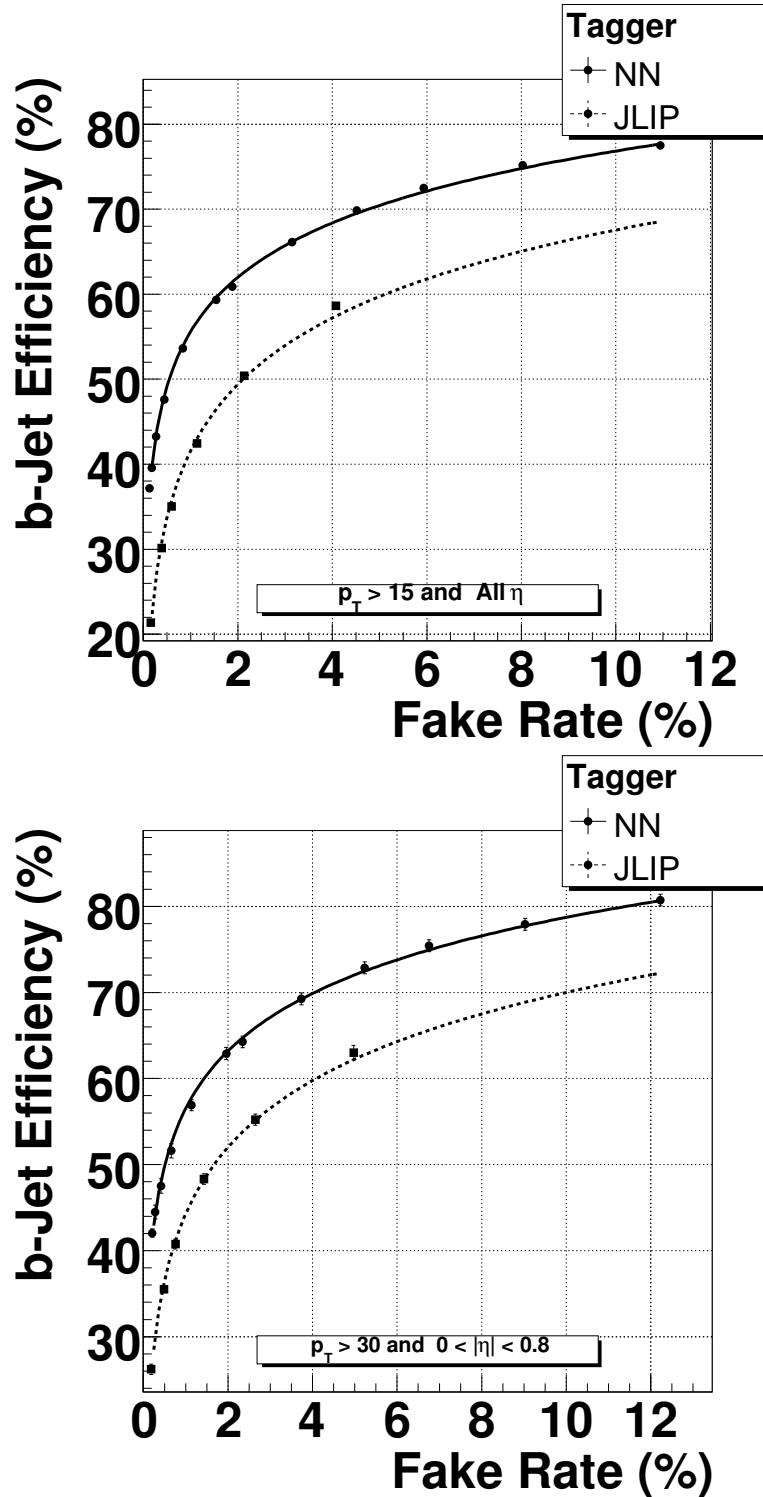


Figure 5.19: Performance profile of NN and JLIP taggers on the BID and COMB skim. The top plot is for all jets and the bottom plot for jets with $|\eta| < 0.8$ and $p_T > 30$ GeV. The error on the plots represents the total uncertainty, statistical and systematic, on the performance measurements. The NN tagger demonstrates large performance gains over the JLIP tagger, with increases in efficiency of up to 50% for a fixed fake rate. Fake rates are typically reduced to between a quarter and a third of their value for a fixed signal efficiency.

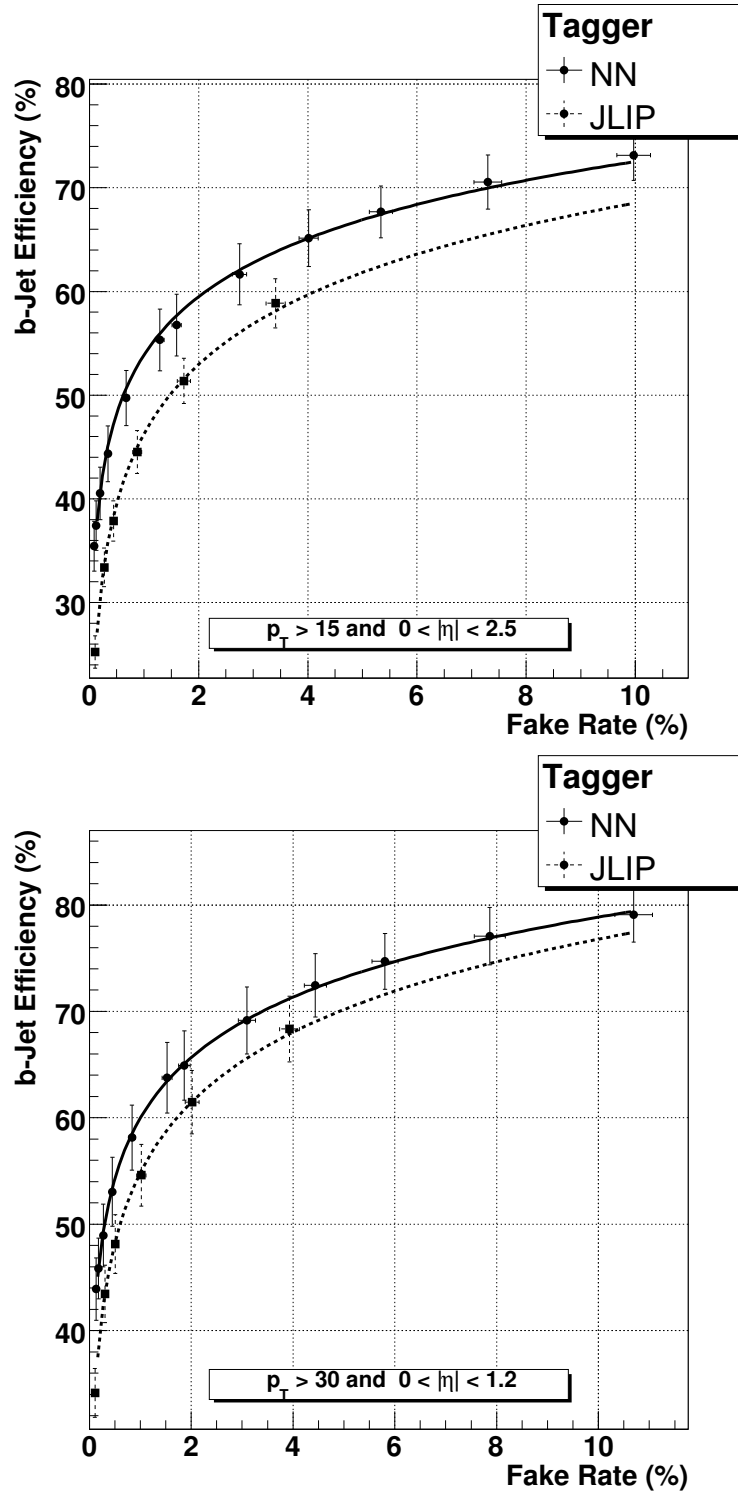


Figure 5.20: Performance of NN and JLIP taggers on the $Z \rightarrow b\bar{b}$ and $Z \rightarrow q\bar{q}$ MC samples (top) and the QCD $b\bar{b}$ and the QCD $q\bar{q}$ MC samples for $|\eta| < 1.2$ and $p_T > 30$ GeV (bottom). The performance is calculated from the NN and JLIP TRFs derived from data on a jet by jet basis. The error represents the full statistical and systematic error due to the uncertainty with which we know the data efficiency and fake rate for the entire sample when calculated per jet.

Chapter 6

Search for WH production in the Muon plus b-Jets Channel

The most sensitive analysis channel at the Tevatron for a Higgs mass below ~ 135 GeV is the associated production of a Higgs boson with a W boson. A search for $W^\pm H$ production in the $e\nu_e b\bar{b}$ decay channel using 174 pb^{-1} of $D\bar{O}$ data has already been published [74]. The search presented in this thesis is based on events with one muon, missing transverse energy \cancel{E}_T to account for the neutrino in the W boson decay, and exactly two jets with at least one of them b-tagged, using about 1 fb^{-1} of data.

In double b-tagged events, the dominant backgrounds to $W^\pm H$ are $W^\pm b\bar{b}$ production, $t\bar{t}$ and single-top quark production. In single b-tagged events, multijet events and W^\pm production in association with c and/or light jets also provide important contributions to the background. The $W^\pm + \text{light jet}$ background dominates if no b-tag is applied.

With only 1 fb^{-1} , it is not possible to observe the presence of Higgs bosons directly [16]. Therefore, we set an upper limit on the cross section.

Outline of the analysis

First, data events containing at least one muon are selected from a data sample acquired with single-muon triggers. The trigger selection and the luminosity determination are described in Section 6.1.

From this dataset events are selected with exactly two jets, one muon and missing transverse energy to account for the neutrino. Events with a second lepton are rejected. Finally, an extra W^\pm selection cut was considered to help reject background. These steps are described in Section 6.2.

The data are compared to predictions for the signal and for various background sources. The signal and most backgrounds are simulated using Monte Carlo. A separate case is the multijet background, where a muon in a jet passes isolation criteria and is seen as an isolated muon. This ‘‘QCD’’ background cannot be simulated very well, and is estimated from data. The same event selection is applied to the simulated events, but instead of applying the triggers, each event is weighted with an efficiency determined from data. The generation of Monte Carlo samples and the weighting are described in Section 6.3. Estimation of the QCD background is described in Section 6.4.

Finally, the NN b -tagger is applied to the jets in the data and background samples. The tagging is explained in Section 6.5.

Systematic uncertainties are discussed in Section 6.6. Based on the dijet mass distributions of the data and the predicted background, an upper limit on the Higgs production cross section is determined in Section 6.7.

6.1 Luminosity and Triggers

6.1.1 Triggers

The trigger requirement for events to pass is an “OR” of different single-muon triggers depending on the running period, indicated by the trigger list version. Table 4.6 shows the triggers used in each trigger list version.

The dataset obtained encompasses seven different trigger lists which are grouped in four different supersets, namely v8-11, v12, v13 and v14. The analysis is performed on each of these supersets separately. The results are combined thereafter.

In the Monte Carlo, the triggers are taken into account by re-weighting the simulated events on an event by event basis with an efficiency derived from data. The efficiency of the “OR”ed trigger has been determined using a tag-and-probe method on di-muon Z events as described in Section 4.3.1. It is parameterised as a function of muon φ and detector η . Because the efficiency is determined on an object-by-object basis (i.e. the “probe” muon must match the muon trigger information), the muon must also be matched to the muon trigger object in the data selection.

The influence of the trigger on the shapes of kinematic variable distributions must be considered. Figure 6.1 shows four important kinematic variables for this analysis: muon E (a), p_T (b), η (c) and φ (d). The background processes are grouped in three categories: the dominant $W^\pm + \text{light jets}$ background, the multijet background (“QCD”) and the other backgrounds (“SM bkgd”). The background contributions are described in more detail in Section 6.3 and Section 6.4. The shape of the data distributions is well described by the expected background.

6.1.2 Luminosity

The luminosity corresponding to the data is determined using the $D\bar{O}$ luminosity system (see Section 3.2.2). The luminosity is computed using the trigger term JT_125TT, which is never prescaled throughout the entire analysed dataset. Table 6.1 shows the luminosity contribution breakdown for the considered trigger ranges. The total luminosity considered is 1.05 fb^{-1} .

The uncertainty on the measured luminosity is 6.1% [75]. The signal and background samples are scaled to the measured luminosity except the $W^\pm jj$ sample, which is normalized to data, and the QCD background which is estimated directly from data. The uncertainty is taken into account in the limit extraction for all the other samples.

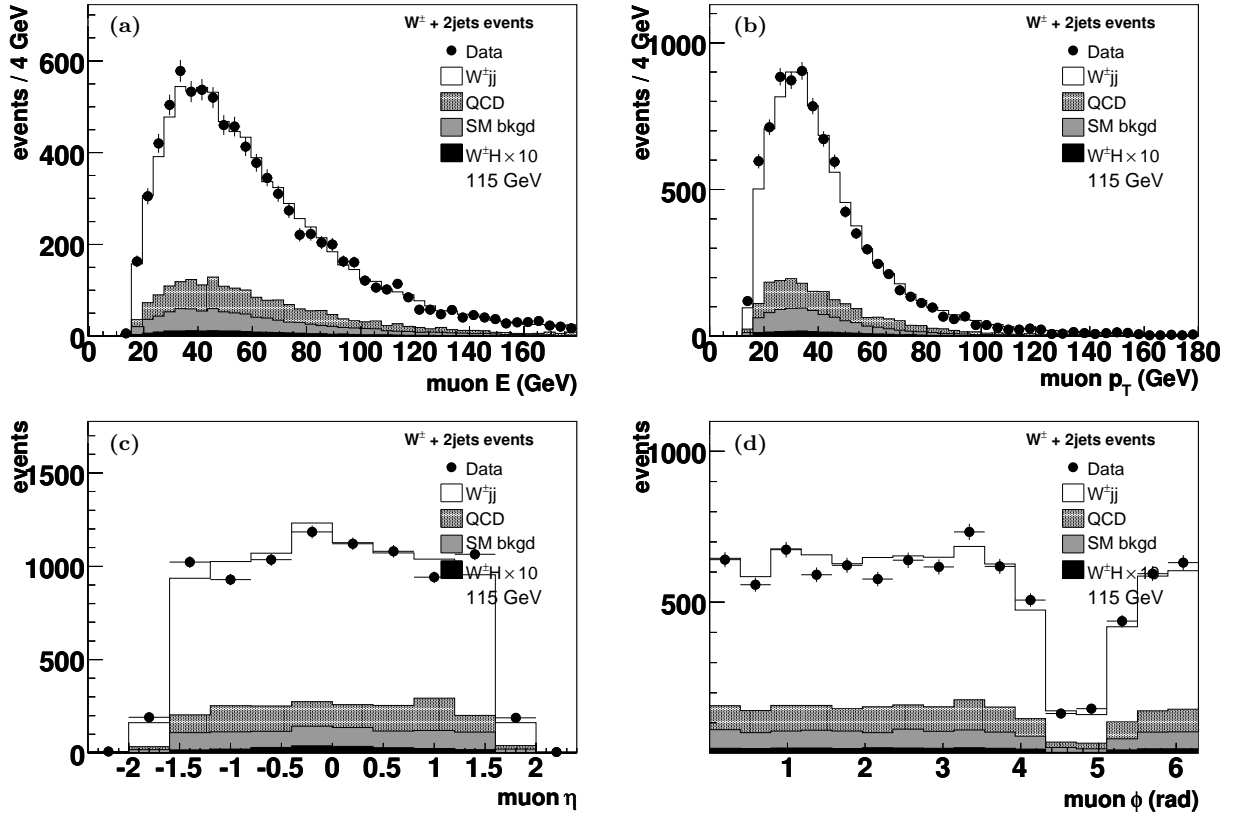


Figure 6.1: Kinematic distributions for muons of the $W^\pm + \text{jets}$ event sample when using the “OR”ed trigger condition: a) muon E ; b) muon p_T ; c) muon η ; d) muon φ .

List	Luminosity (pb^{-1})
v8 - v10.3	31.77
v10.3 - v12	74.75
v12 - v13	231.21
v13 - v13.2	38.05
v13.2 - v14	337.49
v14 - v14.6	142.23
v14.6 - v15	190.77
Total	1046.27

Table 6.1: Recorded luminosity for the v8-v14 trigger lists.

6.2 Event selection

The physics event selection focuses on $W^\pm H \rightarrow \mu\nu_\mu b\bar{b}$ events: one muon, \cancel{E}_T to account for the neutrino, and two jets. Events with an additional lepton isolated from jets and having

a large transverse momentum are rejected to decrease the Z and $t\bar{t}$ dilepton backgrounds. A W^\pm selection cut was used to help reduce QCD background. These cuts are described in the following sections.

6.2.1 Data preselection

Runs marked as “bad” for the calorimeter, muon system or central tracking systems are discarded from the analysis. To ensure a good luminosity measurement only events which do not belong to bad luminosity blocks are selected (see Section 3.2.2). Subsequently, the complete dataset is submitted to the following pre-selections:

- A primary vertex is required with $|z| < 60$ cm and at least three attached tracks;
- At least one muon with $p_T > 15$ GeV must be present;
- There must be at least two jets with $p_T > 15$ GeV and $|\eta| < 2.5$, after JES corrections.

The jets have L1 calorimeter confirmation from the trigger to help reject fake jets. The muons must satisfy the following criteria:

- *medium* quality (see Section 4.4.1);
- matching segments in both the A and BC layer;
- a matching central track with $\chi^2/\text{NDF} < 4$ for the central track fit.

The muon must also match the muon trigger objects that caused the trigger to fire, since the efficiency for the muon triggers was determined taking this match into account. This sample is also used to determine the QCD background in Section 6.4.

6.2.2 Muon isolation

Muons coming from the leptonic decay of W bosons tend to be isolated from jets and they have a relatively high transverse momentum in comparison to muons originating from semi-leptonic decays of heavy flavoured hadrons, which are usually associated with jets. A loose isolation criterion is defined by the spatial separation ΔR between a muon and jets in the (η, φ) plane. Here, the distance between a muon and the nearest good jet is required to be $\Delta R(\mu, \text{jet}) > 0.5$. The *loose* event sample is defined as the sample of events passing the preselection cuts and having one muon satisfying the loose criterion.

However, the jets from heavy flavoured hadrons are not always reconstructed properly and a muon originating from a semi-leptonic decay of a heavy flavoured hadron may seem isolated. These muons constitute the main background. Therefore, tight isolation criteria are applied. To this end, the two variables Halo and TrkCone are introduced:

- Halo(0.1, 0.4) is the scalar sum of transverse calorimeter energy clusters in a hollow cone around the muon between $\Delta R = 0.1$ and $\Delta R = 0.4$. Only electromagnetic and fine hadronic calorimeter cells are taken into account in the calculation of this variable, since there is significantly more noise in the coarse hadronic calorimeter.

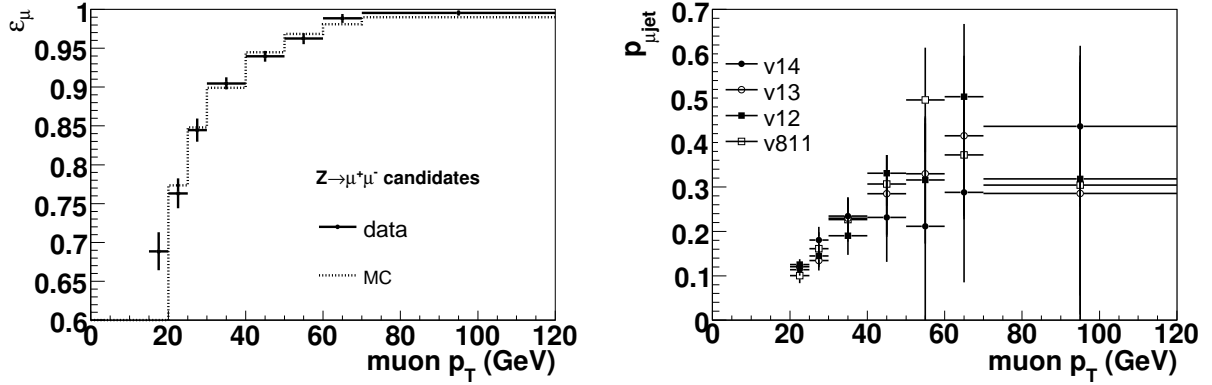


Figure 6.2: Efficiency (left) and fake rate (right) of the tight muon isolation criteria as a function of p_T .

- TrkCone(0.5) is the scalar sum of the transverse momentum of all tracks within a cone of radius $\Delta R = 0.5$ around the muon. The track matched to the muon is excluded from this sum.

The separation between muons originating from W boson decays and those coming from semi-leptonic heavy flavor hadron decays can be improved by exploiting the difference between their transverse momentum spectra [76]. Therefore, the ratio of the halo and track cone isolation criteria and the muon transverse momentum

- $\text{Rat11} = \text{Halo}(0.1, 0.4)/p_T(\mu) < 0.08$
- $\text{RatTrk} = \text{TrkCone}(0.5)/p_T(\mu) < 0.06$

are used to define *tight* muons. In combination with the kinematic cuts described above, the tight isolation criteria reject 89% of QCD background while having an efficiency of 88% for $W^\pm jj$ events.

Efficiency of muon isolation criteria

To determine the QCD background, the efficiency and fake rate of the muon isolation criteria were determined by looking at events with two jets with $p_T > 20$ GeV and $\cancel{E}_T < 10$ GeV, and one muon passing loose isolation criteria. Remaining W^\pm events were subtracted statistically. In those events no real isolated muons should be present. The fake rate $p_{\mu,\text{jet}}$ was given by the fraction of events in which the muon passed the tight isolation criteria. The efficiency for real isolated muons $\varepsilon_{\text{tight}}$ was determined using the tag-and-probe method in $Z \rightarrow \mu\mu$ events with two jets. Previous studies found a strong dependence of the fake rate on the lepton p_T [77]. The dependence of the isolation efficiency $\varepsilon_{\text{tight}}$ and fake rate $p_{\mu,\text{jet}}$ is shown in Fig. 6.2.

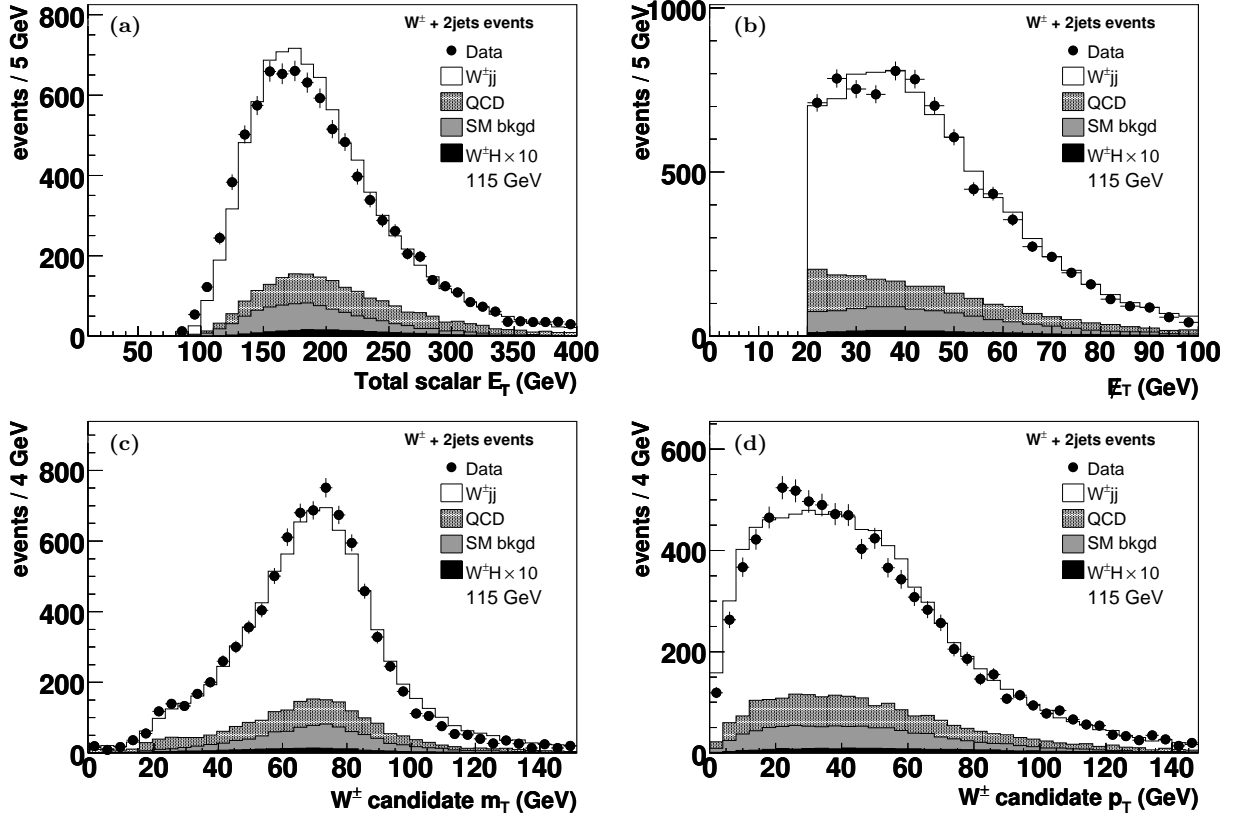


Figure 6.3: Distributions for scalar and missing transverse energy compared to the simulated expectation (ALPGEN): total scalar (a) and missing (b) transverse energy in each event, transverse mass m_T (c) and transverse momentum p_T (d) of the W^\pm candidates.

6.2.3 Missing E_T requirement and W boson transverse mass

Since W boson decays are produced in the searched process, large transverse missing energy, $\cancel{E}_T > 20$ GeV, is required. The calorimetric missing transverse energy is determined according to the CALGO/MET prescription that does not use unclustered energy in the coarse hadronic (CH) calorimeter for the calculation of \cancel{E}_T [52]. \cancel{E}_T is also corrected for the presence of any muons. All corrections to muons and jets are propagated into \cancel{E}_T .

The distributions of the scalar and missing transverse energy are shown in Fig. 6.3a and b and compared to the expected background distributions.

W bosons can be produced in conjunction with jets. The transverse momentum and transverse mass of the W boson can be reconstructed from the muon and \cancel{E}_T kinematics. The transverse mass m_T is defined as

$$m_T^2 = 2\cancel{E}_T \cdot p_{T\mu}(1 - \cos \Delta\phi(\mu, \hat{\cancel{E}}_T)), \quad (6.1)$$

where $\Delta\phi(\mu, \hat{\cancel{E}}_T)$ is the azimuthal angle between the muon and the \cancel{E}_T direction. The distribution of m_T forms a Jacobian peak, an asymmetric distribution which peaks just below

the W boson mass. Figure 6.3c shows the transverse mass distribution of the muon and \cancel{E}_T when two jets with p_T above 20 GeV are required in the final state. The Jacobian peak of the partly reconstructed W boson is clearly visible and provides evidence for $W^\pm + 2$ jets production. The transverse momentum of the reconstructed W boson is shown in Fig. 6.3d. Agreement in shape and normalisation is observed between data and simulation.

In the transverse momentum distribution the QCD background becomes more important for values above roughly 40 GeV. This is due to the selection cuts of 20 GeV transverse momentum on the candidate muon and 20 GeV on \cancel{E}_T . Those events passing the two kinematic cuts, concentrate at low “W” transverse masses [77]. These events can be removed by applying a cut on the angle between the muon and the \cancel{E}_T , as described in Section 6.2.6.

6.2.4 Jet properties

The reconstruction and selection of jets used in this analysis is described in Section 4.4.2. Differences in energy scale and resolution between data and MC have been further reduced using the JSSR algorithm [46] (see Section 4.2.2).

The jet properties in the $W^\pm jj$ sample are well reproduced by the simulation. The distributions of jet properties and kinematics in the simulation compared to those in data are shown in Fig. 6.4–6.7. The distributions of the main jet properties (EMF , CHF , f_{90}) in data and simulation are shown in Fig. 6.4. The kinematic distributions of the leading jet and next to leading jet are shown in Fig. 6.5 and Fig. 6.6.:

Figure 6.7 shows the combined distributions for the two jets in each event. Figure 6.7a shows the scalar sum of the p_T of the jets, H_T . Figure 6.7b shows the distance ΔR between the two jets. The data peak for a distance around π , meaning that the jets are often back-to-back in azimuth. Figure 6.7c shows the invariant mass of the two jets. There is a reasonable agreement in normalisation and shape for masses above 60 GeV.

6.2.5 Second lepton veto

To reduce $t\bar{t}$ background, any event containing more than one “loose” muon is rejected. Events with an electron candidate are rejected if it passes the following criteria:

- Transverse momentum must be larger than 18 GeV;
- A large fraction of energy must be deposited in the electromagnetic section of the calorimeter ($EMF > 0.9$);
- The cluster must be isolated in the calorimeter (isolation < 0.15);
- It must have a matched track within $\Delta R < 0.05$;
- The shower shape must be consistent with that of an electron;
- The electron likelihood (see Section 4.4.3) must be larger than 0.85. $p_T > 18$ GeV.

This cut reduces the $t\bar{t}$ background by about 16% while being almost 100% efficient for $W^\pm H$ events.

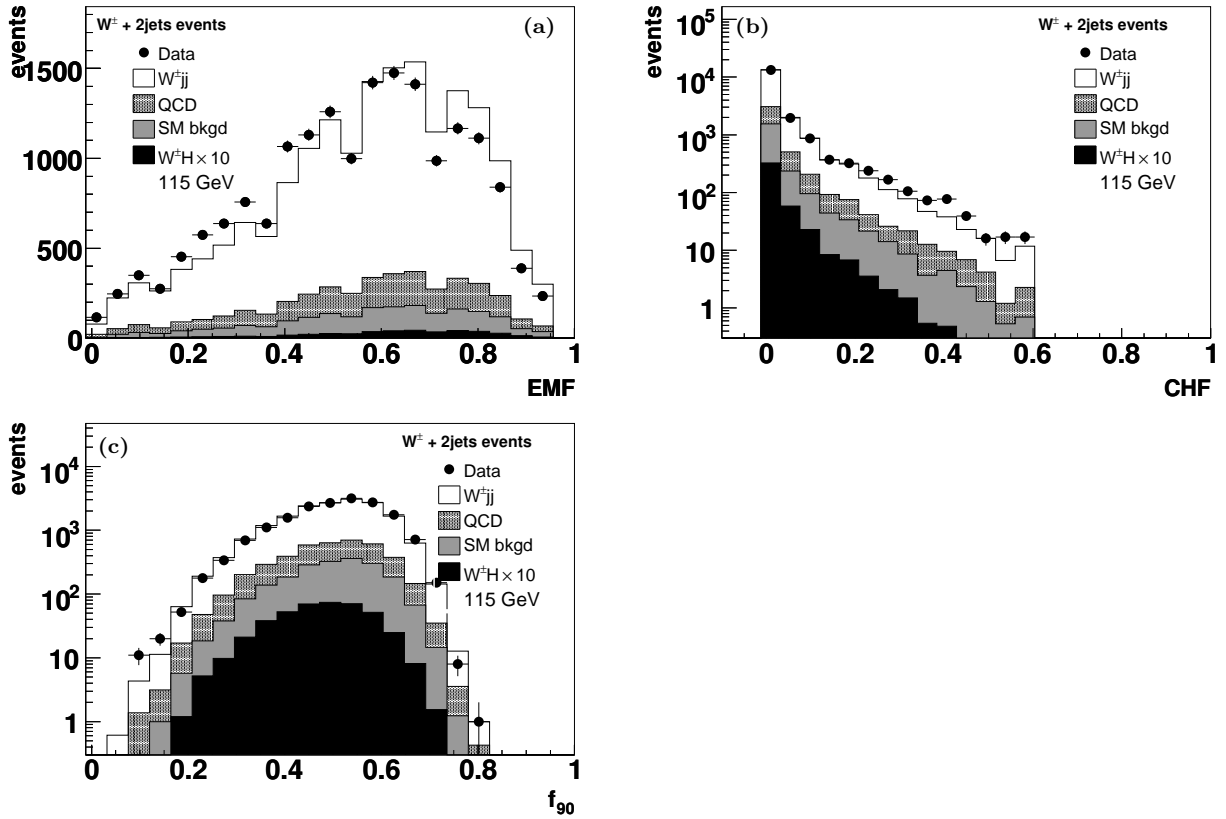


Figure 6.4: Jet ID parameters EMF (a), CHF (b) and f_{90} (c) for data and simulated background.

6.2.6 W selection cut

To further reduce the background, a cut was applied on the angle between the muon and the missing transverse energy of $\Delta\phi(\mu, \hat{E}_T) > 1.1 - (1.1/80) \times \hat{E}_T$. The distribution of $\Delta\phi(\mu, \hat{E}_T)$ is shown in Fig. 6.8. The cut is very efficient for the QCD background, rejecting 64% of QCD events before tagging (but after applying tight muon isolation criteria) and keeping 94% of $W^\pm H$ events. Although the cut is not efficient against the $W^\pm jj$ and top quark backgrounds the final performance was still improved.

6.3 Simulated Event Samples

The Monte Carlo samples used in the analysis are described in Section 4.2.1. The simulated events have been re-weighted with the trigger efficiencies, and corrected for differences in reconstruction and tagging efficiencies and resolution between data and Monte Carlo. These differences are taken into account by applying scale factors, which are constant or have a kinematic dependence depending on the scale factor considered. The uncertainties associated with the scale factors are described in Section 6.6.

The simulated background processes are absolutely normalised to the SM prediction of

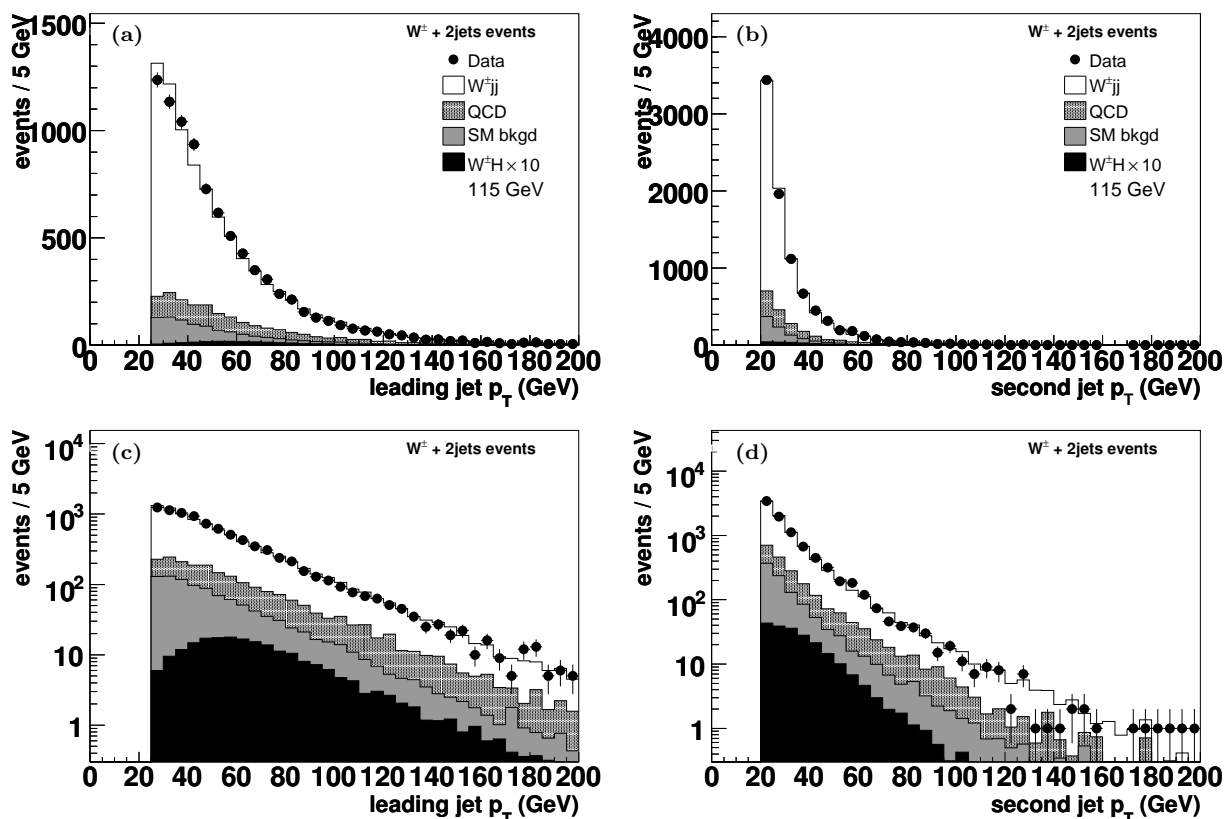


Figure 6.5: Distributions of the transverse momentum of the jets of each event compared to the simulated expectation. a) leading jet; b) second jet, ordered in p_T ; c) as a), in logarithmic scale d) as b), in logarithmic scale

their cross section as given in Tables 4.1 to 4.4, except for the $W^\pm jj$ sample. The $W^\pm jj$ sample is normalised to data after first subtracting the other expected background and signal processes from the data. When we use the NLO theoretical K-factor of 1.35, the normalisation factor data/MC is 0.99.

For clarity of presentation, some samples have been grouped together:

- $W^\pm H$ includes the $W^\pm H \rightarrow \mu\nu_\mu b\bar{b}$ and $W^\pm H \rightarrow \tau\nu_\tau b\bar{b}$ samples;
- $W^\pm Z$ includes all the diboson processes (WW , $W^\pm Z$ and ZZ);
- $W^\pm b\bar{b}$ also includes $Zb\bar{b}$;
- $W^\pm jj$ includes $W^\pm jj \rightarrow \ell\nu jj$ and $Zjj \rightarrow \ell^+\ell^- jj$ ($\ell = e, \mu$);
- $W^\pm c\bar{c}$ also includes $Zc\bar{c}$ and $Zjj \rightarrow \tau\tau jj$.

The remaining Monte Carlo samples are the $t\bar{t}$ and single top samples.

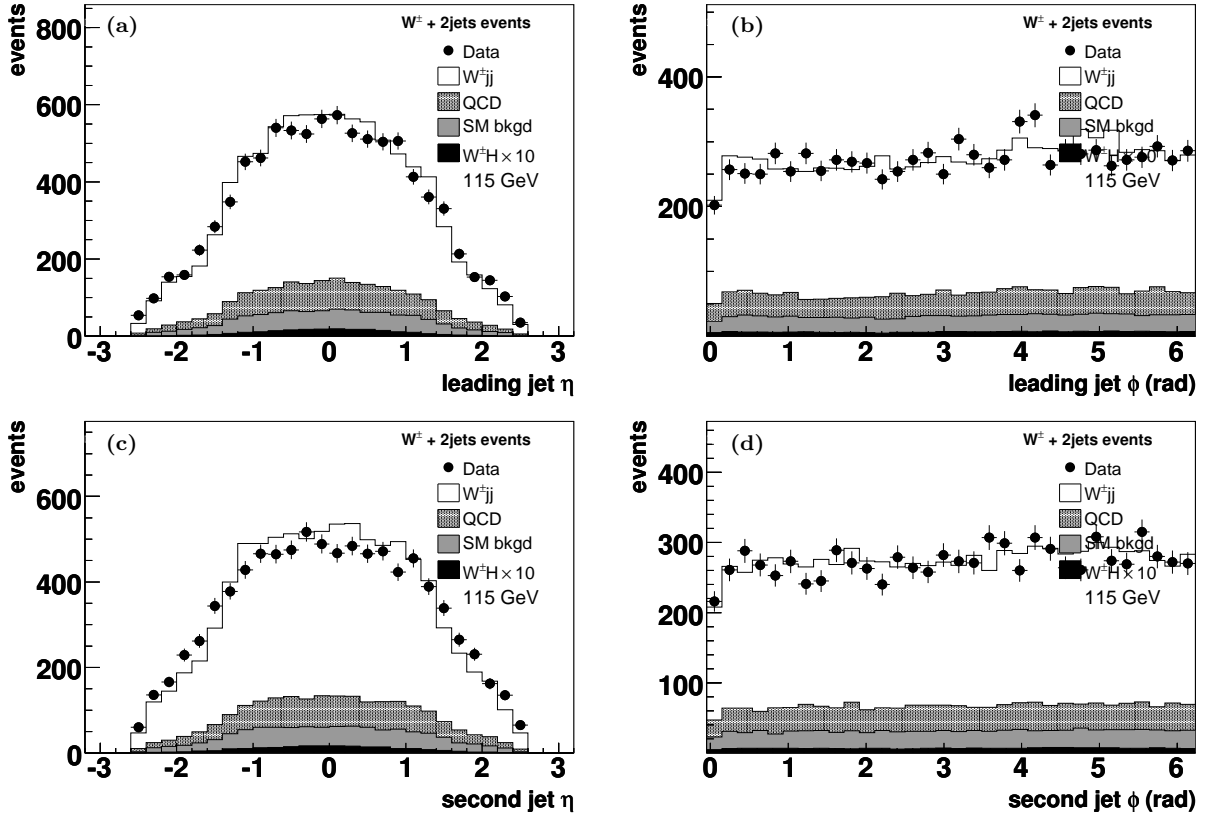


Figure 6.6: Distributions of η and φ of the leading and second jet compared to the simulated expectation. a) η of leading jet; b) φ of leading jet; c) η of second jet; d) φ of second jet;

6.4 Multijet (QCD) background

To estimate the number of multijet (QCD) events with a muon originating from a jet and passing the muon identification criteria, the probability $p_{\mu\text{jet}}$ for such a muon passing the *tight* muon isolation criteria is used (see Section 6.2.2). The dependence of $p_{\mu\text{jet}}$ on p_T is slightly different for the different trigger list versions, thus the muon from jet fake rates are applied consistently to each trigger list sub-sample separately. The QCD background is then estimated for every differential distribution applying the p_T dependent muon from jet rate in the matrix method [78] that has been applied to the tight event sample (containing N_{tight} events) and to the loose event sample (containing N_{loose} events). Defining the number of signal and QCD background events as N_μ and N_{QCD} , the equations

$$N_{\text{loose}} = N_\mu + N_{\text{QCD}} \quad (6.2)$$

$$N_{\text{tight}} = \varepsilon_{\text{tight}} N_\mu + p_{\mu\text{jet}} N_{\text{QCD}} \quad (6.3)$$

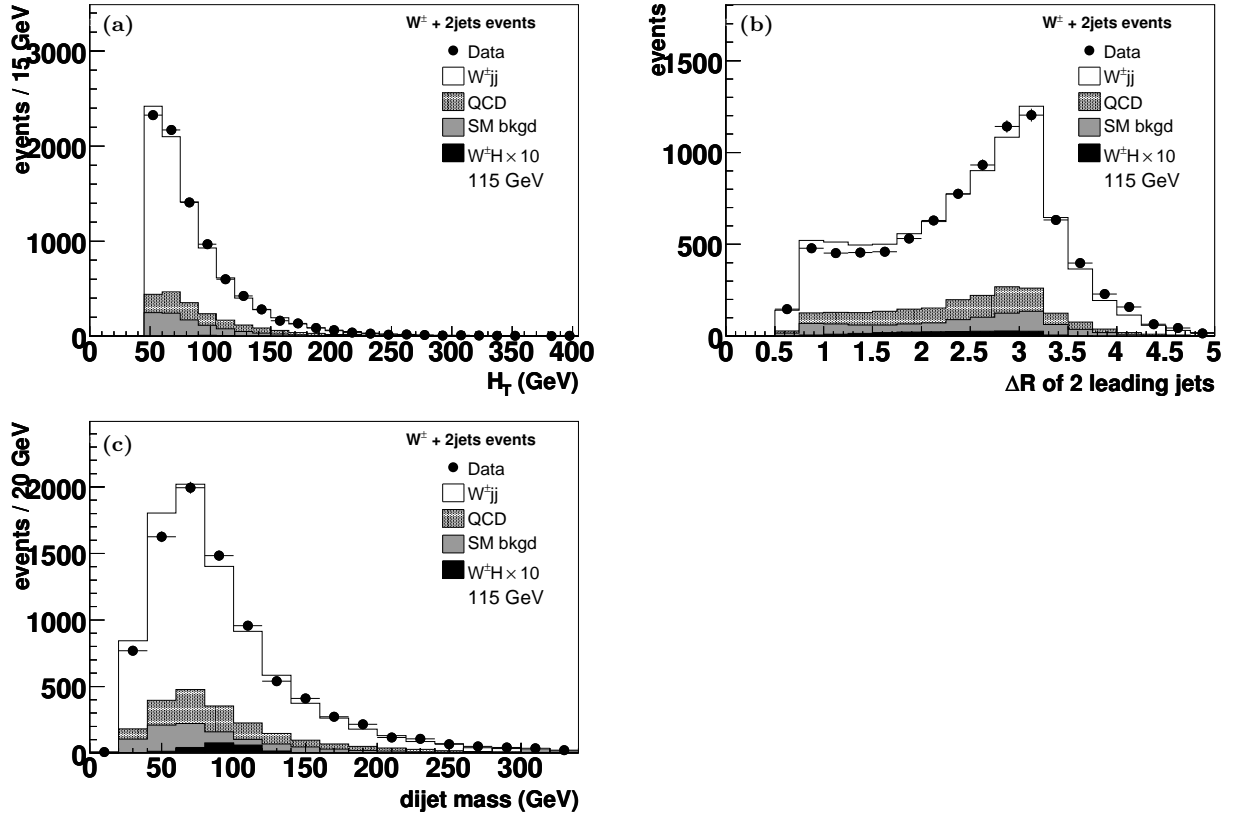


Figure 6.7: Distribution of H_T (a), ΔR (b) and dijet mass (c) between the two leading jets.

can be formulated and subsequently solved. Their solution is given by

$$N_\mu = \frac{N_{\text{tight}} - p_{\mu\text{jet}} N_{\text{loose}}}{\varepsilon_{\text{tight}} - p_{\mu\text{jet}}} \quad (6.4)$$

and

$$N_{\text{QCD}} = \frac{\varepsilon_{\text{tight}} N_{\text{loose}} - N_{\text{tight}}}{\varepsilon_{\text{tight}} - p_{\mu\text{jet}}} \quad (6.5)$$

The distributions of the energy, p_T , η and φ of the muons are shown in Fig. 6.1. The p_T distribution is described by the sum of the simulation and the QCD background derived from the data.

6.5 *b*-Tagging

For tagging heavy flavoured jets the Neural Net *b*-tagging algorithm (see Chapter 5) has been used. To optimise the number of signal events, two separate tagged samples are created: a double tag sample and a single tag sample.

The NN tag operating point is first set to L3 (NN cut > 0.25), which corresponds to a fake rate of about 4.5% for a jet p_T of 50 GeV. If two jets are tagged, the event is selected as

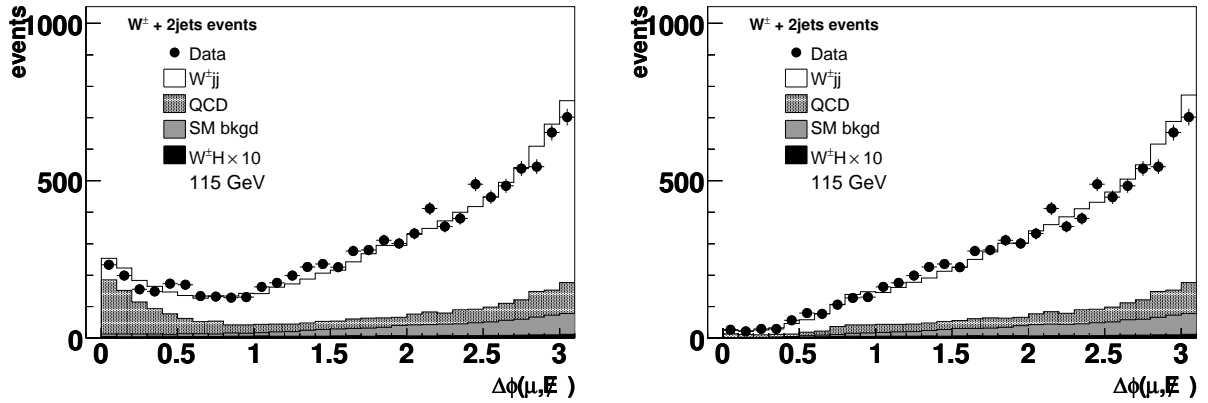


Figure 6.8: Distribution of the angle between the muon and the \cancel{E}_T direction, $\Delta\phi(\mu, \cancel{E}_T)$, before (left) and after (right) applying the W^\pm selection cut.

double-tagged. Otherwise the cut is tightened to “Tight” (NN cut > 0.775), corresponding to a fake rate of about 0.5%, and the event can then be selected as an “exclusive” single b-tag, simply called single b-tag in the following. We are thus left with two disjoint samples, one loose double-tag (DT) and one tight single-tag (ST). The operating points have been selected to optimise the $W^\pm H$ search, based on the quadratic sum of S/\sqrt{B} obtained in the ST and DT samples.

In this way the single and double-tagged subsamples are independent, which simplifies their combination, made to improve the significance of a potential signal. The efficiencies of the L3 and Tight operating points are $(70 \pm 1)\%$ and $(48 \pm 1)\%$, respectively (see Table 5.9; the fake rates are given in Table 5.20.)

The NN tagging algorithm works on taggable jets (see Section 5.1.5). The taggability is a bit higher in MC than in data. The taggability was measured in the $W^\pm + 2$ jets events in data and simulation to determine the ratio between the expected taggability and the taggability in data. The ratio was used to re-weight (per jet) the simulated events in which one or more jets are tagged.

Figure 6.9 shows the taggability scale factors as a function of $|\eta|$ and p_T for $|z_{\text{vtx}}| < 30$ cm and for $30 < |z_{\text{vtx}}| < 60$ cm. In the second bin, $30 < |z_{\text{vtx}}| < 60$ cm, a constant factor has been chosen. The taggability scale factors are applied to the simulated jets which are probed by the NN b-tagger, assuming they can be factorised in $|\eta|$ and φ as has been verified in the b-tagged $t\bar{t}$ cross section measurement [79].

To correct the tagging efficiency of the simulated events, we use an η dependent data over Monte Carlo scale factor, determined in Section 5.4.5. This scale factor is available only for b and c quarks. Applying them to the mis-tagged light quarks leads to an overestimation of this component if the tagging operating point is tight, as determined in p14 [80]. So for light quarks the scale factor is rescaled to match the prediction given by the tag rate function on the subsample of light jets only from our $W^\pm jj$ simulated sample. The rescaling factor was determined to be 0.42 ± 0.05 (statistical uncertainty only) for the exclusive single-tag point. Since the Tight operating point is slightly looser than in p14, we increase the systematic

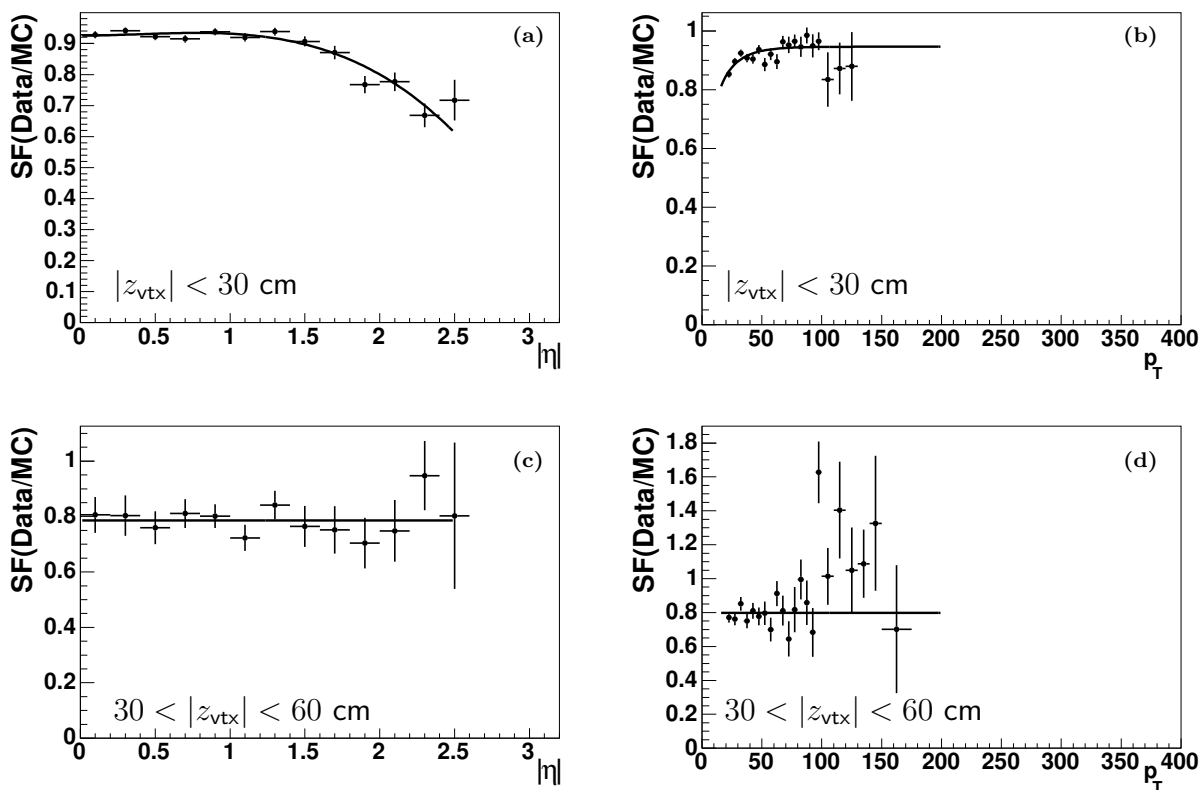


Figure 6.9: Jet taggability scale factors versus pseudorapidity η (a,c) and versus transverse momentum p_T (b,d). The parameterisations of the upper plots (a,b) apply to the $|z_{\text{vtx}}| < 30$ cm bin. The lower plots (c,d) show the $30 < |z_{\text{vtx}}| < 60$ cm bin where no tendency versus η and p_T can be observed. Thus just the average number is used as scale factor in this bin.

error to 25% on this factor. For the L3 operating point we do not apply any rescaling factor, as for the loose operating points the efficiency in data is well determined for the simulation, and no uncertainty on the scale factor is included for this operating point.

Figure 6.10a and b show the distributions of p_T and H_T of the b-tagged jets for the $W^\pm + 2$ jet events. The observed agreement in both cases indicates that the simulation, which includes the different Standard Model processes, describes well the data. In Fig. 6.10c and d the distributions of ΔR and the dijet invariant mass are shown for the same sample of events. The data are compared to the sum of the simulated Standard Model processes added to the multijet background. The QCD background is estimated with the standard matrix method, as for the untagged sample.

When requiring only one b-tagged jet, the background due to $W^\pm jj$, top and QCD processes is still over a factor four larger than the processes which have not yet been observed and which can be studied with the upgraded Tevatron: $W^\pm b\bar{b}$ and Higgs production [74], as well as the recently observed single top quark production process [81]. If two looser b-tags are required, more background events can be rejected and the signal to background ratio is

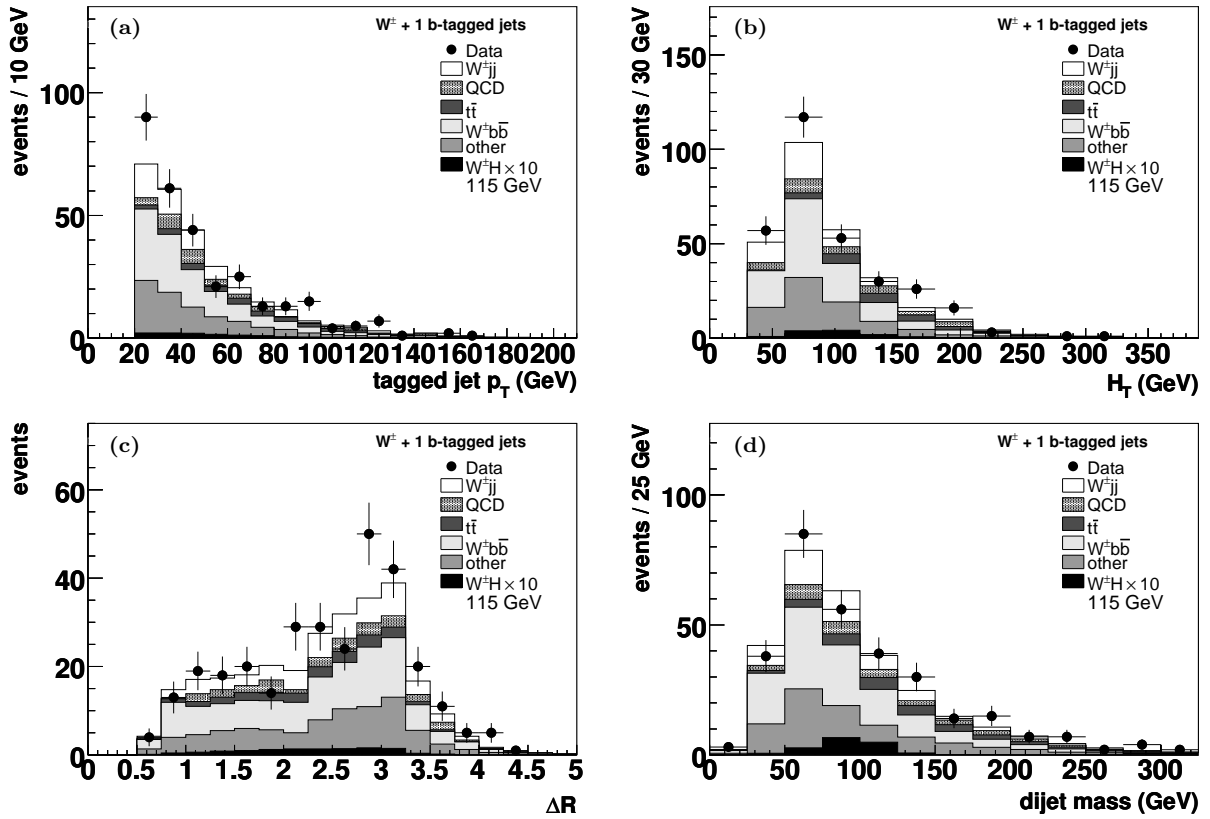


Figure 6.10: Distributions when exactly one jet is b-tagged, compared to the expectation for (a) the leading b-tagged jet transverse momentum and (b) H_T ; (c) ΔR between the two jets; (d) Invariant mass of the two jets in the single b-tag $W^\pm + 2$ jets event sample.

improved.

Figure 6.11a shows the p_T distribution of all the b-tagged jets from the $W^\pm + 2$ b-tagged jet events, compared to the simulated expectation. The distributions of η , ΔR and invariant mass obtained from the two b-tagged jets are shown in Fig. 6.11b and c respectively.

In total, we observe 303 single b-tagged events to be compared to 295 ± 35 expected events, as detailed in Table 6.2. In the double tagged sample, the 74 events observed are to be compared to an expected Standard Model background of 65.8 ± 8.5 events.

These results and distributions show that the simulation of the Standard Model processes describes the data. To estimate our present sensitivity, after reviewing the systematic uncertainties, we can derive a cross section limit for $W^\pm H$ production.

6.6 Systematic Uncertainties

The experimental systematic uncertainties due to efficiencies (i.e. the uncertainty on the ratio data/simulation of the efficiencies) or to the propagation of other systematic uncertainties

	no tag	single tag	double tag
$W^\pm H$	2.15 ± 0.21	0.81 ± 0.08	0.60 ± 0.06
$W^\pm Z$	165 ± 17	9.3 ± 1.0	2.68 ± 0.31
$W^\pm b\bar{b}$	355 ± 83	110 ± 26	27.8 ± 6.6
$W^\pm jj$	6722 ± 424	49 ± 7	4.8 ± 0.8
$W^\pm c\bar{c}$	1072 ± 251	61.3 ± 7.7	7.0 ± 0.9
$t\bar{t}$	64 ± 13	24.0 ± 4.8	12.3 ± 2.5
single top	45 ± 8	17.4 ± 3.2	5.9 ± 1.1
QCD	346 ± 187	23.95 ± 6.7	5.3 ± 1.1
Total expected	8768	295 ± 35	65.8 ± 8.5
Observed events	8768	303	74

Table 6.2: Summary for the $W^\pm + 2$ jet final state. Observed events in data are compared to the expected number of $W^\pm + 2$ jet events without tagging, with one tight b-tag, and with two loose b-tags. The Higgs mass for the sample table is $m_H = 115$ GeV. The untagged $W^\pm jj$ sample is normalised to data, after subtracting the other backgrounds.

(trigger, energy calibration, smearing), which affect the signal and Standard Model backgrounds are detailed in Table 6.3 and 6.4 and described here. Unless described otherwise, they are determined by varying the source of the uncertainty and looking at the resulting event counts for the untagged, single tagged and double tagged samples.

The shapes of the kinematics distributions and of the dijet invariant mass did not change significantly when varying the parameters within their uncertainties. As an example, the dijet invariant mass distributions in the single tag sample are shown in Fig 6.12 for the JES, QCD background and tagging efficiency fluctuations.

Since the $W^\pm jj$ sample is normalised to data on the untagged sample, there is no uncertainty given on the prediction of the total number of untagged events. For the total number of single-tagged and double-tagged events, the uncertainties on the luminosity, the cross sections and the K-factors were also evaluated by varying each $\pm 1\sigma$ and looking at the total number of events. They affect the total number of tagged events because they affect the amount of heavy flavour in the untagged sample.

Most “experimental” uncertainties are correlated between all simulated samples, except the $W^\pm jj$ sample. Because the $W^\pm jj$ sample is normalised to data *after* subtraction of the other samples, the effect is anti-correlated to that in the other samples.

Luminosity

The simulated samples, except the $W^\pm jj$ sample, are scaled to their cross section for the given luminosity. Therefore, the uncertainty on the luminosity of 6.1% is applied as a fully correlated uncertainty between these samples. A small anticorrelated uncertainty is expected on the $W^\pm jj$ sample, as it is normalized to the data after all the other samples are subtracted. Because the $W^\pm jj$ sample dominates the background before tagging is applied, this is a very small effect (about 1.5%) and it is not included in the calculations. No scaling is applied to

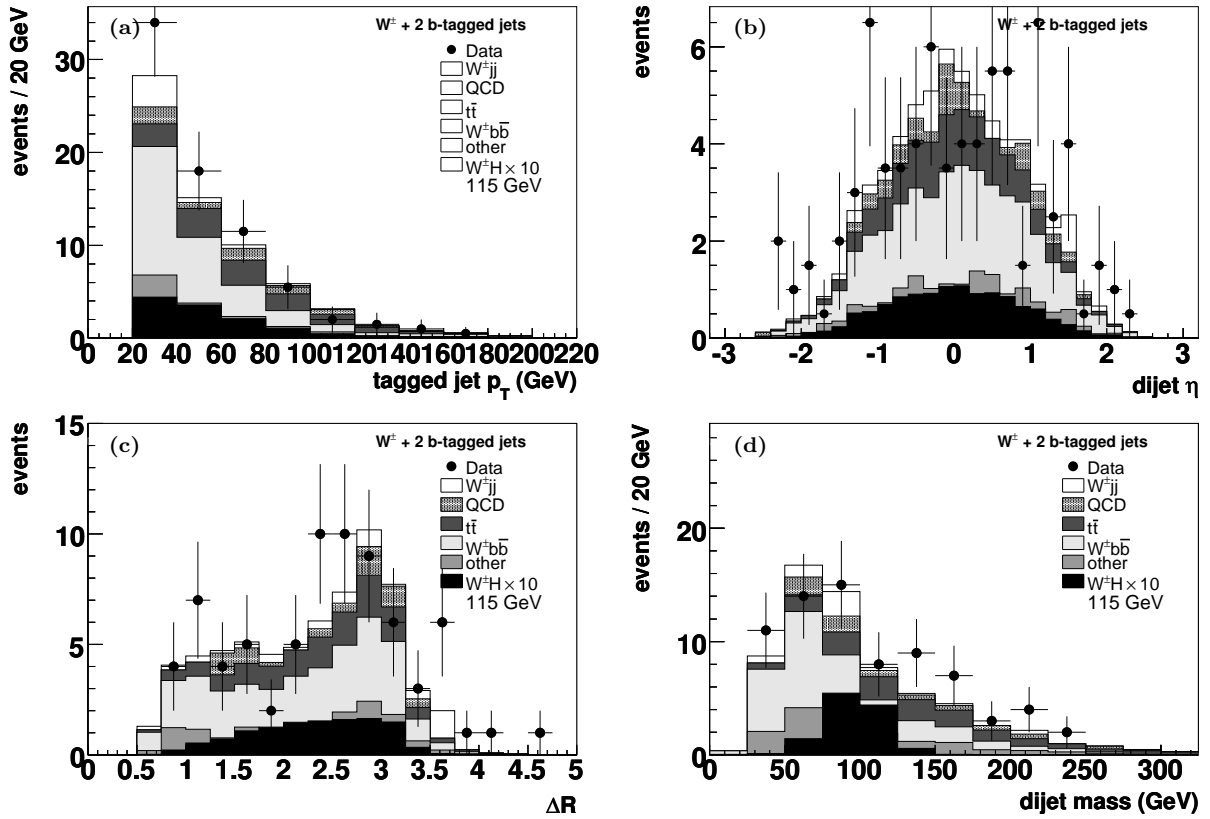


Figure 6.11: Distributions for events with both jets b -tagged: a) b -tagged jets momentum; b) dijet η ; c) ΔR between the two leading jets. d) dijet invariant mass. The data are compared to the different simulated processes.

the QCD background, since it is determined directly in data; therefore, the uncertainty on the luminosity does not apply to this sample.

Trigger efficiency

The Monte Carlo events are weighted with the efficiency of the “OR” single muon trigger. The uncertainty due to the uncertainty on the trigger efficiency is evaluated by varying the efficiency by $\pm 1\sigma$ and comparing the number of events to the number without variation. The uncertainty is applied as a fully correlated uncertainty between all the samples except the $W^\pm jj$ sample, and except the QCD sample where no trigger weight is applied.

ID and reconstruction of muon and jet

In the Monte Carlo samples, the muon reconstruction efficiency and resolution are corrected to agree with data. An uncertainty of 5% is added for the uncertainty on these corrections [50, 82]. The uncertainty due to jet resolution smearing and jet efficiency corrections in the Monte

	$W^{\pm}H$	$W^{\pm}Z$	$W^{\pm}b\bar{b}$	$W^{\pm}jj$
Trigger	1.2%	1.6%	0.3%	2.6%
Muon efficiency	5%	5%	5%	5%
Jet corrections	1.5%	1.2%	0.3%	1.8%
Jet ID	0.5%	1.6%	0.2%	0.9%
Jet multiplicity	2%	2%	2%	2%
JES	1.2%	2.8%	0.6%	8.6%
Taggability	1.3%	1.2%	0.69%	0.67%
Tagging scale factor	1.4%	2.8%	0.73%	8.8%
Total experimental	6.1%	7.3%	5.5%	13.9%
Luminosity	6.1%	6.1%	6.1%	—
Cross section	6.0%	6.0%	9.0%	—
K-factor	—	—	20%	—
Total uncertainty	10.5%	11.2%	23.4%	13.9%
	$W^{\pm}c\bar{c} + Z$	$t\bar{t}$	single top	QCD
Trigger	0.8%	1.3%	2.2%	—
Muon efficiency	5%	5%	5%	—
Jet corrections	1.4%	1.8%	1.8%	—
Jet ID	0.8%	0.6%	1%	—
Jet multiplicity	2%	2%	2%	2%
JES	0.74%	0.39%	1.36%	6.4%
Taggability	1.15%	0.83%	1.5%	—
Tagging scale factor	2.0%	0.6%	1.6%	—
QCD background	—	—	—	27%
Total experimental	6.2%	6.0%	6.7%	27.8%
Luminosity	6.1%	6.1%	6.1%	—
Cross section	9.0%	18.0%	16.0%	—
K-factor	20%	—	—	—
Total uncertainty	12.5%	19.9%	18.4%	27.8%

Table 6.3: Systematic uncertainties for the single tagged sample.

Carlo was determined by changing the smearing and efficiency parameters in the simulation by $\pm 1\sigma$. These uncertainties are applied as fully correlated uncertainties between all the Monte Carlo samples (except $W^{\pm}jj$).

Jet multiplicity

The effect of differences in jet multiplicity in the Monte Carlo and in data was studied by including 3 jet events and looking at the normalisation factor for $W^{\pm}jj$ events. The normalisation factor changed by about 2%, which was taken into account as a fully correlated systematic uncertainty between all the samples (anti-correlated for $W^{\pm}jj$).

	$W^{\pm}H$	$W^{\pm}Z$	$W^{\pm}b\bar{b}$	$W^{\pm}jj$
Trigger	0.22%	1.6%	0.7%	4.1%
Muon efficiency	5%	5%	5%	5%
Jet corrections	0.6%	2.1%	0.4%	1.9%
Jet ID	0.5%	1.1%	0.5%	2.3%
Jet multiplicity	2%	2%	2%	2%
JES	0%	2.4%	0.13%	12.9%
Taggability	2.3%	2.1%	2.1%	1.8%
Tagging SF	2.5%	4.0%	3.1%	5.8%
Total experimental	6.4%	8.0%	6.6%	16.1%
Luminosity	6.1%	6.1%	6.1%	—
Cross section	6.0%	6.0%	9.0%	—
K-factor	—	—	20%	—
Total uncertainty	10.7%	11.7%	23.7%	16.1%
	$W^{\pm}c\bar{c} + Z$	$t\bar{t}$	single top	QCD
Trigger	1.1%	0.1%	0.8%	—
Muon efficiency	5%	5%	5%	—
Jet corrections	1.7%	0.9%	1.5%	—
Jet ID	1.8%	0.3%	1.3%	—
Jet multiplicity	2%	2%	2%	2%
JES	1.5%	0.8%	1.0%	4.0%
Taggability	2.0	1.2	1.5	—
Tagging SF	2.3%	2.8%	3.5%	—
QCD background	—	—	—	19%
Total experimental	7.0%	6.3%	7.0%	19.8%
Luminosity	6.1%	6.1%	6.1%	—
Cross section	9.0%	18.0%	16.0%	—
K-factor	20%	—	—	—
Total uncertainty	12.9%	20.0%	18.5%	19.8%

Table 6.4: Systematic uncertainties for the double tagged sample.

Jet Energy Scale

The uncertainty due to the change in acceptance due to the jet energy scale was evaluated by varying the scale by $\pm 1\sigma$ and comparing the number of events to the number without variation. Because the $W^{\pm} + jj$ sample is scaled to the data and the number of data events also changes when the jet energy scale correction is varied, the variation in the number of events for this sample is compensated for the change in the number of data events. The uncertainty is applied as a fully correlated uncertainty between all the samples.

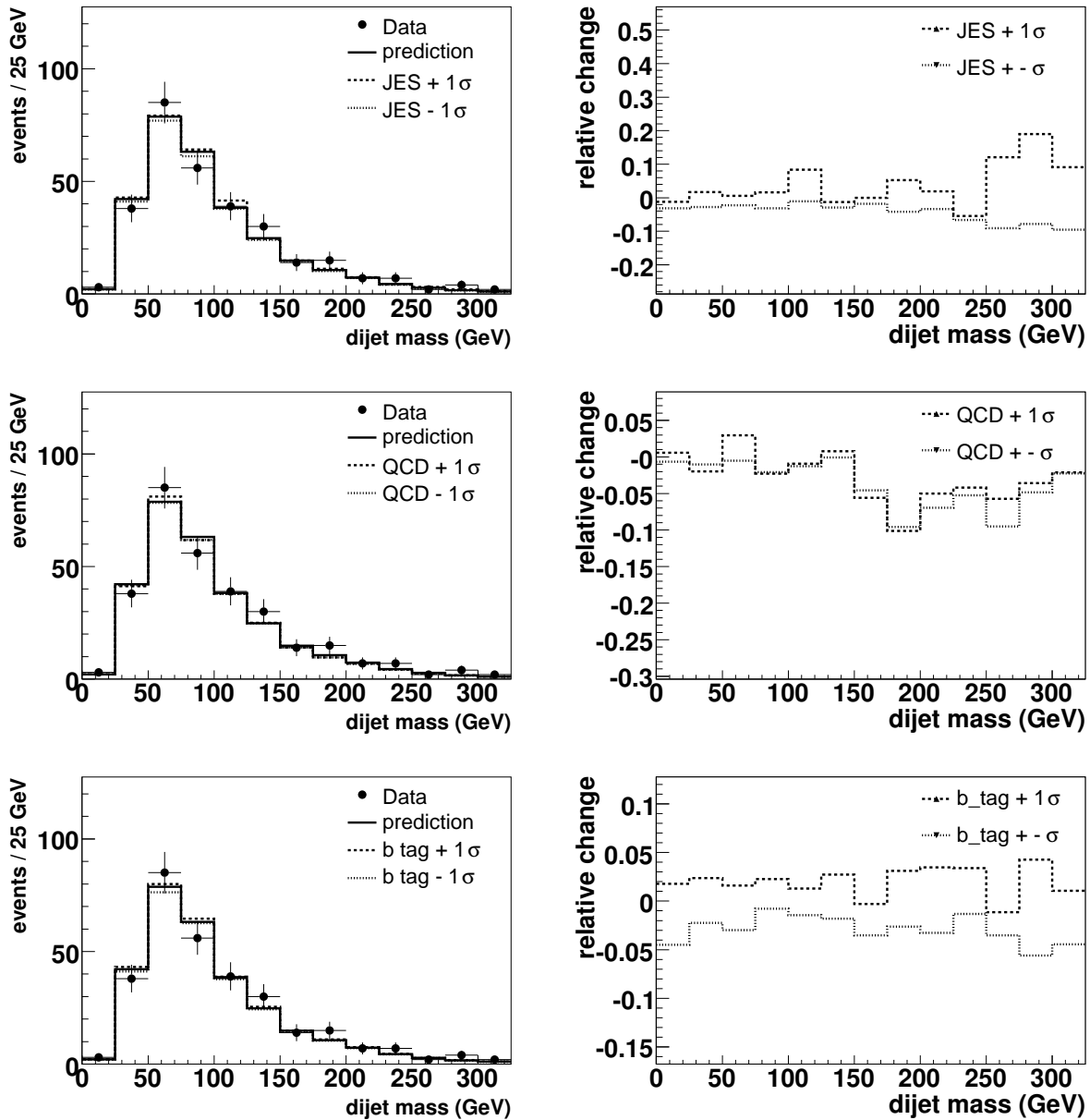


Figure 6.12: Dijet invariant mass distribution in the single tag sample after fluctuating the Jet Energy Scale (top), QCD background (middle) and NN tagging efficiency (bottom) by $\pm 1\sigma$.

b tagging

In the Monte Carlo samples, scale factors are applied to account for the difference in taggability and tagging efficiency in data and Monte Carlo. The uncertainty due to the uncertainty on the tagging scale factor in the Monte Carlo samples is determined by varying the scale factor by $\pm 1\sigma$. For the light jet scale factor for the Tight operating point, the scale factor was

varied by 25% as described in Section 6.5. The uncertainty due to the uncertainty on the taggability scale factor was determined by varying the scale factor by $\pm 1\sigma$. These uncertainties are applied as a fully correlated uncertainty between all the Monte Carlo samples.

Cross section and K-factor

The sources of uncertainties on the cross sections of the background processes are described in [83] and include the uncertainties on the calculations, PDFs and measured parameters on which the cross sections depend, like the top quark mass. The uncertainties used here are 18% for $t\bar{t}$ production, 16% for single-top production, 6% for $W^\pm Z$, $W^\pm H$ and $W^\pm(Z)$ inclusive production and 18% for $W^\pm b\bar{b}$ ($W^\pm c\bar{c}$) production. A separate uncertainty of 20% is assigned for the K-factor of 1.75 used to scale the W^\pm , $Zb\bar{b}$ and W^\pm , $Zc\bar{c}$ cross sections to the NNLO cross section, as described in Section 4.2.1.

The uncertainties are directly applied on the individual samples. The uncertainty on the total number of predicted signal+background events was estimated by varying the K-factor and the cross sections separately by $\pm 1\sigma$ and looking at the number of predicted events, giving an uncertainty of 9% in the single-tagged sample and 10% in the double-tagged sample.

QCD background

The systematic uncertainty on the QCD background due to the uncertainty on the muon isolation fake rate and efficiency is estimated by varying the fake rate $p_{\mu\text{jet}}$ and the efficiency $\varepsilon_{\text{tight}}$ by their uncertainty when determining the QCD background. The resulting variation of the QCD background determined by the matrix method is taken as a systematic uncertainty.

6.7 Upper Limits on $W^\pm H$ Production

The invariant mass distribution provides separation between signal and background, because the invariant mass peaks for values just below the Higgs mass. The dijet invariant mass of the double-tagged events is shown in Fig 6.13 in linear and in logarithmic scale to see more precisely the different contributions. A summary of the number of expected events compared to the observed events is given in Table 6.2. The number of events in data is well described by the expected background, and no hint of a signal is observed. Therefore, using the dijet invariant mass distributions for signal, background and observed data, we set an upper limit on the cross section for associated $W^\pm H$ production, $\sigma(p\bar{p} \rightarrow W^\pm H)$. A Higgs signal is excluded at 95% confidence level (CL) if no events are observed and the likelihood of seeing no signal events (i.e. the observed event are compatible with background), given the assumption that a signal should be present, is less than 5%. This confidence level is determined using the semi-Frequentist CL_s approach, also known as the ‘‘LEP method’’ [84–86]. The Poisson log-likelihood ratio is used as the test statistic, the variable that is used to separate the signal+background and background-only hypotheses. This test statistic is translated into a confidence level using many simulated ‘‘pseudo-experiments’’.

6.7.1 Limit calculations

The likelihood ratio that is used as a test statistic for a single bin i is defined as the ratio of the Poisson likelihoods $Q = L(\text{data}|s + b)/L(\text{data}|b)$,

$$Q_i = \frac{e^{-s_i+b_i}(s_i + b_i)^{d_i}}{d_i!} / \frac{e^{-b_i}b_i^{d_i}}{d_i!}, \quad (6.6)$$

where s_i and b_i are the predicted signal and background and d_i is the observed data in bin i . The likelihood ratio is combined for all the bins in the invariant mass distributions for the single tag and double tag samples:

$$Q = \prod_i Q_i. \quad (6.7)$$

To make the computation more efficient, the log-likelihood ratio (LLR) $\chi = -2 \ln(Q)$ is used. For bin i with d_i events, χ_{d_i} is given by

$$\chi_{d_i} = -2 \ln(Q_i) = 2(s_i - d_i \ln(1 + \frac{s_i}{b_i})). \quad (6.8)$$

The confidence level for the signal+background hypothesis is given by

$$CL_{s+b} = P_{s+b}(\chi \leq \chi_d) = \int_{-\infty}^{\chi_d} \frac{dP_{s+b}}{d\chi} d\chi, \quad (6.9)$$

where $\chi_d = \sum_i \chi_{d_i}$ and the probability distribution function (PDF) P_{s+b} is defined by the distribution of χ_d . This distribution is found by running many pseudo-experiments to simulate the outcome of repeated experiments measuring the value of d . The value of χ_d is calculated for each pseudo-experiment to get the distribution.

Because the CL_{s+b} estimator can lead to exclusion of signals even when there is no experimental sensitivity [87], a modified Frequentist confidence level CL_s is used, defined as:

$$CL_s = CL_{s+b}/CL_b, \quad (6.10)$$

where CL_b is the confidence level for the background only-hypothesis, given by equation 6.9 when P_{s+b} is replaced by P_b . The signal hypothesis is excluded at 95% confidence level if $CL_s < 5\%$.

The values of s_i and b_i are also simulated for each pseudo-experiment. The systematic uncertainties are taken into account by including them in the PDFs P_{s+b} and P_b as a Gaussian smearing. All correlations are maintained between bins and between signal and background. In practice, this is done by changing the per-bin signal or background prediction p_i for each pseudo-experiment,

$$p'_i = p_i \prod_{k=1}^K (1 + \sigma_k^i S_k), \quad (6.11)$$

where p'_i are the systematically varied predictions for bin i and the σ_k^i is the contributed size of each of the K sources of uncertainty. The value S_k is a stochastic variable that is distributed according to a normal Gaussian distribution. The p'_i are cut off at zero so that negative

values of signal and background are not permitted. Correlations can be taken into account by introducing a matrix of correlation coefficients into equation 6.11. For fully correlated uncertainties, it is sufficient to ensure that each correlated uncertainty is calculated only once per iteration.

This smearing procedure “broadens” the distributions and makes the separation between the two smaller. To reduce the degree to which the two PDFs are smeared the “profile likelihood” technique is used [87, 88]. For a given set of predictions, observations and systematic uncertainties, the likelihood that the background PDF predicts the data is maximised over the space of all possible values of the systematic uncertainties to find the “best fit” model for the data. The “best fit” optimises the data-prediction comparison given the Gaussian constraints on the p'_i . It is performed by minimising

$$\chi^2 = 2 \sum_i \left[(p'_i - d_i) - d_i \ln \left(\frac{p'_i}{d_i} \right) \right] + \sum_k S_k^2. \quad (6.12)$$

The S_k are fit to minimise this equation. For this “best fit”, only bins are used for which $s_i/b_i < 10^{-3}$.

A measure of the sensitivity of the experiment is the median expectation of the limit, i.e. the limit for which as many experiments would have a result above it as below it, in the absence of signal. This limit is obtained by doing the calculation for a pseudo-experiment in which b_i is substituted for d_i in Equation 6.6. The resulting confidence level is referred to as CL_s^{med} . The confidence level for the observed data in the experiment is referred to as CL_s^{obs} .

6.7.2 Results for Higgs production

For the calculation, each distribution is binned to a 5 GeV mass resolution over the range $20 < m_{jj} < 200$ GeV. The expected background and signal distributions are smoothed via Gaussian kernel approximation to lessen the impact of limited Monte Carlo statistics [89].

The confidence level is calculated given the dijet invariant mass distributions for data, signal and background. If the CL is greater than 5%, the signal is multiplied by a factor until $CL_s < 5\%$ (in fact, the factor is changed until $4.9\% \leq CL_s \leq 5.1\%$). This factor is the ratio of the upper limit of the Higgs production cross section to the predicted cross section: $\sigma^{\text{limit}}/\sigma^{\text{predicted}}$, where $\sigma^{\text{predicted}}$ is the cross section used to generate the signal distribution.

All upper limits are calculated using 10^5 simulated outcomes and requiring an accuracy better than 0.1% in the confidence levels, i.e. $4.9\% \leq CL_s \leq 5.1\%$.

Figure 6.14 shows the log-likelihood ratio (LLR) distribution (single- and double-tags combined). Included in this figure are the LLR values for the signal+background hypothesis (LLR_{s+b}), background-only hypothesis (LLR_b), and the observed data (LLR_{obs}). The shaded bands represent the 1 and 2 standard deviation (σ) departures for LLR_b . These distributions can be interpreted as follows:

- The separation between LLR_b and LLR_{s+b} provides a measure of the overall power of the search. This is the ability of the analysis to discriminate between the signal+background and background-only hypotheses where the signal hypothesis assumes the Standard Model Higgs production cross section.

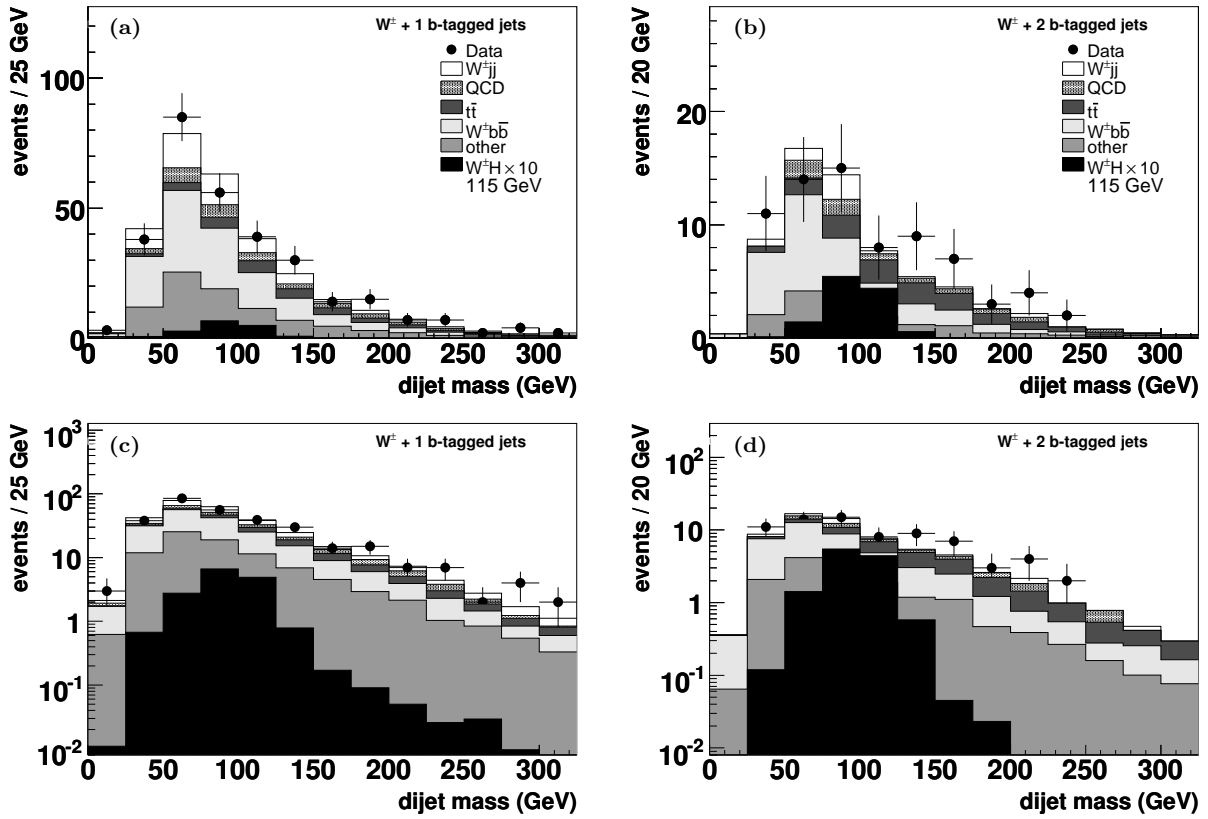


Figure 6.13: Dijet invariant mass distributions in the single tag (left) and double tag (right) samples. The data are compared to $W^\pm b\bar{b}$, $t\bar{t}$, $W^\pm jj$ and other smaller expectations. The backgrounds labelled as “other” in the figure are dominated by single-top production. Also shown is the contribution expected from the 2 b jets originating from the decay of a 115 GeV Higgs Boson produced via $p\bar{p} \rightarrow W^\pm H$. The bottom plots show the same distributions as the top plots on a logarithmic scale.

- The width of the LLR_b distribution (shown here as 1 and 2 standard deviation (σ) bands) provides an estimate of how sensitive the analysis is to a signal-like fluctuation in data, taking account of the presence of systematic uncertainties. For example, when a $1\text{-}\sigma$ background fluctuation is large compared to the signal expectation, the analysis sensitivity is limited.
- The value of LLR_{obs} relative to LLR_{s+b} and LLR_b indicates whether the data distribution appears to be more signal-like or background-like. As noted above, the significance of any departures of LLR_{obs} from LLR_b can be evaluated by the width of the LLR_b distribution.

Figure 6.15 shows the ratio of the cross section limit times branching ratio $\sigma(p\bar{p} \rightarrow W^\pm H) \times B(H \rightarrow b\bar{b})$ to the Standard Model expectation for the $W^\pm H \rightarrow \mu\nu b\bar{b}$ events (single and double tags combined). The ratios for five mass points are given in Table 6.5. Reported are both expected and observed upper limits, wherein the expected limit is obtained using the CL_s^{med} method described above.

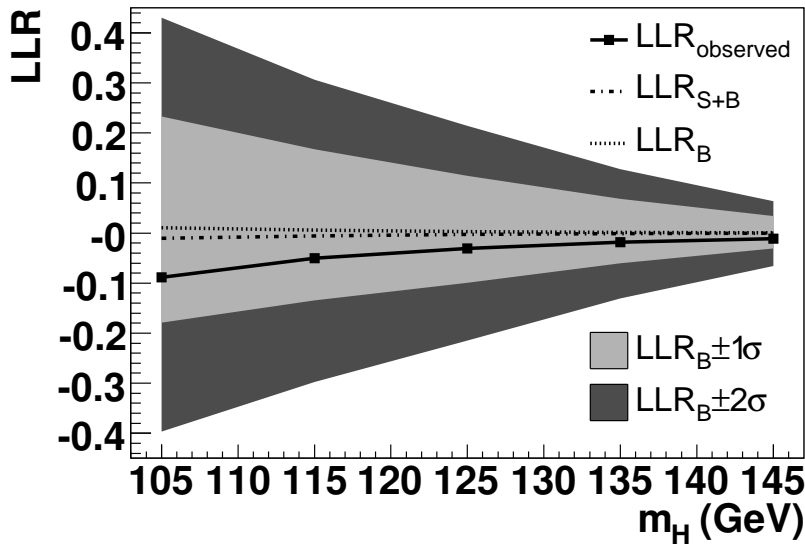


Figure 6.14: Log-likelihood ratio distribution for the $W^\pm H \rightarrow \mu\nu_\mu b\bar{b}$ analysis.

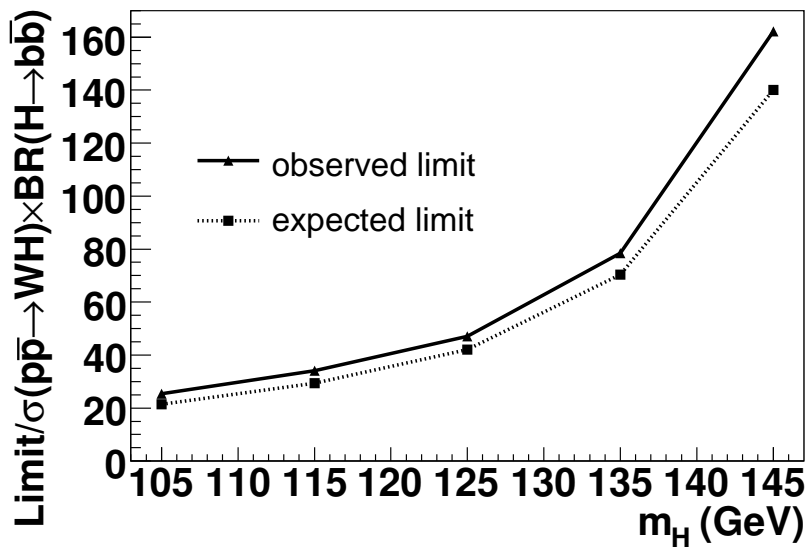


Figure 6.15: Expected (median) and observed 95% CL cross section ratios for the $W^\pm H \rightarrow \mu\nu_\mu b\bar{b}$ analysis (single- and double-tag) in the $m_H = 105 - 145$ GeV mass range.

This translates into a cross section limit for $\sigma(p\bar{p} \rightarrow W^\pm H) \times B(H \rightarrow b\bar{b})$ of 4.4 pb at 95% C.L. limit for a Higgs boson mass of 115 GeV. The corresponding expected upper limit is 3.8 pb. The same study is performed for four other Higgs mass points which are 105, 125, 135, and 145 GeV. The corresponding observed and expected limits are given in Table 6.5. The limits on the cross section times branching ratio, $\sigma(p\bar{p} \rightarrow W^\pm H) \times B(H \rightarrow b\bar{b})$ are shown in the Higgs cross section limit plot, Fig. 6.16, and given in Table 6.6.

m_H	Observed limit $\sigma^{\text{obs}}/\sigma^{\text{pred}}$	Median expected limit $\sigma^{\text{med}}/\sigma^{\text{pred}}$	Observed limit $\sigma^{\text{obs}}(\text{pp} \rightarrow W^\pm H)$	Median expected limit $\sigma^{\text{med}}(\text{pp} \rightarrow W^\pm H)$
105 GeV	25.4	21.4	4.9	4.1
115 GeV	34.1	29.3	4.4	3.8
125 GeV	47.1	42.0	3.7	3.3
135 GeV	78.4	70.4	3.3	2.9
145 GeV	162.2	140	3.0	2.6

Table 6.5: Observed and expected upper limits for Higgs masses between 105 and 145 GeV, presented as a ratio of the upper limit on the cross section $\sigma(\text{pp} \rightarrow W^\pm H)$ to the predicted cross section σ^{pred} and as an absolute upper limit on the cross section for associated $W^\pm H$ production.

m_H	$B(H \rightarrow b\bar{b})$	$\sigma^{\text{obs}} \times B$	$\sigma^{\text{med}} \times B$
105 GeV	0.769	3.9	3.3
115 GeV	0.732	3.2	2.8
125 GeV	0.610	2.2	2.0
135 GeV	0.436	1.4	1.3
145 GeV	0.256	0.76	0.66

Table 6.6: Observed and expected upper limits on the cross section times branching ratio $\sigma(\text{pp} \rightarrow W^\pm H) \times B(H \rightarrow b\bar{b})$.

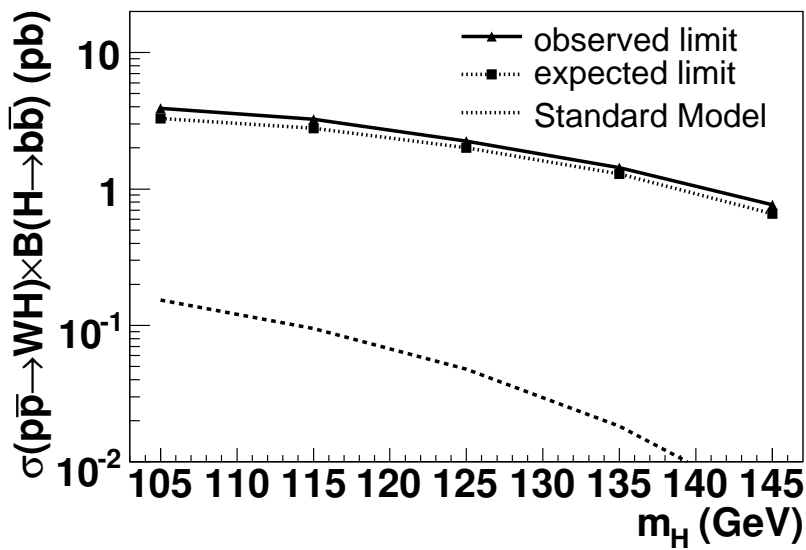


Figure 6.16: Upper limit on associated $W^\pm H$ production as a function of m_H .

Chapter 7

Conclusions

Despite the great successes of our current theory of particles and their interactions, the Standard Model of particle physics, the measurement of the Higgs boson is an important test of its validity. With every study we get closer to a discovery or an exclusion. The work presented in this thesis is an important contribution to this search. A search for the Higgs boson in the $W^\pm H \rightarrow \mu\nu_\mu b\bar{b}$ channel with 1.0 fb^{-1} was done. The analysis relies on selecting events with a clear signature of the $W^\pm \rightarrow \mu\nu_\mu$ decay, and two jets of which one or both are tagged as b-jets.

The b-tagging in this analysis is crucial. To improve on the efficiency of existing tagging algorithms, a Neural Net-based tagging algorithm was developed (see Chapter 5). The NN tagger combines the results of several lifetime-based tagging algorithms and provides an increase in efficiency of up to 50% for a fixed fake rate. The efficiency for the operating points used in this analysis is $(47.6 \pm 0.7)\%$ for a fake rate of $(0.55 \pm 0.05)\%$ and $(69.6 \pm 0.9)\%$ for a fake rate of $(4.7 \pm 0.02)\%$.

As no evidence of a $W^\pm H \rightarrow \mu\nu_\mu b\bar{b}$ signal was observed, an upper limit was set on the cross section. The limit is expressed as the ratio of the measured upper limit to the Standard Model prediction in Table 6.5. The result of our $W^\pm H \rightarrow \mu\nu_\mu b\bar{b}$ analysis is compared in Fig. 7.1 to the previously published results of DØ on 174 pb^{-1} of data [74], CDF on 320 pb^{-1} of data [90], and to the expected preliminary limits of DØ (0.4 fb^{-1} , [91]) and CDF (1.0 fb^{-1} , [92]). The improvement in sensitivity obtained with this analysis is significant, in particular in the region where we have the best sensitivity for a low mass Higgs discovery, i.e. 115–145 GeV.

Additional increase in sensitivity could be gained by the deployment of a system that allows the NN output to be used as a continuous variable. At the moment only specific operating points are used. Other ways the NN tagger could be improved are by creating a new NN to separate b- and c-jets and by creating separate low and high jet p_T NN optimisations. The installation of Layer 0 [93], a new layer of silicon sensors mounted at very small radius around the beampipe, will certainly also improve the b-tagging performance.

The sensitivity of the analysis can be further increased by increasing the amount of data. More than 2 fb^{-1} is being analysed at the moment and the Tevatron is expected to deliver 8 fb^{-1} by the end of 2009. Some efficiency is lost by requiring only muon-only triggers. With the inclusion of “muon+jet” triggers that require the presence of muons and jets, some

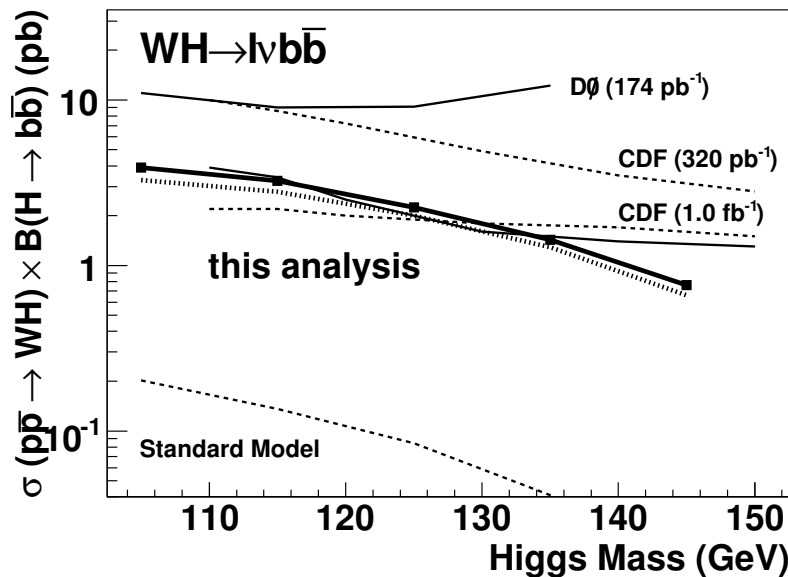


Figure 7.1: Upper limit on $\sigma(W^\pm H) \times B(H \rightarrow b\bar{b})$ compared to previous results from DØ with 174 pb^{-1} of data using electrons [74] and CDF with 320 pb^{-1} [90] and 1.0 fb^{-1} [92] using electrons and muons combined.

increase may be gained. Another way to increase the efficiency is to release the trigger requirement altogether [94], but some aspects of this method are not fully tested yet.

An increase in sensitivity can also be gained by combining different search channels like $W^\pm H \rightarrow e\nu_e b\bar{b}$, ZH production and perhaps even channels where the H decays to $\tau\tau$. If the Higgs mass is higher than about 140 GeV, the $W^\pm H \rightarrow W^\pm W^+ W^-$ and $gg \rightarrow H \rightarrow W^+ W^-$ channels become important as well. In the limit calculation, they can be combined in the same way as the single-tag and double-tag sample [95]. An earlier result of the $W^\pm H \rightarrow \mu\nu_\mu b\bar{b}$ analysis presented in this thesis was combined with a similar search in the $W^\pm H \rightarrow e\nu_e b\bar{b}$ channel, resulting in an upper limit on $\sigma(\text{pp} \rightarrow W^\pm H) \times B(H \rightarrow b\bar{b})$ of 14.7 times the SM prediction for $m_H = 115 \text{ GeV}$ [94]. Combining the results of the DØ and CDF experiments would lead to an increase in sensitivity of about 40% [15].

Further increases in sensitivity are expected from new analysis methods such as multivariate analyses and by improving the dijet mass resolution.

As the understanding of the detector, the algorithms and the analysis strategies improve, tighter limits can be set on the Higgs production cross section. An earlier study indicated that a Higgs boson with $m_H = 115 \text{ GeV}$ can be excluded at 95% CL with about 1.35 fb^{-1} of data, if the results of the DØ and CDF experiments are combined [16]. These studies do not include the impact of systematic uncertainties, which push the luminosity thresholds higher. With 8 fb^{-1} , the Tevatron experiments should be able to observe a 3σ excess for Higgs masses up to almost 130 GeV. With increased luminosity and sensitivity, exclusion or discovery of a low mass Higgs becomes a real possibility.

References

- [1] P. W. Higgs. Broken symmetries and the masses of gauge bosons. *Phys. Rev. Lett.* 13 (1964) 508.
- [2] R. Barate et al. Search for the standard model Higgs boson at LEP. *Phys. Lett.* B565 (2003) 61.
- [3] The LEP Electroweak Working Group. A Combination of Preliminary, Electroweak Measurements and Constraints on the Standard Model. LEP EW WG Plots for the Winter 2007 (2007).
- [4] S. Eidelman et al. Review of particle physics. *Phys. Lett.* B592 (2004) 1.
- [5] F. Halzen and A. D. Martin. Quarks and Leptons: An Introductory Course in Modern Particle Physics. Wiley, New York, USA (1984).
- [6] S. L. Glashow. Partial symmetries of weak interactions. *Nucl. Phys.* 22 (1961) 579.
- [7] S. Weinberg. A model of leptons. *Phys. Rev. Lett.* 19 (1967) 1264.
- [8] G. 't Hooft. Renormalization of massless Yang-Mills fields. *Nucl. Phys.* B33 (1971) 173.
- [9] G. 't Hooft. Renormalizable lagrangians for massive Yang-Mills fields. *Nucl. Phys.* B35 (1971) 167.
- [10] J. F. Gunion, H. E. Haber, G. L. Kane and S. Dawson. The Higgs Hunter's Guide. Westview Press, New Ed edition (July 2000) edition. ISBN-13: 978-0738203058 (2000).
- [11] A. Djouadi, J. Kalinowski and M. Spira. HDECAY: A program for Higgs boson decays in the Standard Model and its supersymmetric extension. *Comput. Phys. Commun.* 108 (1998) 56.
- [12] O. Brein, A. Djouadi and R. Harlander. NNLO QCD corrections to the Higgs-strahlung processes at hadron colliders. *Phys. Lett.* B579 (2004) 149.
- [13] K. Riesselmann. Limitations of a standard model Higgs boson. Hep-ph/9711456 (1997).
- [14] The Tevatron Electroweak Working Group. A combination of CDF and DØ results on the mass of the top quark. FERMILAB-TM-2380-E, DØ internal note 5378 (2007).

- [15] The TEVNPB Working Group. Combined DØ and CDF upper limits on standard-model Higgs-boson production. DØ internal note 5227 (2006).
- [16] L. Babukhadia et al. Results of the Tevatron Higgs sensitivity study. FERMILAB-PUB-03-320-E (2003).
- [17] Fermilab Beams Division. The Tevatron Accelerator Complex.
URL http://www-bdnew.fnal.gov/operations/rookie_books/rbooks.html
- [18] Fermilab Beams Division. Collider Run II Peak Luminosity.
URL <http://www-bdnew.fnal.gov/operations/lum/lum.html>
- [19] D. A. Crane et al. Status report: Technical design of neutrino beams for the Main Injector (NuMI). FERMILAB-TM-1946 (1995).
- [20] V. Abazov et al. The Upgraded DØ Detector. *Nucl. Inst. Meth.* A565 (2006) 463.
- [21] The DØ Operations Group. Daily Data Taking Efficiency.
URL [http://d0server1.fnal.gov/Projects/Operations/D0RunII/DataTaking.htm](http://d0server1.fnal.gov/Projects/Operations/D0RunII>DataTaking.htm)
- [22] C. T. Autermann. Resonant second generation slepton production at the Tevatron. Ph.D. thesis, Tech. Hochsch. Aachen. FERMILAB-THESIS-2006-46 (2006).
- [23] S. Klimenko, J. Konigsberg and T. M. Liss. Averaging of the inelastic cross sections measured by the CDF and the E811 experiments. FERMILAB-FN-0741 (2003).
- [24] T. Andeen et al. The DØ experiment's integrated luminosity for Tevatron Run IIa. FERMILAB-TM-2365 (2007).
- [25] B. Casey and G. Snow. Improved Determination of the DØ Luminosity. DØ internal note 5140 (2006).
- [26] DØ Run Coordination. DØ Operation Webpage 2007.
URL <http://www-d0.fnal.gov/runcoor/>
- [27] S. N. Ahmed. Improved Determination of the DØ Luminosity. DØ internal note 4044 (2002).
- [28] P. Azzi et al. Radiation damage experience at CDF with SVX'. *Nucl. Inst. Meth.* A383 (1996) 155.
- [29] F. Lehner and S. Choi. What do we know about radiation damage in silicon detectors? DØ internal note 3803 (2000).
- [30] R. Lipton. Lifetime of the DØ silicon tracker. DØ internal note 4077 (2002).
- [31] S. N. Ahmed, R. Lipton, D. A. Wijngaarden, S. Duensing, A. Naumann and S. J. de Jong. DØ SMT radiation protection system. DØ internal note 3915 (2001).

- [32] S. N. Ahmed, R. Lipton, D. A. Wijngaarden, S. Duensing, A. Naumann and S. de Jong. DØ SMT Radiation Monitoring System. DØ internal note 4022 (2002).
- [33] S. J. de Jong. Status of the OPAL microvertex detector and new radiation monitoring and beam dump system. *Nucl. Inst. Meth.* A418 (1998) 22.
- [34] P. F. Derwent. Radiation monitoring for vertex detectors at the Tevatron. *Nucl. Inst. Meth.* A447 (2000) 110.
- [35] S. N. Ahmed and L. Berntzon. Background Dose Estimates for DØ SMT. DØ internal note 4043 (2004).
- [36] The DØ Collaboration. Beam tests of the DØ uranium liquid argon end calorimeters. FERMILAB-PUB-92/162, DØ internal note 1434 (1992).
- [37] V. M. Abazov et al. The muon system of the Run II DØ detector. *Nucl. Inst. Meth.* A552 (2005) 372.
- [38] Y. Fisyak and J. Womersley. D0gstar D0 GEANT simulation of the total apparatus response. DØ internal note 3191 (1997).
- [39] M. Goossens et al. GEANT, detector description and simulation and simulation tool. GEANT user's guide CERN, Geneva (1994).
- [40] T. Sjöstrand, L. Lonnblad and S. Mrenna. PYTHIA 6.2: Physics and manual. Hep-ph/0108264 (2001).
- [41] H. L. Lai et al. Improved parton distributions from global analysis of recent deep inelastic scattering and inclusive jet data. *Phys. Rev.* D55 (1997) 1280.
- [42] J. Campbell and K. Ellis. MCFM, Monte-Carlo for FeMtobarn processes.
URL <http://mcfm.fnal.gov>
- [43] M. Mangano et al. ALPGEN, a generator for hard multiparton processes in hadron collisions, version 2.05_d0.
- [44] A. Pukhov et al. CompHEP: A package for evaluation of Feynman diagrams and integration over multi-particle phase space. User's manual for version 33. Hep-ph/9908288 (1999).
- [45] M. Begel, L. Christofek and E. Shabalina. Determination of weighting factors for ALPGEN Monte Carlo signal and background samples. DØ internal note 5016 (2006).
- [46] N. Makovec and J.-F. Grivaz. Shifting, smearing and removing simulated jets. DØ internal note 4914 (2005).
- [47] P. Calfayan. ORing single muon triggers in p17 data. DØ internal note 5329 (2007).

- [48] C. Clément, F. Deliot, T. Golling, K. Haganaki, B. Leonhardt, M. Mulders, E. Nurse, S. Soldner-Remboldt and J. Stark. MuonID certification for p14. DØ internal note 4350 (2004).
- [49] D. Chapin, H. Fox, J. Gardner, R. Illingworth, A. Lyon and J. Zhu. Measurement of $Z \rightarrow e^+e^-$ and $W \rightarrow e\nu$ Production Cross Sections with $|\eta| < 2.3$. DØ internal note 4403 (2004).
- [50] P. Calfayan, T. Gadfort, G. Hesketh, V. Lesné, M. Owen, R. Stroehmer, V. Sharyy and B. Tuchming. Muon identification certification for p17 data. DØ internal note 5157 (2006).
- [51] G. C. Blazey et al. Run II jet physics. In: QCD and weak boson physics in Run II. Proceedings, Batavia, USA, March 4-6, June 3-4, November 4-6, 1999 (U. Baur, R. K. Ellis and D. Zeppenfeld, editors). FERMILAB-PUB-00-297 (1999).
- [52] U. Bassler and G. Bernardi. Towards a coherent treatment of calorimetric energies: Missing transverse energy, jets, E.M. objects and the T42 algorithm. DØ internal note 4124 (2003).
- [53] J.-R. Vlimant, U. Bassler, G. Bernardi and S. Trincaz-Duvoid. Technical description of the T42 algorithm for the calorimeter noise suppression. DØ internal note 4146 (2003).
- [54] G. Bernardi, E. Busato and J.-R. Vlimant. Improvements from the T42 algorithm on calorimeter objects reconstruction. DØ internal note 4335 (2004).
- [55] JES Group. Jet energy scale determination at DØ Run II (final p17 version). DØ internal note 5382 (2007).
- [56] M. Voutilainen and C. Royon. Jet p_t resolution using v7.1 JES for p17 data. DØ internal note 5381 (2007).
- [57] G. Steinbrück. Measurement of the angular distribution of electrons from W boson decays at DØ. Ph.D. thesis, University of Oklahoma (1999).
- [58] L. Wang, J. Hays, C. Schwanenberger and J. Mitrevski. Electron Likelihood efficiency in p17. DØ internal note 5114 (2006).
- [59] G. Borissov. Status of DØ track reconstruction. Talk given at All DØ Meeting, 14 February 2003 (2003).
- [60] G. Borissov. Ordering a chaos or... technical details of AA tracking. Talk given at All DØ Meeting, 28 February 2003 (2003).
- [61] A. Khanov. HTF: histogramming method for finding tracks. the algorithm description. DØ internal note 3778 (2000).
- [62] P. Hough. Machine analysis of bubble chamber pictures. Int. Conf. on High Energy Accelerators and Instrumentation, CERN (1959).

- [63] H. Greenlee. The DØ Kalman track fit. DØ internal note 4303 (2003).
- [64] H. Greenlee. The DØ interacting propagator. DØ internal note 4293 (2003).
- [65] A. Schwartzman and C. Tully. Primary vertex reconstruction by means of adaptive vertex fitting. DØ internal note 4918 (2005).
- [66] Y. Peters, A. Schwartzman and M. Strauss. Certification of the adaptive primary vertex in p17. DØ internal note 5192 (2006).
- [67] M. Narain and A. Schwartzman. Primary vertex selection. DØ internal note 4042 (2002).
- [68] Y. Peters, H. Greenlee, A. Haas and A. Schwartzman. Optimization of the secondary vertex tagger in p17. DØ internal note 5265 (2006).
- [69] A. Schwartzman and M. Narain. Secondary vertex reconstruction using the Kalman filter. DØ internal note 3908 (2001).
- [70] R. Demina, A. Khanov, F. Rizatdinova and E. Shabalina. Measurement of b -tagging efficiency and mis-tagging rates with CSIP method. DØ internal note.
- [71] D. Bloch and B. Clément. Update of the JLIP b -tagger Performance in p14/pass2 with JES 5.3. DØ internal note 4824.
- [72] D. Bloch, B. Clément, D. Gélé, S. Gréder and I. Ripp-Baudot. Performance of the jet lifetime probability method for b -tagging in DØ data. DØ internal note 4158 (2003).
- [73] B. Clément, D. Bloch, D. Gélé, S. Gréder, A. Le Bihan and I. Ripp-Baudot. SystemD or how to get signal, backgrounds and their efficiencies with real data. DØ internal note 4159.
- [74] V. M. Abazov et al. A search for $Wb\bar{b}$ and W Higgs production in $p\bar{p}$ collisions at $\sqrt{s} = 1.96$ TeV. *Phys. Rev. Lett.* 94 (2005) 091802.
- [75] T. Andeen, B. C. K. Casey, K. DeVaughan, Y. Enari, E. Gallas, D. Krop, R. Partridge, H. Schellman, G. R. Snow, S. Yacoob and H. D. Yoo. The DØ experiment's integrated luminosity for Tevatron Run IIa. FERMILAB-TM-2365, DØ internal note 5398 (2007).
- [76] T. Golling. Measurement of the $t\bar{t}$ production cross-section at $\sqrt{s} = 1.96$ TeV in the muon+jets final state using a topological method. DØ internal note 4667 (2004).
- [77] S. Beauceron and G. Bernardi. A search for Wbb and WH production in $p\bar{p}$ collisions at 1.96 TeV. DØ internal note 4633 (2004).
- [78] E. Barberis, T. Golling, I. Iashvili, A. Juste, A. Quadt and P. Schieferdecker. The matrix method and its error calculation. DØ internal note 4564 (2004).

- [79] C. Clément, G. Otero y Garzon, S. Lager, F. Rizatdinova, E. Shabalina and J. Strandberg. Measurement of the $t\bar{t}$ production cross section at $\sqrt{s} = 1.96$ TeV using lifetime tagging. DØ internal note 4900 (2005).
- [80] L. Sonnenschein, S. Trincaz-Duvoid and G. Bernardi. Search for $Wb\bar{b}$ and WH production in the muon channel using pass2 data. DØ internal note 5051 (2006).
- [81] V. M. Abazov et al. Evidence for production of single top quarks and first direct measurement of $|V_{tb}|$. *Phys. Rev. Lett.* 98 (2007) 181802.
- [82] D. Bauer, J. Huang and A. Zieminski. Studies of Upsilon(1S) bottomonium state production with the D0 detector at Fermilab. DØ internal note 4264 (2003).
- [83] G. Bernardi, S. Choi and K. Hanagaki. Cross section errors used in the Higgs searches. DØ internal note 5043 (2006).
- [84] A. L. Read. Presentation of search results: the CL(s) technique. *J. Phys.* G28 (2002) 2693.
- [85] T. Junk. Confidence level computation for combining searches with small statistics. *Nucl. Instrum. Meth.* A434 (1999) 435.
- [86] W. Fisher. Calculating limits for combined analyses. DØ internal note 4975 (2005).
- [87] T. Junk. Sensitivity, exclusion and discovery with small signals, large backgrounds, and large systematic uncertainties. CDF note 8182 (2006).
- [88] W. Fisher. Systematics and limit calculations. DØ internal note 5309 (2006).
- [89] A. L. Read. Linear interpolation of histograms. *Nucl. Inst. Meth.* A425 (1999) 357.
- [90] A. Abulencia et al. Search for H to $b\bar{b}$ produced in association with W bosons in $p\bar{p}$ collisions at $\sqrt{s} = 1.96$ -TeV. *Phys. Rev. Lett.* 96 (2006) 081803.
- [91] G. Bernardi, H. Kim, L. Sonnenschein and J. Yu. A search for WH production at $\sqrt{s} = 1.96$ TeV. DØ internal note 5054 (2006).
- [92] A. Abulencia et al. ICHEP, Moscow (2006) (2006).
- [93] A. Nomerotski. DØ silicon tracker for Run IIb at the Tevatron. *Nucl. Inst. Meth.* A518 (2004) 295.
- [94] C.-M. Anăstăsoaie, G. Bernardi, Y. Enari, F. Filthaut, W. Fisher, V. Kaushik, J. Lellouch, M. Sanders, L. Sonnenschein and J. Yu. Search for WH production at $\sqrt{s} = 1.96$ TeV with 1 fb^{-1} of data. DØ internal note 5357-CONF (2007).
- [95] V. M. Abazov et al. Combined upper limits on Standard Model Higgs boson production for the DØ experiment. DØ internal note 5380-CONF (2007).

Summary

All known experimental results on fundamental particles and their interactions can be described to great accuracy by a theory called the Standard Model. In the Standard Model of particle physics, the masses of particles are explained through the Higgs mechanism. The Higgs boson is the only Standard Model particle not discovered yet, and its observation or exclusion is an important test of the Standard Model. While the Standard Model predicts that a Higgs boson should exist, it does not exactly predict its mass. Direct searches have excluded a Higgs with $m_H < 114.4$ GeV at 95% confidence level, while indirect measurements indicate that the mass should be less than 144 GeV. This analysis looks for $W^\pm H \rightarrow \mu\nu_\mu b\bar{b}$ in 1 fb^{-1} of data collected with the DØ detector in $p\bar{p}$ collisions with $\sqrt{s} = 1.96$ TeV.

The analysis strategy relies on the tracking, calorimetry and muon reconstruction of the DØ experiment. The signature is a muon, missing transverse energy (\cancel{E}_T) to account for the neutrino and two b-jets. The Higgs mass is reconstructed using the invariant mass of the two jets. Backgrounds are $W^\pm b\bar{b}$, $W^\pm c\bar{c}$, $W^\pm + \text{light jets}$ ($W^\pm jj$) (and the corresponding backgrounds with a Z boson), $t\bar{t}$, single top production, and QCD multijet background.

To reduce the background from light jets, one or both jets in the event should be tagged by a b-tagging algorithm. A new, Neural Net-based algorithm was developed. The long lifetime of B-hadrons means that they travel on average some distance from the primary vertex before decaying. Because of the large mass of B-hadrons, their decay tracks do not point back to the primary vertex but have large impact parameters. The NN uses seven input parameters exploiting these properties: the decay length significance, the number of tracks, the mass and the fit χ^2/dof of the decay vertex; a variable constructed from the number of tracks with large impact parameters associated with a jet; and a probability that the jet comes from a background event based on the track impact parameters.

The Neural Net is trained on Monte Carlo simulation, but the efficiency and fake rate are measured in data. A system of 8 equations with 8 unknowns was constructed by comparing the number of tags found by the NN tagger and muon-based tagger in two different samples. The solutions to the equations include the efficiencies of the two taggers on b-jets. The algorithm is up to 50% more efficient at a fixed fake rate than the previous tagging algorithms. The efficiency for two operating points (NN output cuts) used in this analysis, after minimal requirements on the tracks associated with the jets, are $(47.6 \pm 0.7)\%$ for a fake rate of $(0.55 \pm 0.05)\%$ and $(69.6 \pm 0.9)\%$ for a fake rate of $(4.7 \pm 0.02)\%$.

The data used for the analysis are selected with muon triggers. From the triggered sample, events are selected with two jets, one with $p_T > 25$ GeV and one with $p_T > 20$ GeV, a muon

with $p_T > 15$ GeV and separated from any jets, and $\cancel{E}_T > 20$ GeV. Events with a second muon or an isolated electron with $p_T > 18$ GeV are rejected to reduce the $t\bar{t}$ background. A W^\pm selection cut on the \cancel{E}_T and the angle $\Delta\phi(\cancel{E}_T, \mu)$ helps reduce the QCD background. After data selection, there are 8768 data events with an expected signal contribution of 2.15 events for $m_H = 115$ GeV. The background is dominated by $W^\pm jj$. This contribution is normalised to data after subtraction of the other backgrounds.

The QCD multijet background is due to muons-in-jets that are reconstructed as isolated muons. The multijet background is estimated directly in the data sample, using the matrix method. The total number of real isolated muons N_μ and “fake” isolated muons N_{QCD} is determined by solving the equations for the number of events passing “loose” and “tight” isolation criteria, given the efficiency and fake rate for the “tight” criteria which are measured in data.

The background from light jets is reduced by applying the b-tagging algorithm. First, events in which both jets are tagged with an NN cut of 0.25 are selected as a double-tagged (DT) sample. From the remaining events, events are selected with one jet tagged with an NN cut of 0.775. This way, the samples are independent which makes their combination easier. The single tagged sample contains 303 events with an expected signal contribution of 0.81 ± 0.08 and an expected background of 295 ± 35 . The double tagged sample contains 74 events with an expected signal contribution of 0.60 ± 0.06 and an expected background of 65.8 ± 8.5 . The dominant backgrounds in the single tagged sample are $W^\pm + \text{jets}$ (especially $W^\pm b\bar{b}$ and $W^\pm c\bar{c}$), and in the double tagged sample $W^\pm b\bar{b}$ and $t\bar{t}$.

The observed data are consistent with background. Therefore, we set an upper limit on the Higgs production cross section at 95% confidence level (CL). The semi-frequentist confidence level CL_s used in this analysis is determined by integrating the probability distribution functions (PDFs) for a variable that separates the signal+background and background-only hypotheses. The PDFs are determined by running many pseudo-experiments to simulate the outcome of repeated experiments. The upper limit on the cross section is found by increasing the predicted signal contribution until $CL_s = 5\%$.

Systematic uncertainties are taken into account by fluctuating the predicted signal and background contributions for each pseudo-experiment. This smearing procedure “broadens” the signal+background and background-only PDFs and makes the separation between them smaller. The profile likelihood method is used to reduce the impact of systematic uncertainties. For each pseudo-experiment, in the signal sample, the fluctuation of the uncertainties is constrained by determining the “best fit” background prediction to the data.

The observed upper limit ranges from 25 times the SM prediction for $m_H = 105$ GeV to 162 times the SM prediction for $m_H = 145$ GeV. The observed upper limit compares well with the median expected limit in case no signal would be present. This is a significant improvement over earlier analyses at DØ and CDF using less data and different tagging algorithms. The results of an earlier version of this analysis were combined with a $W^\pm H \rightarrow e\nu_e b\bar{b}$ analysis, giving an upper limit of 1.3 pb^{-1} for $m_H = 115$ GeV. Additional channels that may be explored at DØ include ZH production, $W^\pm H \rightarrow W^\pm W^+ W^-$, $g g \rightarrow H \rightarrow b\bar{b}$ and channels where the Higgs boson decays into a pair of tau leptons. To exclude a Higgs boson with a mass $m_H = 115$ GeV, a factor 15 in sensitivity must be gained. The sensitivity will

improve from higher integrated luminosity, the addition of other triggers, improvements in the way the tagging algorithm is used, improvements in the uncertainties and in the analysis techniques and from combination with other channels and experiments. With 8 fb^{-1} , the Tevatron experiments should be able to observe a 3σ excess for Higgs masses up to almost 130 GeV. With increased luminosity and sensitivity, exclusion or discovery of a low mass Higgs becomes a real possibility.

Samenvatting

Het standaardmodel van de hoge-energiefysica beschrijft de elementaire deeltjes en hun interacties. De voorspellingen van het Standaardmodel zijn met grote nauwkeurigheid bevestigd door experimenten. In het model worden de massa's van de deeltjes verklaard door het Higgs mechanisme. Het bijbehorende Higgs-boson is het enige elementaire deeltje in het Standaardmodel dat nog niet direct is waargenomen, en de ontdekking van het Higgs-boson vormt een belangrijke toets van de theorie. Hoewel het Standaardmodel voorspelt dat het Higgs-boson bestaat, geeft het geen exacte waarde voor zijn massa. Dankzij eerdere experimenten om het deeltje waar te nemen kan met 95% zekerheid gezegd worden dat elke massa van minder dan 114,4 GeV is uitgesloten. Metingen van parameters die afhangen van de Higgs-massa geven aan dat de massa kleiner zou moeten zijn dan 144 GeV. In dit proefschrift wordt gezocht naar Higgs-deeltjes die ontstaan zijn samen met een W-boson, waarbij het Higgsdeeltje vervalt in b-anti-b quark paar en het W-boson in een muon en een neutrino. De data zijn verzameld met de DØ detector uit 1 fb^{-1} proton-antiprotonbotsingen in de Tevatron versneller.

Het onderzoek maakt gebruik van de sporen die de deeltjes achterlaten in de detector: de sporen van geladen deeltjes in het binnenste deel van de detector, de energie van deeltjeslawines of “jets” in de calorimeter en de sporen van muonen in het buitenste deel van de detector. De signatuur van de gezochte botsingsproducten is een muon, twee jets die afkomstig zijn van het verval van een b-deeltje en een imbalance in de totale energie, die veroorzaakt wordt doordat het neutrino niet wordt waargenomen. De massa van de twee jets wordt gebruikt om de massa van mogelijke Higgs-deeltjes te berekenen.

Voor elke botsing waarbij een Higgs-deeltje ontstaat, zijn er vele met een bijna identieke signatuur: botsingen waarbij een W- of Z-boson ontstaat samen met twee b-quark jets of met jets van lichtere quarks, botsingen met één of twee top quarks en QCD processen met meerdere jets afkomstig van lichte quarks.

Om deze achtergrondprocessen terug te dringen is het belangrijk jets die afkomstig zijn van b-quarks te onderscheiden van andere jets. Hiervoor is een nieuw algoritme ontwikkeld, dat gebruik maakt van een neurale netwerk. Doordat b-deeltjes iets langzamer vervallen, en dus iets verder vliegen van het botsingspunt dan andere deeltjes, kan hun vervalpunt in de detector worden onderscheiden van het botsingspunt. Door hun grote massa krijgen de vervalproducten bovendien een baan die niet uit het botsingspunt lijkt te komen. Een neurale netwerk maakt gebruik van deze eigenschappen om onderscheid te maken tussen jets van b-quarks en andere jets.

Om het neurale netwerk te trainen is gebruik gemaakt van simulaties van de botsingen en de detector, maar de nauwkeurigheid waarmee b-quark jets van andere jets worden gescheiden is bepaald uit werkelijke botsingsgegevens. De nauwkeurigheid is bepaald door het

aantal b-quark jets gevonden door het neurale netwerk-algoritme en een ander algoritme dat gebruik maakt van muonen te vergelijken in twee data verzamelingen met een verschillend gehalte b-quark jets. De oplossing van het systeem van acht onafhankelijke vergelijkingen en acht onbekende variabelen dat zo kan worden opgesteld omvat ook de efficiëntie van de twee algoritmen. Het neurale netwerk-algoritme vindt $(47,6 \pm 0,7)\%$ van alle b-quark jets bij een kans van $(0,55 \pm 0,05)\%$ om een niet-b-quark jet toch als b-quark jet te identificeren, en $(69,6 \pm 0,9)\%$ van alle b-quark jets bij een kans op een valse b-quark jet van $(4,7 \pm 0,02)\%$, na eisen aan de kwaliteit van de deeltjessporen die zijn geassocieerd met de jet. Het neurale netwerk algoritme vindt tot 50% meer b-quark jets dan eerdere algoritmen.

De data gebruikt voor dit onderzoek zijn online geselecteerd door filters die kijken naar de aanwezigheid van muonen. Uit dit geselecteerde sample zijn vervolgens botsingen gekozen met twee jets, één met een impuls loodrecht op de bundel (p_T) van minimaal $p_t > 25$ GeV en één met minimaal $p_T > 20$ GeV; een muon met minimaal $p_T > 15$ GeV dat niet dichtbij één van de jets ligt, en een energie-imbalance van tenminste $\cancel{E}_T > 20$ GeV. Botsingen waar een tweede muon of een van de jets verwijderd electron met $p_T > 18$ GeV in voorkwam werden verwijderd. Om misreconstructies die lijken op W-bosonen te onderdrukken werd bovendien een snede toegepast op de energie-imbalance en de hoek tussen het muon en de richting van de ontbrekende energie \cancel{E}_T . Na selectie bleven 8768 botsingen over, met een verwacht aantal Higgs-deeltjes van 2,15 als de Higgs-massa 115 GeV bedraagt. W-bosonen met lichte jets maken het grootste deel uit van de botsingen. De voorspelling van deze bijdrage werd genormeerd op het totaal aantal botsingen, na aftrekken van de overige achtergrondprocessen.

De QCD achtergrond van lichte jets komt voort uit muonen die ontstaan in jets, maar die als geïsoleerde muonen worden gereconstrueerd. Het aantal van zulke botsingen werd direct bepaald uit de data-verzameling met de “matrix methode”. De aantallen werkelijk geïsoleerde muonen N_μ en misreconstructies N_{QCD} werden bepaald door het stelsel van vergelijkingen vergelijkingen voor het aantal botsingen dat losse en strikte isolatiecriteria doorstaat op te lossen. De reconstructie-efficiëntie en de kans op misreconstructie werden vooraf in een andere data-verzameling bepaald.

De achtergrond van jets die niet afkomstig zijn van b-deeltjes werd teruggebracht door het neurale netwerk-algoritme toe te passen. Eerst werden botsingen geselecteerd waarin beide jets een neurale net-waarde hadden van minimaal 0,25. Dit was de “dubbel-tag” dataset. Uit de overgebleven botsingen werd een “enkel-tag” dataset geselecteerd waarin tenminste één van beide jets een neurale net-waarde had van tenminste 0,775. Op deze manier werden twee onafhankelijke data-verzamelingen gemaakt, waardoor het eenvoudiger was ze te combineren. De enkel-tag dataset bevatte 303 events met een verwachting van $0,81 \pm 0,08$ Higgs-deeltjes en 295 ± 35 overige botsingen. De dubbel-tag dataset bevatte 74 events met een verwachting van $0,60 \pm 0,06$ Higgs-deeltjes en $65,8 \pm 8,5$ overige botsingen. De belangrijkste achtergrondprocessen in de enkel-tag dataset waren W-boson met b-quark en c-quark jets-botsingen, en in de dubbel-tag dataset W-boson met b-quark jets en top-anti-top botsingen.

De waargenomen aantallen botsingen zijn consistent met de verwachte achtergrond. Daarom plaatsen we een bovenlimiet aan de botsingsdoorsnede voor Higgs-productie, met 95% zekerheid. Dit wil zeggen dat bij deze botsingsdoorsnede 95% van alle experimenten geen Higgs-deeltjes zullen worden waargenomen. Die zekerheid wordt in dit onderzoek bepaald uit

de waarschijnlijkheidsverdelingen van een variabele die verschillende verdelingen heeft voor de “signaal + achtergrond”-hypothese en de nul-hypothese (alleen achtergrond). De waarschijnlijkheidsverdelingen worden bepaald door vele “pseudo-experimenten” te simuleren. De bovenlimiet aan de botsingsdoorsnede wordt gevonden door de verwachte signaalbijdrage te verhogen tot met 95% zekerheid gezegd kan worden dat bij die bijdrage een signaal waargenomen had moeten worden.

De systematische onzekerheden in de verwachte signaal- en achtergrondbijdragen worden in de berekening meegenomen door de verwachte bijdragen binnen de onzekerheid te variëren voor elk pseudo-experiment. Hierdoor worden de waarschijnlijkheidsverdelingen “uitgesmeerd” en wordt het verschil tussen de signaal- en nul-hypothesen kleiner. De “profile likelihood” methode wordt gebruikt om het effect van de systematische onzekerheden te verminderen. Voor elk pseudo-experiment worden de variaties in het verwachte signaal begrensd door de beste vergelijking te bepalen van de achtergrondverwachting en de data.

De waargenomen bovengrens loopt van 25 maal de Standaardmodel-verwachting bij een Higgs-massa van 105 GeV tot 162 maal de Standaardmodel-verwachting bij een massa van 145 GeV. De waargenomen grens komt goed overeen met de verwachte bovengrens in het geval er geen Higgs-deeltjes zouden zijn. De waargenomen bovengrens is een significante verbetering ten opzichte van eerdere analyses van $D\bar{O}$ en CDF die gebruik maakten van minder data en andere b-quark identificatie-algoritmen. De resultaten van een eerdere versie van dit onderzoek werden gecombineerd met een vergelijkbare studie die gebruik maakte van electronen in plaats van muonen, wat resulteerde in een bovengrens aan de botsingsdoorsnede van $1,3 \text{ pb}^{-1}$ bij een Higgs-massa van 115 GeV. Door de resultaten te combineren met andere studies, waar het Higgsboson ontstaat samen met een Z-boson, alleen uit fusie van twee gluonen of waar het vervalt in andere deeltjes dan b-quarks kan een nog lagere grens bepaald worden. Om een ondergrens aan de massa te stellen van 115 GeV moet 15 maal meer gevoeligheid bereikt worden. Verbeteringen worden nog verwacht door het gebruik van meer data, andere online selectie-algoritmen, door het verbeteren van de manier waarop het neurale net-algoritme wordt toegepast, door de systematische onzekerheden te verkleinen, door nieuwe analyse-technieken toe te passen en door de gegevens van $D\bar{O}$ en CDF te combineren. Met een verwachte dataset van 8 fb^{-1} zullen deze experimenten samen een signaal met een significantie van tenminste drie standaarddeviaties waar kunnen nemen als de Higgs-massa kleiner is dan 130 GeV.

Acknowledgements

I would not have been able to finish this thesis without the help and support of a lot of other people. I'll try to mention the people who have influenced me (in a positive way) during this four-year experience.

Frank Filthaut and Sijbrand de Jong proved to be the best combination for me to finish, in time, an analysis which seemed too hard at the beginning. I want to thank to both of them for the trust and the coordination they gave me every time when I needed it most. Even when I was frustrated or angry they knew how to turn this energy into something useful.

Since I came to Nijmegen, Annelies, Marjo and later Gemma were always there to make my life there and in the States easier. Peter Klok, thank you for your kind words and warm teas.

During my stay at Fermilab I had the occasion to learn from so many people who all seemed to know so much, I just tried to be a sponge and absorb all the information which helped me understand and develop the work I was doing. Some of the most interesting things I learned in the Control Room of the DØ experiment. The Run Coordinator at the time, Arnd Meyer, had the patience to answer even the most stupid questions I had in my head. I learned a lot about the detector, the software and even more about life in high energy physics.

When I started on b-tagging I had the luck to start working with Tim Scanlon and later on with Stephen Robinson. The work for the Neural Network b-tagging tool involved a lot of late nights and white hairs, but at the end, completing the studies gave me the first real feeling of satisfaction as a Ph.D. student. It made me say "We did it!". Or, as Tim sang one night, "We are the champions!" The research which gives the title to this work was done together with Jeremie Lelouch. It was hard work, and sometimes I was not able to see the end, but putting things together with him made me give the work I was doing another try every day.

During these four years I made very good friends, who were there every time when I was stressed the most but also when I felt like partying until I crashed. Ana, Helena, Renata, thank you very much for being there every time and I hope we'll be friends for ever. The Dutch DØ group gave good input for my studies but also in my private life. I had the occasion to meet one of the happiest persons on the planet, Pieter Houben. Sharing an apartment with him was a nice experience which seems to go on wherever I live... Axel was always helpful and when I first came to Nijmegen, he made it possible to listen to music on my computer. Pieter VDB, Jeroen, Lucian and Cristina, thanks for your funny or serious words every time we meet.

Miran and Qin helped me finish my thesis faster than I thought. Life without them in Nijmegen was not the same. Even though I still had Folkert and Lucian to discuss how we can destroy or save the planet, I always missed you around.

At Nikhef, I was happy to meet and befriend Claudine, Marcello and Fabio, still my dear friends even though they moved around quite a bit. I am looking forward to more times together with you.

I want to thank Marcela for her open way of being and her readiness to give advice every time I need it. During the commutes to Nijmegen I developed a relaxing ritual meeting Nivea on the train and during the trip we explored lots of subjects from science to travel.

I made many other friends in the real world and in a virtual one, and each of them contributed in some way to finishing my thesis. You know who you are.

When I started my research I left behind some people very dear to me: Eliza, Maria, doamna Rodica Ionescu and my parents. But I knew they were there supporting me every second. My father made me love numbers and science before I knew how to read, and my mother gave me the balance for the romantic side of life. My dear sister Maica Ioana, my brother Viorel and Caroline I missed very much, but I knew they were just a phone call away. The family I gained during my Ph.D., Hans and Wiesje, thank you for giving me the feeling of a family here.

And now, my love, my husband, Bram, I want to thank you for every day you were next to me. There are no words or numbers to describe what I feel for you. But I'll still try during our life together.

Curriculum Vitae

Carmen Miruna Anăstăsoaie was born on May 27, 1978 in Ploiești in Romania. In 1996 she graduated with a baccalaureate degree from the Tudor Vladimirescu Lyceum in Bucharest, specialising in mathematics and physics. She continued her studies at the Physics Faculty of the University of Bucharest. She received her B.Sc. in Physics in June 2000, with a thesis on "The study of luminosity of the meteors" under supervision of Prof. Mircea Rusu. From November 2000 to September 2001 she studied as a Junior Research Fellow at Meudon Observatory in France with an ERASMUS/SOCRATES scholarship awarded by the European Union and a French governmental scholarship. In January 2002 she received her M.Sc. at the University of Bucharest with a thesis on "Fractal dimensions of Unipolar Magnetic Region" under supervision of Dr. Ziad Mouradian and Prof. Rusu. During her studies she was the vice-president of the Association of Amateur Astronomers of the university, strongly connected with the Institute of Astronomy in Bucharest. She was involved in various activities, including supervising seminars, observations and projects. She also attended the "Module D'Etudes Francophones en Astrophysique" and the 24th ISYA International School for Young Astronomers (IAU) in Bucharest, witnessing the 1999 total solar eclipse. From 1998 to 2000 she represented the students in the board of the Physics Faculty and in the senate of the University of Bucharest. From October 2001 to June 2002 she was a teaching assistant at the Physics Faculty of the University of Bucharest. After that, she was employed at the Physics Department of the Polytechnic University of Bucharest.

In August 2003 she started her graduate research at the Radboud University Nijmegen (at the time still known as the University of Nijmegen) under supervision of Prof. Dr. Sijbrand de Jong and Dr. Frank Filthaut. From February 2004 to September 2005 she worked at the Fermi National Accelerator Laboratory (Fermilab) near Chicago in the USA. Initially, she contributed to jet trigger studies and was responsible for the radiation monitoring system of the DØ experiment as an expert. She set a record for data taking efficiency as a DAQ shifter, together with the rest of the shift crew, that stood for more than two years. She then shifted her attention to b-tagging and worked together with colleagues from Imperial College London to develop and deploy a Neural Net-based tagging algorithm, mostly working on the certification of the algorithm in collider data. After returning to Nijmegen she assisted in Bachelor and Master level courses at the university. She presented her work at the annual meeting of the Dutch Institute for High-Energy Physics (Nikhef) in 2005 and at the Dutch Physical Society (NNV) annual meeting for Nuclear and High-Energy physics in 2005 and 2006. In 2003 she attended the international summer school on particle and nuclear astrophysics "NIJMEGEN03" in Nijmegen. She attended the Joint Belgian-Dutch-German summer school on particle physics in 2003 and 2004 and the CTEQ summer school on Rhodes

in 2006.

Her data analysis, presented in this thesis, focused on the search for a Higgs boson signal in events with a muon, missing transverse energy and two b-jets. She worked together with colleagues from LPNHE, Universités Paris VI et VII in France. With the available data, it was not possible to observe the Higgs boson directly. Instead, she set an upper limit on the production rate of Higgs bosons that is competitive with results published by other experiments.